ADAM MICKIEWICZ UNIVERSITY IN POZNAŃ

FACULTY OF CHEMISTRY

THESIS

presented by:

Tomasz Chudziak

„ New generation of sensors based on graphene-functionalized materials”

„Nowa generacja czujników bazujących na sfunkcjonalizowanych materiałach grafenowych”

to obtain the rank: **Doctor of Adam Mickiewicz University in Poznań**

Specialty: **Chemistry**

THESIS supervisor:

Prof. wiz Artur Ciesielski

THESIS co-supervisor:

Dr Dawid Pakulski

I dedicate this work to my to my closest family.

Acknowledgment

It is my great pleasure to express my sincere gratitude to my research supervisor and co-supervisor: Prof. wiz. Artur Ciesielski, ‚Center for Advanced Technologies (Adam Mickiewicz Univeristy in Poznań) & Institut de Science et d'Ingénierie Supramoléculaires UMR7006, (Université de Strasbourg) Dr. Dawid Pakulski, Center for Advanced Technologies (Adam Mickiewicz Univeristy in Poznań) for their guidance, fruitful scientific discussions, and for their help during this period of my research. Without their constant support and encouragement, it would not have been possible to complete my research work and finally this thesis.

I sincerely thank all the faculty members, former and present, post-docs, PhD and M.Sc. students, secretaries and technical staff at both laboratories (Nanochemistry laboratory in Strasbourg and Two-Dimensional Materials Laboratory in Poznań) especially: Prof. Paolo Samori, Dr. Włodzimierz Czepa, Dr. Samanta Witomska, Dr. Iwona Janica and Dr. Cataldo Valentini for the discussions, encouragement, kindness and unforgettable atmosphere during the course of my work.

I would like to especially thank the director of the Doctoral School Prof. dr hab. Piotr Pawluć for the excellent organization of the classes and the high quality of education at the UAM doctoral school.

I would like to thank students especially Maria Stachowiak for countless conversations and motivation to work in the laboratory

Last but not the least I want to specially thank my family for their motivation and support.

This work was partially supported by grants of National Science Centre in Poland (2019/35/B/ST5/01568 and 2021/41/N/ST5/01112).

Streszczenie w języku polskim

Nanotechnologia jest powszechnie uważana za jedną z najbardziej przyszłościowych dziedzin nauki, otwierającą nowe możliwości dla badaczy na całym świecie i bezpośrednio poprawiającą jakość życia ludzkiego. Ta szybko rozwijająca się dyscyplina polega na tworzeniu funkcjonalnych systemów w nanometrycznej skali na poziomie molekularnym, posiadających specyficzne właściwości i zastosowania. W związku z tym, dwuwymiarowe materiały (2DM) są przedmiotem znacznego zainteresowania w środowisku naukowym ze względu na ich niezwykłe właściwości. W ciągu ostatniej dekady, materiały 2D znacząco przyspieszyły rozwój interdyscyplinarnych dziedzin nanonauki i nauki o materiałach, znajdując liczne zastosowania w takich obszarach jak magazynowanie energii, urządzenia optyczne i czujniki. Ogólnie rzecz biorąc, 2DM to materiały, które mają tylko kilka nanometrów grubości lub są nawet zredukowane do pojedynczej warstwy atomów. Ta cecha nadaje 2DM wyjątkowo wysoką powierzchnię właściwą i ultra-wysoką czułość powierzchniową na czynniki środowiskowe, takie jak wilgotność i ciśnienie, co czyni je wysoce pożądanymi w zastosowaniach czujnikowych. Spośród licznych 2DM, grafen wyróżnia się ze względu na swoje niezwykłe właściwości. Grafen definiuje się jako pojedynczą warstwę atomów węgla hybrydyzowanych sp^2, ściśle połączonych w sześciokątną sieć krystaliczną, przypominającą wzór plastra miodu. Grafen wyraźnie wyróżnia się spośród innych materiałów, charakteryzując się wyjątkowo wysoką powierzchnią właściwą (do 2630 m^2/g), modułem Younga wynoszącym 1 TPa i podstawową wytrzymałością na rozciąganie wynoszącą 130 GPa. Pomimo swoich licznych wyjątkowych właściwości, grafen nie ma przerwy energetycznej i wykazuje słabą rozpuszczalność w wodzie, co znacząco ogranicza jego zastosowania w niektórych dziedzinach. Skuteczną strategią przezwyciężenia tych ograniczeń i poszerzenia zastosowań grafenu jest synteza jego pochodnych, takich jak tlenek grafenu (GO) i zredukowany tlenek grafenu (rGO). Spośród wielu metod otrzymywania GO, najpopularniejszą metodą pozostaje utlenienie grafenu metodą Hummersa. rGO można otrzymać licznymi metodami, jednakże najbardziej wydajnymi pozostają termiczne wyprażanie i chemiczna redukcja GO. Każda technika redukcji GO ma inną efektywność, co przyczynia się do zróżnicowania właściwości produktów końcowych. Określenie właściwości otrzymanego rGO ma kluczowe znaczenie dla efektywności sensorów opartych na rGO, w tym czujników ciśnienia, odkształceń i wilgotności.

Summary in English

Nanotechnology is widely regarded as one of the most forward-thinking fields of science, opening new possibilities for researchers globally and directly enhancing human quality of life. This rapidly evolving discipline involves creating functional systems at the nanometric scale on a molecular level with specific properties and applications. Consequently, two-dimensional materials (2DMs) are of considerable interest within the scientific community due to their extraordinary properties. Over the past decade, 2D materials have significantly propelled the interdisciplinary fields of nanoscience and materials science, finding numerous applications in areas such as energy storage, optical devices, and sensors. Generally, 2DMs are materials that are only a few nanometers thick or even reduced to a single layer of atoms. This characteristic endows 2DMs with an extremely high surface area-to-volume ratio and ultra-high surface sensitivity to environmental factors such as humidity and pressure, making them highly desirable for sensor applications. Among the numerous 2DMs, graphene distinguishes itself due to its extraordinary properties. Graphene is defined as a single layer of sp^2 hybridized carbon atoms that are tightly bonded together in a hexagonal crystal lattice, resembling a honeycomb pattern. Graphene distinctly stands out among others, characterized by its exceptionally high specific surface area (up to 2630 m^2/g), a Young's modulus of 1 TPa, and essential tensile strength of 130 GPa. Despite its numerous exceptional properties, graphene lacks a bandgap and exhibits poor water solubility, which significantly limits its applications in certain domains. A viable strategy to overcome these constraints and broaden the applicability of graphene is by synthesizing graphene derivatives such as graphene oxide (GO) and reduced graphene oxide (rGO). Among the various methods for synthesizing GO, the most popular remains the oxidation of graphene using the Hummer's method. rGO can be obtained through various methods. However, the most efficient techniques remain thermal annealing and chemical reduction of GO. Each technique for reducing GO has different levels of efficiency, which contributes to the variation in the properties of the final products. Determining the properties of the obtained rGO is crucial for the effectiveness of rGO-based sensors, including sensors for pressure, strain, and humidity.

Table of Contents

Chapter 1 - Introduction

Nanotechnology is considered one of the most forward-looking fields of science, opening new possibilities for scientists around the world and directly impacting the quality of human life. This rapidly developing field involves creating functional systems at the nanometric scale and give rise to specific properties on a molecular level often with a clear application-oriented vision. Among various materials explored within the filed, two-dimensional materials (2DMs) gained significant interest within the scientific community mostly due to their extraordinary properties. In the last decade, 2DMs have significantly advanced the interdisciplinary fields of nanoscience and materials science and have found numerous applications including energy storage[1, 2], opto-electronic devices[3] and sensors[4-6]. In general, 2DMs are only a few nanometers thick or even thinner, down to a single layer of atoms. Because of that, 2DMs are characterized by extremely high surface area-to-volume ratio and ultra-high surface sensitivity to the environment such as humidity, and factors as changes in pressure, which constitutes a highly desirable attribute in sensory applications. Moreover, 2DMs are distinguished by their exceptional electrical and optical properties, along with their mechanical strength and robustness, rendering them ideally suited as potential active materials for next-generation chemiresistor-based sensors.

One to the most promising 2DMs is graphene and its derivatives. The beginnings of graphene start from the one of allotropic structure of carbon which is graphite. Graphite itself has accompanied humanity since ancient times, when early humans used it to decorate caves and pottery[7]. Whereas the scientific community's awareness of graphene dates back to 1840 when the German scientist Schafhaeutl performed the first exfoliation of graphite using nitric and sulfuric acids[8]. Eleven years later, in 1859, Brodie obtained and described the structure of graphite oxide[9]. Brodie highlighted properties of synthesized material such as: insoluble in water containing acids but slightly soluble in pure water, the acidic nature of graphite oxide and reactivity with alkalies and proposed to name this new material as "Graphon". Moreover, in his article, Brodie described crystals of the graphite oxide examined with the microscope as "perfectly transparent" and "exhibiting beautiful colors" under polarized light. However, better insight into structure comes with times and development of more advanced techniques of characterization. The next step in the development of knowledge about graphite derivatives was the reduction of graphite oxide which was achieved in 1962 by Boehm

and co-workers. These scientists synthesized reduced graphene oxide (GO) by thermal and chemical reduction of graphite oxide[10]. Furthermore, Boehm is one of the three scientists (Boehm, Setton and Stumpp) who designated a single layer of graphite as "graphene" which continues to be utilized to the present day. Following the identification of a single layer of graphite as an individual carbon material between 1969 and 1970, scientific studies emerged showcasing the production of a single layer of graphite on metallic substrates like Pt and Ni[11-13]. Moreover, in 1975 van Bommel *et al.* obtained monolayer of graphite by silicon sublimation[14]. Subsequently, in 1999 Ruoff *et al.* used highly oriented pyrolytic graphite to create single sheets of graphite[15, 16]. However, the most ground-breaking experiment was conducted by Geim and Novoselov in 2004 where single layer of graphene was isolated *via* micromechanical exfoliation of graphite and its outstanding physical properties were studied[17]. This discovery holds immense significance for the scientific community, as evidenced by the Nobel Prize in Physics awarded to the authors in 2010. The method of micromechanical exfoliation introduced by Geim and Novoselov allows for larger-scale production, significantly increasing the number of studies and applications of graphene. Graphene, with its single-atom thickness, is arguably the most esteemed material of the past decade. Its captivating physicochemical properties have not only permeated the academic community but also captured the interest of leading chemical and materials-oriented companies, as well as public institutions.

Graphene is characterized as a single layer of sp^2 hybridized carbon atoms tightly bonded together arranged in hexagonal crystal lattice resembling a honeycomb pattern. Single layer of graphene is referred to as single-layer graphene, while two or three layers are identified as bilayer or trilayer graphene sheets, respectively. Moreover, atomic structure of graphene can serve as a fundamental building block for various other carbon-based materials of all other dimensionalities, such as 0D fullerenes, 1D nanotubes, or stacked into 3D graphite[5]. The properties of these materials are determined by chemical bonds, shape, and dimensionality. In its ground state, carbon possesses four valence electrons, with two in the 2s and two in the 2p subshells. Upon the migration of one of the 2s electrons to an unoccupied 2p orbital, carbon establishes bonds with other carbon atoms through sp hybrid orbitals. These hybrid orbitals, including sp, sp^2, and sp^3, facilitate the formation of bonds between adjacent carbon atoms. Among the reported 2D carbon materials such as: graphyne[18], graphdiyne[19] and graphenylene[20], graphene

stands out as it consists of sp^2 hybridized carbon atoms organized into planar hexagonal units within two dimensions. For many years, graphene was viewed as merely a theoretical material, since earlier theories suggested that perfect two-dimensional graphene would be unstable in reality due to thermal fluctuations, which would inhibit long-range crystalline order at finite temperatures[21]. For this reason, it was assumed that 2D materials could not exist without a 3D substrate. However, in 2004, graphene and other free-standing 2D atomic crystals were experimentally discovered[17, 22]. Since these discoveries, significant research efforts have been dedicated to understanding graphene's properties. Numerous fascinating characteristics of graphene have been revealed, including an unusual half-integer quantum Hall effect, a non-zero Berry phase, and a strong ambipolar electric field[6, 23]. Inspired by the potential applications of graphene's unique characteristics, considerable research has been undertaken to investigate a wide array of new graphene-based devices. This phenomenon, referred to as the "graphene rush", has catalyzed the exploration of atomically thin sheets of other layered materials, including semiconducting transition metals dichalcogenides (TMDCs)[4], MXenes[24-26] and hexagonal boron nitride[27, 28] and black phosphorous or phosphorene. In general, 2DMs are categorized into various groups, including elements, metallic compounds, nonmetallic compounds, organics, and salts.

2DMs demonstrate advantageous characteristics, including mechanical properties, which dictate the requisite strength for targeted applications and integration. For example, examining the mechanical properties of monolayer MoS_2 using the Young's modulus, values were obtained of ≈280 GPa and a stiffness of ≈183 Nm^{-1}. Following a maximum deflection lower than the critical threshold, it was observed that upon loading, the MoS_2 reverted to its original state, illustrating its elasticity. However, beyond the critical deflection, the MoS_2 failed to return to its initial state, thus demonstrating its plasticity[29]. This feature constitutes a serious limitation in the use of MoS_2 as a potential material in strain and pressure sensors. On the other hand, in the case of a monolayer of h-BN exhibited nonlinear elastic deformation followed by strain softening anisotropic deformation and failure[30]. When considering 2D materials, graphene distinctly stands out among others, characterized by its exceptionally high specific surface area (up to 2630 m^2/g), a Young's modulus of 1 TPa, and essential tensile strength of 130 GPa[31]. These distinctive properties of graphene unequivocally indicate its potential utilization in pressure and strain sensors. Moreover, in graphene, three electrons occupy the 2s, $2p_x$,

and $2p_y$ states, forming hybridized sp^2 electron states. These planar orbitals establish energetically stable and localized σ-bonds with the three nearest carbon atoms. The remaining electron, in the $2p_z$ orbital perpendicular to the graphene sheet, participates in π bonding. The interaction of the $2p_z$ orbital states between neighboring atoms profoundly affects the electronic properties of graphene. This attribute leads to graphene resembles a semi-metal with a distinctive zero band gap[32]. Furthermore, graphene exhibits numerous exceptional properties, such as outstanding thermal conductivity (exceeding 3000 W/mK) and electrical conductivity (approximately 6000 S/m)[33]. Moreover, a single layer of two-dimensional graphene demonstrates electron mobility of approximately 10,000 $cm^2\ V^{-1}\ s^{-1}$[17], whereas theoretical calculations suggest that in a defect-free single layer, it can potentially reach up to 200,000 $cm^2\ V^{-1}\ s^{-1}$[34]. Additionally, the electrical conductivity properties of graphene can be enhanced through nitrogen doping, where the annealed nitrogen-doped graphene exhibited reduced electrical resistance in comparison to GO and reduced graphene oxide (rGO)[35]. For this reason, graphene holds significant promise for sensing applications due to its exceptionally high conductivity and extensive surface area. Moreover, graphene combined with other 2DM which possesses an atomically smooth surface, lattice constant akin to that of graphene, sizable optical phonon modes, and a substantial electrical band gap like hexagonal boron nitride (*h*-BN) can be used to obtain high quality *h*-BN nanosheets for high-performance large-area graphene electronics[36]. Because of the outstanding conductivity properties of graphene, attempts are being made to modify other two-dimensional materials. For example, similar to graphene WS_2 electrical properties can be enhanced by nitrogen doping[37]. Moreover, the electrical conductivity of monolayer MoS_2 can be adjusted, directly achieved through substitutive doping and other TDMCs like $MoSe_2$, $MoTe_2$ can be altered by doping with nonmetal elements such as H, B, C, N, O[38, 39]. Despite efforts to enhance the properties of other two-dimensional materials, graphene remains at the forefront of significant interest and is the subject of numerous research endeavors and applications. Thus, graphene has been extremely investigated in energy storage devices as cathode-anode material for batteries[40] and an electrochemical double-layer supercapacitors[2, 41]. Additionally, graphene has found numerous applications in sensors due to its optoelectronic properties. In general, atomically thin structured 2DMs possess effective optoelectronic properties, rendering them suitable for both electronic and optoelectronic applications. Specifically, their optical transparency and rapid response to external stimuli are pivotal features essential

for optoelectronic and other sensing applications[42]. Two-dimensional materials owe these properties by quantum confinement effect significantly alters the electronic behavior of these materials. Due to this phenomenon 2DMs are ideal for both fundamental research and innovative electronic applications. In case of graphene absorbance results in a universal optical conductivity, equal to $\sigma 0 = e^2/4h$ at zero chemical potential. This is a direct consequence of the charge carriers behaving as massless Dirac fermions[43]. Moreover, even though graphene is only one atom thick, it possesses the greatest tensile strength and elastic modulus of any natural material and remains impermeable in its pristine form. Additionally graphene's impermeability has spurred extensive research into its use as a barrier for liquid and gas permeation[44, 45]. Simultaneously, a graphene layer is capable of complete permeability to water molecules[46]. This specific characteristic indicate further presents G as an ideal candidate for potential applications in humidity sensors. An overview of mass production methods and applications of 2DMs is presented on Figure 1.

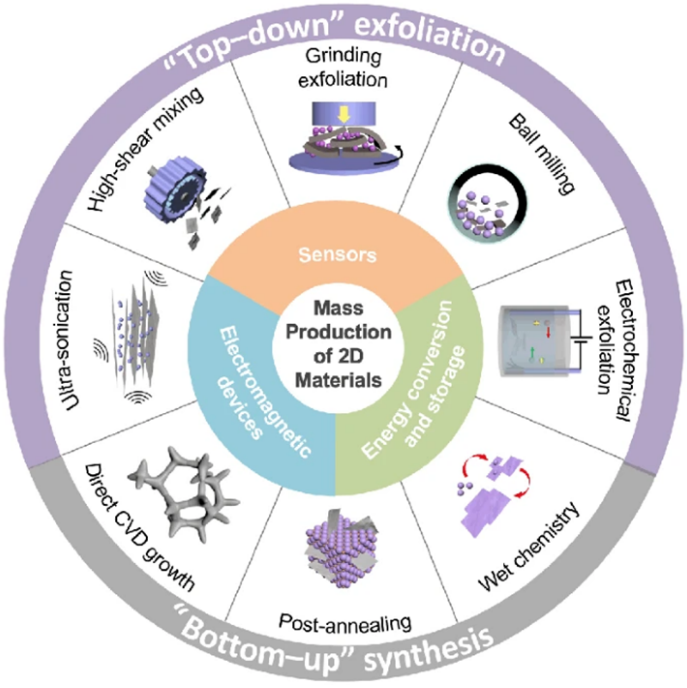

Fig. 1 *An overview of mass production methods and applications of 2DMs[47].*

Graphene's remarkable electrical characteristics make it highly appealing for future electronics applications. These include use in ballistic transistors, transparent conductive electrodes, integrated circuits, field emitters, transparent conductive electrodes, and sensors[48]. With the growing interest in graphene, the demand for this 2D material is also increasing, necessitating the advancement of efficient graphene

production techniques. To date, several techniques for producing graphene have been developed. Additionally, this is worth to mention that using various methods to produce 2DMs obtained material can exhibit varying characteristics owing to the presence of defects. These defects result in distinct behaviors, thereby impacting the performance of the final sensing device. In general, all synthesis processes associated with 2D materials are categorized into either “top-down” or “bottom-up” approaches. In top-down approach, a 2D material is obtained by selectively removing material from larger or bulk solid materials through controlled processes. In case of bottom-up techniques the production of a 2DMs involves the utilization of atomic or molecular precursors. These precursors have the capacity to react and grow, forming the desired 2D material or self-assembling into complex structured 2DMs. In comparison of top-down and bottom-up methods bottom-up is more efficient in mass production of desired 2DMs. The top-down approach employs various methods such as: liquid-phase, ultrasonic, electrochemical, mechanical and lithium-intercalated exfoliation or chemical reduction, whereas the bottom-up technique engages, chemical vapor deposition (CVD), epitaxial growth, wet chemical methods, pulsed laser deposition. However, the most used methods include mechanical cleavage, chemical exfoliation, chemical synthesis, chemical vapor deposition, and epitaxial growth on a silicon carbide (SiC) substrate. In 2DMs production by mechanical exfoliation, the 3D material is transformed into a single layer or a few layers of 2D material through a process of layer-by-layer peeling or interlayer tearing. To obtain high quality of 2DMs by this method two factors correlated with Van der Waals interactions the lateral and normal forces must be considered. Where the normal force is used to overcome the Van der Waals attraction during peeling process and lateral force is to overcome interaction between the layers of starting material[49, 50]. In case of graphene a commercially available highly oriented pyrolytic graphite (HOPG) is used as starting material. Since, Geim and Novoselov[17] mechanically exfoliated thin flakes consisting of single layer or a few layers of graphene from graphite it has resulted in numerous exciting discoveries regarding the electronic and mechanical properties of graphene. Regrettably, while this method produces high-quality flakes, their lateral size is quite limited. The small-scale production associated with mechanical exfoliation can be compensated for using liquid exfoliation and chemical exfoliation techniques. Unfortunately, the use of these methods allows for an increase in production scale but the obtained 2DMs exhibit diminished quality. Besides these approaches of synthesis of 2DMs several promising methods have been reported, such as mentioned epitaxial growth

from silicon carbide (SiC) and chemical vapor deposition on metal surfaces. Among them, the CVD technique is the most promising for the large-scale production of 2DMs with high quality and controlled sizes. CVD entails the high-temperature synthesis of 2DMs which involves decomposing decomposition of hydrocarbons on metal surfaces in vacuum condition[51]. The initial successful synthesis of graphene by CVD method was achieved on Ni surface[52]. Since then, substantial progress has been made in the production of graphene layers on a variety of metal substrates, with precise control over their thickness[51, 53]. In the end of CVD process the metal substrate undergoes chemical etching and the graphene layers are released which can be transferred to a different substrate. Another method of graphene production is thermal decomposition on SiC. This technique takes advantage of differences in sublimation of elements (silicon and carbon). The substrate made of SiC is heated at temperature around 1200°C. When the temperature is achieved silicon atoms starts to sublimate. The elimination of Si atoms results in the reorganization of surface carbon atoms into graphene layers[54, 55]. Even though the method of thermal decomposition on SiC allows to obtain graphene, controlling the thickness of graphene layers in the routine fabrication presents a considerable challenge. Moreover, the quality of produced graphene strictly depends on the standard of the SiC substrate. For this reason there are also reported other subtrates based on metals to fabricate graphene such as Co, Pt, Ni and Ru[56-58]. In last few years numerous techniques have been investigated for the production of 2DMs. However, one of the most promising methods is the electrochemical exfoliation of graphite. In general, the conventional experimental configuration comprises a working electrode and a counter electrode submerged in an electrolyte. Concurrently, the applied electrical potential and the composition of ions are integral factors in adjusting both the thickness and surface characteristics of the exfoliated materials[59, 60]. For example, tetraheptylammonium bromide molecules were used as electrolyte which intercalated MoS_2 crystal[61]. The MoS_2 crystal and the intercalated compound underwent rapid exfoliation, yielding thin MoS_2 nanosheets characterized by high quality and phase purity, rendering them conducive for applications in large-area electronics. In case of graphene to the electrochemical process graphite is used as working electrodes in liquid electrolytes which are aqueous solutions of inorganic salts such as: ($(NH_4)_2SO_4$, Na_2SO_4, K_2SO_4)[62]. Contingent upon the power supply applied to graphite electrodes, exfoliation methods can be delineated as anodic (utilizing a positive bias) or cathodic (employing a negative bias).

Diagrammatic representation elucidating the mechanism of electrochemical exfoliation of graphite is presented on Figure 2.

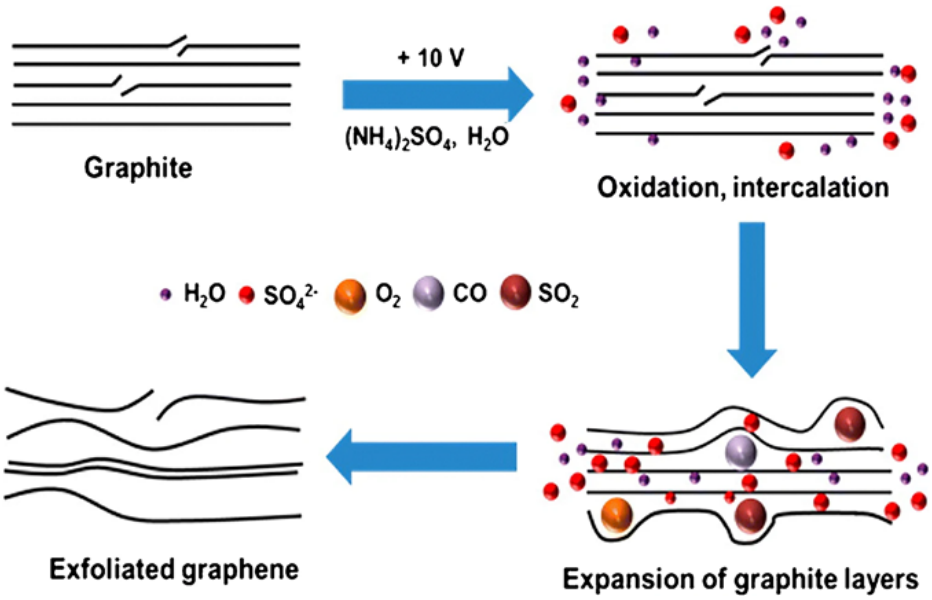

Fig. 2 *Schematic illustration of the mechanism of electrochemical exfoliation of graphite[62].*

The electrochemical exfoliation of graphite has attracted escalating attention in recent years as a method with promising scalability. Unlike other exfoliation methods this technique demands minimal equipment and is typically executed under ambient conditions. Moreover, it is environmentally friendly compared to alternative chemical or sonication-based routes which often entail the use of hazardous reagents or solvents.

Over the past few years, a multitude of techniques have been explored for the synthesis of two-dimensional materials. The development of knowledge about large-scale high-quality production of 2DMs have contributed to the increased utilization of these materials in electronics. However, beyond other 2DMs graphene still plays significant role in both everyday life and the scientific community. Furthermore, the chemical conversion of graphite which was studied due to the increased interest in methods of obtaining graphene has proven to be a feasible method for producing significant quantities of graphene-based single sheets and it has opened the advancement of research on derivatives of graphene materials such as graphene oxide and reduced graphene oxide. Moreover, another element that distinguishes graphene from other 2DM materials is its applications. Graphene has been primarily used as transistors in biomolecular applications. Additionally, graphene-based electrical sensors are utilized for temperature measurement, as photodetectors, and in radio frequency (RF) applications[63-67]. Moreover, the long history of designing and developing strain sensors from various

materials, graphene-based sensors have demonstrated exceptional suitability for strain-sensing applications. The benefit of using graphene instead of other conductive materials for strain sensing is attributed to the creation of a pseudo-magnetic field, which arises from the shift in the Dirac cones and the decrease in Fermi velocity. The utility of this pseudo-magnetic field is found in its application for detecting changes in the electronic structure under strain. Apart from their role as pressure sensors, strain sensors have been utilized for various applications, notably within healthcare devices. These sensors are often integrated into gloves, applied to skin surfaces, and affixed to organs to monitor various physiological parameters. Furthermore, the scope of potential applications for graphene sensors can be expanded by transforming more of these graphene-based sensors into comprehensive sensing systems. These sensors can be incorporated to develop wearable sensing systems for pervasive monitoring of physiological parameters and chronic diseases. Moreover, by enhancing the selectivity and specificity of graphene sensors, numerous everyday applications can enable the resolution of a multitude of everyday applications.

1.1 Chemical derivatives of graphene

It is widely acknowledged that materials play a pivotal role in the advancement of science and technology, with the development of new technologies often depending on the availability of innovative materials. Therefore, the study of materials exhibiting exceptional properties has always been a significant focus in scientific research. Over the past two decades, graphene has garnered significant attention as one of the most extensively studied materials. However, besides its numerous exceptional properties, graphene lacks a bandgap and exhibits poor water solubility, thereby significantly limiting its application in certain domains[5]. A viable strategy to overcome these constraints and broaden the applicability of graphene is by synthesizing graphene derivatives. As an illustration, the treatment of graphite to potent oxidizing agents introduces epoxy, hydroxyl, and carboxyl groups onto the basal plane of graphite layers ultimately leading to the formation of graphene oxide (GO). The oxidation of graphene is typically conducted by strong oxidants such as concentrated sulfuric acid, nitric acid, and potassium permanganate, following the Hummers method[68]. In Hummers method the graphite powder is treated by $NaNO_3$ and $KMnO_4$ dissolved in concentrated H_2SO_4. Presently, the Hummers method stands as the predominant approach for synthesizing graphene oxide. However, for specific application the oxidation level of GO obtained by

Hummers method can by insufficient. Moreover, during oxidation process toxic gases like NO_2 and N_2O_4 are released. For this reason, the modifications of Hummers method were studied. For example it has been proven that replacement of nitric acid by H_3PO_4 in mixture with H_2SO_4 in ratio 9:1 allows for production higher oxidized GO with more hydrophilic nature without toxic gases release[69]. Moreover, recently has been reported synthesis single-layer GO at room temperature by using K_2FeO_4 instead of $KMnO_4$[70]. The GO is the oxide form of graphene, where oxygen is introduced to graphene through chemical oxidation by the Hummers or Marcano methods. Furthermore, GO is characterized by extensive oxygenation, with numerous oxygen-containing functional groups such as epoxide, hydroxyl, carbonyl, and carboxyl groups present on its basal plane. Thus, the presence of these functional groups renders GO hydrophilic, enhancing its interfacial interaction with for example polar polymer matrices. That feature can improve the mechanical and electrical properties for various applications. Moreover, The functional groups introduced by the oxidation of graphene facilitate the dispersion and stabilization of GO in water[7]. Although GO is recognized as an infinitely thin sheet (with atomic-scale thickness) of oxidized graphene, an accurate model of its chemical structure has yet to be developed. The structure of GO is actively debated, with various structural models having been proposed, such as the models of: Dekany[71], Hoffman[72], Ruess[73], Scholz-Boehm[74], Nakajima Matsuo[75], Lerf-Klinowski[76]. The graphical presentation of GO models is presented on Figure 3.

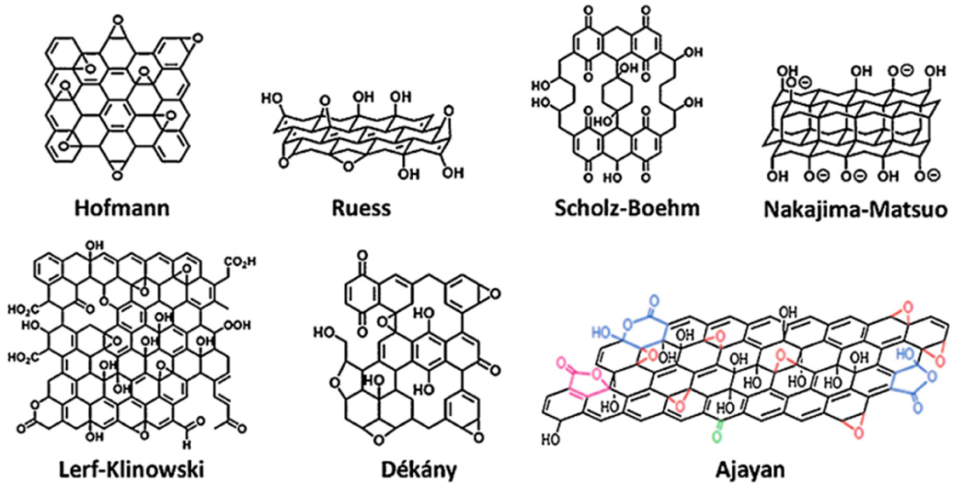

Fig. 3 *Structural models of graphite oxide (and hence GO) proposed[77].*

Regular lattices consist of discrete repeating units, and currently, the Lerf-Klinowski model is the most widely accepted configuration. The introduction of oxygen moieties to

the graphene structure has significant impact on the properties of obtained material. The oxygen functional groups (OFGs) in GO can be used for chemical modifications through established chemical methods. This makes GO potentially useful for applications in chemical sensing[78], solar cells[79], drug delivery[80], water desalination[81], and as an active material in energy storage systems (ESSs)[82]. Moreover, the present of the numerous hydrophilic functional groups on its surface provides efficiency interaction with water molecules from the environment. That feature is especially required in case of humidity sensing devices. Furthermore, the pristine graphite sheet exhibits atomic flatness, with a van der Waals thickness of 0.34 nm. Conversely, graphene oxide sheets are thicker due to the displacement of sp^3 hybridized carbon atoms positioned slightly above and below the original graphene plane, in addition to the presence of covalently bound oxygen atoms. Consequently, the lack of interconnected pathways between sp^2 carbon clusters necessary for classical carrier transport result in, newly synthesized GO sheets or films are typically insulating, exhibiting a sheet resistance of approximately 10^{12} Ω/sq or higher[83, 84]. Furthermore, the presence of oxygen functional groups renders GO thermally unstable, leading to its pyrolysis at elevated temperatures. Moreover, oxidation process causes massive amounts of defects in structure of graphene. Thus, GO exhibits electrical insulation properties due to the disruption of its sp^2 bonding networks. As electrical conductivity can be restored by re-establishing the π-network, one of the crucial reactions of graphene oxide involves its reduction. The reduction of graphene oxide leads to obtaining another graphene derivative which is rGO. The structure of graphene, GO and rGO are presented on Figure 4.

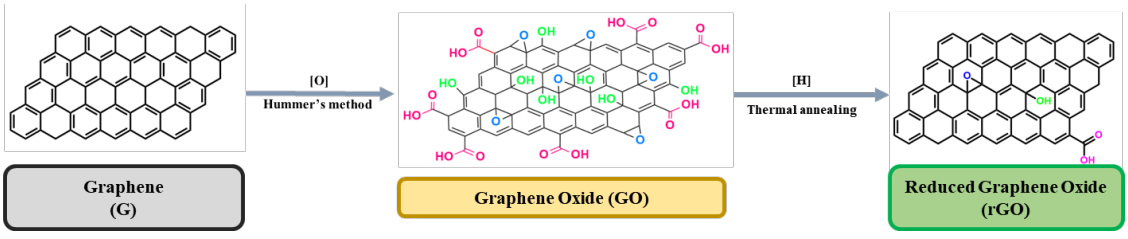

Fig. 4 *Schematic illustration of structure graphene, graphene oxide and reduced graphene oxide.*

When GO is dispersed colloidally, various chemical methods can be utilized to reduce graphene oxide. The chemical reduction is currently the most efficient approach for reducing GO, approaching the electrical characteristics of graphene (8.5×10^4 S m^{-1} is the highest electrical conductivity reported for chemically reduced graphene oxide (CrGO)[85]. Undoubtedly, one of the most prevalent and earliest reported approaches

involved the application of hydrazine monohydrate[86]. While many potent reductants exhibit varying degrees of reactivity with water, hydrazine monohydrate does not, thus rendering it an appealing choice for reducing aqueous dispersions of graphene oxide. Moreover, reduction conducted by hydrazine hydrate causes contamination with nitrogen atoms which has significant impact on conductivity of synthesized material[87]. This result can be explained by CrGO contamination with nitrogen and pyrazole formation, where the nitrogen atoms behave as electron donors and supply p-type holes. Consistently, other reducing agents have been investigated over the last few years. Thus, CrGO can be synthesized by dimethylhydrazine, p-phenylene diamine, ethylenediamine, hydroxylamine[88, 89], sodium borohydride ($NaBH_4$)[90], L-ascorbic acid (AA)[91-93], or sodium dithionite ($Na_2S_2O_4$)[87]. Chemical reduction is presently the most prevalent and efficient method for reducing graphene oxide. From an industrial perspective, chemical reduction is attractive due to its suitability for large-scale commercial production and its low energy requirements, typically operating at temperatures below 100°C. However, the expense of the chemicals, coupled with the substantial quantities of chemical waste generated, makes this approach less favorable for industrial use[94]. Chemical reagents can be circumvented by employing the electrochemical method. In this approach, the reduction process depends on electron exchange between the GO and the electrode and can be performed within an electrochemical cell in the presence of an aqueous buffer solution. Nevertheless, in electrochemical reduction, the deposition and reduction of GO are confined to substrates capable of serving as electrodes. Despite being one of the most efficient and commonly employed solution-processed protocols, chemical reduction is deemed inconvenient due to the generation of a stoichiometric quantity of chemical waste. Hence, thermal reduction emerges as one of the most appealing methods for reduction due to its low environmental impact. Thermal reduction entails the controlled annealing of GO within a specific atmosphere, leading to the desorption of H_2O, CO_2, and CO as desorption byproducts. It is well-documented that, under vacuum conditions and within an annealing temperature range of 100 to 185 °C, interlamellar H_2O molecules are desorbed. Additionally, between 185–300 °C and 500–700 °C, epoxide and carbonyl groups are eliminated, respectively. Subsequently, in the temperature ranges of 700–900 °C and 900–1200 °C, ether and hydroxyl groups are eliminated, resulting in a material characterized by a heightened carbon to oxygen (C/O) ratio[95, 96]. However, such elevated temperatures pose significant energy demands and are incompatible with the thermal reduction of graphene oxide on plastic substrates, particularly in the context

of flexible electronics which is huge limitation for strain and pressure sensor application. There are also different methods of reduction of GO such as: radiation-induced reduction[97], solar mediated reduction[98], the multi-step combined methods assisted reduction[99], photo-assisted[100] and microwave[101]. However, the chemical and thermal reduction techniques still remain the most common use in scientific community. The selection of the reduction method for GO has a significant impact on the electrical properties of the resultant material. This is particularly evident when considering efficiency of reduction in terms of C/O ratio. Comparing graphene and GO, oxygen from OFGs atoms substantially modify the electronic properties of the graphene layer, as observed from the band structure and density of states (DOS). Moreover, the opening of the energy gap is also associated with an increase in the effective masses of both electrons and holes. Therefore, even a minimally effective reduction of the insulating GO profoundly influences the conductive properties of the synthesized rGO. The reduction process of GO entails the elimination of OFGs, inducing the rehybridization of carbon atoms into the sp^2 configuration within regions devoid of oxygen. This process also facilitates the localized restoration of the planar honeycomb lattice structure. The segments comprising pristine graphene within GO layers manifest as graphene quantum dots (GQDs). Therefore, rGO can be characterized as a two-dimensional structure comprising GQDs of varying dimensions, dispersed randomly across the surface of the rGO substrate. The most diminutive GQDs arises from the extraction of a solitary oxygen atom from GO. Due to the complex structure of GO, it is exceedingly challenging to precisely estimate the impact of removal of single oxygen atom on the band gap. However, in the simple quantum models the relationship of oxygen removal can be described as follow Equation 1:

$$E_g(n_v) \approx E_g(0)\exp(-0.25n_v) \qquad Eq.\ 1$$

where $E_g(n_v)$ is the band gap of obtained rGO, $Eg(0)$ is the band gap of fully oxidized graphene and n_v is the number of oxygen eliminated from structure[102]. On the Figure 5 is presented the evolution of the electronic structure change and in the energy gap with the increase of number of oxygen atoms vacancies, (n_v). However, according to experimental results obtained for free GQDs, it is observed that their energy gap varies inversely with their diameter[103]. Nevertheless, still monitoring the impact of oxygen atoms form OFGs elimination on the energy gap and density of states provides a solid foundation for elucidating the disparities in the electrical and optical properties of rGO

with different C/O ratios. That correlation holds particular significance in the utilization of graphene derivatives for devices relying on their electrical properties, such as supercapacitors, batteries, and sensors.

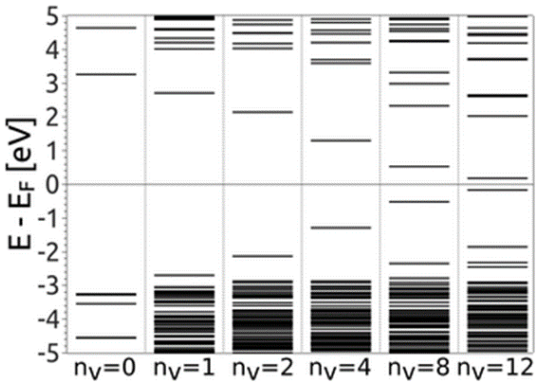

Fig. 5 *Evolution of the electronic structure change and energy gap with the increase of number of O vacancies[102].*

Finding a balance between the conductivity of rGO and the amount of oxygen in the structure by C/O is a crucial factor in designing new electrical devices, particularly chemical sensors. Therefore, further expansion and enrichment of knowledge concerning the reduction of GO are imperative.

1.2 2DMs based pressure sensing

Graphene and other 2DMs continue to be a prominent focus of research in science and engineering, even after more than 15 years since the first isolation of graphene. The extensive data available on the impressive performance of device prototypes clearly demonstrate the potential of 2DMs for their use in applications ranging from electronics and photonics to sensing. Among numerous applications. Recently, there has been considerable interest in both capacitive and transistor-based pressure sensors constructed by making use of 2DMs as active elements. In general, pressure sensors are devices designed to generate electrical signals in response to variations in external pressure[104, 105]. Pressure, defined as the ratio of force to the area over which it is applied, is a fundamental aspect of both natural phenomena and human activities. Pressure sensors that convert applied force into an electrical signal are increasingly in demand across numerous established and emerging applications, including human–machine interfaces[106], robotic technologies[107], wearable healthcare monitors[108-111] and microelectromechanical systems (MEMS)[112, 113] contributing to the development of Internet of Medical Things (IoMT). These applications necessitate sensors with high

sensitivity, particularly in the low-pressure range (<100Pa for detecting slight vibrations; <10kPa for gentle touch). Additionally, these sensors must exhibit rapid response times (in milliseconds), low power consumption (0.1 V – 5 V), adjustable pressure-sensing capabilities, and long-term stability and robustness. Due to these rigorous requirements 2DMs are once again classified as the most promising materials. Generally, pressure sensing devices can be categorized based on their pressure operating range such as: ultra-low pressure (<1 Pa), subtle-pressure (1 Pa – 1 kPa), low pressure (1 – 10 kPa) and medium-pressure (10 – 100 kPa) and high pressure (>100kPa). The range below 1 Pa is defined as the ultra-low pressure regime. Although such ultra-low pressures are infrequently encountered in everyday situations. However, the advancement ultra-sensitive pressure sensors is crucial in developing MEMS, microphones and others[114]. In case of other ranges numerous pressures resulting from minor interactions and small-scale objects fall within the subtle-pressure regime (1 Pa–1 kPa). Moreover, sensors designed to detect subtle pressures also underpin the development of highly responsive touch screen devices prevalent in mobile phones and artificial skin[115]. The pressures in low and medium pressure regime are more common in daily life and recently, considerable attention has been devoted to the development of pressure sensors for various applications in these pressure ranges like for example pulse monitor devices and medical diagnosis systems[116-118]. To advance understanding of sensor device performance across all possible pressure ranges, a variety of electroactive materials, including graphene[119, 120], nanoparticles[121], conductive elastomers[122] and single walled carbon nanotubes (SWCNT)[123, 124] have been employed as active components. Regardless of the type of active materials employed as sensory component, pressure sensors operate through one of three main transduction mechanisms, *i.e.*, capacitance, piezoelectricity and piezoresistivity. The schematic representation of transduction mechanisms of pressure sensors is presented on Figure 6.

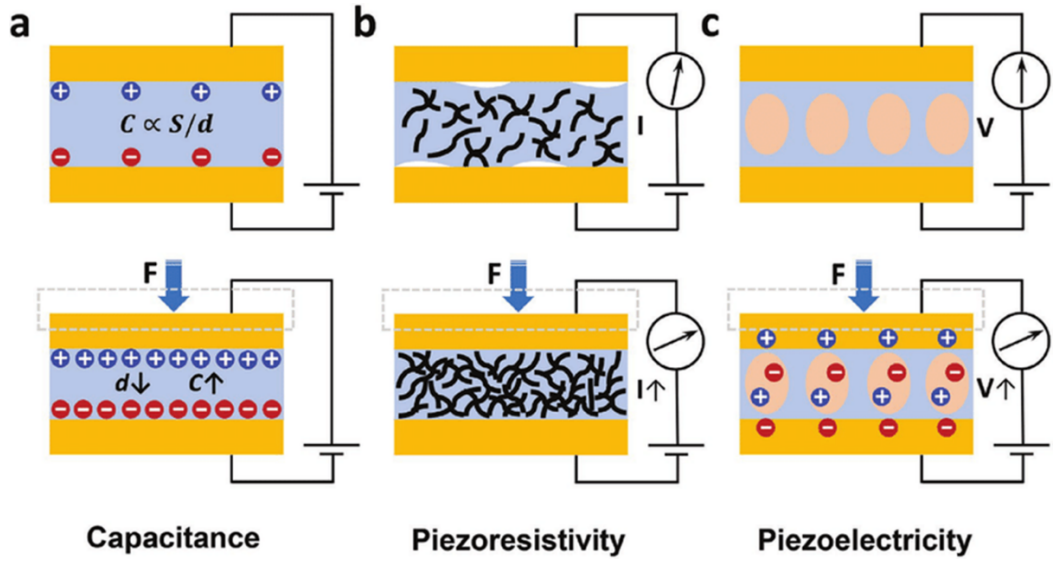

Fig. 6 *Schematic of transduction methods of pressure sensors: a) capacitance, b) piezoresistivity, and c) piezoelectricity[125].*

Capacitance transduction mechanism is based on the ability to store electrical charge and transfer this charge along the device system. Capacitive pressure sensors utilize the principle of altering the capacitance of a capacitor in response to applied pressure. A capacitor consists of two conductive plates separated by a dielectric material. When pressure is applied to the sensor, it causes a deformation of the plates and the dielectric, leading to a change in the distance between the plates and the permittivity of the dielectric. This change in capacitance can be measured using an electrical circuit, and the magnitude of the capacitance change is proportional to the applied pressure. The capacitance C of a parallel plate capacitor can be described by follow Equation 2:

$$C = \varepsilon_0 \varepsilon_r A / d \qquad Eq.\ 2$$

where ε_0 is the free space permittivity (usually electric constant), ε_r is the relative permittivity of material between the plates, A is the area of overlap of the two plates in square meters and d is the distance between electrodes in meters[105]. From the equation is clear to see that causing defects into the plates surface and distance between these plates by applied pressure provide significant change into capacitance. However, this change can be not linear which is serious disadvantage towards recyclability of working senor device. Capacitive pressure sensors offer high accuracy, stability, and a wide operating range. They are less sensitive to temperature fluctuations compared to resistive sensors. Moreover, capacitive tactile pressure sensing is considered as one of the most sensitive techniques for detecting small deflections of structures[126]. Moreover, one the most

promising application of capacitance transduction mechanism is the Organic Field-Effect Transistor (OFET). The OFET sensor device is constructed by active material with semi-conductor properties, a gate dielectric layer and three electrodes which are source, gate and drain[127-129]. In the OFETs system the transistor acts like a switch that controls the flow of electricity whereas applying a voltage (gate voltage) to a special electrode (gate) allows triggering a control signal for the switch. To establish a conducting pathway, a brief pulse of voltage is applied to the gate electrode when charge carriers aggregate at the interface between two layers within the transistor: the dielectric and organic layers. This process generates a temporary conductive channel. Once formed, this channel facilitates the flow of electricity from one electrode (the source) to another (the drain), akin to current flow in a closed circuit. By modulating the gate voltage through pulsing, it becomes feasible to regulate the timing and magnitude of the electric current flowing through the OFET, presenting a significant advantage for low-voltage applications in sensor devices. Within the operational framework of the device, the dielectric layer functions as a capacitor. The gate voltage modulates the charge state accumulated within this capacitor. This approach enables OFETs to exhibit low power consumption and high sensitivity. In case of 2Ms capacitive pressure sensors graphene and graphene-polymer composite materials have been extensively utilized in the design of electrodes for capacitive pressure sensors. However, certain researchers have introduced flexible capacitive pressure sensors employing graphene-polymer composites and graphene-based materials as the dielectric[130-134]. Nonetheless, OFETs and capacitive sensors, in general, entail higher costs and complexity due to the requisite precision in fabrication and signal conditioning circuitry.

Piezoelectricity transduction mechanism is based on generation of variations in electric charge within specific crystalline or ceramic materials subjected to mechanical stress[135]. Where the presence of electric dipole moments within a solid material is a fundamental factor underlying the piezoelectric effect. When mechanical stress (force or pressure) is applied to the piezoelectric material, the crystal structure deforms. This deformation disrupts the arrangement of the electric dipoles, causing them to no longer cancel each other out. As a result, a net positive or negative charge accumulates on opposite surfaces of the material, creating a voltage potential. To form electrical signal electrodes are attached to the piezoelectric material's surfaces and the voltage potential generated due to the stress difference creates an electric field across the electrodes. This

electric field can be measured by an external circuit, converting the mechanical stress into a measurable electrical signal. In general, piezoelectric materials are classified as smart materials due to their inherent ability to function as both sensors and actuators. This versatility stems from their remarkable sensitivity, generating a significant voltage output in response to applied mechanical force[136, 137]. Piezoelectric materials exhibit the property of becoming electrically polarized when subjected to external strain and, conversely, can undergo deformation in response to an applied voltage[138, 139]. Piezoelectricity can only occur in materials that exhibit non-centrosymmetric structures and possess a bandgap, thus excluding metallic substances. Notably, several materials that are centrosymmetric and thus not piezoelectric in their bulk form lose their inversion center when reduced to a monolayer, resulting in the emergence of piezoelectricity. Consequently, 2DMs like MoS_2[140, 141], BN[139], graphene[138] and GaS[142] are ideally suited for devices employing piezoelectric transduction methods.

Piezoresistivity transduction mechanism converting the change in resistance of a device into a measurable electrical signal. The intensive research focus on these sensors stems from their advantageous characteristics: simple device structures, straightforward readout mechanisms, and the potential for achieving high pixel densities, where each pixel is for example an organic thin film transistor[122]. Moreover, piezoresistive sensors exhibit compatibility with a broad spectrum of pressure ranges. This attribute translates to the reliable measurement of significant strain levels also. In general, piezoresistive sensors operate based on the principle of piezoresistivity. This principle describes the alteration in electrical resistance exhibited by a material when subjected to mechanical deformation. The resistance of a piezoresistor can be calculated by follow Equation 3:

$$R = \frac{\rho\, l}{t\, \omega} \qquad Eq.\ 3$$

Where where ρ, l, t, and ω denote the resistivity, length, thickness of the piezoresistor, and the width of the contact, respectively[143]. The confluence of advantageous features in piezoresistive technology, including low cost, high sensitivity, straightforward construction, exceptional long-term stability with minimal noise, and demonstrably high accuracy and reliability, underscores its maturity. While the favorable characteristics of piezoresistive materials facilitate straightforward fabrication and integration with electronic circuits, it is important to note that these sensors are typically limited to single-point contact measurements and require an external power source for operation. Resistive

sensors based on the first type, are either made of two-dimensional grid of sensing elements or the design employs two flexible sheets coated with a resistive material (typically possessing a finite resistivity of around 100 ohms per square). Piezoresistivity transduction mechanism is one of the most common appealing from others three main methods in working sensing pressure device. Simplicity and ease in creating devices based on piezoresistive materials is a key factor in popularity in scientific community, especially in devices based on chemiresistor structure. The pressure sensors based on piezoresistivity are precise, reliable, and their work is resistance for many various conditions.

Regardless of transduction methods the development of highly sensitive pressure sensors is critical to the realization of electronic skin and the integration of health monitoring capabilities into novel wearable devices. Moreover, pressure sensors with various structures will improve the intelligence and convenience of our professional and daily activities across various domains. Significant research efforts are currently directed towards enhancing sensor sensitivity, often through the implementation of microstructured electrodes or the incorporation of specialized active materials. However, these methods can be quite complex. Wherefore, 2DMs have significant impact in advanced sensor development. On Table 1 are presented few examples from literature of 2DMs based pressure sensors and their performance.

Tab. 1 Examples of 2DMs based materials as pressure sensors.

Material	Detection range	Sensitivity	Response time	Reference
MXene	10.2 Pa~30 kPa	0.55 kPa^{-1}	11 ms	[144]
rGO	9 Pa	0.26 kPa^{-1}	-	[119]
MoS_2	1-120 kPa	0.011 kPa^{-1}	180 ms	[145]
MXene/cotton fabric	10.25–40.73 kPa	0.57 kPa^{-1}	-	[146]
MXene/Ag NWs composite electrodes	0-600 kPa	3.65 – 418.2 MPa^{-1}	-	[147]
MXene-coated carboxylated carbon Nanotubes (CCNTs)/carboxymethyl chitosan (CCS)	0-80.9 kPa	0.18 kPa^{-1}	-	[148]
GO-doped PU nanofibers/Ni-coated cotton yarn elastic composite yarn	>0.001N	1.59N^{-1}	50ms	[149]
rGO/cotton	<500kPa	0.21 kPa^{-1}	681 ms	[150]
GO	0–0.7 m/s	1.22 $\Omega/(ms^{-1})$	5 s	[151]

Graphene / CNT	0–0.3 kPa	19.8 kPa^{-1}	16.7 ms	[152]
GO/Graphene	>0.15 g	0.032 kPa^{-1}	0.1 ms	[153]
MXene/CS/PU	>30 μN	0.014 kPa^{-1}	19 ms	[154]
Xene-sponge/PVA NWs	5.37–18.56 kPa	442 kPa^{-1}	138 ms	[155]
Graphene/PDMS	<70 kPa	0.23 kPa^{-1}	-	[156]

For example, MXenes are currently employed as strain and pressure sensors because of their electronic responses to strain induced by external forces. MXene pressure sensors demonstrate piezoresistive behavior, wherein external pressure induces a change in resistance. Rationally, the conductance of MXenes rises (falls) as the interlayer space contracts (expands). The 2D nature of MXenes facilitates their interaction with other 2D materials via van der Waals heterostructures, leading to intriguing electronic properties. In particular, MXene like ML-$Ti_3C_2T_x$ was implemented into working pressure sensor device[157]. The conductance of MXenes exhibited a monotonically increasing trend with rising pressure, accompanied by a notably high gauge factor (GF). Moreover, the sensitivity and stability of MXenes as active material in pressure sensors can be enhanced by addition other 2DMs like rGO[158] and CNT[159]. Due to this modification after 10 000 cycles, the MXene/rGO aerogel still shows a sensitivity of 22.56 kPa^{-1} to external force. Pressure sensors utilizing MXenes have attracted considerable attention owing to their exceptional performance and straightforward fabrication processes. To further enhance the sensing capabilities of MXene-based pressure sensors, meticulous material selection and meticulous design of the composite/foam structure are imperative. Similar to the case of composites comprising MXenes and graphene-based materials, employing two different two-dimensional materials may yield a beneficial effect on the device's efficiency. For example the sandwich structure composed of a BN/graphene/BN nanofilm results in the sensor's pressure detection range extends from 130 to 180 kilopascals, while boasting a maximum sensitivity of 24.85 microvolts per volt per millimeter of mercury[160]. The sandwich structure in this case is beneficial because of the lower BN layer is employed as a substrate for graphene, while the upper BN layer serves the purpose of a protective coating. Moreover, it has been empirically validated that the utilization of a boron nitride protective layer substantially enhances the performance stability of the graphene pressure sensor. In recent years, the continuous progress in mechanical materials research has led to the increasing exploration of potential applications for graphene and its derivatives especially graphene oxide, reduced graphene oxide, and carbon nanotubes. The linear piezoresistive effect of graphene has been employed in

creating various chamber pressure sensors, where strain-induced alterations in the bandgap width led to a notable decrease in carrier mobility. For the first time, a closed pressure cavity type suspended graphene pressure sensor was fabricated by suspending a monolayer of graphene over a cavity in the SiO_2 layer[161]. The maximum pressure detection limit reached 0.1 MPa, and the sensitivity (2.96×10^{-5} kPa^{-1}) was approximately 20 to 100 times greater than that of conventional silicon piezoresistive pressure sensors. Nevertheless, this sensor type encounters a substantial linearity issue, which could be addressed through the development of a field effect transistor-based circuitry[162]. Moreover, a suspended graphene sensor utilizing a cylindrical cavity structure, where pressure is exerted on the graphene film via the conduction of cylindrical contacts, has been devised. This configuration notably enhances sensor sensitivity[163]. Nonetheless, the manufacturing process is complex, and the sensor is prone to mechanical failure. Over recent years, the scientific community has introduced numerous adaptations to graphene-based pressure sensor configurations to fully exploit its potential[120, 164-170]. Despite the significant advancements in graphene-based technologies and numerous research endeavors conducted the potential of graphene remains an open question due to its inherent properties, which the full utilization of graphene's potential remains an ongoing inquiry. Hence, graphene derivatives have also been explored for their potential in piezoresistive pressure sensor applications. Graphene derivatives display a varied array of properties in contrast to pure graphene, owing to differences in their structure and chemical composition. For example, graphene oxide features a unique honeycomb carbon structure decorated with oxygen-containing functional groups on its surfaces which significantly affects its conductive properties, resulting in an electron mobility of approximately 10 000 cm^2 V^{-1} s^{-1}, while its mechanical properties remain largely unaffected. Moreover, rGO obtained from GO demonstrates an augmented electrical conductivity and mechanical resilience. Its room temperature mobility attains a notable value of up to 15 000 cm^2 V^{-1} s^{-1} and remains unaltered by fluctuations in temperature. Furthermore, doping and chemical modifications are strategies utilized to enhance graphene derivatives. Through manipulation of the bandgap value and the development of novel solutions and composite materials, GO and rGO have been employed in piezoresistive pressure sensors. Additionally, the utilization of graphene and its derivatives enables the development of sensors spanning different pressure ranges, where they can mutually complement one another. For example graphene based pressure sensor operating in 100–200 kPa whih sensitivity 24.85 μV/V/mmHg has been reported[160],

whereas sensor based on rGO is working in 100 – 200 Pa pressure range with sensitivity 178 kPa^{-1}[171] and according to GO 0-30 kPa with 0.13 kPa^{-1} sensitivity[172]. Notwithstanding significant strides in this arena, multiple impediments persist in the widespread utilization of flexible sensors derived from graphene. Complex and costly manufacturing procedures represent a substantial hurdle. Therefore, there is a pressing need to devise cost-effective and streamlined manufacturing techniques to facilitate their practical deployment. Moreover, the presence of other 2DMs and oxygen containing functional groups can substantially undermine the material's properties, especially in the case of graphene. In broad terms, graphene and its derivative materials maintain a wide-ranging application outlook and considerable market potential, thus warranting robust research endeavors and proactive promotion in the field of pressure sensor applications.

1.3 2DMs based strain sensing

A strain sensors generally consist of active sensing elements adhered to a flexible, elastic support substrate. These flexible and oftentimes stretchable sensors are capable of detecting both low and high stress levels. The choice of stretchable materials is crucial in the fabrication of flexible strain sensors. 2DMs possess substantial potential in the domains of flexible electronics devices, owing to their unique properties arising from their specialized structures. The examination of the mechanical properties of 2DMs is pivotal for the advancement of next-generation flexible strain electronic device applications. Due to the vast array of potential configurations, strain sensors lack a unified classification system. Most reported flexible strain sensors are single-functional and incapable of measuring mechanical deformations resulting from complex multidirectional impacts, such as detecting intricate movements involving tensile stress, twisting, or bending. Sensors with specific characteristics are typically tailored for particular application. For example, a sensor designed to measure small strain with high sensitivity is suitable for detecting heartbeats. Sensors with high stretchability and low sensitivity are ideal for detecting high-amplitude joint movements. Additionally, the strain sensor must conform to the surface of the human body and ensure a certain level of comfort. Beyond their application as pressure sensors, strain sensors have been utilized in various fields, including healthcare devices[173-175], human–machine interaction[176, 177], in motion detection[159, 178, 179]. Moreover, the intelligent wearable electronic devices demonstrate excellent interaction with the human body, providing significant advantages for personalized medicine, rehabilitation and disease

diagnosis[180, 181]. When wearable sensors are incorporated into clothing and affixed to human skin, they seamlessly adapt to the skin's contours, enabling precise real-time measurement of various signals[182, 183]. In recent years, flexible strain sensors have been extensively reported and have garnered significant attention as a crucial element of intelligent wearable sensors.

Due to the demands for flexibility, the critical issue lies in selecting an appropriate substrate for the active material in the sensor. For conventional rigid pressure sensors, substrates such as silicon (Si), silicon dioxide (SiO_2), or glass are typically employed, and they are not deemed pivotal in determining device characteristics. However, the selection of the substrate material becomes a critical factor in the efficiency of flexible strain sensors. Both substantial mechanical flexibility and minimal roughness are highly sought-after attributes. Numerous commercially available polymers and elastomers such as: polyethylene terephthalate (PET), polyimide (PI), polyurethane (PU) polydimethylsiloxane (PDMS), polyethylene (PEN) are suitable substrates for strain sensors. Each of these substrates possesses its own set of merits and drawbacks. The choice of substrate may hinge not only on its elastic characteristics but also on its polarity, affinity, and interactions with the deposited active material. For example, PDMS boasts several additional advantages, such as high transparency and exceptional stability over a broad temperature range. Moreover, the intrinsic flexibility and extensibility of PDMS allow devices made from it to easily respond to torsional, tensile, and compressive strains[184]. However, due to its polarity, it is challenging to deposit non-polar materials on PDMS which is huge limitation in the development of devices based on PDMS. PEN and PET are also regarded as promising substrates. For example, an ultra-lightweight plastic electronic device (3 g/cm^2) has been fabricated using an ultra-thin PEN foil, 1 mm thick, capable of enduring repeated bending to a 5 mm radius and paper-like crumpling. By integrating pressure-sensitive rubbers with organic field-effect transistors on a PEN substrate, strain-sensing matrices have been developed, demonstrating their promising potential in electronic skin applications[185]. PI exhibits exceptional stability, insulating properties, and mechanical characteristics. Additionally, PI is resistant to corrosion from various chemical solvents, which is crucial in subsequent device processing steps. Moreover, even ultra-thin PI films remain undamaged by high mechanical forces, and its outstanding bending stability renders it as an appropriate option for compliant devices. However, these synthetic materials mentioned above serve effectively as sensor

substrates, yet their limited biodegradability raises environmental concerns with extensive device deployment. Hence, research endeavors are focused on exploring and developing natural materials for sensor substrates. Cellulose paper possesses inherent flexibility, porosity, cost-effectiveness, recyclability, biodegradability, and biocompatibility. Moreover, it has been employed in test strips for medical diagnostics as strain sensor[186, 187]. In general, in practical sensing applications, it is essential to consider the thermal resistance, chemical resistance, transparency, and flexibility of a material[188]. The creation of flexible sensors necessitates innovative materials design approaches, encompassing active materials and conductors, along with the selection or synthesis of flexible substrates. Rigid bulk materials can be rendered deformable by reducing their thickness and organizing them into nanostructures. For active materials, cost-effective, print-compatible, solution process able, and lightweight π-conjugated organic semiconductors have been employed. Non-transition metal oxides that demonstrate high sensitivity and favorable conductivity, such as ZnO, In_2O_3, SnO_2, and Ga_2O_3, have also been utilized as active materials[189, 190]. Among the new potential active materials for flexible sensors, 2DMs involving transition-metal dichalcogenides[191], black phosphorus[192], MXene[159], MXene/rGO[158] and graphene[193] because of their great electrical performance. Moreover, conductive materials, which enable interconnection between different components of electronic devices, are indispensable for the functionality of said devices. Nanoparticles, nanotubes, nanowires, and thin films can serve as core materials for specific processing conditions[194, 195]. The characteristics of strain sensors are typically determined by the materials and substrate used and their structure. The main physical properties of foams, films, or textile materials present inherent challenges and advantages in their application for strain measurement. Due to their structure and properties, strain sensors can be categorized into several subtypes, including yarns, fiber, fabrics, films, foams and gel[196]. Regardless of the subtypes, the operating principle of strain sensors functions similarly. As the bending radius decreases and the level of deformation increases, the relative change in sensor resistance alters both externally and internally. The sensing mechanism of the flexible strain sensor is illustrated on Figure 7.

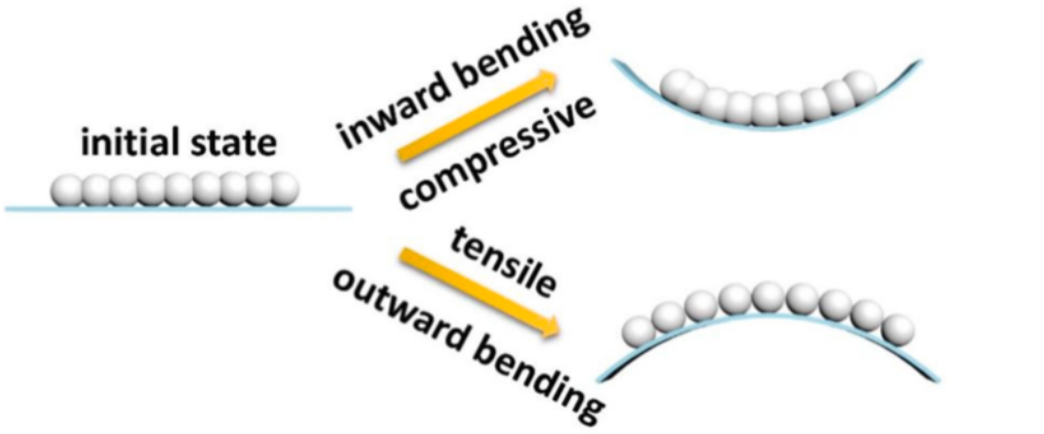

Fig. 7 *Sensing mechanism of the flexible strain sensor[197].*

Regardless of the application, strain sensors can utilize various types of transduction mechanism, including capacitive[198], piezoelectric[199, 200] and piezoresistive[201, 202], where the most prevalent still remains piezoresistive transduction method. Piezoresistive sensing, which converts mechanical displacement into an electrical signal, is advantageous for monitoring minor structural deformations in flexible support layers over time. In this scenario, variations in conductance or resistance can be measured from a specific active matrix, either with or without an on/off switchable transistor. Furthermore, the majority of traditional strain sensors are constructed using metal foil and semiconductor materials. However, gauge factor of metal strain sensors' sensitivity does not exceed 5, which is inadequate for detecting signals pertinent to human health[203]. Wearable strain sensors necessitate a sensing range of 55% strain, representing the upper limit of deformation within the human skin[204]. Moreover, strain sensors integrated into health monitoring systems must demonstrate the capacity to stretch in accordance with diverse human movements, including breathing, joint articulation, and muscle contractions. In the other hand, semiconductor strain sensors exhibit higher sensitivity compared to metal strain sensors, attributable to their distinctive piezoresistive effect. However, their limitations, including low flexibility, narrow detection range, and high fabrication costs, constrain their widespread applications. Recently, researchers have made significant efforts and conducted extensive experiments to investigate novel strain sensors composed of various functional sensing materials, owing to their superior performance. Moreover, the main characteristics of strain sensors are typically determined by the implemented materials and their structure. The inherent physical properties of foams, films, or textile materials pose natural challenges and

advantages in their application for strain sensing. The 2DMs and their heterostructures have garnered considerable attention due to the many fascinating material properties that emerge from their layered structure. On Table 2 are presented few examples from literature of 2DMs based strain sensors and their performance.

Tab. 2 Examples of 2DMs based materials as strain sensors.

Material	Detection range	Sensitivity	Response time	Reference
α-Bi_2Se_3	-	GF ~ 237	-	[205]
GaSe		GF ~ -4.3	-	[206]
rGO	0.1%–400%	GF ~ 2.5	60 ms	[207]
Graphene	-	GF ~ 2.6	-	[208]
	~80%	GF = 0.97		[209]
	0-0.3%	GF = 389		[210]
MoS_2	<−5.23%	GF ~ 72.5	-	[211]
Graphene/PDMS	70%	GF ~ 24	-	[212]
MXene/CNT	0–30%	GF ~ 64.6	-	[213]
MXene nanoparticle–nanosheet hybrid	0–53%	GF > 178.4	130 ms	[214]
MXene/PVA	0.5–3.0%	GF~25	-	[215]
MXene nanocomposite hydrogel	<350%	GF = 44.85	-	[216]
InSe	±0.25 %	GF = 36	-	[217]
In_2Se_3	-0.39% - 0.39%	GF = 237	-	[205]
SnS_2	0-1.4%	GF = 3933	-	[218]

The benefit of utilizing graphene over other conductive materials for strain sensing is the creation of a pseudo-magnetic field caused by the shift in the Dirac cones and the reduction in Fermi velocity. The utility of this magnetic field lies in its utilization to ascertain the alteration in electronic structure under strain. Moreover, graphene-based sensors incorporate various materials amalgamated during fabrication. The change in unit resistance relative to the change in unit length induced by the strain determines the extent of strain to be considered for the material. Furthermore, the relative amount of strain is greater when applied parallel to the C-C bonds compared to its application perpendicular to the C-C bonds, primarily due to a more significant increase in the band gap. To these days numerous research groups developed many graphene films on polymer substrates, including for example PDMS, PET, and PI[219-221]. In terms of the performance of flexible pressure sensors, researchers propose various innovative designs primarily focused on structural and material enhancements. For example, incorporating micro- and nanostructures into traditional thin-film pressure sensors can significantly enhance their

sensitivity and stability. As an illustration, the integration of micro- and nanostructures into conventional thin-film pressure sensors can markedly enhance their sensitivity and stability. Moreover, the utilization of a multilevel structure can enhance their ability to adapt to various environmental conditions. Enhancements in material selection also play a pivotal role in this context. At present, frequently employed materials for flexible pressure sensors encompass polymers and metal films. However, these materials may demonstrate limitations such as inadequate durability and other issues. Consequently, capitalizing on the exceptional mechanical properties and other advantages provided by graphene and its derivatives proves highly beneficial in addressing these challenges.

1. 4 2DMs based humidity sensing

A gas sensor is a device capable of identifying the presence and measuring the concentration of specific gases in the atmosphere, such as water vapor (humidity), organic vapors, and hazardous gases[222]. Gas sensing is increasingly important in our society due to the necessity for rapid detection of toxic gases and organic vapors. This is crucial for environmental and human safety, the industrial sector, emission control and medical diagnosis. In general, chemiresistors and chemi-capacitors are other prevalent gas sensing devices, wherein the sensing material is positioned between two electrodes. The presence of gas molecules adsorbed on the material's surface prompts a modification in its resistance or capacitance, which can be precisely measured. Gas sensor performance is typically evaluated using various metrics, with sensitivity, selectivity, stability, response and recovery times, cost, dimensions, and flexibility being among the most significant factors. The response $R(\%)$ of a particular device is calculated as the ratio between the change in resistance (or another output) observed when the device is exposed to the sensed gas ($R_{(i)}$) and when it is not, divided by the resistance observed in the absence of the sensed gas (R_0). The response can de descried by follow Equation 4:

$$R(\%) = \frac{R_{(i)} - R_0}{R_0} \times 100\% \qquad Eq.\ 4$$

At present, several materials, including metal oxides such as SnO_2, In_2O_3 and CuO[223], conducting polymer[224] and for example CNT[225], are employed as active materials for gas detection, including humidity sensing. In particular, metal oxides have exhibited superior properties regarding response and sensitivity among other materials. Moreover, their low cost and ease of production render them widely utilized in

commercially available gas detection devices. However, resistive metal oxide-based gas sensors generally function at high temperatures (exceeding 100°C), leading to significant power consumption. Furthermore, the elevated operating temperatures cause fluctuations in gas sensing responses due to the growth of metal oxide grains. Moreover, another limitation of metal oxide-based gas sensors is their insufficient selectivity[226, 227]. Hence, the gas sensing research community is focused on developing new materials capable of detecting gases at room temperature, under standard environmental conditions, with high selectivity and sensitivity. Because of these requirements, two-dimensional materials have attracted significant attention from researchers. Due to their exceptional features, 2D materials emerge as promising candidates for gas sensors, boasting an intrinsically high surface-to-volume ratio. Moreover, the 2DMs such as for example phosphorene[228], black phosphorus[229] TMDs like MoS_2[230-233], $MoSe_2$[234] and WS_2[235-237] featuring either a direct or indirect bandgap, which can be adjusted according to the number of layers. On Table 3 are presented few examples from literature of 2DMs based humidity sensors and their performance.

Tab 3 Examples of 2DMs based materials as humidity sensors.

Material	Detection range	Sensitivity	Response time	Reference
GO	10 – 98 RH%	79.3 (ΔV/RH%)	19 s	[238]
	15 – 95 RH%	37757 (ΔC/C)	10.5 s	[239]
	40 – 88 RH%	120000 (ΔI/I)	6 s	[240]
MoS_2	0 – 60 RH%	150 (ΔR/R)	9 s	[241]
WS_2	40 – 80 RH%	3750 (ΔR/R)	13 s	[242]
rGO	30 – 90 RH%	-	28 s	[243]
Graphene	1 – 96 RH%	0.31 (ΔR/R)	0.6 s	[244]
VS_2	0 – 100 RH%	30 (ΔR/R)	30 s	[245]
$TiSi_2$	0 – 100 RH%	63 (kΩ/RH%)	8 s	[246]
GO/MWNTs	10 – 90 RH%	1000% (ΔZ/Z)	10.7 s	[247]
MoS_2 Ink	10 – 95 RH%	-	8 s	[248]
$ZrSe_2$	15 – 80 RH%	68 (kΩ/RH%)	1 s	[249]
Ti_3C_2/TiO_2	7 – 33 RH%	280 (pF/RH%)	-	[250]
MXene/GO	3–90 RH%	-	1.07 s	[251]

Despite numerous examples of various two-dimensional materials applications in the literature, graphene and its derivatives remain at the forefront of interest. Graphene has garnered considerable attention for gas sensing applications due to its morphological characteristics, notably its high surface-to-volume ratio. However, its zero or quasi-zero bandgap may pose a challenge when employing it as an active material in sensing devices.

Hence, graphene derivatives such as GO and rGO are being contemplated. Which demonstrated that graphene and its derivatives could function as efficient sensing materials for next-generation humidity sensing systems. Graphene-based gas sensors operate on the principle that the introduction of gas molecules alters the local charge carrier concentration in graphene, either increasing or decreasing the concentration of electrons depending on the nature of the gas species (electron donor or acceptor) whether they are oxidizing or reducing. Oxidizing gases function as electron acceptors, while reducing gases serve as electron donors., resulting in a corresponding decrease or increase in electrical conductivity[252, 253]. In case of H_2O molecule acts like as an acceptor on the graphene surface[254]. If the oxygen atom is oriented towards the graphene surface, there is a slight charge transfer to the graphene, whereas if the hydrogen atoms are oriented towards the surface, there is a minor charge transfer to the water molecule. This arises from the configuration of the highest occupied molecular orbital (HOMO) and lowest unoccupied molecular orbital (LUMO) of H_2O and their respective positioning relative to the Dirac point[253]. The calculated density of states of orbital meanwhile the water molecule is adsorbed on graphene surface is presented on Figure 8.

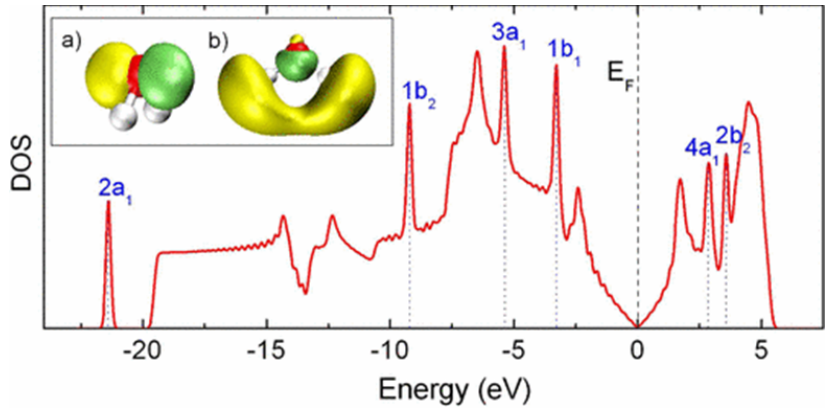

Fig. 8 *Density of states during the adsorbed H_2O molecule. Color online H_2O on graphene. Inset: a) representation of the HOMO and b) the LUMO of H_2O. The H atoms are depicted in white, the oxygen atom in red; green and yellow denote different signs of the orbital wave function. The blue dotted lines indicate the positions of the molecular orbitals of H_2O[253].*

The adsorption energy is primarily determined by the orientation of the water molecule (upright (*u*), downward (*d*), normal (*n*), and vertical (*v*)) relative to the graphene surface. When the highest occupied molecular orbital ($1b_1$) is entirely situated on the oxygen atom, while the lowest unoccupied molecular orbital ($4a_1$) is predominantly located on the hydrogen atoms. In the *u* orientation, the HOMO predominantly influences the interaction, and by slightly mingling with the graphene orbitals above the Fermi level,

it transfers some charge to the graphene. Similarly, there's a more pronounced mingling with the orbitals below the Dirac point due to their closer energy levels, although this does not result in any charge transfer as all these orbitals are occupied. In the *d* and *v* orientations, the LUMO of H_2O engages more prominently with the surface and can, *via* a slight overlap with the graphene orbitals beneath the Dirac point, acquire some charge from graphene. Additionally, there is a more significant interaction with the orbitals above the Dirac point; however, this does not result in any charge transfer since all these orbitals are vacant. In the *n* orientation, once again, the HOMO will exhibit stronger interaction, but there will also be some interaction with the LUMO. This will result in a transfer of charge from the molecule to graphene, although the interaction with the LUMO will diminish this transfer to some extent. The presented interactions and effects of water molecules on changes in the DOS of graphene orbitals provide the basis for understanding the operation of humidity sensors based on graphene. However, pristine graphene has a significant limitation, especially in applications in devices employing a chemiresistor configuration. This limitation arises from its semimetallic, rather than semiconducting, properties, which prevent the formation of a Schottky barrier with metals. In the chemiresistive configuration of humidity sensors, changes in resistance occur due to electron exchange when gas molecules interact with the semiconductor sensing layer or metal electrodes. In a semiconductor sensing layer interfacing with a metal electrode, the alignment of Fermi levels (E_F) between the two materials is imperative for equilibrium. The Fermi level characterizes the thermodynamic energy needed to add an electron to a solid-state material, without considering the energy needed to remove the electron from its source. In a semiconductor, the Fermi level typically resides within the bandgap. The minimum energy needed to extract an electron from a specific point within a solid-state material is denoted as the work function Φ, which equals the energy disparity between the Fermi level and the vacuum level. If the work function of the metal electrode surpasses that of the semiconductor ($\Phi_M > \Phi_{SC}$), electrons with high energy from the semiconductor's conduction band (E_C) migrate from its bulk to the metal surface, creating an electron depletion layer (EDL) at the interface. In n-type materials, where the Fermi level (E_F) is close to the conduction band (E_C) and electrons are the dominant charge carriers, the resulting depleted junction is termed a Schottky barrier. If $\Phi_{SC} > \Phi_M$, a Schottky barrier is also established for p-type materials, where the Fermi level (E_F) is near the valence band (E_V) and electron holes (h+) predominate as the charge carriers. In this scenario, electrons transition from the metal surface to the

unoccupied states within the valence band of the semiconductor bulk, resulting in the formation of an electron-accumulation layer/hole-depletion layer. Conversely, ohmic contacts may be established. Nonetheless, these appear to be of lesser significance for implementation in chemiresistive gas sensors. For this reason, the semimetallic nature of graphene precludes the formation of a Schottky barrier with metals. Consequently, there arises a necessity to establish a Schottky junction, either by interfacing pristine graphene with various semiconductor materials or by employing oxygen-functionalized graphene derivatives. On Figure 9 are presented examples of the effects of the interaction for the Schottky barrier between gold and n-type semiconductor MoO_2, as well as reduced graphene oxide of p-type.

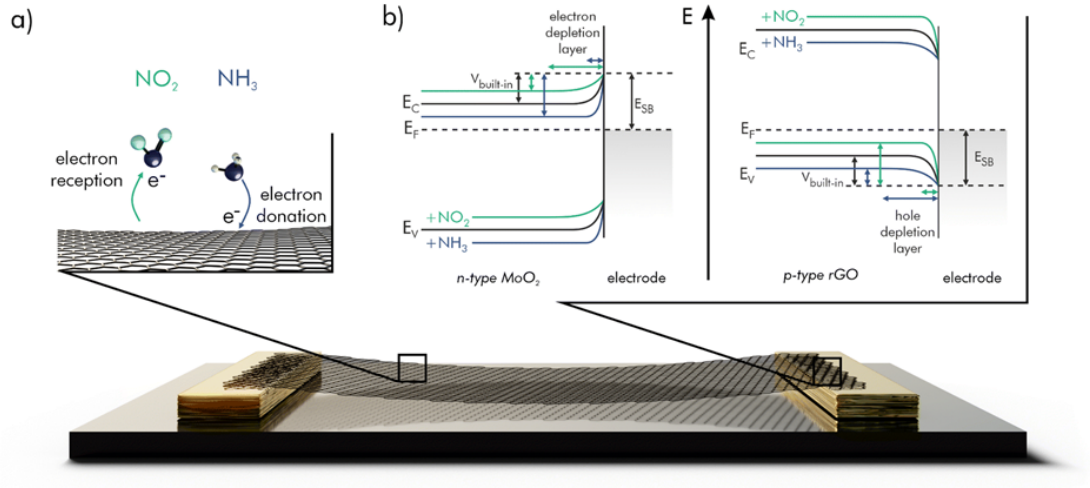

Fig. 9 *Gas sensing mechanisms on a semiconducting material, such as a graphene derivative, involve two main processes: (a) electron exchange between gas molecules and the receptor material, and (b) the shift of the band structure at the semiconductor-electrode contact[255].*

The utilization of graphene derivatives such as graphene oxide and reduced graphene oxide in humidity sensors offers a substantial advantage over pristine graphene owing to the presence of oxygen containing functional groups. The physisorption of molecules onto a surface is contingent upon the attributes of both the analyte and the surface itself. For instance, graphene exhibits an extended lattice structure composed of sp^2 hybridized carbon atoms, characterized by extensive π-conjugation. Therefore, the involvement of noncovalent intermolecular interactions within π-systems is crucial in recognition phenomena, as even subtle changes in the electronic properties of these systems can induce alterations in both structure and properties[256, 257]. However, water, being polar in nature, will be attracted only by interactions of a similar character, which implies that pristine graphene lacking polar functional groups will be an inefficient

humidity sensor. GO and rGO, in particular, are receiving significant attention due to their scalable industrial production, low cost of raw materials, straightforward preparation process, processability in environmentally friendly solvents, and high chemical stability. These attributes make them even more suitable for humidity sensing applications[258-261]. The exceptional humidity-sensing ability of GO arises from the abundance of hydrophilic functional groups on its surface, such as epoxide rings, hydroxyl, and carboxyl groups, which effectively interact with water molecules in the surrounding environment. Nevertheless, due to the strong interactions between water molecules and the mentioned functional groups of GO, humidity sensors based on GO experience significant hysteresis and inconsistent behavior over time[262]. Furthermore, their sensing capabilities often exhibit slow response and recovery times[263]. Moreover, due to the low conductivity of GO (often below 1×10^{-4} S m^{-1}) substantial electrical potentials are necessary to generate measurable currents, consequently resulting in heightened power consumption. Alternatively, rGO exhibits conductivity levels that are 6 to 7 orders of magnitude higher than those of GO thus enabling the production of energy-efficient devices[264]. However, a notable drawback of rGO is its hydrophobic characteristic. As a result of the removal of oxygen-containing functional groups during the reduction process of GO, its surface becomes hydrophobic, resulting in decreased interaction with water molecules and hence reducing its responsiveness to humidity. To overcome these limitation the functionalization of rGO surface can be provided. Moreover, devices based on rGO typically comprise numerous rGO flakes with varying shapes, thicknesses (few layers of graphene sheets), sizes, and degrees of reduction. This leads to variations in electrical properties among these sheets, and the formation of random junctions between these flakes further exacerbates this variability. Consequently, there are differences in properties between any two devices made of rGO.

Chemiresistive sensors composed solely of graphene exhibit low selectivity and are highly sensitive to humidity when operated in ambient conditions. However, incorporating graphene with other semiconducting materials, can enhance the sensing characteristics, particularly in terms of selectivity, through synergistic effects. Although, attaining genuine selectivity with a high degree of sensitivity, particularly in ambient conditions, continues to pose a significant challenge and is frequently regarded as a fortuitous occurrence. The development of materials tailored for specific gas sensing applications remains a significant challenge, primarily due to the lack of comprehensive

understanding regarding the intricate mechanisms and underlying reasons for certain interactions between sensors and target gases.

1. 5 Key parameters for sensors

Despite extensive and ongoing research on graphene-based sensors and their various forms, creating an effective sensor remains a challenge. To evaluate the performance and effectiveness of a sensing device, it is essential to gather detailed information on the key parameters related to sensors. The performance of sensors can be characterized by several key parameters: sensor response and recovery time, limit of detection (LOD), operating temperature window, selectivity for specific analytes, as well as chemical and physical stability. Ongoing advancements in enhancing and integrating these parameters have further encouraged the development of sensors for an even broader range of applications.

The sensitivity is a critical parameter for sensors, as it determines the measurement accuracy and the overall effectiveness of the device. Sensitivity of a sensor can be defined as the gradient of the output characteristic curve or, more broadly, as the smallest change in physical parameters that produces a detectable change in output. In some sensors, sensitivity is also defined as the magnitude of the input parameter change needed to generate a standardized output signal. In case of pressure sensors, sensitivity presented on Equation 5 is defined as:

$$S = \mathrm{d}X/\mathrm{d}P \qquad Eq.\ 5$$

where S represents the sensitivity, X denotes the quantitative output signal, and P represents the applied pressure. Measurement sensitivity can be influenced by the functional material used, the sensing mechanism employed, and the structural configuration of the sensor. Thus, materials with significant piezoresistive or piezoelectric coefficients are highly desirable. However, utilizing individual elements of nanostructured materials may not be the most favorable approach. In this context, enhancement approaches at the macroscopic scale are more feasible. The tunneling effect and crack/gap structures have been demonstrated to effectively enhance sensitivity in piezoresistive sensors. Additionally, foamed or pyramidal elastomer dielectrics exhibit strong performance in capacitive sensors. Moreover, it is important to note that many highly sensitive sensors exhibit optimal performance within a constrained range of strain.

Therefore, sensors capable of both high stretchability ($\varepsilon \geq 100\%$) and high sensitivity (GF ≥ 50) remain a focal point of research. In case of gas sensors, the site-binding hypothesis posits that atoms present on the surface of sensing materials can function as binding sites for analyte adsorption. Consequently, the change in conductance of the device would correlate with the extent to which analyte molecules occupy these binding sites on the sensing materials. Moreover, the heightened sensitivity of electrically transduced sensors utilizing 2D materials can be attributed to their expansive surface area and abundant active sites that facilitate interactions with analytes.

The limit of detection (LOD) is another critical parameter; nevertheless, its definition rigorously depends on the specific type of sensor employed. In case of humidity sensing the LOD is defined as the lowest concentration of an analyte that can be reliably differentiated from its absence in a sample (blank) with a specified level of precision and reproducibility, typically within a 99% confidence interval. A widely employed experimental method for determining the LOD involves exposing a sensing device to known concentrations of the analyte of interest to produce a calibration curve. The detection limit can be determined by comparing the sensor's resolution to its sensitivity. Various analytical criteria, depending on the techniques used (*e.g.*, the concentration at which the signal is three times the noise level), are utilized to ensure that the recorded analytical signal is meaningful and distinguishable from the baseline. Since the LOD is determined by the sensitivity and resolution of the sensor, it can be enhanced by improving material-analyte interactions, increasing available surface area, implementing surface functionalization, and employing signal amplification techniques. The extensive coverage of functional groups on 2DMs facilitates effective and robust interactions with targeted analytes, thereby achieving high sensitivity. Simultaneously, the intrinsic high conductivities of these materials and the superior quality of their interfaces contribute to reduced signal noise. This combination has made 2DMs highly appealing for the development of gas sensors with low LODs. In case of pressure sensing, the LOD is the lowest pressure that can produce a signal change. Enhancing LOD in pressure sensors is crucial for the advancement of effective ultra-low and subtle-pressure sensors.

Linearity describes the proportional relationship between output signals and input stimuli, and excellent linearity can streamline the calibration and data processing procedures. Linearity is often measured by the extent of deviation from a straight regression line, expressed as a percentage. Nevertheless, achieving both high sensitivity

and excellent linearity simultaneously poses a significant challenge. For instance, piezoresistive sensors frequently demonstrate varying gauge factors across different strain ranges due to nonlinear and heterogeneous deformation. Meanwhile, capacitive sensors employing microstructured dielectrics also encounter similar challenges. For practical applications, it is highly advantageous to develop sensitive pressure sensors that exhibit wide linear operating ranges, as their responses are more accurate and reliable within these ranges.

Response time is a critical factor in assessing the dynamic performance of sensors. For pressure sensing, the response time of a pressure sensor refers to the duration it takes for the sensor to complete its response process, from the application of pressure to the generation of a stable signal output. Both advancements in instant-response displays and real-time healthcare monitoring systems necessitate reducing response times. Consequently, numerous devices capable of quick responses (response time <100 ms) have been developed. In the other hand for gas sensing, response time is defined as the interval during which the analytical signal reaches a specified percentage (*e.g.*, 90-95%) of its ultimate value following an abrupt change in the input signal. In general, the response time heavily relies on the device's design, the components responsible for recognition, and the analytical techniques employed to produce the signal.

Reproducibility refers to the capability of an analytical device to generate consistent signal outputs when experimental conditions are modified. Reproducibility can be evaluated by examining how consistent the calibration data is when obtained from different devices under the same test protocols and using identical equipment. In sensors incorporating 2DMs, the reproducibility between devices depends largely on the precision of nanomaterial synthesis and its effective integration into functional devices. For example, CVD has proven effective for large-scale production of graphene or MoS_2, providing precise control over the structure of the synthesized materials. Advancements in synthetic methods enabling direct deposition of 2DMs onto sensing devices can enhance and ensure signal reproducibility in analytical measurements.

Selectivity is another crucial parameter especially for gas sensing. Selectivity refers to the ability of an analytical method to differentiate and quantify specific analytes of interest in complex mixtures, without being affected by interference from other components. The selectivity of analytical devices is typically achieved through the

incorporation of recognition elements that can selectively interact with a specific analyte of interest. Depending on the sensor type, selectivity can be enhanced by adjusting experimental parameters such as temperature or pressure, or by employing alternative materials that, for instance, can exclude interferents based on their size or binding affinity. Achieving selectivity in complex mixtures of interferents is a fundamental objective of sensor research and a motivating factor in the exploration of new materials that offer novel selective host-guest surface chemistries.

In summary, the specific parameters required for the sensing system are mainly determined by its intended application. For example, sensors designed for continuous sample or pressure monitoring must demonstrate excellent sensitivity, respond time LOD and linearity over extended periods.

1. 6 Functionalization of two-dimensional materials

The physicochemical properties of 2DMs can be systematically tailored to fully exploit or broaden their applications across various disciplines. It is widely recognized that surface modification of a material can be employed to alter its properties. This is particularly true for 2DMs due to their exceptionally high surface to volume ratio. The ubiquitous surface nature of 2DMs, particularly MXenes, renders them highly sensitive to environment and external stimuli. This sensitivity creates opportunities to modify, control, and fine-tune their physical and chemical properties. In general, functionalization involves imparting new functions or capabilities to a material that were originally absent. In this context, functionalization is understood as the process of enhancing a material's properties or introducing new functionalities in response to external stimuli. Many researchers suggest hybrid materials as a solution for addressing gas sensing requirements under conditions of low power and ambient temperatures. Combining the strengths of both domains is expected to yield a synergistic effect, leveraging the exceptional conductivity of 2D carbon materials along with the selectivity of nanomaterials derived from metals, semiconductors, or organic compounds. All these materials exhibit varying adsorption behaviors towards specific gases. A common requirement is that changes in their electrical properties must alter the conductivity of the composite material.

Spatial positioning is a crucial factor in the functionalization of 2DMs, as it dictates the specific reaction mechanisms between functional groups and the material's surface sites. The enhancement of edge sites on 2DMs has been extensively

investigated[265, 266]. In particular, in the case of chemically stable 2DMs such as graphene and *h*-BN, the edges have a tendency to spontaneously bond with other molecules or atoms[267, 268]. For instance, techniques such as sonication in water or ball milling in NaOH solution are employed to introduce hydroxyl groups (–OH) for the functionalization of *h*-BN[269]. Same method can be used for functionalization with *i.e.* NH_2 group and halogens[270, 271]. Moreover, even in 2DMs with high crystallinity, the presence of vacancy defects is unavoidable. Thus, molecules containing thiol groups (–SH) are a prominent example of functional groups that can bond effectively with sulfur vacancies in MoS_2, provided that the geometry of the molecule allows for favorable chemical interactions without disrupting bonding[272-274]. Moreover, healing or passivation of defects can also be achieved through vacancy functionalization. For instance, thiol functionalization can repair sulfur vacancies on the MoS_2 surface by forming bonds between the sulfur atoms of the thiol groups and the vacancies, subsequently breaking the sulfur-carbon bonds[275].

In general, hybrid materials typically comprise two or more components: one that offers good conductivity and others that exhibit selective interactions with specific gases. On a graphene surface, the adsorbed nanomaterial acts as a mediator, gathering information about gas composition through specific interactions with its components. This can amplify the signal due to the high surface-to-mass ratio, which creates more binding sites. Specifically for carbon materials like graphene derivatives, these functionalities can be covalently attached to the crystalline structure through nucleophilic or electrophilic substitution, condensation, or addition reactions[276]. Despite its significant potential for applications, it is important to note that graphene itself lacks a band gap and is inert to reactions, thereby limiting its competitiveness in the fields of semiconductors and sensors. This is one of the primary reasons for the substantial increase in research projects focused on functionalizing graphene. These projects involve reactions of graphene (and its derivatives) with organic and inorganic molecules, chemical modification of the extensive graphene surface, and comprehensive exploration of various covalent and noncovalent interactions with graphene[277-280]. The functionalization of pristine graphene sheets with organic functional groups has been developed for various purposes. The primary objective is to improve the dispersibility of graphene in common organic solvents, which is generally achieved by attaching specific organic groups. Dispersing graphene sheets in organic solvents is a critical step towards

creating nanocomposite materials incorporating graphene. Moreover, organic functional groups like chromophores introduce new properties that can be integrated with graphene's existing properties, such as conductivity. Typically, when organic molecules are covalently bonded to the graphene surface, the disruption of its extended aromatic structure allows for the modification of its electronic properties. Furthermore, creating a band gap through chemical doping is an effective approach for enabling the use of graphene in nanoelectronic devices[281]. The organic covalent functionalization of graphene can be achieved through two primary methods such as: forming covalent bonds between free radicals or dienophiles and the C=C bonds of pristine graphene and forming covalent bonds between OFGs and the oxygen groups present in GO. The covalent functionalization of graphene materials can be classified according to reaction type, including single-atom reactions (such as oxidation, hydrogenation, and halogenation), radical reactions, and cycloaddition reactions[282]. Furthermore, polymers are commonly used materials that are often covalently bonded to graphene. Oxidation of graphene leads to the formation of graphene oxide, a process that has been described in the Hummers method and its modifications. The most basic atom that can be attached to a carbon compound is hydrogen, making hydrogenation a fundamental example of covalent functionalization. The hydrogen atom that is covalently bonded modifies the hybridization of the attached carbon atom from sp^2 to sp^3, transforming zero-bandgap graphene into hydrogenated graphene with a bandgap of 3.5 eV[283]. Similar to hydrogenation, halogenated graphene exhibits a wider bandgap and lower charge mobility and conductivity compared to pristine graphene. During the halogenation process, halogen atoms are covalently attached to graphene using methods such as halogen-plasma treatment, photochemical reactions, or reagents containing halogens (like XeF_2)[284]. Furthermore, notwithstanding covalent halogenation, chlorination resulted in an increase in charge carrier density and a decrease in the resistance of the graphene sheets[285]. Cycloaddition is primarily conducted through the Diels-Alder reaction, where the hybridization of a pair of carbon atoms shifts from sp^2 to sp^3, forming a new ring by combining with an electron-rich organic diene. This process results in an increased band-gap of the graphene[286, 287]. Moreover, aryl radicals generated through the reduction of diazonium salts can engage in addition reactions on the surface of the graphene structure. Aryl diazonium cations accept electrons from the graphene and release nitrogen gas, resulting in the formation of an aryl radical that subsequently reacts with the aromatic rings in graphene. This method of modification can achieve a high degree of

functionalization, and the resulting products are stable under various conditions[288, 289]. Despite numerous methods for covalent functionalizing graphene, the absence of functional groups in its structure remains a significant limitation in terms of modification. However, graphene can be modified in a non-covalent manner. Non-covalent attachment of various molecules to graphene has been extensively studied. The π-π stacking interaction is the most common and effective method for non-covalent modification. Alternative methods of non-covalent modification of graphene include Van der Waals forces, as well as hydrogen and ionic bonds, along with coordination bonds. However, due to its chemical composition, GO and rGO have significant advantages over graphene in terms of functionalization.

GO can be produced on a large scale and its surface is exposed to various oxygen containing functional groups (*e.g.*, epoxide, hydroxide, and carbonyl). These groups can bind metal ions through chelation mechanisms and electrostatic interactions, serving as anchoring points for additional chemical functionalizations[290-293]. An optimal strategy for chemically modifying graphene oxide would employ orthogonal reactions that selectively target specific functional groups, enabling the modification of one site while preserving others. However, demonstrating the selectivity of these chemical transformations remains challenging. The epoxy groups can undergo modification *via* ring-opening reactions under diverse conditions. A probable mechanism for this reaction entails nucleophilic attack at the α-carbon, *i.e.,* by the amine. However, amine groups can undergo reaction with carboxylic acid groups of graphene oxide through the amidation process. Additionally, besides the carboxylic acids decorating the edges of graphene oxide, the platelets also contain chemically reactive epoxy groups on their basal planes. This draws inspiration from numerous examples of cross-linking reactions observed in synthetic polymer chemistry. For example, poly(allylamine), a main-chain aliphatic polymer with pendant amine groups, was utilized to cross-link graphene oxide platelets by stitching together the epoxy groups of two or more platelets[294]. In the other hand, a diverse set of reactions utilizing carboxylic acids has been developed in the field of small molecule organic chemistry, and many of these methodologies have been successfully adapted for use with GO. The coupling reactions often necessitate the activation of the acid group using 1-ethyl-3-(3-dimethylaminopropyl)-carbodiimide (EDC)[295], thionyl chloride $SOCl_2$[296] and N,N'-dicyclohexylcarbodiimide (DCC)[297]. After activating the acid group, subsequent addition of nucleophilic species such as amines or hydroxyls

results in the formation of covalently attached functional groups on GO platelets through the formation of amides or esters. Besides activating and amidating/esterifying the carboxyl groups on GO, it is also feasible to convert them into other reactive groups. For example, to generate amide and carbamate ester groups from the carboxylic acid and hydroxyl groups, respectively, of graphene oxide platelets, one can achieve this through the addition of isocyanate derivatives bearing various aliphatic and aromatic groups[298]. Moreover, various material composites incorporate both a p-type semiconductor (*e.g.,* rGO) and an n-type semiconductor. When these composites interface, they create p–n junctions, which are highly responsive to the adsorption of gas molecules and significantly influence the overall electrical resistance of the sensor substrate[299, 300]. Furthermore, GO can also engage in non-covalent interactions such as π–π stacking, cation-π interactions or van der Waals forces with the sp^2 networks that remain unoxidized or are not involved in hydrogen bonding[301]. In case of rGO, functionalization proceeds similarly to that of GO due to the similar chemical composition of the remaining OFGs. In the literature, there are numerous examples of hybrids based on GO and rGO with various molecules employed, *i.e.,* tin dioxide[302, 303], Cu, Pt and Au nanoparticles[304-306], zinc oxide[307, 308], polypyrrole[309], poly(methyl methacrylate)[310], poly(3,4-ethylenedioxy-thiophene)[311], polyaniline[312], MoS_2[313] and MXene[314] which found their application in sensing device.

In summary, graphene materials and their composites provide a promising approach for creating sensor devices capable of detecting various gases and pressure. These sensors based on graphene demonstrated superior performance relative to all other sensors in aspects such as sensitivity, detection limit, and reversibility. Moreover, these sensors outperform others due to their low energy consumption and capability to function at room temperature. Graphene's distinctive properties, including its high surface area, mechanical strength, and superior electrical and thermal tolerance, make it an ideal candidate for developing gas sensors that can function in harsh environments. Furthermore, functionalization of graphene and its derivatives open new possibilities for manipulation of band gap and detection limit. Despite numerous advantages, several challenges must be overcome to commercially fabricate graphene sensors. Thus, utilization of GO and rGO presents a viable solution to this issue in sensor device application.

1. 7 Active film formation - techniques of deposition of materials for application in sensing

With the advancement of smart and digital healthcare, wearable sensors are gaining significant interest for their portability and ability to provide real-time monitoring. Notably, gas sensors, capable of detecting gas markers from the human body as well as hazardous gases from the environment, are attracting significant attention. However, conventional fabrication techniques such as lithography and CVD are often incompatible with flexible substrates because these substrates cannot withstand the harsh conditions required during fabrication, such as high temperatures. Therefore, there is a critical need for summarizing the available fabrication techniques for wearable pressure and gas sensors, given the limitations posed by conventional methods. There are few fabrication techniques with promising outcomes such as: coating, printing, spinning, dry transferring and Layer-by-Layer (LbL) deposition. The schematic diagram illustrating representative fabrication techniques for sensors is presented on Figure 10.

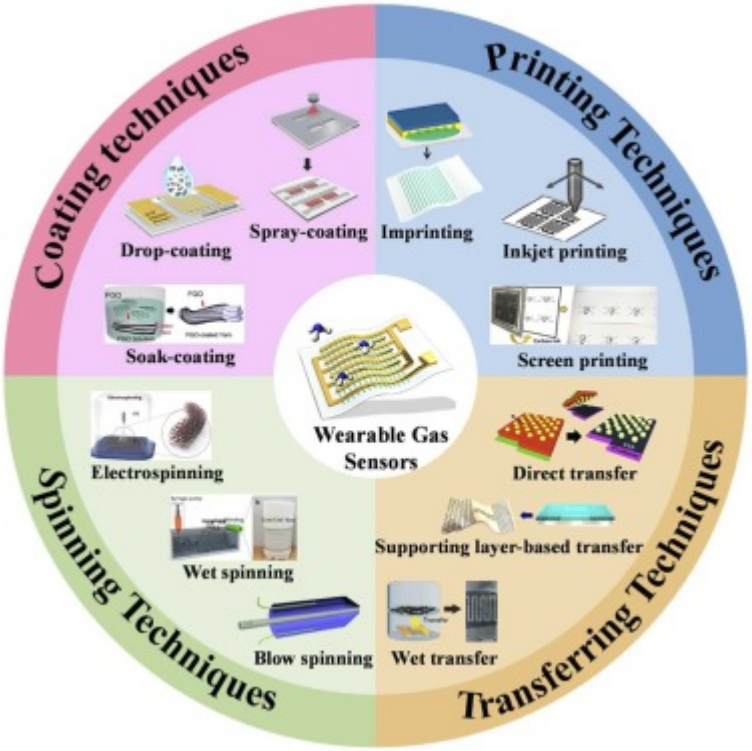

Fig. 10 *The schematic diagram illustrating representative fabrication techniques for sensors[315].*

Lithography is a physical top-down approach that employs photons, electrons, and ions to produce nanostructures[316]. It has been a preferred method for creating patterned nanostructures by transferring a mask pattern onto a substrate. The most prevalent

technique is optical lithography, which utilizes ultraviolet light to transfer a specified pattern from a mask onto a light-sensitive material called photoresist, applied to the semiconductor substrate. The substrate undergoes chemical changes when exposed to a particular wavelength of light through the mask, resulting in the creation of a pattern. This pattern is then typically transferred to the substrate through etching[317]. However, this method is not sufficient for large-scale production of advanced sensors.

A coating technique is a straightforward, convenient, and highly efficient method used to apply soluble sensitive materials onto the surface of a substrate in the form of thin films[318, 319]. However, the process of preparation using this technique does not require expensive equipment or harsh fabrication conditions, making it suitable for most flexible substrates particularly when there are no strict requirements on the boundary range of the sensitive material film. Therefore, this method is widely employed in the fabrication of sensors device. There are also few types of coating such as: spray, spin, soak, drop, dip coating and others. Spray coating method is an economical and effective approach to prepare uniform sensitive films from both hydrophobic and hydrophilic sensing materials. This method offers the flexibility to adjust parameters for depositing various types of material dispersions[320-322]. Although, masking procedures are essential to ensure precise control over the deposition process, thereby safeguarding specific regions from unintended coating and ensuring the integrity of the final film's structural characteristics. Despite this limitation the spray coating method can utilize to produce pressure and humidity sensor based on GO[323]. In the other hand, spin coating entails depositing materials onto a rotating surface, where centrifugal force spreads them evenly, ensuring consistent film thickness and quality upon drying. In this process, only a portion of the soluble material remains on the substrate to form a film, while the majority is ejected off due to centrifugal force[324]. However, this method requires solubility or dispersibility of active material in solvent which is huge limitation in case of 2DMs. Dip coating is a method used to prepare thin films by immersing substrates in a solution containing the coating material. The substrate is then withdrawn from the solution at a controlled rate, facilitating the evaporation of the solvent and resulting in the deposition of a uniform film on the substrate surface. This technique is valued for its versatility and cost-effectiveness in thin film fabrication processes[325, 326]. By this technique it is possible to produce, *i.e.,* humidity sensor which exhibits the most significant sensing response to humidity within the range of 30% to 90% relative humidity (RH) based on

GO[327]. In comparison with the coating methods mentioned above, this technique has a broader range of application fields, including both regular and irregularly shaped substrates. Drop coating is one of the simplest methods for preparing sensors based on soluble sensitive materials. In this technique the sensitive active material is deposited onto a substrate by dripping and then dried either at room temperature or under controlled heating conditions. This procedure ultimately affixes the sensitive material onto the substrate in the form of a film. However, it is challenging to precisely control the thickness and the boundaries of sensitive material films prepared using the drop coating method. Despite many disadvantages, coating methods are still widely utilized in the production of both pressure and humidity sensors.

Transfer techniques are of significant importance in the manufacturing of sensors, as they enable the application of traditional manufacturing processes, which are typically restricted to rigid substrates. The transfer method can be divided by dry and wet transfer. The dry transfer exploits the varying adhesion properties between the film layer and substrate to move the film from the original substrate to the desired target substrate. Successful transfer requires that the adhesion strength at the recipient substrate and device interface exceeds that at the donor substrate and device interface, which can be accomplished through surface chemical modification or hydrophilic treatment. Because this method does not involve etching agents or solvents during the transfer process, it is gaining popularity in the industrial fabrication of flexible devices based on 2DMs. Unfortunately, this method has significant limitations due to differences in polarity between the deposited material and certain substrates, rendering it inefficient for sensor production. In the other hand, wet transfer involves transferring individual sensitive layers onto various substrates using solution-based media. During the wet transfer process, the sensitive film initially deposited on the donor substrate is immersed in a solvent, facilitating its removal and subsequent deposition onto the receiving substrate. However, due to the low solubility and limited interaction with solvents of 2DMs, the wet transfer method is not as popular as dry transfer in sensing device applications.

An alternative approach for fabricating efficient miniaturized electrochemical devices involves leveraging the versatility and modularity of the LbL method to construct hierarchical nanomaterials[328, 329]. The LbL method was first introduced by Decher *et al.* in the early 1990s as a technique for fabricating nanostructured materials[329]. After first utilization of LbL, it has undergone rapid development, and in its current state, it

enables the fabrication of nanomaterials by combining various mutually interacting species. These species can be assembled using a wide range of interactions, such as electrostatics, charge transfer interactions, coordination interactions, host-guest interactions, π-π interactions, hydrogen bonding and others[330]. In general, LbL technique is a straightforward and economical approach for producing nanostructured layered materials. The method employed for this purpose involves sequentially dipping a substrate into solutions containing materials with complementary functionalities. Therefore, it is feasible to produce layered materials under gentle conditions on substrates of various types. Thus, the LbL represents a precise solution-based deposition technique for creating thin films, membranes, and 2DMs based sensors. However, the widespread use of dip coating deposition, particularly on an industrial scale, is hindered by the lengthy time needed to achieve films of optimal quality and the large amount of material necessary for assembling each individual layer, leading to significant waste during the fabrication process. Despite these drawbacks, the versatility and simplicity of dip coating deposition have driven its evolution as a critical method for assembling LbL materials. Currently, various automated dipping devices facilitate the fabrication of LbL materials, significantly reducing the time required for the assembly process. The LbL method has proven to be highly efficient for electrochemical devices based on 2DMs, as evidenced by numerous examples in the literature[331-335].

Chapter 2 Characterization methods

This chapter will discuss the various characterization techniques employed in this study to structurally analyze graphene and GO-based hybrid materials. Due to its atomic thinness and typically microscopic size, graphene is challenging to detect. The capacity to identify and characterize graphene-based materials is crucial for its discovery and ongoing success. For practical uses and quality assurance, it is essential to determine the number of layers, structure, and electronic quality. Thankfully, a variety of methods, ranging from subjective observation to precise spectroscopic analysis, each provide unique benefits. Often, multiple complementary techniques are employed simultaneously to achieve thorough and reliable characterization.

2.1 Morphological characterization

2.1.1 Scanning Electron Microscopy

Scanning electron microscopy (SEM) has been utilized by numerous researchers as the approach for morphologically characterizing graphene-based materials due to the simplicity in specimen preparation. In this method a tungsten filament (cathode) releases thermionic electrons that are accelerated across a potential difference of 1.0 to 30.0 kV towards the anode. Under a vacuum of less than 10^{-5} Pa, the electron beam is directed towards the sample using condenser and objective electromagnetic lenses. During the scan, secondary and back-scattered electrons, along with Auger electrons and X-rays, are emitted. These emissions interact with detectors, which send signals to the software that converts them into grayscale images. Secondary electrons are primarily outer shell electrons generated through inelastic scattering, whereas backscattered electrons arise from significant-angle elastic scattering interactions between the incident electrons and the sample. Usually, Energy Dispersive X-ray Spectroscopy (EDS) complements SEM by providing qualitative and semi-quantitative results. Because of, detectors for secondary and backscattered electrons produce visual images of the specimen, whereas the X-ray spectrometer reveals details about its chemical composition. Together, these techniques offer fundamental insights into the material composition of scanned specimens. In general, similarly to how an electron beam scans line by line in a cathode ray tube, in a vacuumed microscope column, the focused electron beam scans across the specimen's surface. During this process, interactions between the beam and the sample

generate signals that are electronically detected and amplified using appropriate equipment. The schematic illustration of SEM is presented on Figure 11.

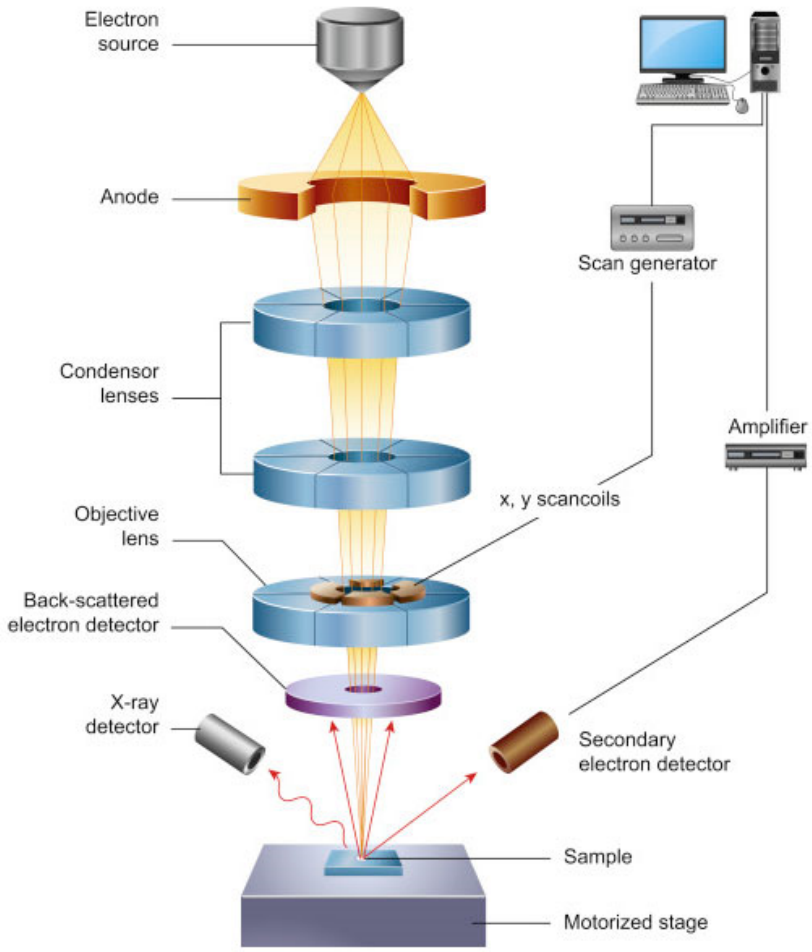

Fig. 11 *Schematic illustration of SEM[336].*

Typically, the resolution of the SEM image depends on both the size of the electron probe focused onto the sample surface and the interaction of the primary electrons with the sample. The maximum resolution achievable in SEM is influenced by several factors, primarily the size of the electron beam spot and the interaction volume of the beam with the sample. Some advanced SEMs can resolve features below 1 nanometer in size. These capabilities make SEMs valuable tools for imaging and analyzing the surface morphology and composition of materials at very high magnifications and resolutions, albeit not at the atomic scale. Furthermore, samples that are not conductive need to undergo surface pretreatment. Typically, a specimen is coated with a thin layer of gold or carbon using a process called sputter coating. This involves placing the specimen in a chamber with Argon gas at ultra-high vacuum and a target made of gold or carbon. A high voltage

potential difference ionizes the Argon gas, and the resulting ions are accelerated towards the target. As they strike the target, atoms are ejected and travel to coat the specimen surface, enhancing its visibility under detailed visualization. Typical graphene flakes exhibit a shiny, layered structure, whereas GO shows wrinkles resulting from the oxidation process[337, 338]. SEM is extensively employed to study the surface structure of graphene and GO samples synthesized using various methods display distinct morphologies when observed under SEM imaging. In general, SEM images of GO typically show a layered or lamellar structure with diverse surface formations[339]. On Figure 12 are shown examples of SEM images for graphene and GO.

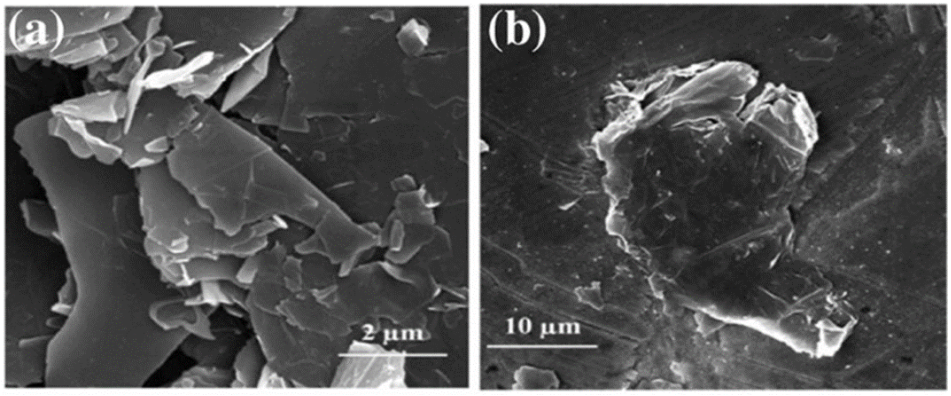

Fig. 12 *SEM imagines of a) graphene and b) GO[340, 341].*

Alternatively, GO often forms densely packed nanoplatelets with OFGs that contribute to high surface roughness. However, studies employing SEM techniques must be conducted cautiously because mishandling can lead to inaccurate data and misinterpretation of the results obtained.

In this thesis, SEM was employed to observe morphological changes following functionalization reactions in hybrid materials and to track the progress of GO reduction.

2.2 Qualitative characterization

2.2.1 X-ray photoelectron spectroscopy

X-ray photoelectron spectroscopy (XPS) is a widely utilized quantitative spectroscopic surface analysis technique that is instrumental in determining the elemental composition of a material and providing information about chemical bonding. In general, XPS is a surface-sensitive analytical technique where X-rays are directed onto the surface of a material, and the kinetic energy of the emitted electrons is measured. Two key

attributes of XPS that enhance its analytical prowess are its surface sensitivity and its capability to provide chemical state information about elements within the sample. XPS can detect all elements except hydrogen and helium, and it has been employed extensively to analyze the surfaces of a wide range of materials, including plastics, textiles, soils, and semiconductors. XPS is rooted in the photoelectric effect, initially discovered by Heinrich Hertz in 1887. Hertz observed that electrons were ejected from surfaces when illuminated with light. Albert Einstein provided a formal explanation of this phenomenon in 1905, earning the Nobel Prize in Physics in 1921 for his work. The application of photoemission with x-ray irradiation was first observed by Robinson and Rawlinson in 1914. Steinhardt and Serfass presented the first practical use of photoemission as an analytical technique in 1951[342]. However, the significant advancements that transformed X-ray photoelectron spectroscopy into the technique we recognize today were primarily accomplished by Kai Siegbahn during the 1950s and 1960s. Siegbahn's pioneering work laid the foundation for high-resolution electron spectroscopy, originally known as electron spectroscopy for chemical analysis (ESCA). His contributions were so profound that he was awarded the Nobel Prize in Physics in 1981 for his achievements in this field.

In XPS, the sample is exposed to soft X-rays (typically energies below approximately 6 keV), and then the kinetic energy of the emitted electrons is analyzed. The emitted photoelectron results from the complete transfer of the X-ray energy to a core level electron. This phenomenon can be described by follow Equation 6:

$$h\nu = BE + KE + \Phi_{spec} \qquad Eq.\ 6$$

where, hν is energy of X-ray, *BE* is the binding energy of the electron, *KE* is the kinetic energy of the electron that is emitted and Φ_{spec} is constant which represents spectrometer work function. To find the binding energy of an electron, Equation 6 can be rearranged as follows (Equation 7):

$$BE = h\nu - KE - \Phi_{spec} \qquad Eq.\ 7$$

It's important to note that the binding energy of the photoelectron is measured relative to the sample's Fermi level, not the vacuum level. This is why Φ_{spec} is taken into account. In XPS peaks are labeled according to the element and orbital from which the electrons were ejected. For instance, O 1s refers to electrons emitted from the 1s orbital of an oxygen atom. Any electron with a binding energy lower than the energy of the X-ray source can be emitted from the sample and detected using the XPS technique. The binding

energy of an electron is an intrinsic property of the material and remains constant regardless of the x-ray source used to eject it. However, when experiments are conducted using different x-ray sources, the kinetic energy of the emitted photoelectrons may vary, as described in the earlier equations. The schematic representation of an XPS system is illustrated on Figure 13.

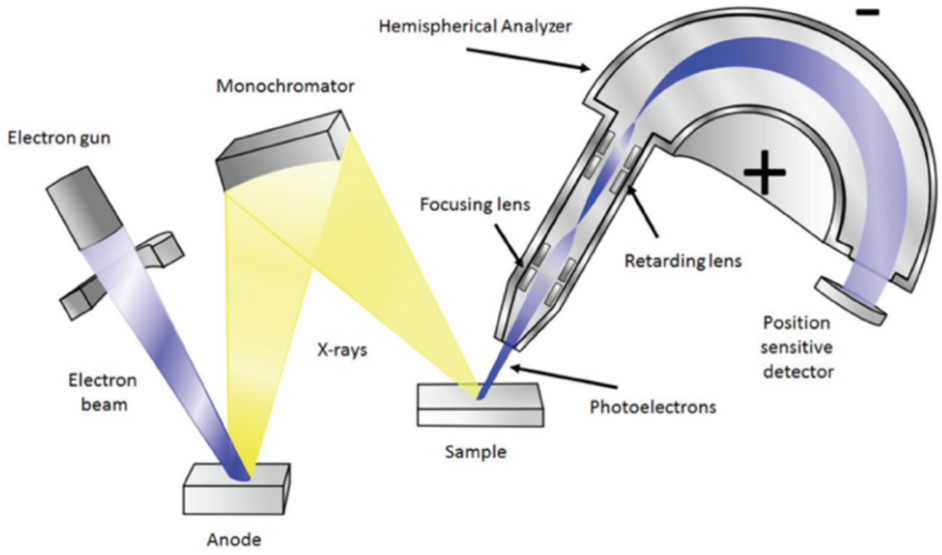

Fig. 13 *Schematic representation of an XPS system[343].*

In general, the *BE* of an electron is dependent on the element from which it is emitted, particularly the specific orbital, as well as the chemical environment of the atom. By measuring the *KE* of the electrons that reach the detector, the *BE* of the electrons can be calculated. This allows for the identification of the various elements present on the surface of the sample and their chemical states. Consequently, a comprehensive analysis of the surface composition of the examined area will be achieved. Moreover, XPS can also be employed to detect contaminants in the sample. While X-rays can penetrate the material to several hundred nanometers, the emitted photoelectrons originate from only a few nanometers of the surface layer. This makes the technique particularly relevant for analyzing nanometer thin 2DMs and functionalized 2DMs.

XPS is widely recognized and highly effective techniques for analyzing the chemical surface composition of graphene and its derivatives, particularly in terms of carbon content and oxygen, and the binding energy (eV) of functional groups[344]. Determining the carbon and oxygen content through elemental analysis is a meticulous process, particularly challenging due to the difficulty in completely removing moisture

from a GO sample. The C 1s spectrum of GO is typically analyzed by fitting it with five components: aromatic rings and hydrogenated carbons (C=C/C–C, C–H, 284.6–284.9 eV), hydroxyl groups (C–OH, 285.9 eV), epoxy groups (C–O–C, 286.9 eV), carbonyl groups (C=O, 288.2 eV), and carboxyl groups (C=O(OH), 289.3 eV). The hump observed at 290.6 eV is attributed to a π–π* shake-up satellite[345, 346]. On Figure 14 is presented example of XPS survey spectrum obtained for GO and rGO and its hybrid by various amines. On Figure 15 is illustrated example of C 1s XPS spectra for the same set of samples.

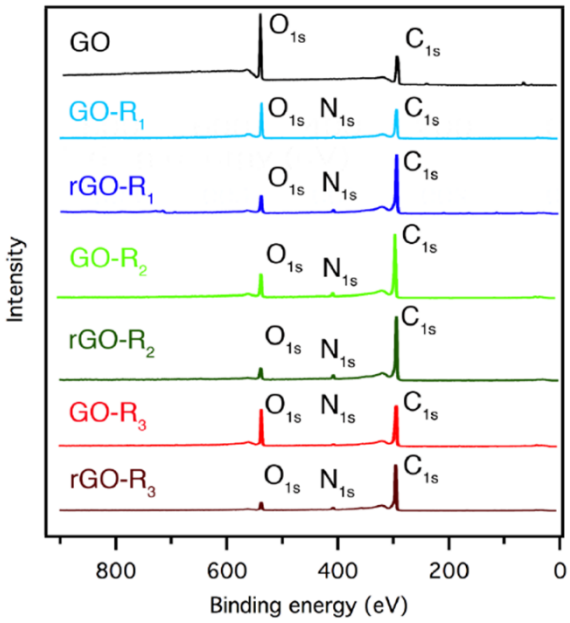

Fig. 14 *XPS spectra of GO, GO-R1-3, rGO-R1-3[117].*

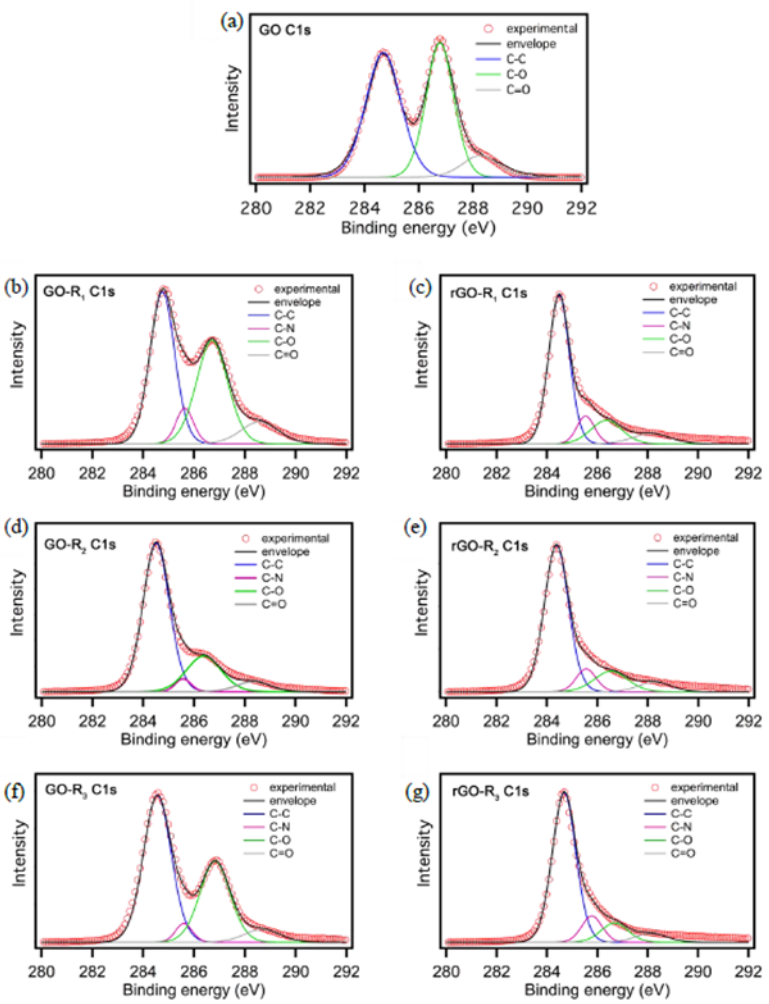

Fig. 15 *C1s XPS spectra of (a) GO; (b), (d), (f), GO-R1-3; (c), (e), (g), rGO-R1-3[117].*

In this dissertation, XPS analysis was employed to assess the chemical composition of the graphene-based materials and to monitor post-reaction changes and evaluate the degree of reduction in graphene oxide samples.

2.2.2 Raman spectroscopy

Raman spectroscopy (RS) is a non-destructive chemical analysis method that offers comprehensive information about chemical structure, phase and polymorphism, crystallinity, and molecular interactions. It relies on the interaction of light with the chemical bonds present within a material. RS is a method based on the phenomenon of light scattering, where molecules scatter incident light from a high-intensity laser source. Most of the scattered light retains the same wavelength (or color) as the laser source and does not convey significant information which is referred to as Rayleigh scattering. However, a minute fraction of the incident light (typically 0.0000001%) is scattered at

wavelengths (or colors) different from the laser source, and these wavelengths are characteristic of the chemical structure of the analyte. This phenomenon is known as Raman scattering. A Raman spectrum displays several peaks that indicate the intensity and wavelength position of the Raman scattered light. Each peak corresponds to specific molecular bond vibrations, encompassing individual bonds such as C-C, C=C, N-O, C-H, and collective vibrations like benzene ring breathing modes, polymer chain vibrations, lattice modes, and others. Moreover, RS investigates the chemical structure of a material and provides insights into chemical structure, phase and polymorphism, contamination and impurity. A Raman spectrum typically serves as a unique chemical fingerprint for a specific molecule or material, allowing for rapid identification of the material or differentiation from others. Raman spectral libraries are frequently utilized to identify materials based on their Raman spectra. These libraries contain thousands of spectra that are quickly searched to find a match with the spectrum of the sample being analyzed. Moreover, when combined with mapping (or imaging) Raman systems, it becomes feasible to produce images that are based on the Raman spectrum of the sample. These images illustrate the distribution of individual chemical components, polymorphs, and phases, as well as variations in crystallinity. This technique is typically employed for the analysis of molecules. However, since 2006, when Ferrari *et al.* first utilized Raman characterization for graphene, it has been extensively used to evaluate the quality and structural integrity of exfoliated 2DMs, including determining the number of layers in nanosheets. Thus, RS has been widely employed to investigate the extent of disorder in graphite-like materials.

In general, RS is extensively utilized for characterizing carbon-based materials due to the presence of conjugated and double carbon-carbon bonds, which result in high Raman intensities[347]. In the case of the graphene, RS provides valuable information such as the number of graphene layers and the presence of defects in the sheets. Furthermore, RS is a promising tool for characterizing the reduction of GO to rGO[348]. The notable structural changes that occur during the oxidation of pristine graphite to GO and subsequently the reduction of GO to rGO are evident in the Raman spectra[86]. In the Raman spectrum of pristine graphite exhibits a prominent G peak at 1581 cm^{-1}, which corresponds to the first-order scattering of the E_{2g} mode[349]. In the other hand, in GO, the G band exhibits broadening and shifts to 1594 cm^{-1}, accompanied by the appearance of a D band at 1363 cm^{-1}. These changes are attributed to the reduction in size of the in

plane sp^2 domains. The Raman spectrum of rGO shows both G and D bands (at 1584 and 1352 cm^{-1}, respectively), but with a higher D/G intensity ratio in comparison with GO. This indicates a decrease in the average size of the sp^2 domains following the reduction of GO. Moreover, this phenomenon can be attributed to the formation of numerous smaller graphitic domains during reduction, compared to the larger domains present in GO before reduction. On Figure 16 is presented of Raman spectra obtained for graphene, GO and rGO form literature.

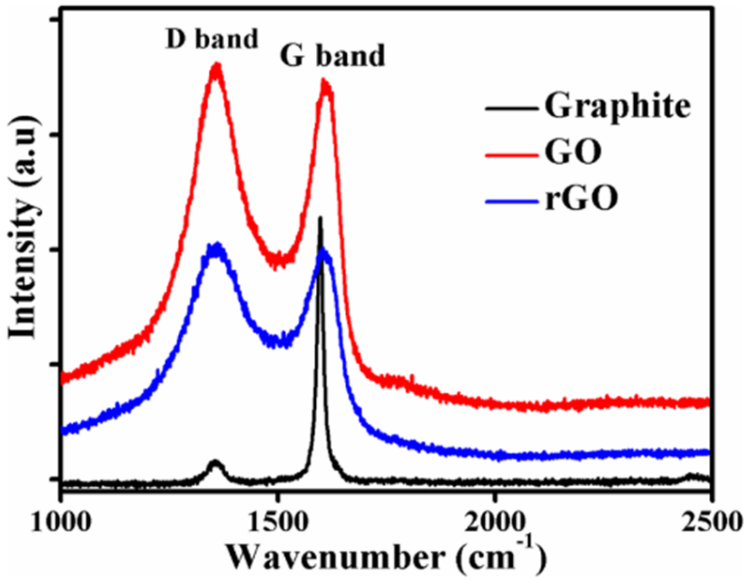

Fig. 16 *Raman spectra of graphite, GO and rGO[350].*

In this dissertation RS was utilized to follow influence of reducing agents on GO samples during the reduction process. Moreover, RS was employed to determine number of defects in structure and assess quality of obtained materials.

2.2.3 X-ray diffraction

X-ray diffraction (XRD) is a versatile non-destructive analytical method used to examine physical properties such as phase composition, crystal structure, and orientation of powdered materials. It is a widely used technique for determining the composition or crystalline structure of a sample. For larger crystals, such as macromolecules and inorganic compounds, it can be employed to determine the arrangement of atoms within the sample. X-rays, which are highly energetic ionizing radiation, are produced when electrons are scattered and interact with matter. XRD serves as a method for investigating the atomic structure of the specimen[351]. Moreover, XRD analysis utilizes

monochromatic radiation. This specific wavelength of intense X-radiation is generated when electrons from a source (such as a tube filament) eject inner-shell electrons from atoms in a metal target. The immediate filling of the vacancy left by the dislodged electron with another electron from a specific lower energy shell leads to the emission of energy in the form of X-rays at a distinct wavelength. This phenomenon is referred to as characteristic radiation. In XRD, the characteristic radiation known as Kα is generated when K shell electrons are replaced by L shell electrons. The Kα wavelength (λ) is specific to each element and is determined by the atomic number of the target element in the X-ray tube. The most frequently used target is copper, producing Cu Kα radiation with a wavelength of λ = 1.54Å. Other metallic targets and their corresponding radiations include Cr Kα with λ = 2.28Å, Fe Kα with λ = 1.94Å, and Mo Kα with λ = 0.71Å. The atoms act as scattering centers, re-emitting X-rays at the same wavelength as the incident radiation in all directions through coherent scattering. The regular arrangement of atoms causes the scattered X-rays within the crystal to be in first, in phase in specific directions determined by symmetry and atomic spacings, and in second, out of phase in all other directions. The in-phase X-rays constructively interfere, emerging from the crystal as intense, diffracted beams, while the out-of-phase X-rays destructively interfere, resulting in minimal emergence. This systematic interplay of constructive and destructive interference, due to the periodic arrangement of atoms in the crystal, constitutes X-ray diffraction. Moreover, XRD takes place when the radiation is scattered by the atoms in the specimen, which then reemit X-rays at the same wavelength as the incident radiation[352]. A simplified way to intuitively understand the relatively complex phenomenon of XRD is to envision regularly spaced planes of atoms within mineral structures. The distance between a specific set of planes is referred to as d-spacing. Despite being on the scale of Angstroms, d-spacing can be determined with high accuracy using XRD. The principles behind this determination are elegantly articulated by the Bragg Equation 8:

$$n\lambda = 2d \sin \theta \qquad \textit{Eq. 8}$$

where n is an integer, λ is the wavelength of the radiation, d is the d-spacing, and θ is the angle between the planes and the incident X-ray beam. The schematic representation of Bragg law equation is presented on Figure 17.

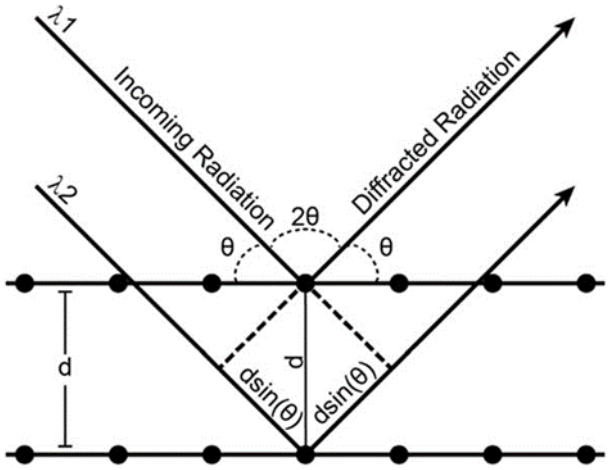

Fig. 17 *Schematic representation of Bragg's law conditions[353].*

Therefore, for a given radiation wavelength and a constant interlayer distance, diffraction will occur at a specific angle.

The powder XRD can provide useful information form solid state materials. In the powder XRD two types of instruments have been employed to carry out diffraction analysis: the XRD powder camera and the X-ray diffractometer. In the powder camera method, diffraction maxima or cones are recorded on cylindrical photographic film placed around the specimen. In contrast, the diffractometer electronically records the intensity of the diffracted beam at precise angles as the specimen is scanned over an angular range. The powder XRD is particularly useful for identifying the structure of two-dimensional materials, especially graphene derivatives that are insoluble. Moreover, this method can be utilized for investigation oxidation level of GO and rGO. For instance, a partially oxidized GO where the peak at $2\theta = 12°$ corresponds to the (001) plane of GO, while the additional peak at $2\theta = 26°$ corresponds to the (002) plane of graphite. Furthermore, the peak at 2θ around 42° corresponds to the (111) plane of GO[338, 354]. Moreover, the functionalization and oxidation level can be examined by the changes in interlayer distance (d form Bragg law). For example, the interlayer distance of graphite is typically around 0.335 nm. In the case of GO, due to the introduction of covalently attached oxygen functional groups, this distance can vary from 0.6 to 1.1 nm. Importantly, this variation is proportional to the degree of oxidation[355-358].

In this dissertation the XRD method was used to investigate the structure changes and number of defects obtained during the reduction process of GO. Moreover, the

interlayer calculations were performed to show post reactions modification in the graphene hybrids structures.

2.2.4 Fourier Transform Infrared Spectroscopy

Fourier Transform Infrared Spectroscopy (FTIR) is a technique used for qualitative characterization. In general, in this method the infrared radiation is employed to cause vibration in molecule. Vibrations can be either symmetric or asymmetric and are classified as stretching (ν) and bending (δ). Stretching vibrations involve a continuous change in distance along the bond axis, whereas bending vibrations involve changes in the angle between two bonds. The four types of bending vibrations are scissoring, rocking, wagging, and twisting. The deformation of the first two occurs "in-plane", while the deformation of the latter two occurs "out-of-plane". The types of vibrations are illustrated on Figure 18.

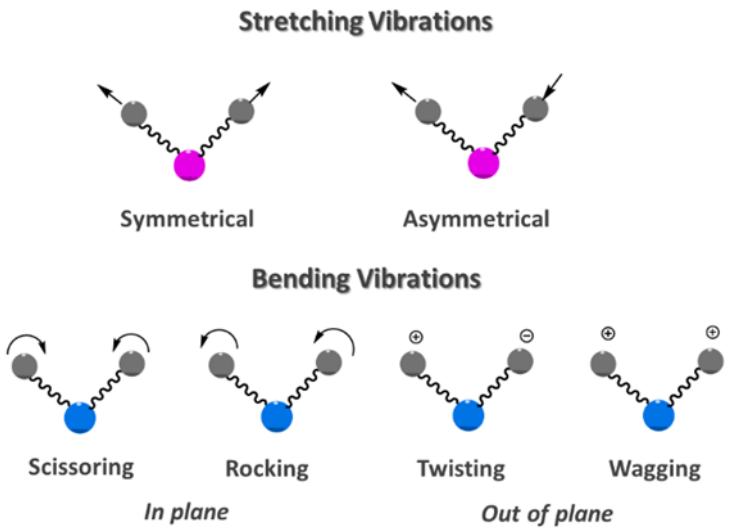

Fig. 18 *Major stretching and bending vibrational modes[359].*

A molecule with more than two atoms can exhibit all the aforementioned types of vibrations. When a molecule absorbs infrared radiation, its dipole moment changes. The intensity of the peaks in the spectrum depends on these changes. The energy difference between the two vibrational states matches the energy of the absorbed radiation's wavelength. It is the infrared region of the electromagnetic spectrum that contains frequencies corresponding to the vibrational frequencies of organic bonds. However, a particular vibration frequency might be shared by more than one molecule, and vibrations with very small differences (less than 1 cm^{-1}) can overlap.

In the FTIR method of analysis, the reflection technique involves the reflection of the IR beam after it interacts with the sample. That technique is given specific names based on the reflection process, such as attenuated total reflectance (ATR). Moreover, that reflectance method function with different optical properties and has the advantage of not requiring the traditional sample preparation needed for transmission FTIR spectroscopy. J. Fahrenfort was the pioneer in demonstrating the effectiveness of the ATR method[360]. In this method of reflection, an infrared beam is directed at an optically dense crystal (like ZnSe, ZnS, Ge, or diamond) with a high refractive index, at a precise angle[361]. The internal reflection produces an evanescent wave that reaches beyond the crystal's surface into the sample placed in contact with it. In regions of the IR spectrum where the sample absorbs energy, the evanescent wave is weakened. The detector registers this attenuated IR beam as an interferogram signal, which is then used to generate an IR spectrum[362]. The primary advantage of ATR sampling stems from its extremely shallow sampling path length and depth of IR beam penetration into the sample, typically ranging from 0.1 to 5 micrometers. Moreover, this allows for sampling of aqueous solutions and solid-state samples with minimal or no need for sample preparation. Thus, ATR is currently the most widely used FTIR sampling technique, especially for graphene-based materials.

The GO comprises graphitic sp^2-hybridized domains surrounded by disordered oxidized domains (sp^3 C-C), whereas the characteristic peak of graphite is typically found at around 1557 cm^{-1} (C=C). After oxidation, hydroxyl groups (O-H) in GO appear around 3400 cm^{-1}, carbonyl groups (C=O) are located at approximately 1730 cm^{-1}, carboxyl groups (C-OH or O=C-OH) are observed at about 1400 cm^{-1}, and the band at approximately 1044 cm^{-1} corresponds to alkoxy groups (C-O)[363-365]. Furthermore, the rGO spectrum exhibited a decreased peak intensity at 3430 cm^{-1} and the absence of peaks at 1785, 1707, and 1105 cm^{-1}, indicating the reduction of GO[346].

In this dissertation FTIR was used to investigate the chemical composition changes during the reduction and functionalization of GO process.

2.3 Instrumental techniques used for characterizations of experimental section

In the Chapter 3,4,5 and 6 the structural data were obtained by XRD with the use of Bruker AXS D8 Advance diffractometer in Bragg-Brentano geometry with CuKα1

radiation (λ = 1.5406 Å). XPS analyses were performed with a Thermo Scientific Kα X-ray Photoelectron Spectrometer system equipped with an Al Kα X-Ray source (photon energy Eph = 1486.6 eV, beam spot size ~100 μm. SEM was performed on an FEI Quanta 250 FEG Scanning Electron Microscope operating at an accelerating voltage of 5 keV incident beam energy. Raman spectra were performed using a Renishaw InVia Reflex system. The spectrograph used a high-resolution grating (2400 grooves cm^{-1}) with additional bandpass filter optics, a confocal microscope, and a 2D-CCD camera. The excitation was carried out using a 532 nm laser excitation beam, with a 100× objective, 0.2 mW maximum power and 1 s acquisition time. FTIR spectra were recorded within the mid-IR range (500–4000 cm^{-1}) using a PerkinElmer spectrometer (spectrum two) equipped with ATR Diamond. The UV-Vis absorption spectra were recorded using a Jasco V-670 UV-Vis spectrophotometer. Thicknesses of the obtained layers were determined by means of an Alpha-step KLATencor Alpha-Step IQ Profilometer. Elemental Analysis (EA) was performed on an Elementar Analyser Vario EL III.

In Chapter 3 for the nuclear magnetic resonance (NMR) spectroscopy ^{1}H and ^{13}C spectra were recorded on a Bruker Avance III HD spectrometer coupled to an 11.7 T wide bore superconducting magnet operating at 500 MHz ^{1}H Larmor frequency and 125.76 MHz ^{13}C Larmor frequency. All spectra were recorded at 298 K stabilized temperature using the magic-angle spinning technique for high-resolution NMR spectroscopy in solid-state using 4 mm zirconia rotors. The spinning frequency was equal to 12 kHz for ^{1}H and ^{13}C nuclei. A speed synchronized spin-echo was included inside the experimental pulse sequences for the ^{1}H and ^{13}C spectra, recoded with direct polarization to get undistorted line shapes and filter out background probe signals. The echo time was kept identical for all ^{1}H and ^{13}C spectra and equal one rotation period. The total echo time was 83 μs, the recycle delay was 5 s, and the number of scans was 512 for proton spectra. Due to the very high conductivity of studied samples, no cross-polarization experiment was possible, owning to non-effective energy transfer. Therefore, the ^{13}C spectra were recorded using the direct polarization method with recycle delay equal to 10 s and 8192 scans, leading to almost 23 hours of data accumulation per spectrum. Pore-size distribution and specific surface area of CrGO samples were investigated by the nitrogen adsorption–desorption isotherm (Autosorb iQ, Quantachrome) using Barrett-Joyner-Halenda (BJH) and Bruanauer-Emmett-Teller (BET) techniques, respectively.

The electrical conductivity measurements were conducted on pelletized samples: 50 mg of GO or CrGO were pressed under 10 tons with a Specac press machine. Films electrical resistivity were measured with Jandel, Model RM3000, limit of detection 107 Ω sq^{-1}. The resistivity (ρ) was obtained by follow Equation 9:

$$\rho = Rs \cdot l \qquad Eq.\ 9$$

Where *Rs* is the sheet resistance and *l* is thickness of the film.

The calculation of the average defect distance (L_D) were obtained by utilizing follow Equation 10:

$$L_D^2 = (1.8 \pm 0.5) \times 10^{-9}\, \lambda_L^4 \left(\frac{I_D}{I_G}\right)^{-1} \qquad Eq.\ 10$$

Where, λ_L is the laser wavelength (nm). Calculation of defect density (n_D) were perfumed using descried Equation 11:

$$n_D = \frac{(1.8 \pm 0.5) \times 10^{22}}{\lambda_L^4} \left(\frac{I_D}{I_G}\right) \qquad Eq.\ 11$$

From the XRD diffractograms the peak position has been calculated using the Bragg's law (Equation 8) presented above.

The crystallite dimension has been derived from the Scherrer formula presented on Equations 12 and 13:

$$L_C = \frac{K\lambda}{\beta_a \cos\theta_a} \qquad Eq.\ 12$$

and

$$L_a = \frac{1.84\,\lambda}{\beta_b \cos\theta_b} \qquad Eq.\ 13$$

Where *Lc* is the crystallite thickness (Å), *La* is the crystallite size (Å), K is the shape factor equal to 0.89, β is the FWHM of the (100) and (002) peaks θ_a and θ_b are the corresponding scattering angles.

The SkinEthic™ Reconstructed Human Epidermis (reconstructed human epidermis (RhE), provided by EpiSkin; Lyon, France), was used for evaluating skin irritation potential of rGOs, following the OECD Test Guideline (TG) No. 439. According to the TG, before being used for the experiments, RhE tissues were checked for quality control criteria (mean optical density, O.D., of 3 negative controls = 1.15 ±

0.05; mean viability of 3 positive controls, 5% SDS = 1.3 ± 0.1%; exposure time inducing 50% viability using Triton X-100 1%, ET50 = 8.7 ± 0.3 h), that were all within the acceptance range. Technical proficiency was assessed testing the ten proficiency substances listed in Annex 3 of the OECD TG 439, as previously reported[366]. In addition, unspecific interaction of rGOs with the MTT readout was preliminary evaluated on "killed" RhE, obtained by freezing treatment at - 80°C for 48 h and none of the materials significantly increased MTT conversion, suggesting no unspecific interactions for rGOs

The assessment of irritation potential of rGOs on SkinEthic™ RhE model was performed following the skin Irritation Test-^{42bis} , in compliance with the OECD TG 439, as previously reported for other graphene-related materials (Fusco *et al*., 2020). Briefly, after being wetted with 10 µL of distilled water, RhE tissues (dimensions of 0.5 cm^2, at day 17) were topically exposed to 16 mg of each rGO (concentration of 32 mg cm^{-2}) in triplicate for 42 min at room temperature (RT). As negative and positive controls, RhE tissues were exposed to phosphate buffered saline (PBS) or 5% w/v sodium dodecyl sulphate (SDS), respectively. After exposure, RhE tissues were washed 25 times with 1 mL PBS and transferred in a 6-well plate with 2 mL growth medium for 42 h at 37 °C and 5% CO_2. Tissue were then transferred in a 24-well plate containing 300 µL of MTT solution (1 mg mL^{-1}) for 3 h at 37 °C and 5% CO_2 and the resulting formazan salts were extracted with isopropanol (1.5 mL per well, for 2 h at RT) and measured at 570 nm using the FLUOstar® Omega microplate reader (BMG LABTECH, Ortenberg, Germany). Tissue viability is reported as % of negative controls and are the mean ± standard error (SD) of three independent experiments.

Moreover, after 42 minutes of exposure to rGO or positive control followed by 42 hours of post-incubation time, culture media were collected and stored at -80 °C. Interleukin (IL)-1α was quantified using a specific sandwich ELISA kit from Diaclone (Tema Ricerca, Milan, Italy) following the producer's instructions. Results are expressed as pg/mL of IL-1α released by the tissues in the growth medium and are the mean ± SD of three independent experiments.

Furthermore, for skin irritation (OECD TG 439), the results are expressed as % of tissue viability with respect to negative controls and are the mean ± SD of three independent experiments. As a threshold given by OECD TG 439, viability ≤ 50% defines

an irritant material. Statistical analysis was performed by a one-way ANOVA followed by Bonferroni's post-test (GraphPad Prism version 8.00) and statistical significance was considered for $p < 0.05$.

In Chapter 4 the specific surface area was measured using a Micromeritics ASAP 2050 surface area and porosity analyzer. Before the Brunauer–Emmett–Teller (BET) measurements, the samples were outgassed for 12 hours at 95 °C. Adsorption isotherms were calculated for nitrogen adsorption at 77 K and a pressure up to 1 bar. For ssNMR All experiments were performed at room temperature on an AVANCE 500 MHz wide bore spectrometer (Bruker™) operating at a frequency of 500.12 MHz for ^{1}H NMR and 188.5 MHz for ^{13}C NMR. As GO is generally barely protonated the classical cross-polarization magic angle spinning (CP/MAS) proves ineffective in obtaining ^{13}C quantitatively. Then a direct polarization with magic angle spinning (DP/MAS) pulse scheme was preferred by using a speed synchronized spin echo sequence with proton decoupling during acquisition. The latter allows us to obtain undistorted line shapes and filter out background probe signals, giving integrable spectra providing recycling delays that fulfill quantitative rules, *i.e.* equal to *ca.* 3 to 5 times that of the longitudinal relaxation time (^{13}C T_1). Under our conditions (speed and fields) T_1s were measured to be less than 300 ms (saturation/recovery method, data not shown). ^{13}C spectra were recorded using a triple resonance MAS probe (Bruker™), allowing the samples to be spun at 22.5 kHz after packing them inside 3.2 mm o.d. zirconia rotors (closed with Vespel caps). Recycle-time delays were set to 1.5 seconds and 10 240 transients over 8192 time-domain points separated by 2 µs dwell time were added, leading to a 61.035156 Hz pt^{-1} spectral resolution (spectral width = 250 kHz and total acquisition time per spectrum = 4 hours 30 min). ^{13}C NMR and ^{1}H NMR RF-fields were 60 kHz and 95 kHz, respectively. For the 300 °C thermally treated samples, the conductivity was such that it was very difficult to tune the probe. The concern was fixed by dispersing these powders in silica. Raw data were processed with a 150 Hz Lorentzian filter followed by Fourier transformation without zero filling. Chemical shifts are referenced to TMS by the substitution method using adamantane as an external reference. Spectral deconvolution was performed within Topspin™ software suite from Bruker™ using a CSA (chemical shift anisotropy) model.

To perform electrical experiments the GO films were produced. The GO water solution (0.4 mg mL^{-1}) was spray coated onto PET substrates at 90 °C (2.5 × 1.2 cm^2). Subsequently, the GO films were immersed in 30 mL aqueous solution of the reducing

agent at the desired concentration (dilution 1:10 of the amount indicated in Table 4) for 2 hours. In case of thermal reduction for bending characterization GO water solution (0.4 mg mL^{-1}) was spray coated onto PET substrates at 100 °C (2.5 × 1.2 cm^2, 125 μm thick) and annealed at 150 °C for 24 h in air. The reduced film of GO on PET was allowed to contact electrically with conductive copper tape. The sheet resistance of the film was 40 kΩ sq^{-1}. The stability test of the TrGO and CrGO conductive films to fatigue bending was carried out by performing 2000 bending cycles with a bending radius of 6 mm using a digital force gauge (Mark-10, M7-025E, ~25 N) equipped with a motorized test stand (Mark-10, ESM-S-8 303E). All the above-mentioned tests were performed by applying a bias voltage of 1 V by means of a Keithley 2635B.

2.4 Preparation of samples

2.4.1 Preparation of rGO samples

In Chapter 3 to synthetize rGO samples an aqueous dispersion containing 30 mL of GO at a concentration of 10 mg mL^{-1} was diluted with 270 mL of Milli Q water and sonicated for 20 minutes in an ultrasonic bath cleaner (140 W). Subsequently, a reducing agent was added without further purification and the pH adjusted to 9-10. The reaction mixture was stirred for a specified time (refer to Table 4) at 95 °C. The CrGO was collected by filtration and thoroughly washed with deionized water and ethanol. The resulting black precipitate was then freeze-dried under vacuum for 72 hours.

Tab. 4 Synthetic conditions studied for the preparation of CrGO.

Reducing agent	Concentration (g/L)	pH adjusting reagent	Reaction time (h)	Reaction temperature (ºC)
$NaBH_4$	8	5 wt% K_2CO_3	2	95
$NaBH_4$	8	5 wt% K_2CO_3	12	95
Ascorbic Acid	8	25 wt% NH_3	2	95
Ascorbic Acid	8	25 wt% NH_3	12	95
N_2H_4	10	-	2	95
N_2H_4	10	-	12	95
$Na_2S_2O_4$	7.5	25 wt% NH_3	2	95
$Na_2S_2O_4$	7.5	25 wt% NH_3	12	95

2.4.2 Preparation of TrGO samples

In Chapter 4 solid GO was obtained by lyophilization from the commercially available GO solution using a freeze dryer (GO, 4 mg mL^{-1}, monolayer content >95%, Graphenea). To produce GO films the 4 mg mL^{-1} aqueous dispersion of GO was diluted to a concentration of 0.4 mg mL^{-1}, then drop-cast on glass slides, and finally dried under air.

The thermal annealing of GO was performed by follow protocol. GO (solid) and GO films were annealed at different temperatures for 4 or 24 h in a muffle oven (16 cm × 16 cm) under air (1 bar) or in a tubular oven (100 cm × 7 cm) under argon (continuous flow 1 bar) before the measurements. Moreover, GO powders were annealed from a mg scale to a gram scale.

2.4.3 Preparation sensor devices by LbL method

In Chapter 5 all chemicals such as GO solution (4 mg mL^{-1}), 4-aminotiophenol, sodium citrate, tetrachloroauric (III) acid trihydrate ($HAuCl_4$) were delivered by commercially available sources. Preparation for production of sensor device was preceded by dilution GO solution to 2 mg mL^{-1} with Milli-Q water. Obtained solution was vigorously shaken and sonicated in sonic bath for 15 min. Meanwhile, the solution 1 x 10^{-3} M of 4-aminotiophenol in ethanol was prepared. The gold nanoparticles (AuNPs) were synthesized as follows: a solution of 2.2 mM sodium citrate in Milli-Q water (150 mL) was heated until boiling under vigorous stirring. After 15 min, 1 mL of $HAuCl_4$ (25 mM) was injected while the solution was boiling. The color of the solution changed from yellow to bluish grey and then to soft red in 10 min.

Fabrication pressure sensing device was proceeded by LbL method with specially designed dipping machine presented on Figure 19.

Fig. 19 *The photography of projected dipping machine.*

The ITO-glass substrates 25 mm x 75 mm (slide thickness 1.1 mm) with ITO thickness of 100 nm and roughness 1.8 nm with 20 Ω m^{-1}, were purified by sonication in acetone and isopropanol for 15 min. Each substrate was automatically dipped into the prepared GO solution at a speed of 2500 mm per minute, then withdrawn and dried for an hour in air. After drying the deposited GO layer, the dry substrate was dipped again at the same speed for 10 minutes in the prepared ethanolic solution of 4-aminotiophenol. It was then dried for 30 minutes and subsequently immersed at the same speed in the prepared solution of AuNPs. This cycle was repeated six times. The processing is illustrated on Figure 20.

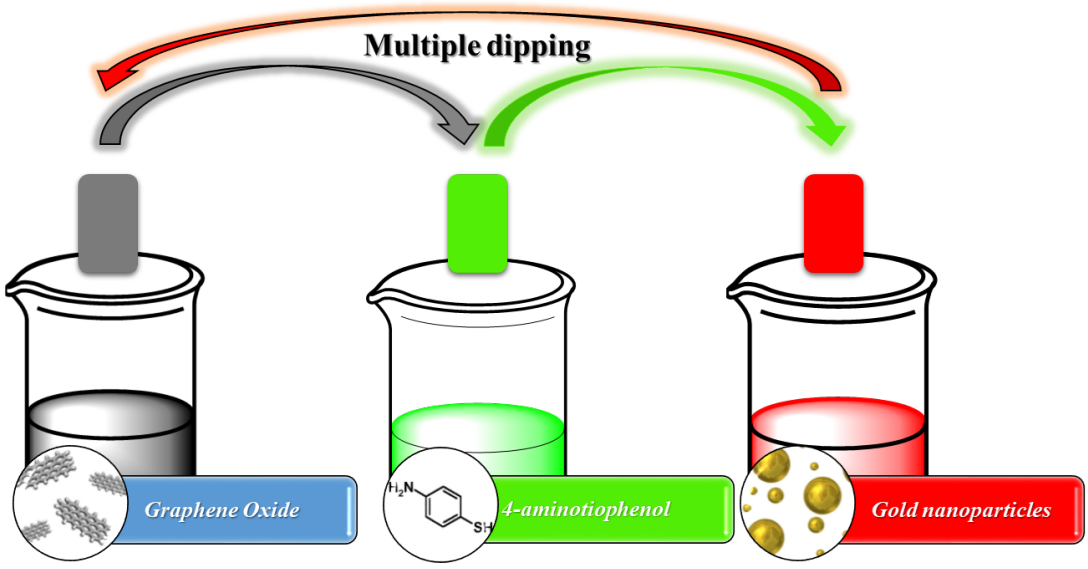

Fig. 20 *The schematic illustration of the fabrication of sensor device.*

For sensors, the top layer was retained on the GO layer GO(L1). To identify the quality of material deposition, substrates with gold nanoparticles as the top layer were prepared GO(L2). For fabrication of strain sensors similar protocol of dipping was utilized. Yet, the base substrate was change to ITO-PET foil. The material prepared in this manner, with a graphene top layer, underwent thermal reduction of GO to obtain reduced sample rGO(L1). The thermal reduction process was conducted in a tube furnace under vacuum at a temperature of 150 °C for 4 hours. Due to temperature necessary to effectively reduce GO (see Chapter 4) it is difficult to investigate reduction of GO(L2) because of high volatility of thiols, which without top layer of graphene vaporize in this temperature.

2.4.4 Preparation of water swellable material, rGO and sensor assembling

In Chapter 6 the water swellable material (WSM) was synthesized by radical mechanism to create the cross-lined water swellable polymer. All chemicals used for reaction were purchased from commercially available sources. The itaconic acid (IA) was used as the monomer and the 1,4-diethenylbenzene (DVB) (stabilized with 4-tert-butylpyrocatechol) was utilized as linker. To initiate the polymerization reaction the benzoyl peroxide (with 25% H_2O for stabilization) was used as catalyst. The 624.48 mg of IA was dissolved in the 694.45 μL of DVB, then the 116.25 mg of benzyl peroxide was added carefully under stirring. After dissolving of benzyl peroxide the heat was initiated into the reaction under vigours stirring. Polymerization occurred within short period of time. When the temperature reach 60 °C the gel starts forming, where under 70 °C the solid of itaconic-divinylbenzene polymer (poly(itaconic acid – divinylbenzene) (IDP) participated. At the end of the reaction, the mixture was diluted with 150 mL of hot ethanol, then filter and without further purification was dried in a hot air oven at 120 °C for 48h.

The solid GO was obtained by lyophilization process from the commercially available GO solution using a freeze dryer (GO, 4 mg mL^{-1}, monolayer content >95%, Graphenea). Then the GO was reduced by thermal annealing in 200 °C under vacuum in 24 h. (see Chapter 2.4.2.)

In the construction of the humidity sensor, the synthesized polymer was finely ground in a mortar, similar to the obtained rGO. Then, 50 mg of rGO was evenly deposited onto a polytetrafluoroethylene (PTFE) filter with a diameter of 47 mm and a pore size of 0.2 micrometers. The evenly deposited 50 mg of rGO on the filter was compressed using a

hydraulic press with a force of 10 kPa and held at this pressure for 10 minutes. After obtaining the compressed rGO, 50 mg of the previously ground polymer was sprayed onto its surface using spray coating with air, without any solvent. Subsequently, the material with the polymer top layer underwent the same compression process. Another 50 mg of rGO and polymer was then deposited using the same methodology. This cycle was repeated four times to obtain the rGO(IDP) sensor. After constructing the layered material, gold electrodes were applied using an evaporating process. In Chapter 6 the RH was varied by changing the hydration of nitrogen flux inside the box. The flux rate was fixed to maintain the pressure constant.

Chapter 3 Chemical reduction of graphene oxide

3.1 Introduction

GO is extensively studied as a 2DM because of its cost-effective large-scale production and straightforward processing capabilities[78, 367, 368]. The OFGs such as hydroxyl, epoxy, carbonyl, and carboxylic groups, located on both the basal plane and edges, confer unique physicochemical properties to GOs. These properties include excellent dispersibility and colloidal stability in various solvents, including water. Crucially, these OFGs can act as active sites for chemical modification with various molecules, thereby rendering GO suitable for applications in chemical sensing[222, 255, 260], pressure sensing[171, 181], energy storage[2, 49, 100, 354] and healthcare[117, 369]. Although, the presence of OFGs in GO disrupts the continuous sp^2 network typical of graphene, leading to an insulating material that is unsuitable for applications involving electrical conductivity[370]. Fortunately, this limitation can largely be mitigated by reducing the OFGs in GO, which increases the degree of conjugation in the carbon network by forming sp^2 species, thereby significantly improving the material's electrical properties. To achieve the electroactive form of GO, *i.e.*, rGO, various methods such as thermal (TrGO) and chemical (CrGO) treatments can be employed. These methods are still the most extensively utilized[371, 372].

Thermal reduction is an appealing method due to its low environmental impact, but the high temperatures needed (over 1000°C) make it energy-intensive and unsuitable for use with plastic substrates, which are often preferred for flexible sensing electronic applications[373]. Conversely, chemical reduction is presently the most effective method for reducing GO, achieving electrical properties close to those of graphene. Moreover, the highest reported electrical conductivity for CrGO is 8.5×10^4 S m^{-1}[85]. Chemical reduction is industrially attractive due to its compatibility with large-scale production and low energy consumption, as the reduction temperature is typically below 100 °C. Various reducing agents can be used to obtain CrGO, including hydrazine hydrate (N_2H_4), dimethylhydrazine, p-phenylenediamine, ethylenediamine, and hydroxylamine, sodium borohydride ($NaBH_4$), ascorbic acid (AA), sodium dithionite ($Na_2S_2O_4$) and others. However, numerous reducing agents and protocols have been documented in the literature, making it challenging to evaluate and compare these methods in terms of their structure-performance relationships. For example, in electronic applications, it is crucial

to maximize the removal of OFGs to achieve CrGO with the highest electrical conductivity. Unfortunately, some reducing agents, or their oxidized forms, can introduce doping or contamination in the CrGO. While CrGO synthesized with hydrazine hydrate is generally regarded as closely resembling pristine graphene in terms of electronic and structural properties, whereas films of CrGO produced using sodium borohydride have been reported to exhibit significantly lower sheet resistance. This outcome can be attributed to CrGO contamination with nitrogen and the formation of pyrazole, where nitrogen atoms act as electron donors and create p-type holes[374, 375]. Ascorbic acid, despite being one of the most extensively studied "green" reducing agents for producing CrGO, also faces the same issue of contamination[91]. AA undergoes oxidation initially to dehydroascorbic acid (DHA), and subsequently to oxalic and guluronic acids. These compounds can then interact supramolecularly with the remaining carboxylic groups of pristine GO[376-378]. Contrary to applications in electrical fields, the situation is more intricate when addressing applications in sensing device. Alternative strategies, such as heteroatom doping, have also been extensively utilized to enhance the conductivity of pristine GO[379, 380]. Nonetheless, the electrical performance of rGO as an active material in sensing is superior to that of pristine GO substrates because the removal of OFGs is accompanied by other physicochemical and structural changes in rGO, such as increased conductivity, surface area, and pore size. Therefore, the optimal reduction conditions for electronics applications may vary. Moreover, a systematic study comparing the physicochemical and structural properties of CrGO with its performance in electronics using various reducing agents and reduction times has not been conducted. To address this significant knowledge gap, the study investigates the optimization of GO reduction by varying reduction conditions, particularly focusing on the choice of reducing agent and reaction time (2 or 12 hours). Regarding reducing agents, the study focuses attention on four of the most commonly employed agents, *i.e.*, hydrazine hydrate, sodium borohydride, AA, and a sulfur-containing compound such as sodium dithionite. This study aims to systematically investigate how these factors influence the toxicity, physicochemical and structural properties of CrGO, ultimately enhancing their performance for electronic devices.

3.2 Results

3.2.1 Chemical composition of chemically reduced graphene oxide

The successful chemical reduction of GO was then monitored using FTIR spectroscopy. The FTIR spectrum of synthesized material is presented on Figure 21.

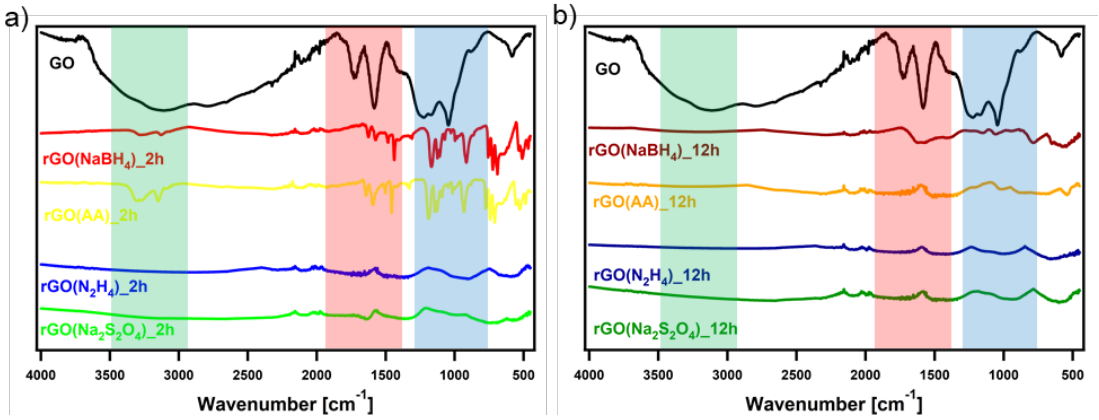

Fig. 21 *FTIR spectra of chemically reduced GO with different reducing agents at a) 2 hours and b) 12 hours reaction time.*

The black curve displays the distinctive vibration bands of GO, including: 2500–3500 cm^{-1} (OH stretching vibration), 1722 cm^{-1} (C=O stretching vibration), 1620 cm^{-1} (aromatic C=C stretching vibration), 1400 cm^{-1} (C–OH bending vibration), 1220 cm^{-1} and 1046 cm^{-1} (breathing vibrations), and ~1000 cm^{-1} (stretching vibrations from epoxy, ether, or peroxide groups). After 2 hours of chemical reduction, the vibrations associated with the various OFGs were significantly diminished in rGO(N_2H_4) and rGO($Na_2S_2O_4$). However, achieving the same degree of reduction in rGO(AA) or rGO($NaBH_4$) required 12 hours of reduction. FTIR analysis provided initial insights into the reduction efficacy of the four studied reducing agents, ranking N_2H4 and $Na_2S_2O_4$ as the most potent, followed by AA, and $NaBH_4$ as the least effective reducing agent.

The extent of GO reduction is typically quantified by the C/O ratio derived from XPS analysis. However, as XPS is a surface-sensitive technique (*i.e.*, the penetration depth of the XPS beam ranges only between 1 and 10 nm). Thus, firstly was performed elemental analyses of obtained CrGO. The results of elemental analyses are presented on Table 5.

Tab. 5 Elemental analysis of chemically reduced GO samples.

Sample	%C	%O	%N	%S	%H	C/O
GO	46.10	46.60	0.03	2.00	5.27	0.99
rGO($NaBH_4$)_2h	65.00	31.94	0.17	1.17	1.73	2.04
rGO($NaBH_4$)_12h	66.72	30.29	0.58	1.11	1.30	2.20
rGO(AA)_2h	75.51	20.59	1.99	0.88	1.03	3.67
rGO(AA)_12h	70.74	26.32	0.97	0.92	1.05	2.69
rGO(N_2H_4) _2h	80.28	14.62	3.35	1.01	0.74	5.49
rGO(N_2H_4)_12h	83.50	11.60	3.63	0.74	0.54	7.20
rGO($Na_2S_2O_4$)_2h	81.47	14.89	0.72	2.16	0.77	5.47
rGO($Na_2S_2O_4$)_12h	84.78	12.07	0.41	2.09	0.65	7.02

As can be seen in Table 5 the C/O ratio ranges from 0.99 for pristine GO to 7.20 for rGO(N_2H_4)_12 h. Based on the C/O ratio, the reducing agents rank in strength as follows: $Na_2S_2O_4 \approx N_2H_4 >$ AA > $NaBH_4$, consistent with FTIR analyses. Notably, the nitrogen content is slightly elevated in the samples reduced with N_2H_4, suggesting potential contamination due to the reaction between GO and N_2H_4 (*e.g.*, pyrazole formation). From the XPS survey spectra presented for GO on Figure 22 and for rGO samples on Figure 23, the C/O ratio was estimated ranging from 0.86 for pristine GO up to 11.21 for rGO($Na_2S_2O_4$)_12 h. The detail data obtained from XPS survey is presented on Table 6.

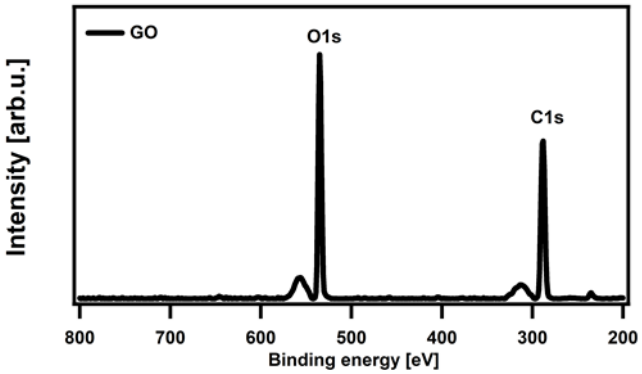

Fig. 22 *Survey spectra of GO.*

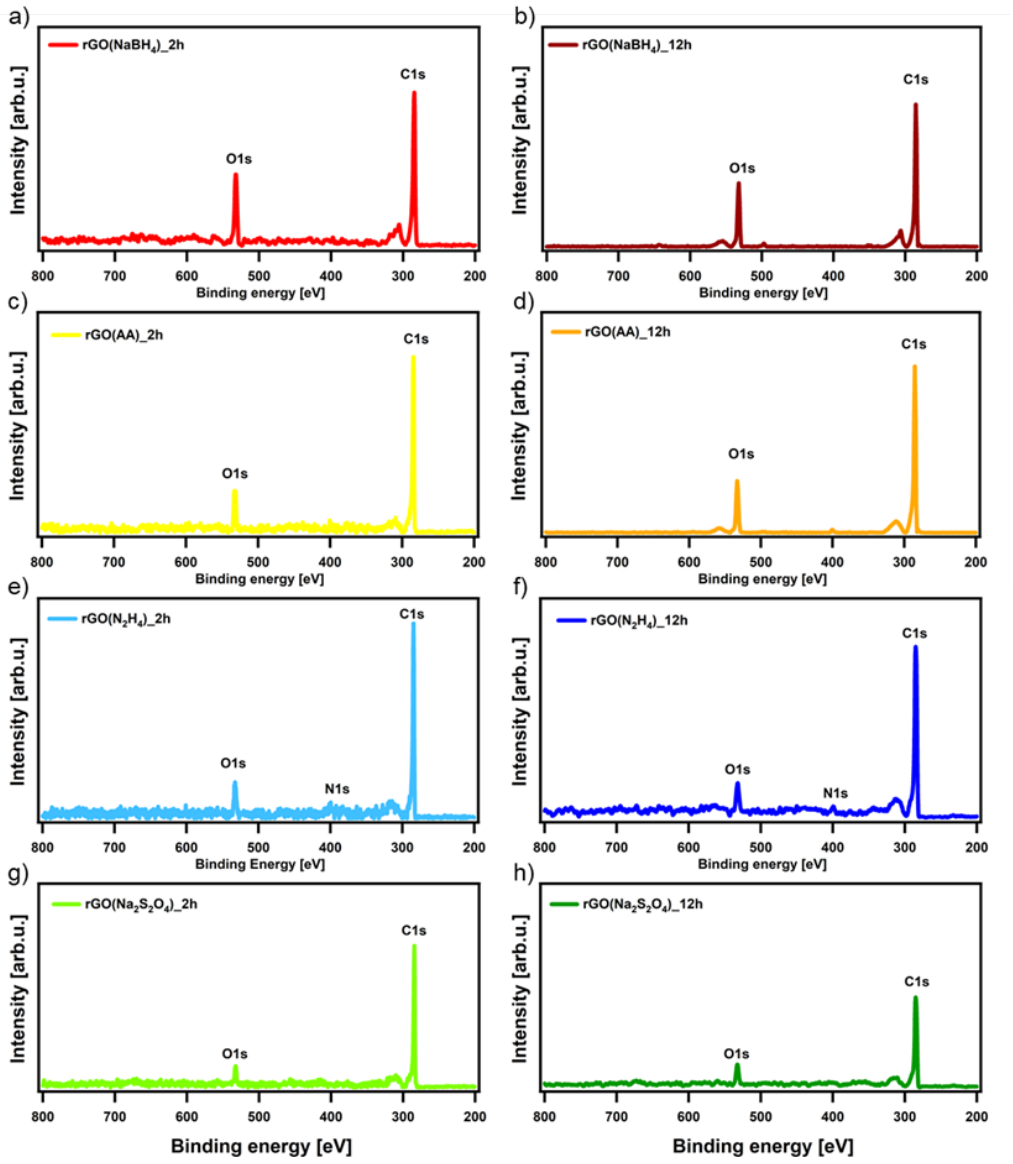

Fig. 23 *Survey spectra of CrGO with different reducing agents and a), c), e), g) 2 hours and b), d), f) h) 12 hours of reaction time.*

In full agreement with FTIR and EA, the strength of the reducing agents followed the same trend. Likewise, the nitrogen element was also present in the rGO(N_2H_4) samples, and its amount was proportional to the reaction time (2.70% after 12 hours of reaction). Traces of sodium element (~1%) were found in the rGO ($NaBH_4$) samples, yet, their levels were so low that they could not be detected in elemental analysis. No detectable contamination of sodium or sulfur was observed in the rGO($Na_2S_2O_4$) samples. Concerning the reaction time, a minimal difference (*i.e.*, maximum 5% increase) was observed between 2 and 12 hours of reaction for all the reducing agents.

Tab. 6 Elemental analysis of chemically reduced GO samples from XPS survey.

Sample	%C	%O	%N	%Na	C/O
GO	46.10	53.87	0.03	-	0.86
rGO($NaBH_4$)_2h	81.12	17.50	-	1.37	4.64
rGO($NaBH_4$)_12h	82.10	17.25	-	0.65	4.76
rGO(AA)_2h	87.37	12.63	-	-	6.92
rGO(AA)_12h	87.80	12.20	-	-	7.20
rGO(N_2H_4) _2h	89.79	8.45	1.76	-	10.63
rGO(N_2H_4)_12h	88.50	8.60	2.90	-	10.29
rGO($Na_2S_2O_4$)_2h	91.39	8.61	-	-	10.62
rGO($Na_2S_2O_4$)_12h	91.81	8.19	-	-	11.21

Although FTIR, EA and XPS survey spectra exhibited similar trends in the effectiveness of the reducing agents, further analysis was required to understand the impact of reaction time. To gain insight into the chemical aspects of the reduction process by each reducing agent, high-resolution XPS spectra of C 1s and O 1s were deconvoluted. The deconvoluted spectra for GO sample of C 1s and O 1s is presented on Figure 24.

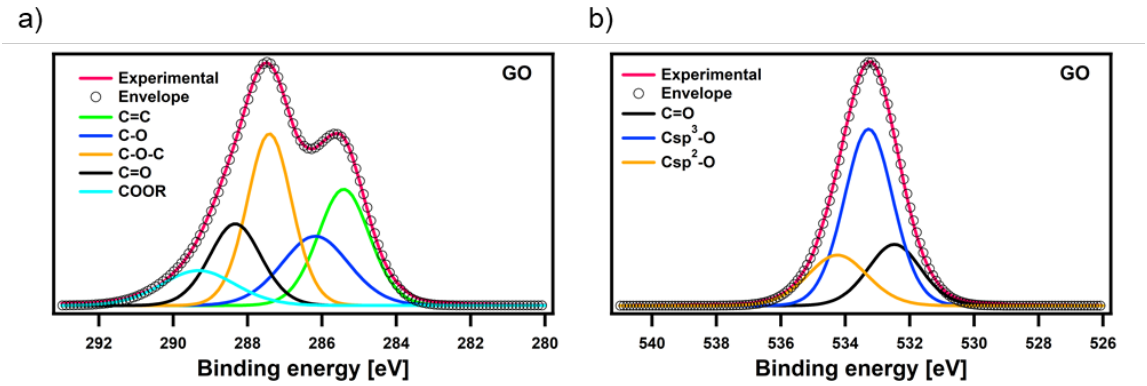

Fig. 24 *Fitted XPS of GO for a) C 1s and b) O 1s.*

The high-resolution C 1s spectra were analyzed by fitting them with 5 Gaussian–Lorentzian curves corresponding to different chemical environments: 284.5 eV for C–C (Csp^2–Csp^2), 285.15 eV for C–O (encompassing Csp^2–O–Csp^2, Csp^3–OH, and Csp^2–OH), 286.5 eV for C–O–C (Csp^3–O–Csp^3), 287.40 eV for C=O, and 288.50 eV for COOR (including COOH and lactone). The C 1s deconvoluted spectra obtained from XPS is illustrated on Figure 25. Likewise, the high-resolution O 1s spectra were fitted with 3 Gaussian–Lorentzian curves: 531.08 eV C=O, 532.03 eV Csp^3–O (including Csp^3–O–Csp^3, and Csp^3–OH), and 533.43 eV Csp^2–O (including Csp^2–O–Csp^2 and Csp^2–OH), (see Figure 26).

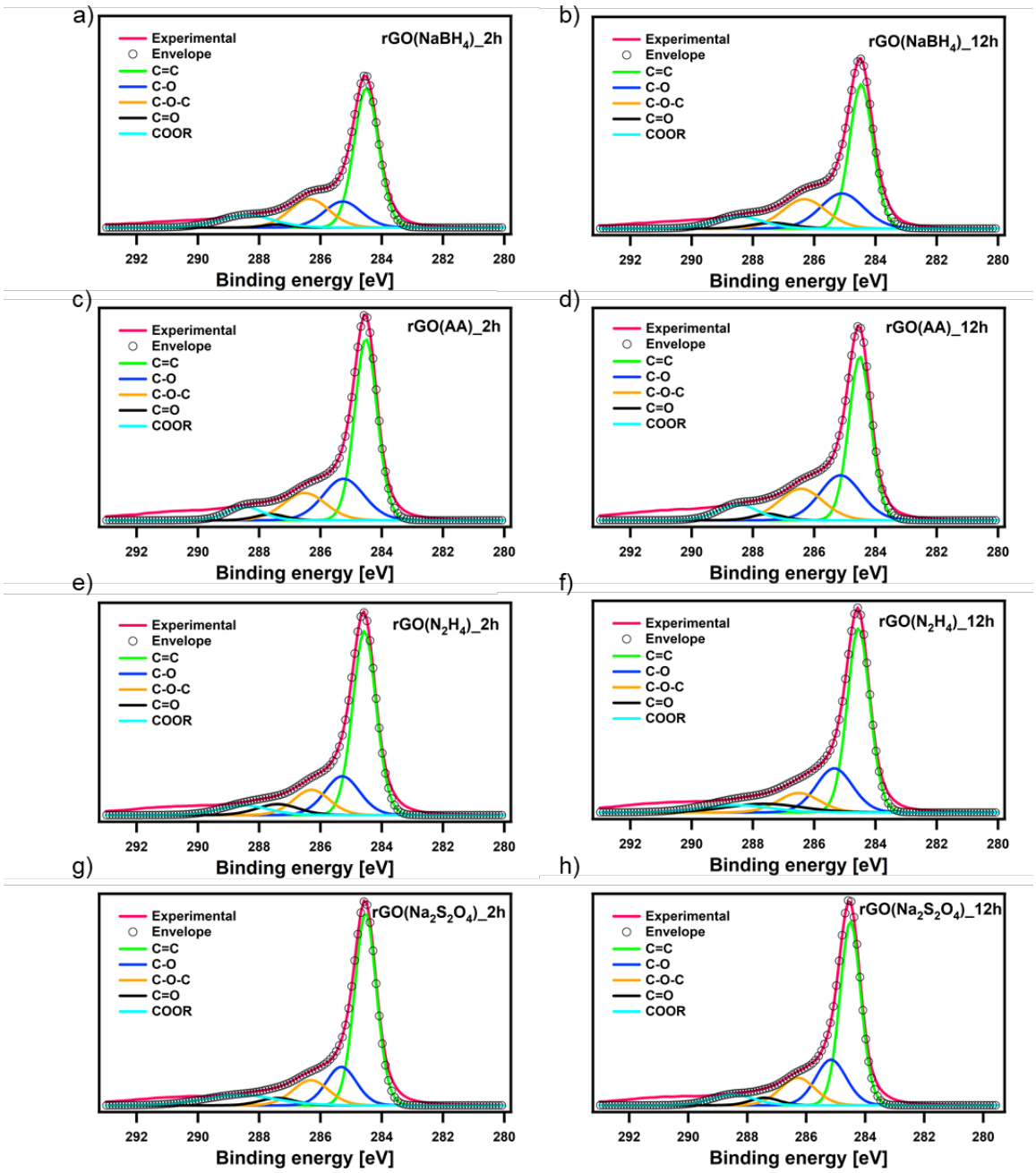

Fig. 25 *High-resolution XPS spectra of C1s for the CrGO with different reducing agents and a), c), e), g) 2 hours and b), d), f) h) 12 hours of reaction time.*

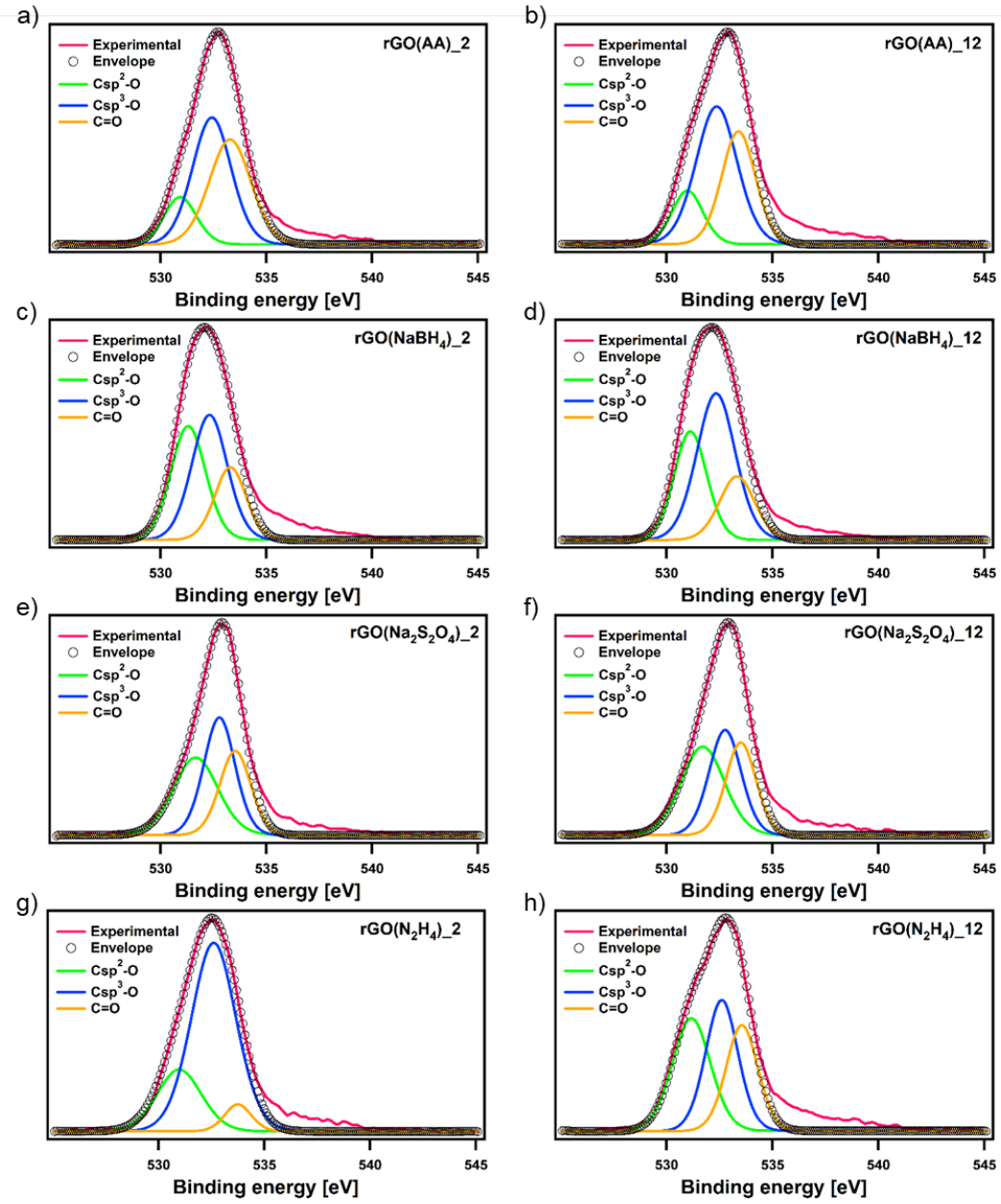

Fig. 26 *High-resolution XPS spectra of O 1s for the CrGO with different reducing agents and a), c), e), g) 2 hours and b), d), f) h) 12 hours of reaction time.*

Moreover, to demonstrate the reactivity between GO and N_2H_4, the high-resolution N 1s XPS spectra were obtained (see Figure 27) at 2 and 12 hours of reaction. Figure 27 shows the formation of a pyridine ring, C–N–C and a pyrrole or diazine ring (N–C=O)[381, 382]. Moreover, carbonyl groups, whether in the form of C=O or COOR, constituted the lowest percentage among the various OFGs present in GO. The results indicate that N_2H_4 is particularly effective in reducing COOR groups, whereas all reducing agents resulted in similar amounts of C=O moieties. The changes in the area corresponding to the four distinct C–O species present in GO were observed throughout

the reduction process. Furthermore, the area corresponding to C–O species, including both Csp^3–O–Csp^3 and Csp^3–OH peaks, decreased uniformly after chemical reduction, with no significant variations observed among the different reducing agents or reaction times. However, $Na_2S_2O_4$ showed a higher decrease (nearly 30% compared to GO). Finally, the most intriguing findings pertained to the Csp^2–O species, encompassing both Csp^2–O–Csp^2 and Csp^2–OH.

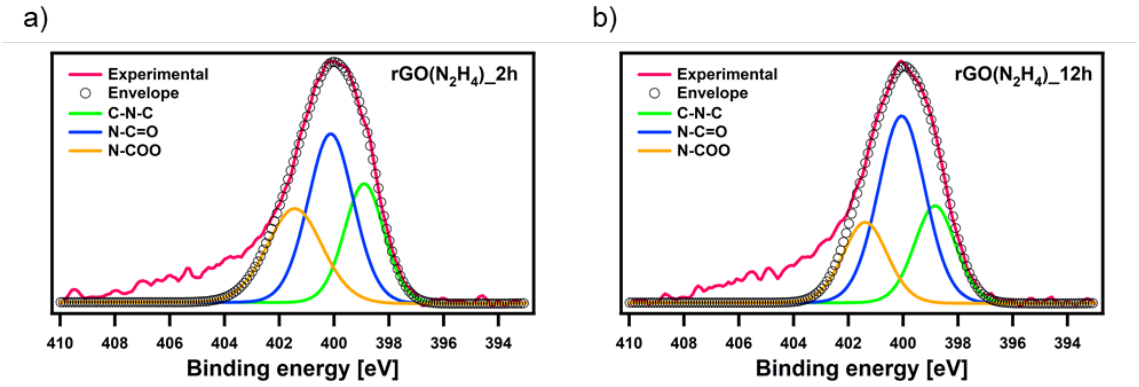

Fig. 27 *XPS analysis of 1Ns spectra of CrGO with hydrazine at a) 2 and b) 12 hours of reduction*.

To complete analyses the solid-state NMR magic angle spinning (ssNMR-MAS) was performed and also deconvoluted. The ssNMR-MAS spectra were deconvoluted in eight curves: 60.4 ppm ($^{13}Csp^3$–O–$^{13}Csp^3$), 70.6 ppm ($^{13}Csp^3$–OH), 78.9 ppm (^{13}Csp3–OH, close to defects), 100.2 ppm (^{13}C–OOR), 126.7 ppm ($^{13}Csp^2$–$^{13}Csp^2$), 134.7 ppm ($^{13}Csp^2$–$^{13}Csp^2$ close to defects), 162.4 ppm (Csp^2–O (including Csp^2–O–Csp^2 and Csp^2–OH)) and 187.9 ppm (^{13}C=O). The obtained NMR spectra are presented on Figure 28 for GO and on Figure 29 for synthesized rGO samples.

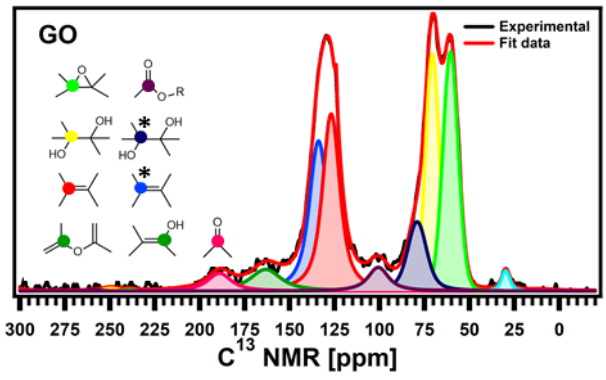

Fig. 28 *Solid-state MAS-NMR of GO sample.*

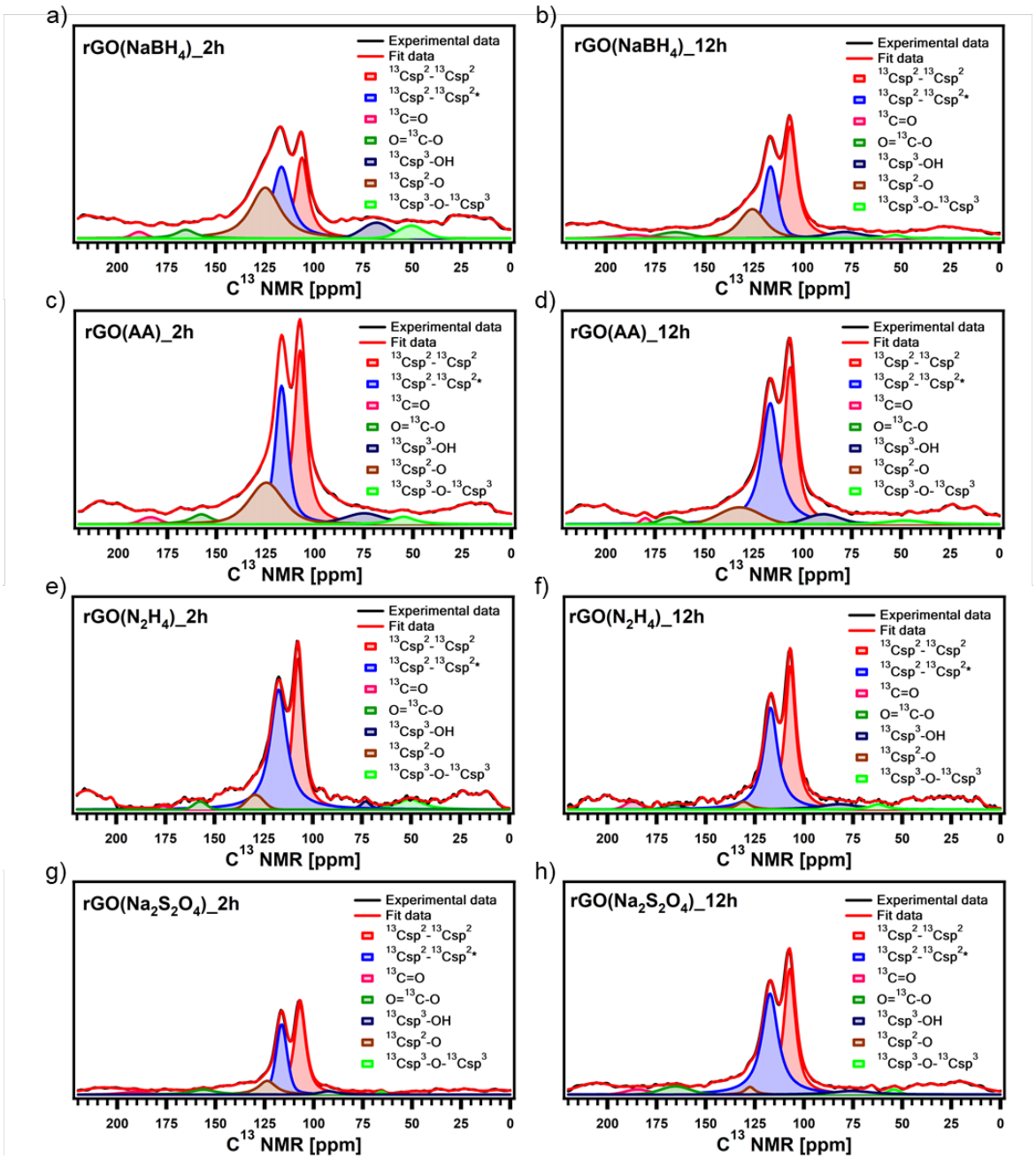

Fig. 29 *Solid-state MAS-NMR of CrGO samples for a), c), e), g) 2 hours and b), d), f) h) 12 hours of reaction time.*

By combing the evolution of the area of each component in XSP and ssNMR spectra to function of reducing agents and reaction time significant dependencies can be observed. On Figure 30 are presented relatives contributions of C 1s and O 1s peaks and NMR spectra components estimated by dividing the area under each component by whole areas of these peaks as a function of the reducing agents and reaction time. Thus, as expected, the area of the C=C and Csp^2–Csp^2 peaks increased in all the cases as the reduction process restored the π-conjugation of the carbon sheets. While the largest C=C

and Csp^2–Csp^2 peak areas were obtained for rGO ($Na_2S_2O_4$)_2 h, the smallest C=C and Csp^2–Csp^2 peak areas were observed for rGO($NaBH_4$)_2 h. The reaction time only played a major role when $NaBH_4$ was used as a reducing agent. The area of Csp^2–Csp^2 close to the defects (Csp^2–Csp^2*) increased with the reduction process. Interestingly, we observed a decrease of the Csp^2–Csp^2* peak area after 12 hours of reaction, when $NaBH_4$ and N_2H_4 were used. This can be directly correlated with the contamination with the sodium and nitrogen elements, respectively, which reacted with the defects present in the GO sheets.

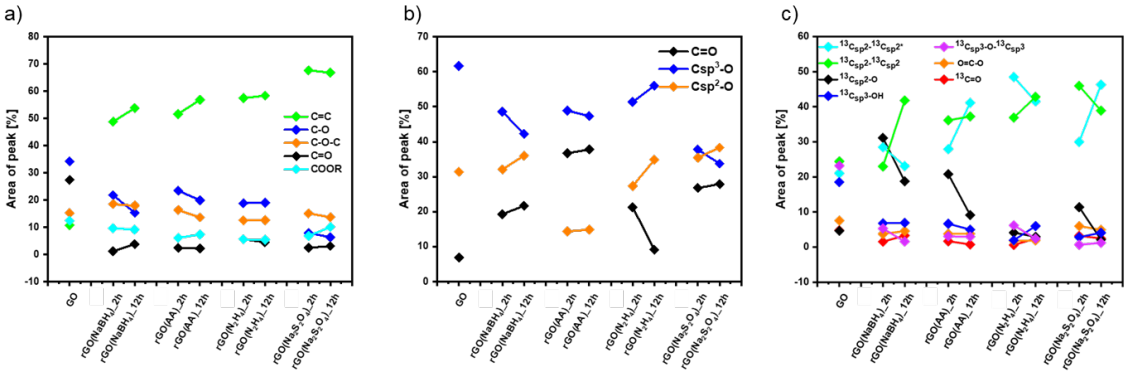

Fig. 30 *Comparison of the relative contribution of a) C 1s XPS b) O 1s and c) NMR spectra components as a function of the reducing agents and reaction time estimated by dividing the area under* each *component by the whole peak area.*

In case of hydrazine, as previously demonstrated, the reduction process induced a structural reorganization from Csp^3–O to Csp^2–O, resulting in an initial increase in the peak area of the Csp^2–O species. However, with continued reduction, the OFGs were progressively eliminated, leading to a subsequent decrease in the peak area of the Csp^2–O species. However, when the reduction continued, the OFGs were eliminated, leading to a decrease in the peak area of the Csp^2–O species. This phenomenon can be clearly observed by ssNMR. For the mildest reducing agent rGO($NaBH_4$)_2 h, there was a sharp increase of the Csp^2–O peak area compared to that of pristine GO, which then decreased when the reduction was performed for 12 hours. The same trend was observed when rGO(AA)_2 h, the following reducing agent by strength, was used. However, the peak area increase was lower than that in rGO($NaBH_4$)_2 h and when the reduction was performed for 12 hours the peak area of Csp^2–O was comparable to that of pristine GO. Interestingly, when N_2H_4 was used, no increase in the peak area of Csp^2–O was observed, independent of the reaction time. Finally, rGO($Na_2S_2O_4$)_2 h followed the same trend as rGO(AA) but with a lower peak area increase. Therefore, ssNMR unequivocally proves that the strength of the reducing agents varies as follows: $Na_2S_2O_4 \approx N_2H_4 > AA > NaBH_4$.

Besides, the reaction time plays a role for three of the reducing agents, $Na_2S_2O_4$, AA and $NaBH_4$.

3.2.2 Structure and morphology of chemically reduced graphene oxide

Raman spectroscopy confirmed not only the chemical composition of CrGO but also that the different Raman features (*e.g.*, band position, intensity ratio and width) were related to structural parameters such as crystallinity, reduction degree of GO and oxygen content[383]. The Raman spectra of GO and CrGO were deconvoluted by using five Lorentzian curves, which consist of the first-order Raman modes, namely: D, D″, D′, D* and G (Raman results are presented on Figure 31 and on Figure 32 deconvoluted spectra for CrGO samples).

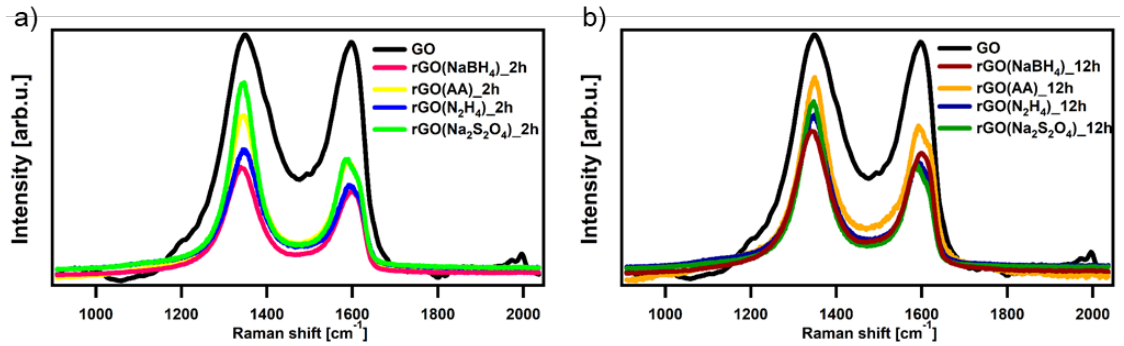

Fig. 31 *Overlapped Raman spectra of GO and CrGO with different reducing agents at a) 2 and b) 12 hours of reaction time.*

While the D band (~1350 cm^{-1}) is associated with the breathing modes of photons of A_{1g} symmetry, the G band (~1585 cm^{-1}) is related to the first-order scattering of E_{2g} phonons of the sp^2 carbon structure[384]. Commonly, the relative intensity of the D band with respect to the G band (I_D/I_G ratio) is an insightful parameter to estimate the degree of defects in GO derivatives and it has been correlated with the inverse of the crystallite size on basal planes (1/La) by Tuinstra and Koenig[349]. Investigating the I_D/I_G ratio for synthesized samples allows for identification for all used reducing, grow of the ratio. The comparison of I_D/I_G ratio is illustrated on Figure 33 (a).

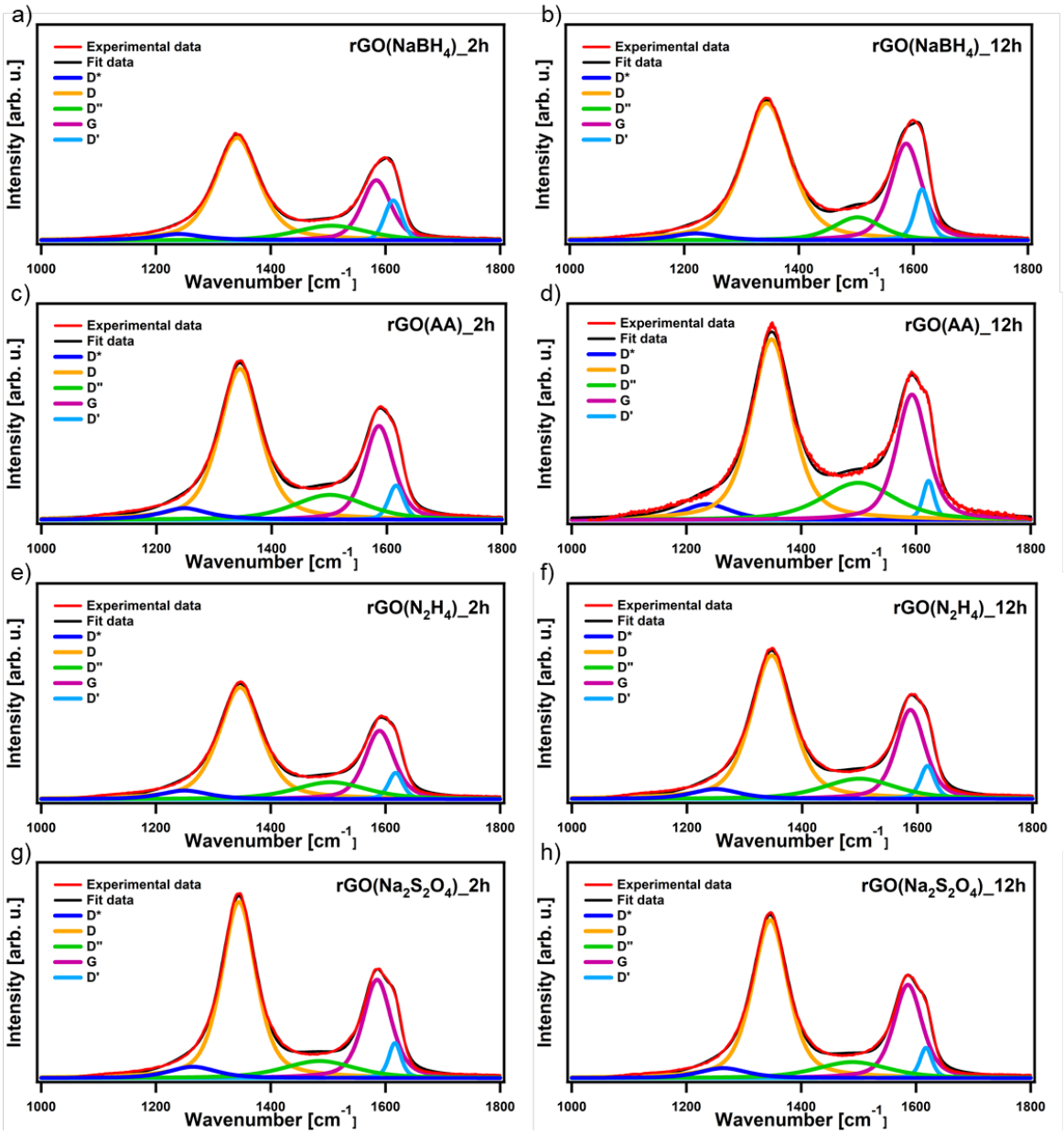

Fig. 32 *Fitted Raman spectra of CrGO with different reducing agents and a), c), e), g) 2 hours and b), d), f) h) 12 hours of reaction time.*

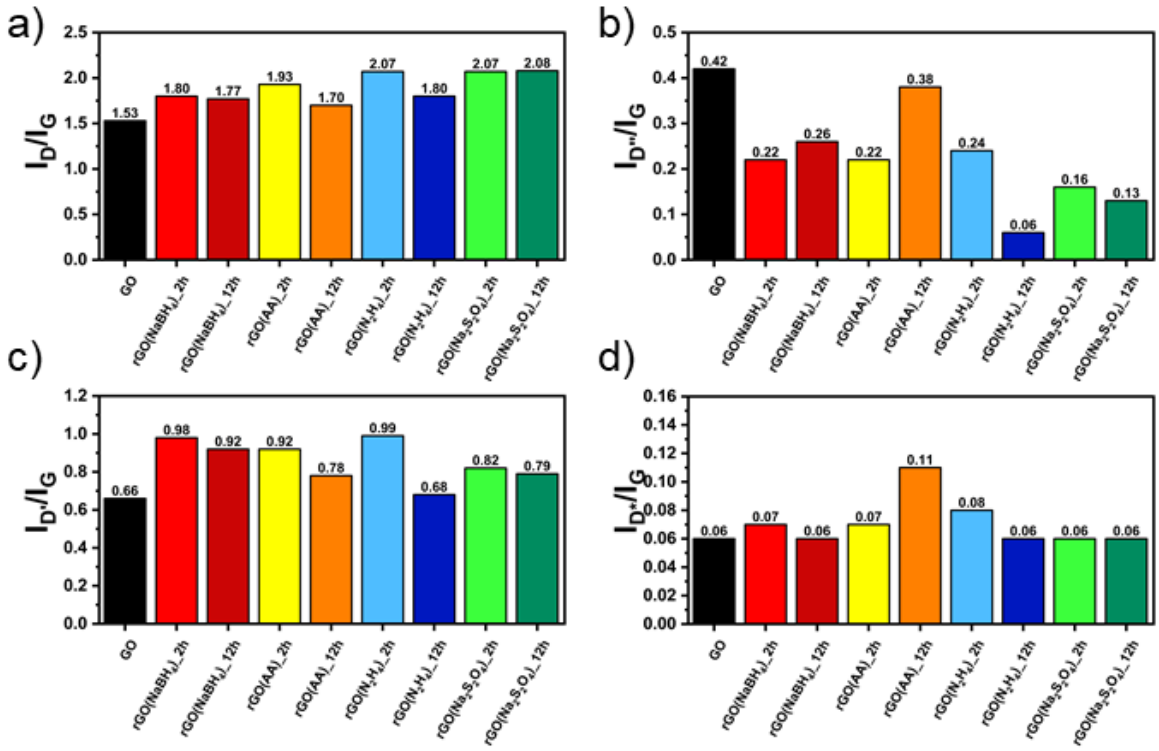

Fig. 33 *Ratio of the band intensities a) I_D/I_G b) $I_{D''}/I_G$ c) $I_{D'}/I_G$ d) I_{D*}/I_G of CrGO with different reducing agents and different reaction times.*

Investigating the I_D/I_G ratio for synthesized samples allows for identification for all used reducing, grow of the ratio. The comparison of I_D/I_G ratio is illustrated on Figure 33. That feature clearly indicate the restoration of sp^2 conjugation due to the removal of the oxygen functional groups from GO[385, 386]. The increase in the I_D/I_G ratio is proportional to the strength of the reducing agent, in full agreement with previous characterization results. In addition, the I_D/I_G ratio decreases after 12 hours of reaction when AA and N_2H_4 are employed, which is related to undesired contamination. The additional bands (D′′, D* and D′) arise from the defects present in the graphitic structure of the carbon material[383, 387, 388]. The $I_{D''}/I_G$, I_{D*}/I_G, and $I_{D'}/I_G$ ratios are shown in Figure 33 (b), (c) and (d) respectively. Ideally, all these ratios should decrease with the reduction degree. However, the $I_{D'}/I_G$ and I_{D*}/I_G ratios increased slightly in all the cases; therefore, it can be concluded that the chemical reduction process creates defects in the graphitic structure of the carbon material. In contrast, the $I_{D''}/I_G$ ratio decreases in all the cases and the decrease is proportional to the strength of the reducing agent.

Moreover, the Raman spectrum was utilized to unravel the number of defects present in the pristine GO and CrGO. First, the average defect distance (L_D) was

calculated. The obtained values for GO and CrGO are illustrated on Figure 34 (a). From the results it is indicated that, the L_D of pristine GO amounts to 9.64 ± 1.11, which upon reduction only decreases slightly to 8.27 ± 0.95 for the strongest reducing conditions (rGO($Na_2S_2O_4$)_12 h). Furthermore, the number of defects was also calculated from Raman analysis. The results are presented on Figure 34 (b). As $L_D \approx 10$, the estimated number of defects in each case in GO and CrGO is between 7.8×10^{10} and 10.6×10^{10}.

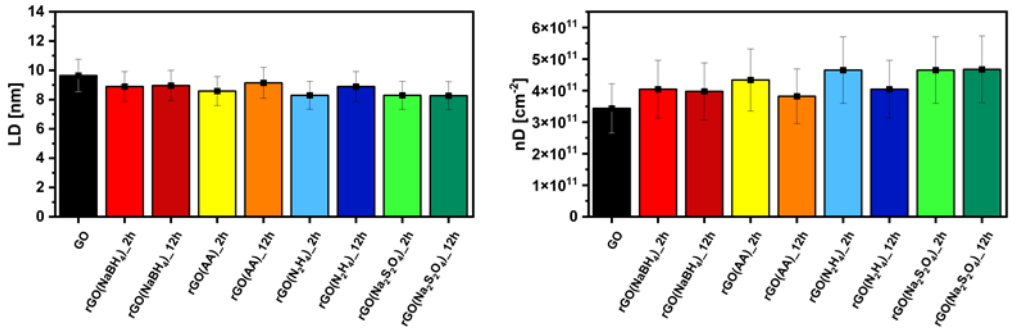

Fig. 34 *a) Average defect distance and b) defect density of CrGO with different reducing agents and different reaction times.*

The effect of the different reducing agents on the crystallinity of CrGO was investigated using powder X ray diffraction. The XRD spectra and obtained calculated values are presented on Figure 35. The pristine GO diffraction pattern displays one characteristic peak at 2θ = ∼10° (peak I) with a Full-Width at Half Maximum (FWHM) of 0.81 related to the (002) family of planes. After the chemical reduction, the CrGO exhibits one characteristic peak at 2θ = ∼25° (peak II), with a larger FWHM of 4.4–5.81°, related to the smaller crystallite sizes and a second at about 42.8° related to the (100) family of planes. After two hours of the reaction, peak I completely disappears when $Na_2S_2O_4$, N_2H_4, and AA reducing agents are used. However, peak I remains present even after 12 hours of reaction when $NaBH_4$ is used. This observation is consistent with the results obtained by Shin et al.[90]. From the scattering angle (2θ) of each peak we can quantify the d-spacing, average crystalline size (La), crystalline thickness (Lc), and graphene layer number (n) for GO and all CrGO using the Debye–Scherrer equation. On Table 7 are presented all calculated values form XRD spectrum. The d-spacing of pristine GO amounts to 8.79 Å and after its chemical reduction, it decreased to ∼3.76 Å [389, 390]. The significant reduction in the interlayer distance is associated with the partial removal of OFGs from the GO sheets. Although the d-spacing slightly decreases with reaction time, there are no substantial differences observed between the different reducing

agents used. The crystal thickness (*Lc*) notably decreases from 97.32 Å for pristine GO to approximately 15.5 Å after chemical reduction. Interestingly, no significant differences are observed between the various reducing agents used and reaction time for both *Lc* and *La* (see Fig. 35 c)).

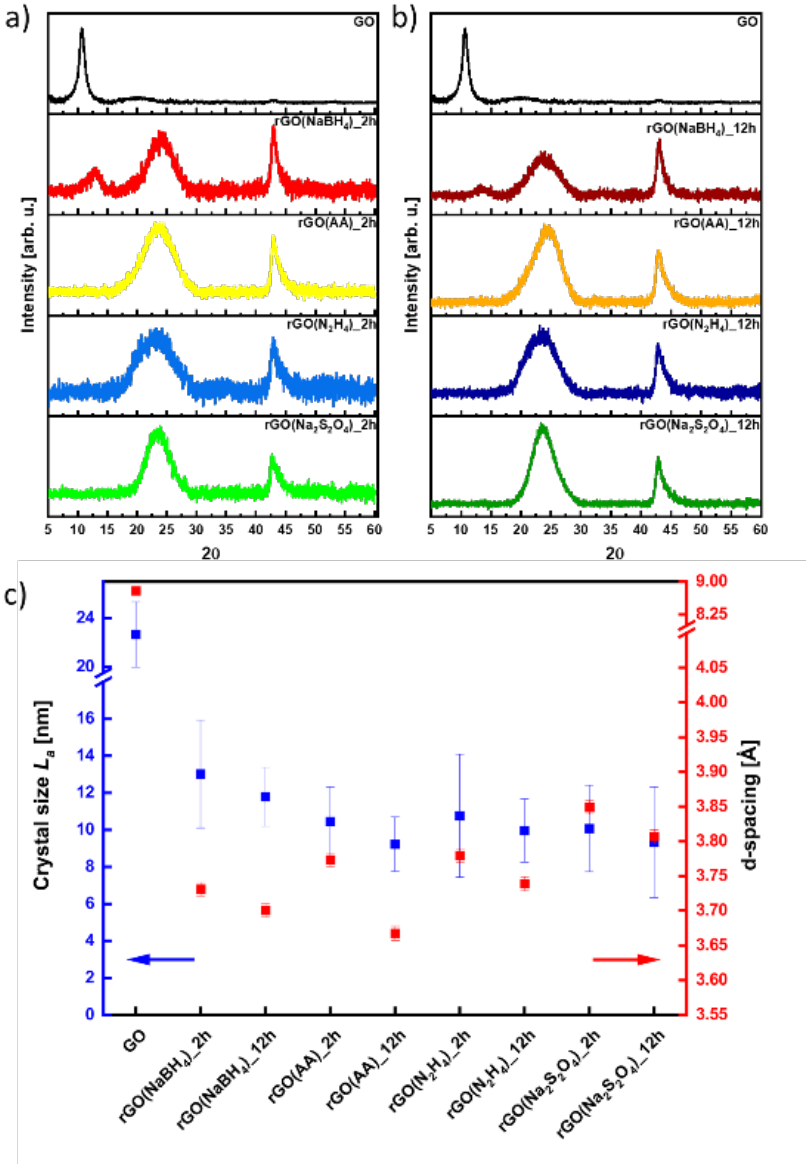

Fig. 35 *XRD patterns of rGO reduced for (a) 2 hours and (b) 12 hours, and (c) dependence on crystal size (La) and d -spacing in correlation with the reducing agent.*

Tab. 7 The XRD peak position, d-spacing, crystallite size (L_a), crystalline thickness (L_c) and average graphene layer number (n_c) calculated for the (002) and (100) planes for all measured samples.

Sample	Reactant	Reaction time [h]	(0 0 2) position [°]	(1 0 0) position [°]	*d*-spacing [Å]	L_a [Å]	L_c [Å]	Number of layers n_c
GO	-	-	10.05	-	8.79 ±0.01	226.59 ±2.68	97.32 ±3.05	11.07
rGO($NaBH_4$)_2h	$NaBH_4$	2	24.02	42.94	3.73 ±0.01	130.19 ±2.91	17.53 ±0.92	4.74
rGO($NaBH_4$)_12h		12	23.82	943.08	3.70 ±0.01	117.93 ±1.59	14.75 ±0.49	3.95
rGO(AA)_2h	AA	2	23.55	43.01	3.77 ±0.01	104.49 ±1.88	13.81 ±0.67	3.66
rGO(AA)_12h		12	24.24	42.85	3.67 ±0.01	92.28 ±1.46	15.24 ±0.70	4.16
rGO(N_2H_4)_2h	N_2H_4	2	23.08	42.97	3.85 ±0.01	93.30 ±2.99	12.52 ±0.77	3.25
rGO(N_2H_4)_12h		12	23.34	42.74	3.81 ±0.01	100.77 ±2.33	14.19 ±0.71	3.73
rGO($Na_2S_2O_4$)_2h	$Na_2S_2O_4$	2	23.51	42.79	3.78 ±0.01	107.64 ±3.32	18.23 ±0.79	4.82
rGO($Na_2S_2O_4$)_12h		12	23.77	42.85	3.74 ±0.01	99.66 ±1.71	17.95 ±0.69	4.80

Notably, the theoretical number of layers (n_c) indicates that few-layer thick CrGO sheets (3–5 layers) can be produced even with mild reducing agents such as AA. Therefore, we can conclude that the choice of reducing agent and the reaction time do not significantly affect the crystallinity of the resulting CrGO.

The scanning electron microscopy was utilized for investigation of morphological changes upon the chemical reduction of GO. The obtained SEM images are presented on Figure 36. The SEM investigation clearly indicate the absence of morphological changes upon the chemical reduction of GO for all the reducing agents and reaction times employed.

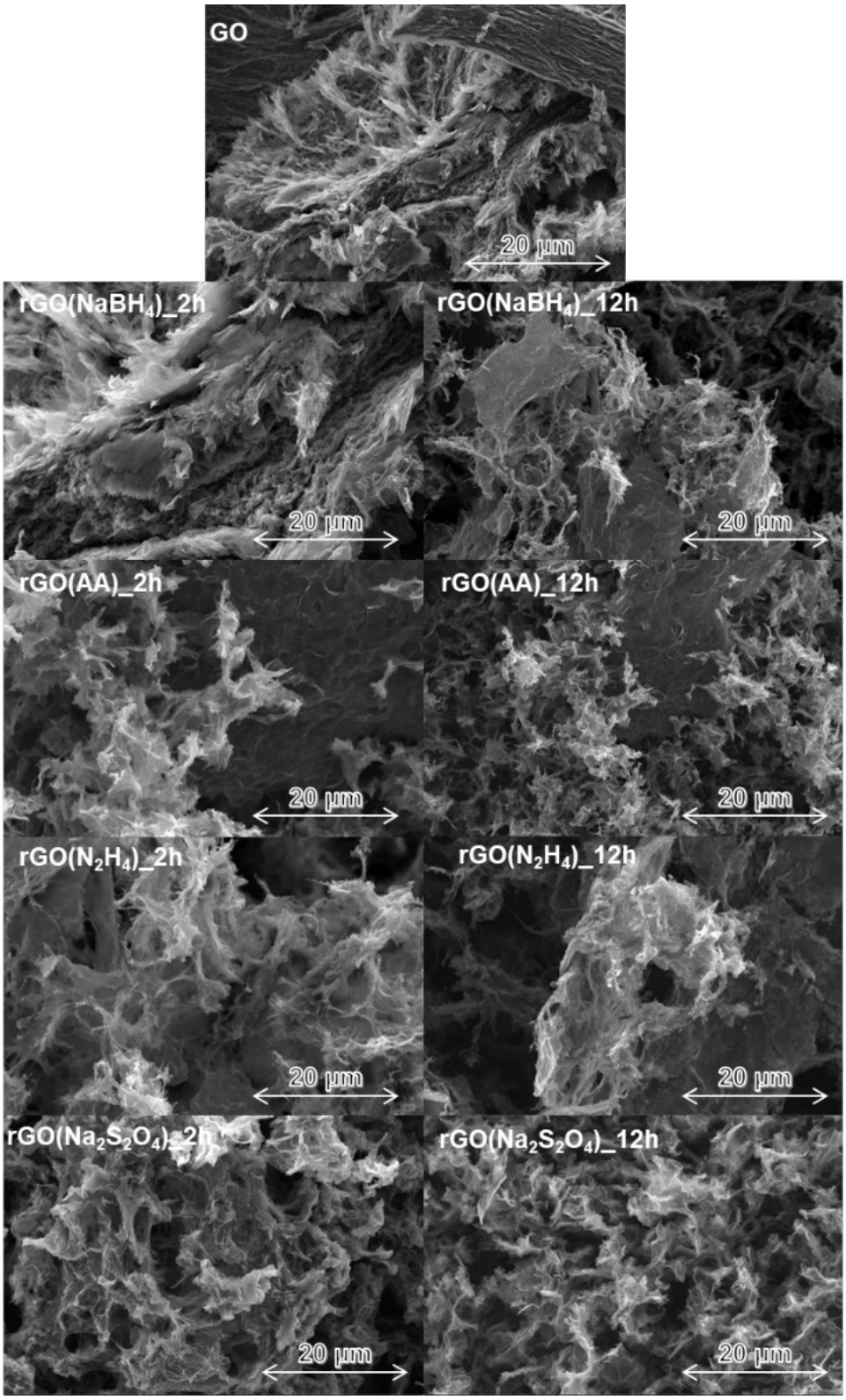

Fig. 36 *SEM images of GO and CrGO with different reducing agents and different reaction times.*

The specific surface area and average pore size of CrGO were evaluated by recording N_2 adsorption–desorption isotherms at 77 K. The adsorption isotherms of the CrGO exhibited type-I sorption isotherms, with steep rises appearing at low relative

pressure and type-IV sorption features with adsorption/desorption hysteresis at higher pressure. The obtained isotherms are presented on Figure 37 for GO and 38 for CrGO. The calculated Brunauer–Emmett–Teller (BET) surface area of CrGO revealed significant differences between the reducing agents used (presented on Figure 39 (a)). In all cases, the surface area increased with reaction time, showing an increase between 25% and 97%. Interestingly, the two reducing agents that produced CrGO with the highest carbon-to-oxygen (C/O) ratio, $Na_2S_2O_4$ and N_2H_4, resulted in the lowest surface areas, measuring 140.91 m^2/g and 96.41 m^2/g, respectively, after 2 hours of reaction. In contrast, when the mildest reducing agents AA and $NaBH_4$ were used, CrGO exhibited the highest surface areas (394.90 and 555.63 m^2/g, respectively, after 12 hours of reaction) compared to pristine GO (12.61 m^2/g). he same trends were observed for the average pore size of CrGO (see Figure 39 (b)) ranging from 1.40 nm when $Na_2S_2O_4$ was used for 2 hours of reaction time, to 13.70 nm when AA was used for 12 hours of reaction time.

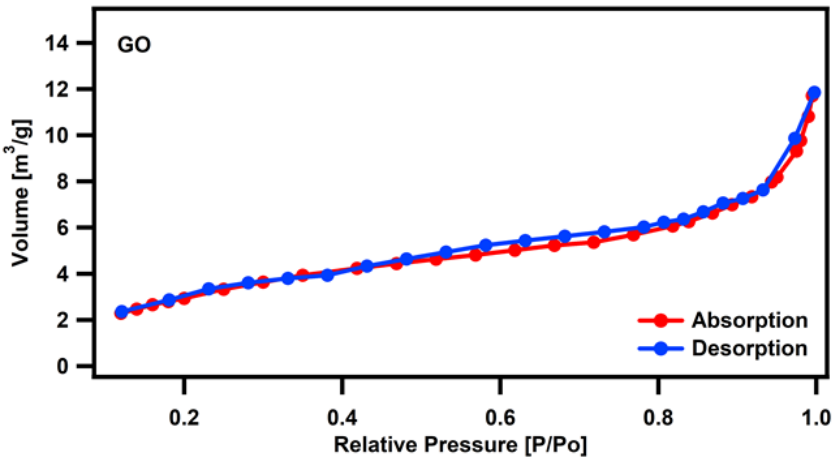

Fig. 37 *BET surface area for GO.*

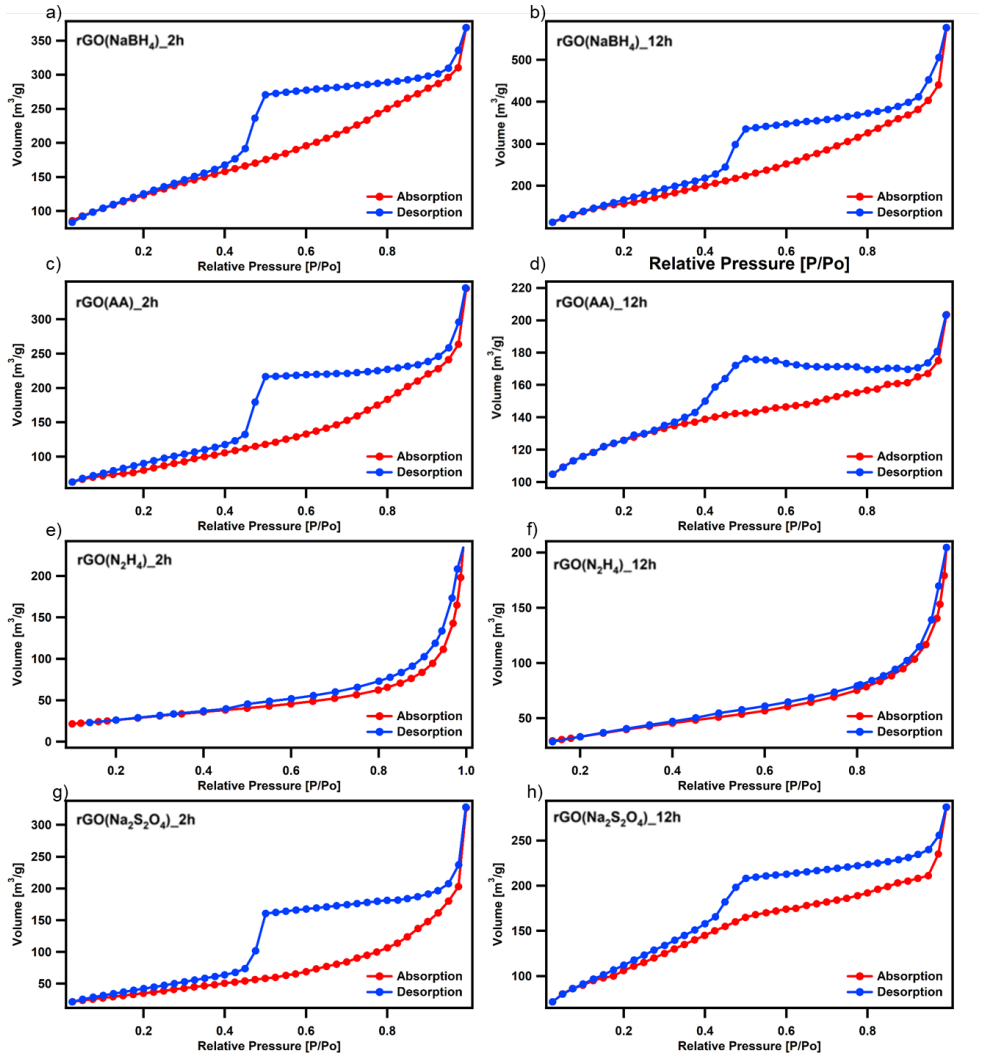

Fig. 38 *BET surface area for CrGO with different reducing agents and a), c), e), g) 2 hours and b), d), f) h) 12 hours of reaction time.*

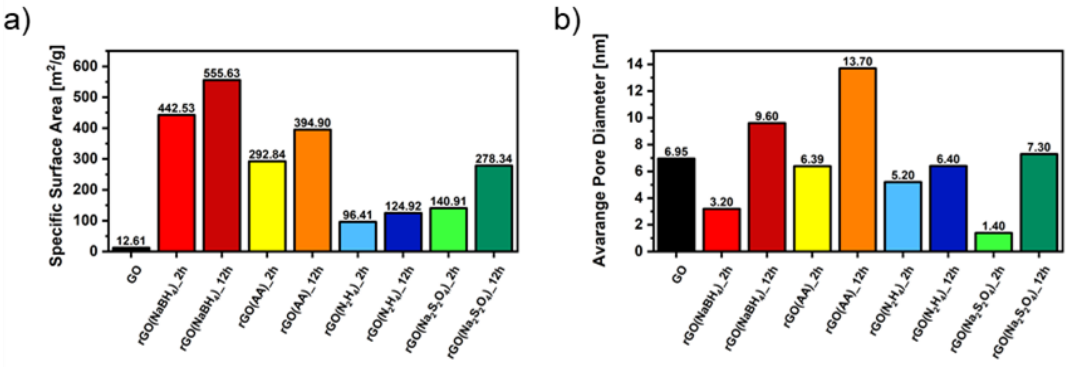

Fig. 39 *a) Specific surface area and b) average pore diameter obtained from BET isotherms of CrGO samples.*

3.2.3 Conductivity properties of chemically reduced graphene oxide

To gain a greater insight into the electrical performance of CrGO, thin film conductivity measurements were performed. Pellets of different materials were prepared, and the film resistivity was measured with a four-point probe (FPP). Due to its insulating character, the film resistivity of the pristine GO material was above our instrument's detection limit. The film conductivity of CrGO, ranging from 2.7 × 101 S m^{-1} (rGO($NaBH_4$)_2 h) to 4.3 × 103 S m^{-1} (rGO($Na_2S_2O_4$)_2 h), gradually increased with the strength of the employed reducing agent, following a trend in full agreement with the previous characterization results. Therefore, for electrical applications, rGO(AA)_12 h, rGO(Na_2S_2O) and rGO (N_2H_4) represent the best choices, as their performance is comparable. The obtained values for all CrGO samples are presented on Figure 40.

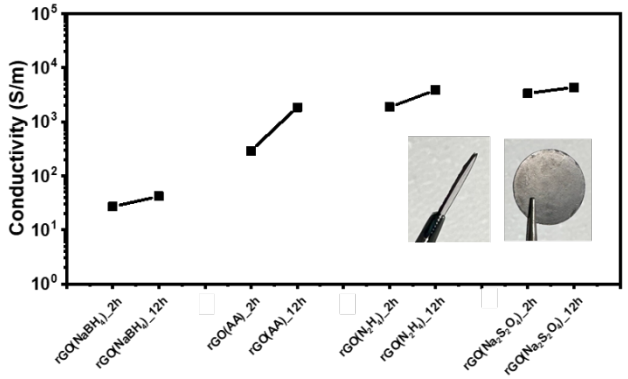

Fig. 40 *Film conductivity of CrGO with different reducing agents and different reaction times. Inset, lateral and frontal side of a representative pellet.*

Moreover, to explore the compatibility of our reduction process with substrates employed in flexible electronics such as flexible strain sensor device, the reduction of a film GO deposited on PET is performed using the four reducing agents. As can be seen in Figure 41 only the CrGO films reduced with AA and $Na_2S_2O_4$ are stable and homogeneous. Furthermore, the mechanical stability of the films was tested by performing 2000 bending cycles. The resistance of the film was constant for the 2000 bending cycles performed with subtle variations below 1% presented on Figure 42.

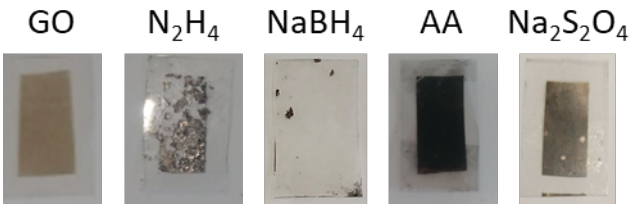

Fig. 41 *Optical images of the films of GO and CrGO with different reducing agents.*

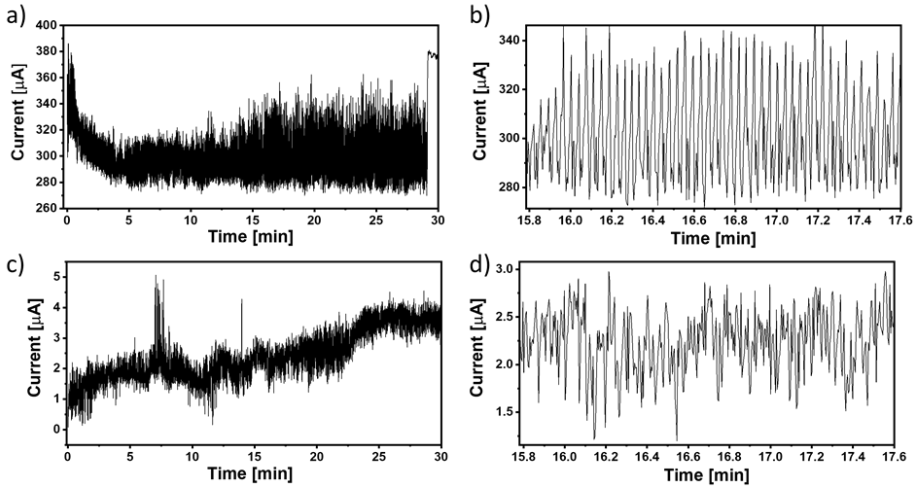

Fig. 42 *Resistance of the CrGO film obtained with a) $Na_2S_2O_4$ and c) AA, as a function of time during the application of 2000 bending cycles. Magnification of the film resistance of CrGO obtained with b) $Na_2S_2O_4$ and d) AA, as a function of time.*

Moreover, surface area, porosity and oxygen content have been identified as the key properties that strongly influence the conductivity of synthesized rGO samples. Figure 43 presents correlation between all aforementioned factors and conductivity of CrGO. The increase in surface area is directly proportional to the electrical conductivity. Moreover, surface area and conductivity follow nearly the same trend for the different reducing agents and reaction times. As in the case of surface pore size and conductivity follow the same trend. The presence of electrochemically active groups (*e.g.*, OFGs) is advantageous, as they can provide a large additional interaction with the analyte in case of gas sensors device. During the reduction process, OFGs are eliminated and therefore this is detrimental to the electrical conductivity. Thus, the two reducing agents that produce CrGO with lower oxygen content (*i.e.*, N_2H_4 and $Na_2S_2O_4$) also show the highest conductivity values. In contrast, AA and $NaBH_4$ produce CrGO with higher oxygen content, but only after 12 hours is the electrical conductivity boosted. Pristine GO, despite having the highest amount of OFG, exhibits the lowest conductivity which was under detection limit of the utilized instrument.

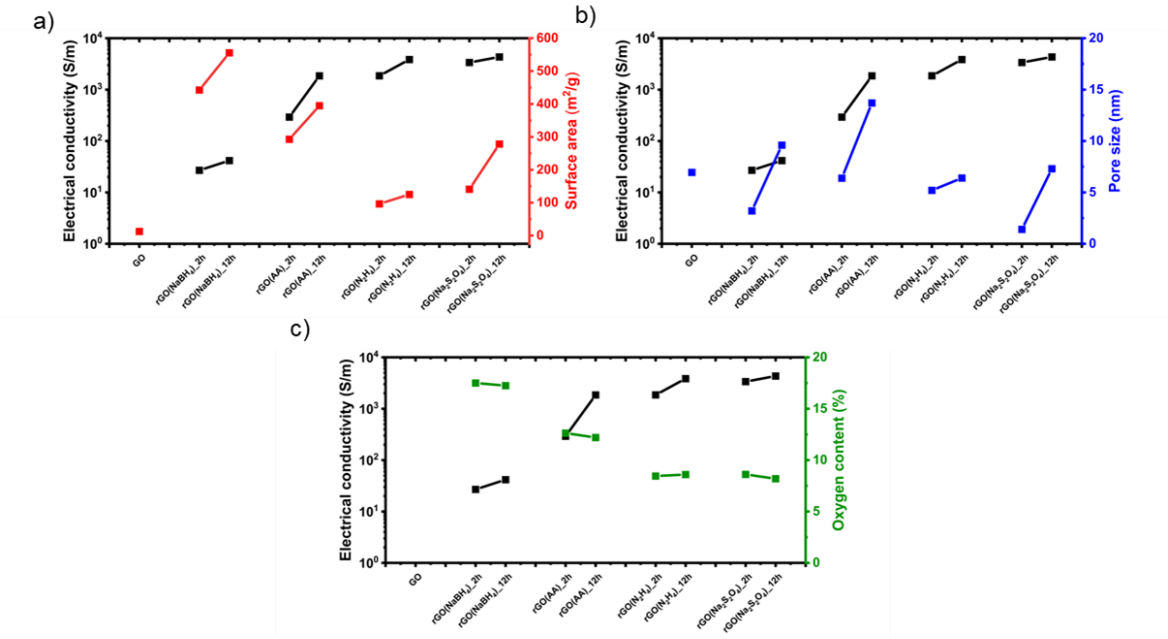

Fig. 43 *Conductivity of CrGO with different reducing agents and reactions times compared with their corresponding a) surface area, b) pore size and c) oxygen content.*

3.2.4 Toxicology of chemically reduced graphene

Considering the importance of reduced rGO in wearable devices, which inevitably come into contact with human skin, the toxicology tests were conducted specifically focused on assessing its potential to cause skin irritation, a common concern at the cutaneous level. The irritation potential of rGO was evaluated using the OECD TG 439 standard, employing the SkinEthic™ Skin Irritation Test (42 minutes exposure + 42 hours post-incubation), which is already fruitfully adopted for graphene-related materials[366]. RhE tissues were exposed to 16 mg of each material in powder form at the air-liquid interface for 42 minutes. After exposure, the tissues were incubated for 42 hours without the materials. The irritation potential was evaluated based on tissue viability, with values ≤50% indicating potential irritation. The MTT reduction assay was used to measure the reduction in tissue viability caused by rGOs, as depicted in Figure 44.

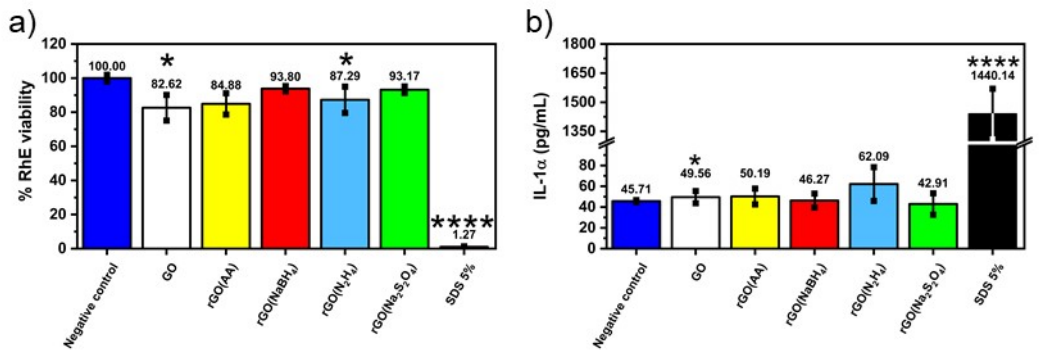

Fig. 44 *Assessment of skin irritation properties of chemically reduced GOs (a) using the SkinEthic™ Skin Irritation Test*$^{-42bis}$ *(OCED TG 439). Results represent tissue viability reductions induced by rGOs evaluated using the MTT reduction assay with respect to negative controls (RhE exposed to PBS); 5% SDS was used as the positive control. Results are the mean ± SE of three independent experiments. Statistical differences vs. negative controls: *p < 0.05; ****p < 0.0001 (one-way ANOVA and Bonferroni's post-test) and (b) the release of IL-1α from RhE exposed to chemically reduced GOs. IL-1α was measured using a specific sandwich ELISA in growth media collected from RhE after exposure to each material; 5% SDS was used as the positive control. The data, reported as pg mL−1 of IL-1α released in the media, are the mean ± SE of three independent experiments. Statistical differences vs. negative controls (RhE exposed to PBS): ****p < 0.0001 (one-way ANOVA and Bonferroni's post test).*

In general, none of the material's RhE viability was reduced to levels lower than the threshold value given by the OECD TG 439 (tissue viability ≤50%) and, therefore, they can be considered as non-irritant materials. Among the different samples, the rGO(AA)_2 h (reduction of cell viability by 15%; $p < 0.05$), rGO(N_2H_4)_12 h (reduction of cell viability by 20%; $p < 0.05$) and GO (reduction of cell viability by 17%; $p < 0.05$) were able to slightly reduce RhE viability, even though at levels not predicting the irritant potential. In contrast, the positive control (5% SDS) significantly reduced RhE viability by 99% ($p < 0.0001$), resulting in an irritant compound. The absence of skin irritation was confirmed by the analysis of IL-α release from treated RhE, as an additional biomarker to classify skin irritants using 3D models of the epidermis[391]. Indeed, despite minor variations, none of the materials significantly increased IL-α release from RhE in contrast to the positive control (1440.1 pg mL^{-1}), increasing by more than 30 fold its release with respect to the negative control (45.7 pg mL^{-1}). By and large, these results also suggest that the different chemical reductions, possibly leading to chemical reagent residues and/or changes in the material structure, do not appear to affect the good biocompatibility of graphene-related materials previously reported by both in vitro[392-396] and in vivo[397] studies.

3.3 Conclusions

In summary, the study introduced, developed and optimized, scalable, easily controllable, and energy-efficient method for producing chemically reduced CrGO with customizable electrical properties. This research, corroborated by ssNMR, indicate that the peak area corresponding to Csp^2–O species serves as an excellent indicator of the reduction strength of the employed reducing agents. Specifically, the following trend was observed: $Na_2S_2O_4 \approx N_2H_4 > AA > NaBH_4$, which aligns with the outcomes of FTIR analysis, elemental analysis, and XPS analysis. Furthermore, the peak area of the Csp^2–O species revealed the influence of the reaction time on GO reduction for three of the reducing agents, namely $Na_2S_2O_4$, AA, and $NaBH_4$.

Moreover, that investigations using EA and XPS revealed that the utilization of N_2H_4 during the GO reduction process resulted in nitrogen contamination and pyrazole formation. Similarly, $NaBH_4$ led to sodium contamination, while AA induced a supramolecular interaction with DHA within the CrGO structure. Notably, these results demonstrate that CrGO with excellent electrical conductivity (>1800 S m^{-1}) can be synthesized using AA (with a 12 hour reaction time), $Na_2S_2O_4$, or N_2H_4 (regardless of reaction time). CrGO produced with AA or N_2H_4, exhibiting reduced hydrophilicity, enabled the fabrication of films on flexible plastic substrates, maintaining resistance even after enduring 2000 bending cycles. This feature, clearly indicate that CrGO can be utilized for flexible pressure and humidity sensing electronics.

Furthermore, skin irritation tests demonstrated that all variants of CrGO could be considered non-irritating materials, affirming that the reduction process does not compromise their biocompatibility at the cutaneous level. These findings represent a significant advancement in the application of rGO, particularly in wearable and flexible electronics with skin-level interactions.

Chapter 4 - Thermal reduction of graphene oxide

4.1 Introduction

Over the past fifteen years, extensive research has focused on converting electrically insulating GO into its conductive form, rGO by removing OFGs and (partial) restoring sp^2 conjugation. This scalable and low-cost method produces materials with graphene-like properties. Among the various protocols, thermal annealing stands out as an appealing, environmentally friendly approach compatible with industrial processes. However, the high temperatures typically required to accomplish this process are energetically demanding and are incompatible with the use of plastic substrates often desired for flexible electronics applications such as pressure and strain sensors. Thus, a systematic study on the low-temperature annealing of GO by optimizing different annealing conditions, *i.e.*, temperature, time, and reduction atmosphere is needed.

The GO is a distinctive multifunctional 2DM consisting of carbon, oxygen, and hydrogen atoms in varying ratios. It was first synthesized nearly 150 years ago[398]. However, at present GO is primarily produced by treating natural graphite flakes with strong oxidants, predominantly utilizing a modified version of the Hummers' method[68]. The presence of various OFGs like epoxy, hydroxyl, and carbonyl on both the basal plane and the edges gives GO a distinctive combination of mechanical and optical properties. Additionally, these functional groups contribute to GO's excellent dispersibility and colloidal stability in many solvents, particularly in water[399-403]. Furthermore, utilizing well established chemical strategies, these OFGs can be utilized as sites for chemical modification, thereby enhancing GO potential applications in sensing application. Due to the use of strong oxidants like potassium permanganate in most GO production methods, GO typically contains a considerable number of defects in its crystalline structure. This results in a reduction in electrical conductivity, which hinders the direct application of GO in electronics[404, 405]. Significant efforts have been dedicated to removing OFGs from GO through reduction processes. The aim is to enhance the degree of conjugation in the carbon network by forming sp^2 species, thereby improving the material's electrical properties with the goal of approaching the characteristics of graphene[5]. GO reduction yielding electroactive rGO can be achieved through a variety of chemical (CrGO) or thermal (TrGO) methods. Chemical reduction is still the most common and efficient approach for reducing GO using a plethora of reducing agents including hydrazine,

sodium borohydride ($NaBH_4$), hydrogen iodide, or AA[91, 92, 375, 376, 406, 407]. However, the cost of chemicals and the substantial amount of chemical waste generated render this methodology industrially undesirable[94]. Chemical reagents can be avoided by using the electrochemical method. In this approach, the reduction of GO depends on the exchange of electrons between the GO and the electrode, which takes place inside an electrochemical cell in the presence of an aqueous buffer solution. However, electrochemical reduction is limited to substrates that can serve as electrodes. While chemical reduction remains one of the most efficient and widely used solution-based protocols, it is inconvenient due to the production of a stoichiometric amount of chemical waste. Thus, thermal reduction stands out as one of the most appealing reduction methods due to its minimal environmental impact. Thermal reduction involves annealing GO under controlled atmospheric conditions, resulting in the desorption of products such as H_2O, CO_2, and CO. It is widely acknowledged that under vacuum and annealing temperatures ranging from 100 to 185 °C, interlamellar H_2O molecules are removed. At temperatures between 185 and 300 °C, epoxide and carbonyl groups are eliminated, followed by the removal of ether and hydroxyl groups at temperatures ranging from 700 to 1200 °C. This sequential process results in a material with a higher carbon to oxygen ratio[95, 408]. However, these high temperatures are energetically demanding and unsuitable for thermal reduction of GO on plastic substrates used in flexible electronics. Typical substrates for flexible and wearable electronics include materials such as polyethylene terephthalate and polyimide which retain their mechanical properties at temperatures up to 175 °C for PET and 232 °C for PI. That feature is huge limitation according to flexible sensing application. Thus, there is a strong demand for the thermal reduction of GO at relatively low temperatures. In recent years, a few studies have reported achieving the thermal reduction of GO at relatively low temperatures (<300 °C)[409-413]. For example, it has been discovered that the reduction temperature can be lowered to 150 °C at atmospheric pressure when GO is dispersed in propylene carbonate or in a mixture of water and organic solvents[412]. Grossman et al. measured the sheet resistance of GO films annealed at 50 and 80 °C in air. After five days of annealing at 80 °C, the sheet resistance dropped from 1010 Ω sq^{-1} of pristine GO to 105 Ω sq^{-1} mainly due to the interlamellar H_2O desorption[414]. Chhowalla *et al.* reported that GO films reduced under ultra-high vacuum (UHV) for 15 minutes at 150 and 200 °C have a resistivity of about 10 and 10^{-2} Ω m, respectively, and when the reduction is performed in Ar/H_2 for 15 minutes at 200 °C, a resistivity of 10^{-2} Ω m was obtained[410]. Nazarov

et al. investigated thermal reduction in air at temperatures ranging from 130 to 200 °C with an annealing time of 15 minutes. They observed a decrease in resistivity from 4×10^5 Ω m to 4×10^{-2} Ω m. This reduction was attributed to an initial desorption of H_2O, followed by the desorption of oxygen-containing functional groups, releasing CO and CO_2[415]. These examples emphasize that regardless of the reduction atmosphere, annealing at 200 °C for 15 minutes consistently reduces resistivity to approximately 10^{-2} Ω m. Sun *et al.* investigated the kinetics and thermodynamics of GO deoxygenation under argon using thermogravimetric analysis coupled with a mass detector. They observed a dramatic increase in CO and CO_2 signals near 180 °C, with traces of CO_2 detected as early as 130 °C[413]. While these examples demonstrate that thermal reduction of GO can be achieved at relatively low temperatures, the relationship between changes in conductivity and other parameters such as chemical composition, surface area, or crystallinity of TrGO remains unclear. There is no systematic study has explored and optimized the annealing conditions and correlated them with changes in GO's structure and functions. To address this significant gap the thermal reduction of GO at various low temperatures (100, 130, 150, 200, 250, and 300 °C) under both air and inert atmospheres has been studied. Moreover, the effect of annealing conditions on the chemical structure, various physico-chemical parameters, and the conductivity has been investigated. Furthermore, to demonstrate the full compatibility of the reduction strategy with the use of plastic substrates, the proof-of-concept devices consisting of *ca.* 66 nm thick TrGO films supported on flexible PET substrates were fabricated and monitored their resistance during 2000 bending cycles.

4.2 Results

4.2.1 Chemical composition of thermally reduced graphene oxide

To gain insight into the chemical composition of TrGO, XPS analyses were performed on the GO powders annealed for 4 hours. The XPS spectra obtained from TrGO samples are presented on Figure 45. The with C/O ratio analysis in the function of temperature utilized is illustrated on Figure 46. From the survey spectra, a C/O ratio of 2.5 is estimated for pristine GO.

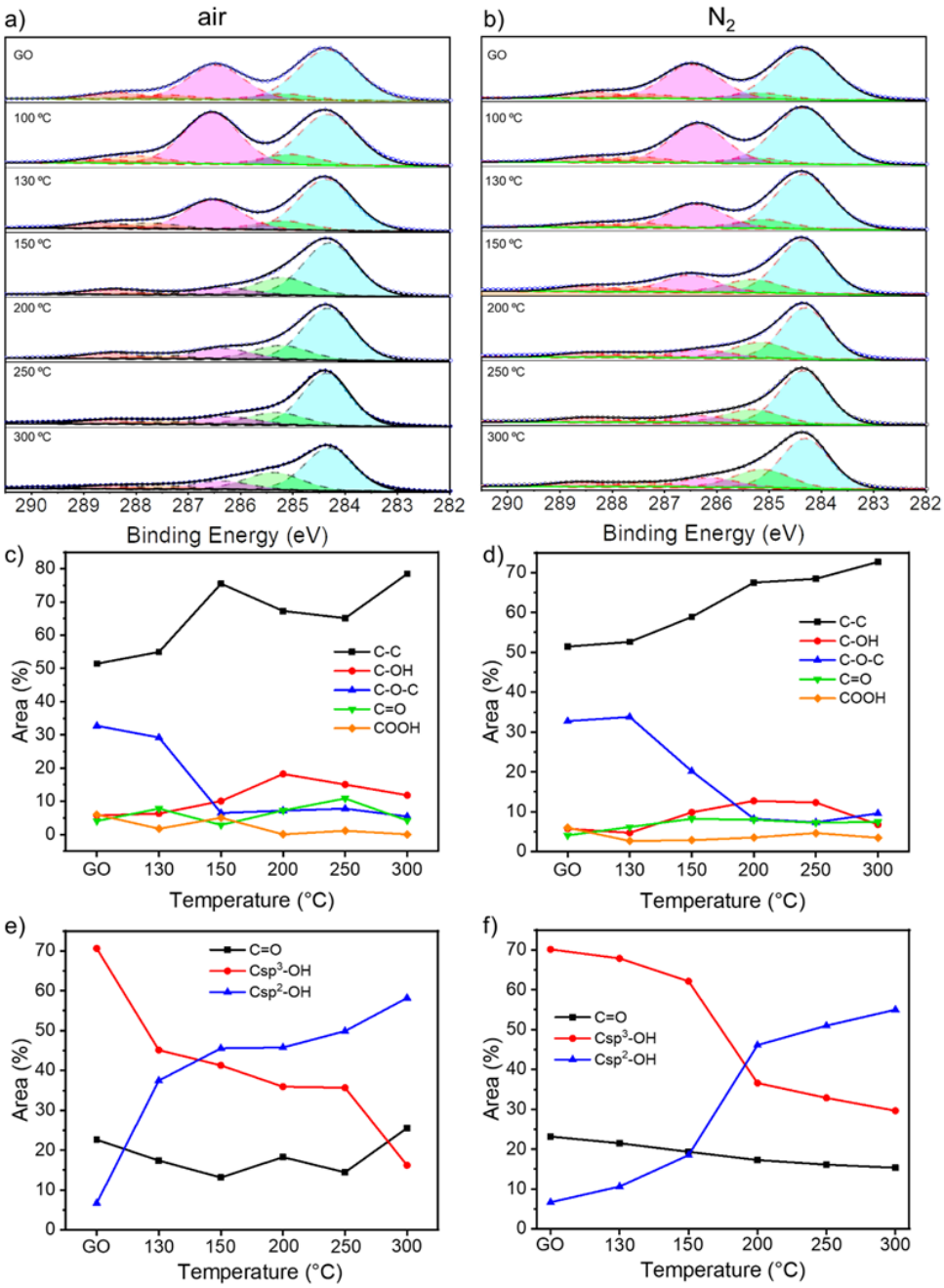

Fig. 45 *High-resolution XPS C 1s peaks of thermally reduced GOs under (a) air and (b) N_2; temperature dependence of the relative contribution of C 1s peak components estimated by dividing the area under each component by the whole C 1s peak area for (c) air and (d) N_2; temperature dependence of the relative contribution of O 1s peak components estimated by dividing the area under each component by the whole O 1s peak area for (e) air and (f) N_2.*

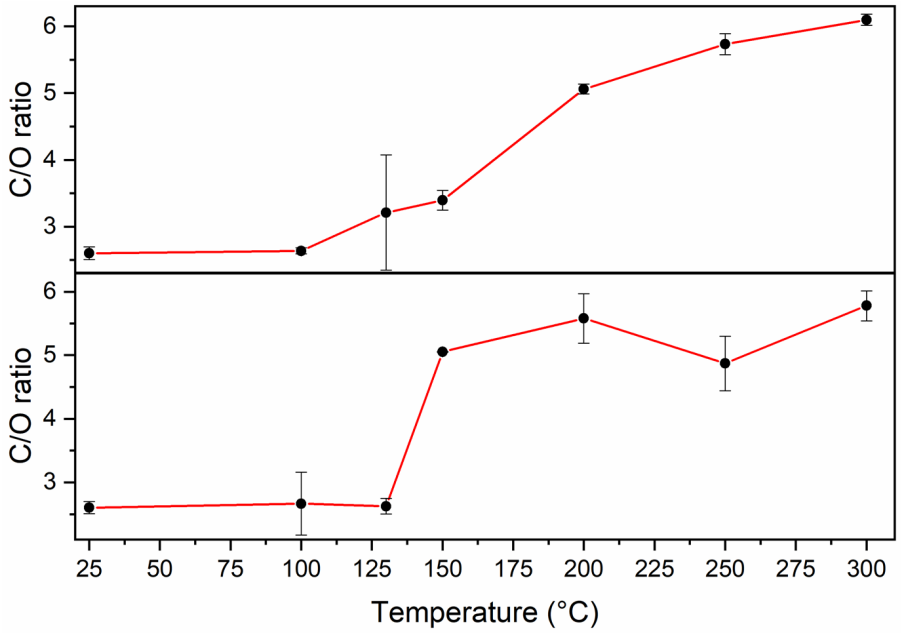

Fig. 46 *C/O ratio obtained from the XPS analysis of the TrGO under N_2 (top) and air (bottom).*

During the annealing, H_2O, CO and CO_2 are released and, consequently, the C/O ratio increases, indicating the reduction process. The C/O ratio increases between 130 and 200 °C for the samples annealed either under air or nitrogen; however, while the C/O ratio increases gradually when the annealing is performed under N_2, more rapid changes are monitored when the annealing is performed in air. For example, at 150 °C, the C/O ratio is 5.05 in air compared to 3.40 in a N_2 environment, indicating that the reduction process at lower temperatures is more efficient in air. The high-resolution C 1s spectrum is fitted with five Gaussian-Lorentzian curves representing five chemical environments such as: at 284.4 eV C–C (Csp^2–Csp^2), 285.15 eV C–O (including Csp^2–O–Csp^2, Csp^3– OH and Csp^2–OH), 286.48 eV C–O–C (Csp^3–O–Csp^3), 287.38 eV C=O, and 288.50 eV COOR (including COOH and lactone). On Figure 45 (c) and (d) is shown the evolution of the area of each component as a function of annealing temperature. As expected, the area of the C–C peak increases with annealing temperature in both atmospheres due to the reduction of oxygen content in the sample. Conversely, the area of the C–O–C peak sharply decreases at 150 °C when annealing in air and at 200 °C when annealing in N_2. However, the areas of the other three peaks remain relatively constant. To gain a greater understanding of the nature of the OFGs, the high-resolution XPS of O 1s spectrum is fitted with 3 Gaussian–Lorentzian curves: 531.08 eV C=O, 532.03 eV Csp^3–O (including Csp^3–O–Csp^3, and Csp^3–OH), and 533.43 eV Csp^2–O (including Csp^2–O–Csp^2 and Csp^2–OH) which are presented on Figure 47.

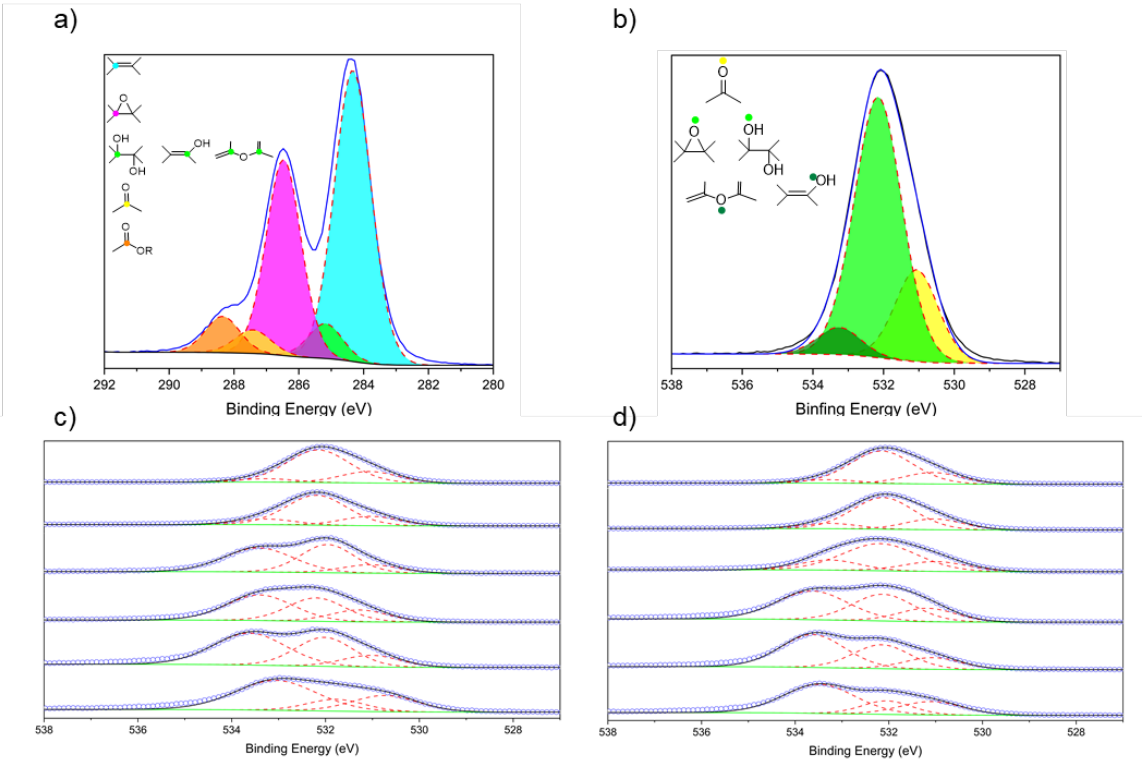

Fig. 47 *Fitted XPS a) C 1s and b) O 1s spectrum of GO and their corresponding chemical groups. XPS analysis of O 1s for the TrGO under (c) air and (d) N_2*

Figure 45 (e) and (f) show how the relative area of each component varies with the annealing temperature. The area of the Csp^3–OH peak decreases starting from 150 °C when the reduction is performed under air and from 200 °C under N_2, following the same trend as the C–O–C peak. In parallel, the relative area decrement of the Csp^3–O peak is accompanied by a drastic increase in the area of the Csp^2–O peak, indicating the inclusion of oxygen atoms in the conjugated carbon network. From XPS analysis, we can conclude that the threshold temperatures for the thermal reduction of GO under air and N_2 amount to 150 °C and 200 °C, respectively.

Further insight into the chemistry of the reduction process was obtained by solid-state NMR magic angle spinning (ssNMR-MAS) analyses, which is presented on Figure 48.

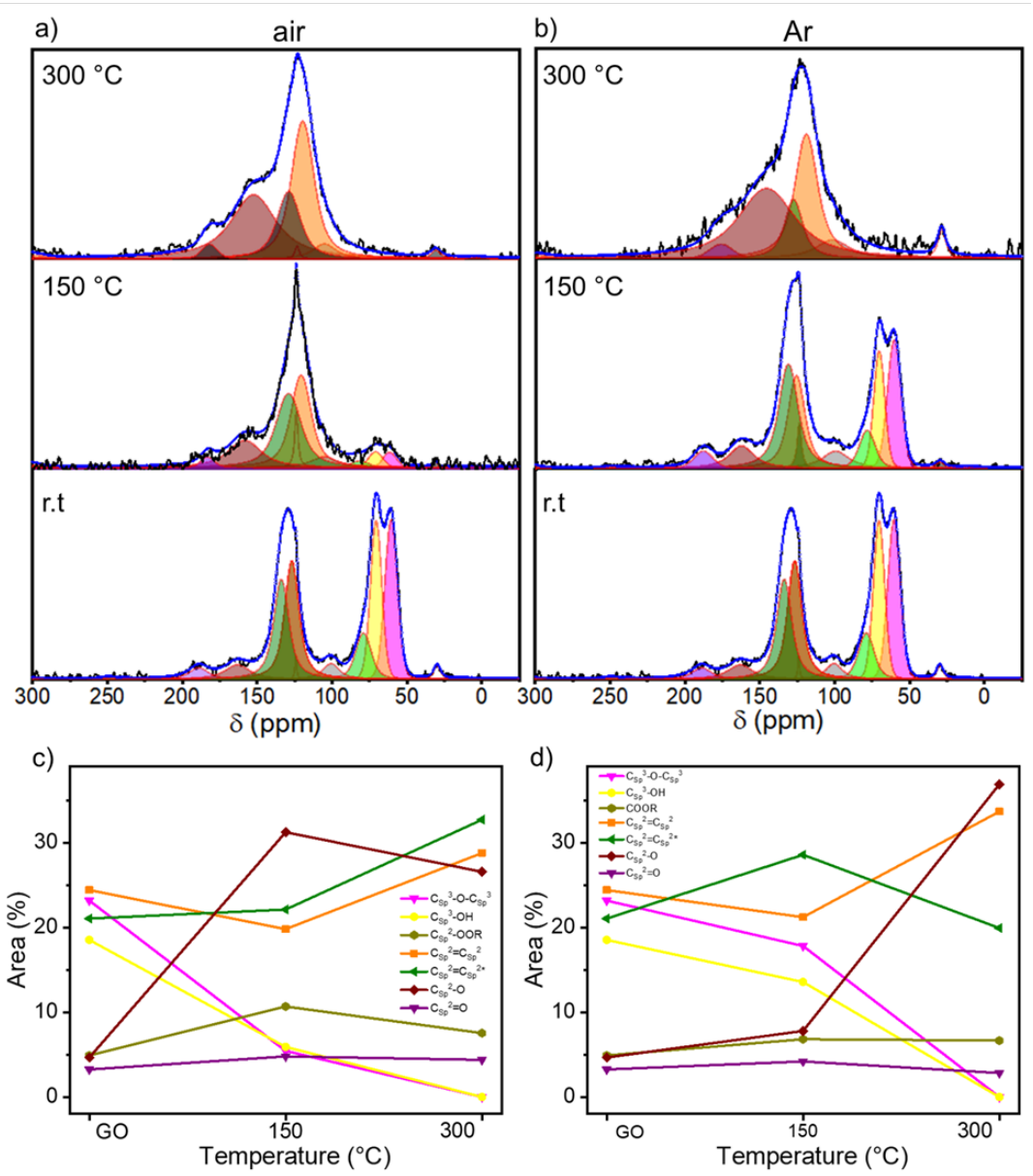

Fig. 48 *Solid-state MAS-NMR C 1s spectra of thermally rGO under (a) air and (b) argon; temperature dependence of the relative contribution of NMR spectral components estimated by dividing the area under each component by the whole peak area for (c) air and (d) argon.*

As previously reported, the ssNMR spectrum of GO is deconvoluted in eight curves corresponding to 60.4 ppm ($^{13}Csp^3$–O–$^{13}Csp^3$), 70.6 ppm ($^{13}Csp^3$–OH), 78.9 ppm ($^{13}Csp^3$–OH, close to defects), 100.2 ppm (^{13}C–OOR), 126.7 ppm ($^{13}Csp^2$–$^{13}Csp^2$), 134.7 ppm ($^{13}Csp^2$–$^{13}Csp^2$ close to defects), 162.4 ppm (Csp^2–O (including Csp^2–O–Csp^2 and Csp^2–OH)) and 187.9 ppm (^{13}C=O)[416-419]. The deconvoluted GO NMR spectra is illustrated on Figure 49.

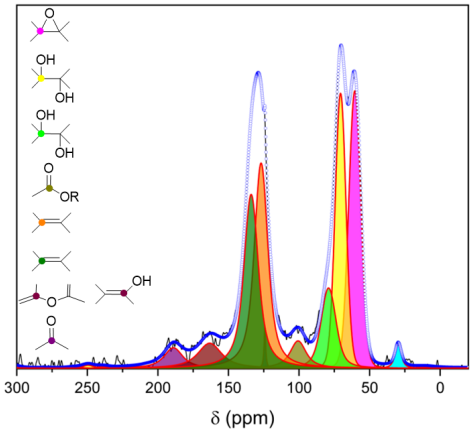

Fig. 49 *Fitted ssNMR spectrum of GO and their corresponding chemical groups.*

Consistent with the XPS analysis, the intensity of peaks related to sp^3 carbons decreases as the annealing temperature increases, while the intensity of sp^2 carbon peaks increases. At 150 °C under argon, there is a slight decrease in the area of the Csp^3–O–Csp^3 and Csp^3–O peaks compared to the pristine GO spectra. However, at 150 °C under air, these peaks are almost completely suppressed, and the Csp^2–Csp^2 peak increases significantly. At 300 °C, the spectra of TrGO under both atmospheres are similar, with the Csp^2–Csp^2 peaks being predominant. As seen in the XPS analysis, the only OFG formed during annealing is Csp^2–O. A quantitative evaluation is performed by plotting the relative areas of the fitted solid-state NMR spectra as a function of the reduction temperature (see Figure 48 (c) and (d)). The $^{13}Csp^2$–O peak increases drastically from 4.7% to 31.2% after the reduction under air at 150 °C and is kept almost constant at 300 °C (27%). However, when the reduction is performed under argon, only at 300 °C the $^{13}Csp^2$–O peak increases sharply to 37%. Moreover, in full agreement with the high-resolution XPS, the ssNMR experiments confirm that the reduction of GO can occur at a lower temperature under air when compared to the inert atmosphere.

As previously documented, the characteristics observed in the Raman spectra of GO and rGO, including band position, intensity ratio, and width can be correlated with structural properties such as oxygen content, crystallinity, and the degree of reduction of GO[383, 384, 419-421]. The Raman spectra of GO and TrGO were deconvoluted using four Lorentzian curves, which consist of the first-order Raman modes, namely: D, G, D″, and D′ bands and are presented on Figure 50 and Figure 51 respectively.

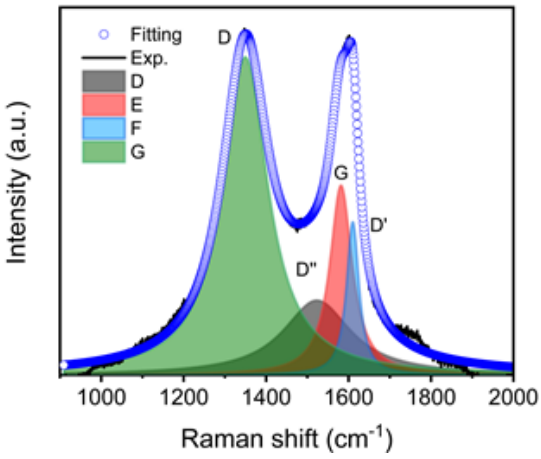

Fig. 50 *Fitted Raman spectra of GO.*

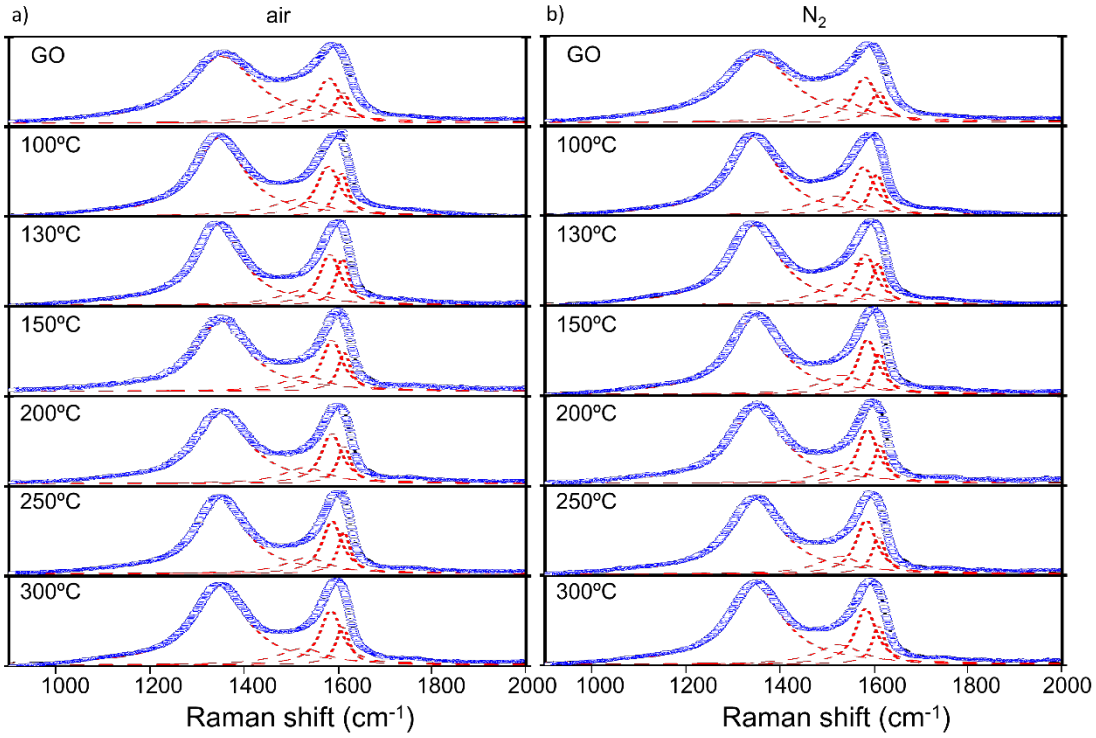

Fig. 51 Fitted Raman spectra of GO and TrGO under (a) air and (b) under N_2 at different temperatures.

The D band, situated between 1330 and 1355 cm^{-1}, originates from the A_{1g} breathing modes of six-membered rings. These modes are activated by defects like vacancies, grain boundaries, and disorder in the carbon lattice, along with double-resonant processes near the K point of the Brillouin zone boundary[383]. The G band, occurring at 1580–1600 cm^{-1}, corresponds to the first-order allowed Raman mode E_{2g}[384]. Additional bands (D′ and D″) arise due to defects in the graphitic structure of the carbon material. The physical origin of the D′ band at 1610–1620 cm^{-1} remains not

fully understood. Some authors have attributed the D′ band to disorder-induced phonon modes caused by crystal defects, while others associate this band with double vacancies that result in pentagonal and octagonal rings, often known as 5–8–5 defects[384]. The D″ band, located at 1500–1550 cm^{-1}, is associated with the amorphous phase, and its intensity decreases as crystallinity increases[422]. The relative intensity of the D band compared to the G band (I_D/I_G ratio) is a well-established parameter for assessing the degree of defects in graphene oxide (GO) derivatives. It has been correlated with the inverse of the crystallite size on basal planes ($1/La$) using the Tuinstra–Koenig model. Upon GO thermal reduction, the intensity of the G peak increases and hence the I_D/I_G ratio decreases with the annealing temperature. The results are presented on Figure 52.

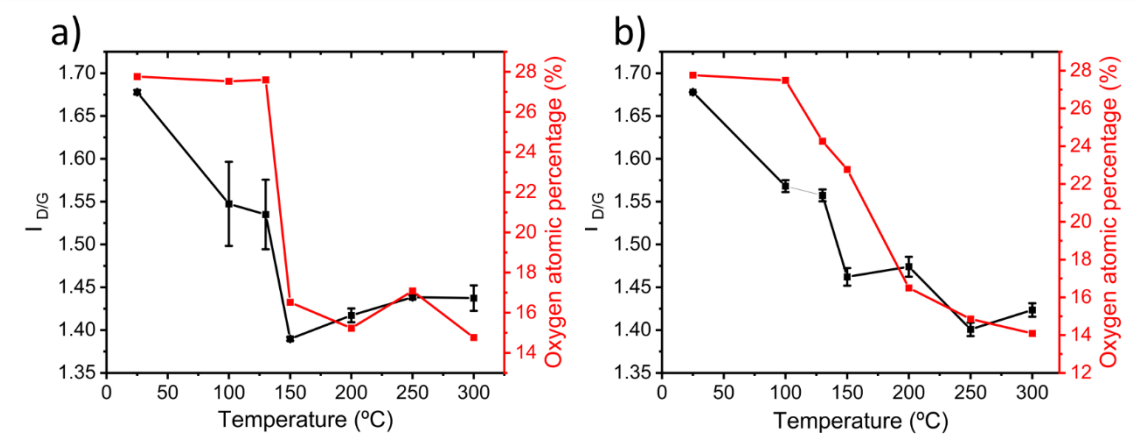

Fig. 52 *Evolution of the I_D/I_G ratio values and the oxygen atomic percentage of TrGO as a function of the annealing temperature under (a) air and (b) under N_2.*

Moreover, the oxygen atomic percentage obtained by XPS is also included on Figure 52 for a better understanding of the degree of GO reduction. This Figure shows that upon thermal reduction under air, an abrupt decrease of both the I_D/I_G ratio and oxygen atomic percentage at temperatures ≥150 °C is observed, with both parameters becoming stable (I_D/I_G = ~1.42 and ~15% oxygen atoms). However, when thermal reduction is conducted under N_2, a slower decrease in both parameters is observed, reaching similar minimum values as reduction under air above 250 °C. The intensities of the D′ and D″ bands also decrease as the degree of reduction progresses, reflecting a reduction in the number of defects on the basal plane of GO. Figure 53 demonstrates that the $I_{D'}/I_G$ ratio and the $I_{D''}/I_G$ ratio decrease with increasing annealing temperature under both air and N_2 atmospheres.

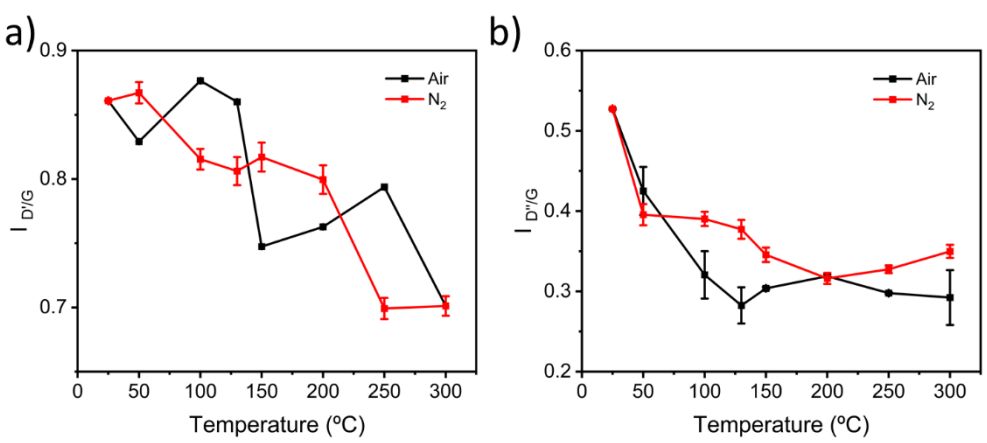

Fig. 53 *Evolution of the (a) $I_{D'}/I_G$ and (b) $I_{D''}/I_G$ ratio values of TrGO as a function of the annealing temperature under air (black curves) and under N_2 (red curves).*

It is also important to note that while the $I_{D'}/I_G$ ratio decreased to ~20% of its initial value, the $I_{D''}/I_G$ ratio decreased ~45% (under air) and ~35% (under N_2) of their respective initial values. From this result two conclusions can be drawn. At first, thermal annealing reduces mainly the defects related to the D″ band. Secondly, this process is more pronounced for annealing under air, leading to a more crystalline structure. Moreover, the effect of temperature on the crystallinity of TrGO is investigated by PXRD presented on Figure 54. Pristine GO diffraction pattern displays one characteristic peak at 2θ = ~11° (peak I) with a full-width half maximum (FWHM) of ~ 1.2° related to the (002) family of planes (see Figure 54 (a) and (b)).

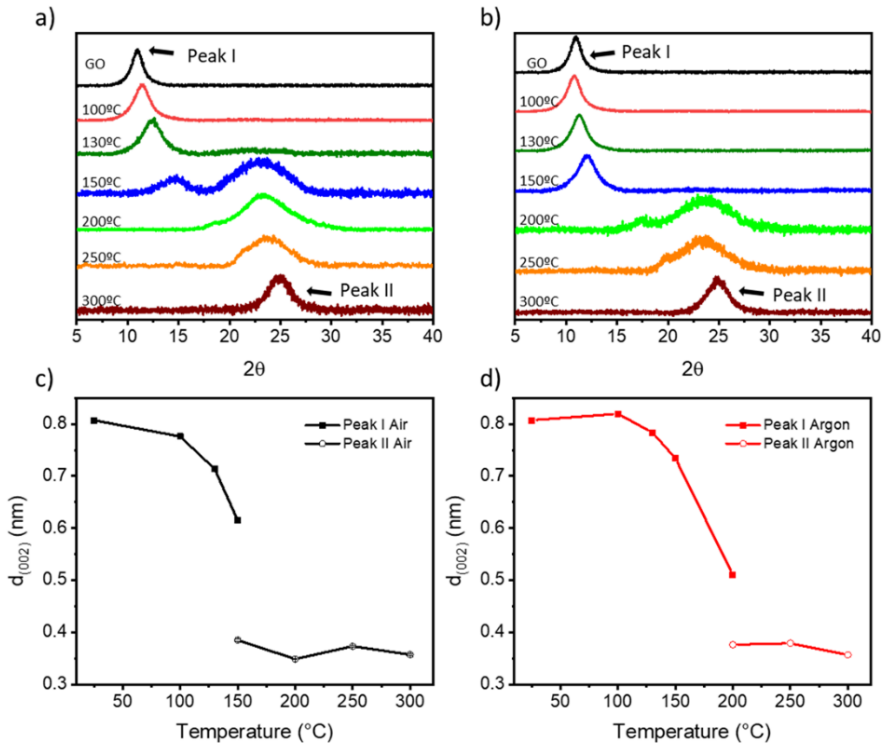

Fig. 54 *(a and b) Diffraction patterns of TrGO under (a) air and (b) argon at different temperatures; (c and d) calculated d-spacing for peak I (full squares) and peak II (empty circles) for the samples annealed under (c) air and (d) argon.*

On the other hand, rGO exhibits one characteristic peak at 2θ = ~25° (peak II) with a larger FWHM of ~5°, five times larger compared to peak I, which indicates a smaller crystallite size. Figure 54 (a) and (b) show a gradual disappearance of peak I and a gradual increase of peak II upon increasing the annealing temperature. In agreement with previous characterization studies, such as XPS and Raman spectroscopy, when the annealing is performed under air, peak II appears at a lower temperature (*i.e.*, 150 °C) compared to annealing performed under argon (*i.e.*, 200 °C), and the full reduction is achieved at 200 °C under both atmospheres. From the PXRD patterns different parameters can be determined (*e.g.*, interlayer distance and the number of GO layers). First, from the scattering angle (*2θ*) of each peak (see Figure 55), the d-spacing parameter was quantified. At 150 °C in air and 200 °C in argon, there is the coexistence of peaks I and II, hence two d-values are determined. The estimated d-spacing of GO is ~0.8 nm, in agreement with the reported values[423]. When GO is annealed under air from 100 to 150 °C, peak I shifts toward higher scattering angles, indicating a contraction of the interlayer spacing. This effect can be attributed to the evaporation of the entrapped H_2O. Conversely, when GO is annealed under argon from 100 to 150 °C, only a slight shift of

peak I from 11° to 12° is recorded. Above 150 °C (under air) and 200 °C (under argon), peak I intensity drops significantly and peak II becomes the major feature in the diffractogram with a calculated d-spacing of TrGO of ~0.3 nm. The further shrinking of the interlayer distance is related to the partial removal of the OFGs from the GO sheets. Furthermore, considering the crystallite size (*Lc*) (see Fig. 55) and the interlayer spacing d (002), and the interlayer spacing d (002) was estimated. This results clearly indicate that for GO annealed in air few layer-thick rGO sheets (4–6 layers) can be produced already at 150 °C. Remarkably, the low-temperature annealing under both atmospheres (*i.e.,* air and argon) allows us to produce high-quality few-layer rGO, starting from commercially available GO with a high percentage of monolayers (>95%) with promising characteristics for integration into electronic devices.

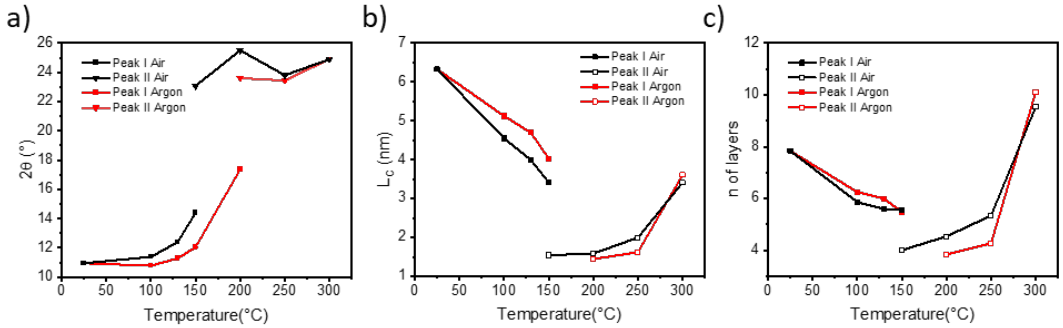

Fig. 55 *a) Main peak position for GO and TrGO under air (black curves) and under argon (red curves), b) crystallite size calculated for GO and TrGO under air (black curves) and under argon (red curves) and c) number of GO layers for GO and TrGO under air (black curves) and under argon (red curves)*

4.2.2 Structure of thermally reduced graphene oxide

The porosity of TrGO annealed at different temperatures under air or argon is evaluated by recording N_2 adsorption–desorption isotherms at 77 K. The results are presented on Figure 56 (a), (b). The adsorption isotherms of TrGO exhibited type-I sorption isotherms, with steep rises appearing at a low relative pressure and type-IV sorption features with adsorption/desorption hysteresis at higher pressure. The calculated BET surface area of TrGO increases gradually with the rising annealing temperature up to 300 °C, from 12.61 $m^2\ g^{-1}$ for the as-prepared GO to 480.44 $m^2\ g^{-1}$, when the annealing is performed under air. In contrast, when the annealing is performed under argon the surface area abruptly increases at 200 °C to 439.92 $m^2\ g^{-1}$, and then remains roughly constant. The average pore size increases gradually with thermal treatment temperature, following the same tendency as the specific surface area. The Figure 56 (c), (d) shows the

differential distribution of pore volumes *vs* pore sizes for TrGO under air and argon. It reveals that all materials have a predominant mesopore distribution with sizes in the range between 10 and 100 nm.

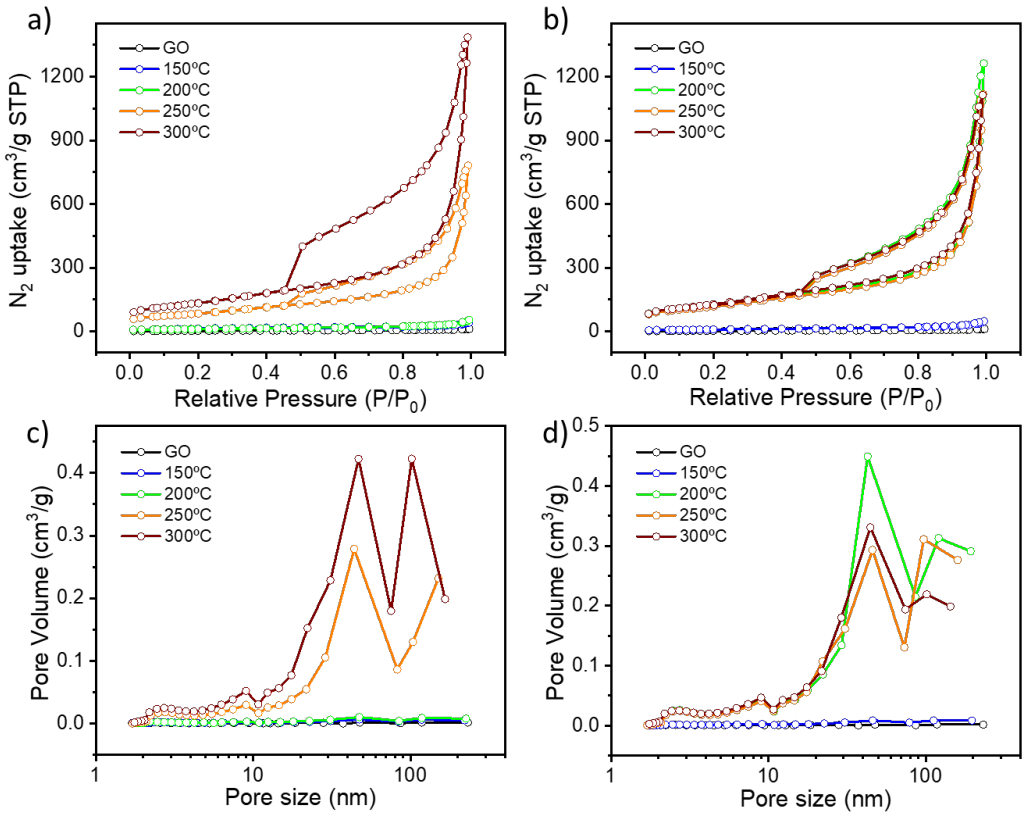

Fig. 56 *BET surface area of GO and TrGO under (a) air and (b) argon. Pore size distribution of thermally reduced GO under (c) air and (d) argon.*

4.2.3 Conductivity properties of thermally reduced graphene oxide

To gain greater insight into the reduction process, the electrical resistivity is used as an internal gauge by performing thin film conductivity measurements. The films of GO (thickness of 66 ± 11 nm) were annealed at 150 and 200 °C under air and under argon, and the film resistivity was measured at different annealing times with a FPP) to follow the kinetics of the reduction process. The results are presented on Figure 57.

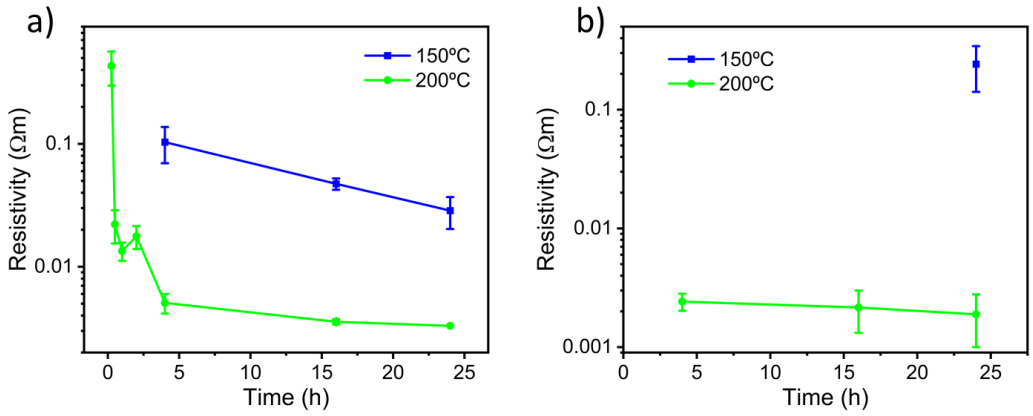

Fig. 57 *a) Kinetic resistivity measurements for the annealing of GO in air at 150 °C and 200 °C for 24 hours and b) for the annealing of GO under argon at 150 ºC and 200 ºC.*

Importantly, N_2 and argon are tested as inert atmospheres and no substantial differences in the electrical characteristics are observed on the resulting TrGO. Under air and inert atmospheres (Ar and N_2), the film resistivity gradually decreases upon annealing at 200 °C with the lowest resistivity being achieved after 4 hours (~3 × 10−3 Ω m). At 150 °C under air, the onset of conductivity in TrGO is observed after 4 hours of reduction with the resistivity continuously decreasing even after 24 hours (~3 × 10−2 Ω m). Conversely, when the annealing is performed under argon, the onset of TrGO's conductivity (~2 × 10−1 Ω m) is observed only after 24 hours. To demonstrate the full compatibility of reduction process with substrates employed in flexible electronics, the annealing of a GO film deposited on PET was performed at 150 °C for 24 h. Then, the mechanical stability of the films was tested by performing 2000 bending cycles. The results for mechanical stability of films are presented on Figure 58.

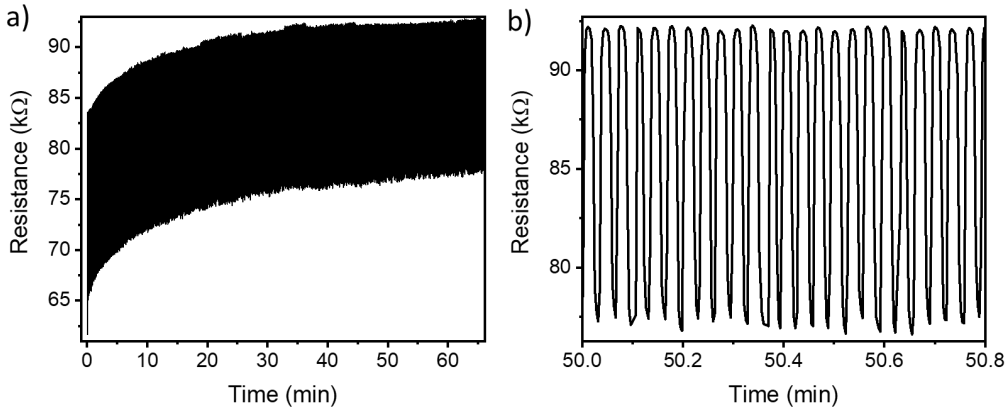

Fig. 58 *a) Resistance of the film as a function of time during the application of 2000 bending cycles with a bending radius of 6 mm, b) magnification of the film resistance as a function of time.*

The resistance of the film is constant for the 2000 bending cycles performed with a subtle increase below 1%. Although 24 hours are needed to produce conductive TrGO when the annealing is executed at 150 °C, the reduction time can be reduced to 4 hours when the annealing is performed at temperatures ≥ 200 °C.

Moreover, on Figure 59 is shown the room-temperature resistivity of 66 nm thick films of TrGO prepared under air and argon at different annealing temperatures. The resistivity measured for TrGO is above the detection limit of the employed instrument (*i.e.* 107 Ω sq^{-1}) for temperatures below 150 °C under argon and below 100 °C under air. Under an argon atmosphere, from 200 °C to 300 °C, the resistivity of TrGO decreases from 3×10^{-3} to 4×10^{-4} Ω m, thereby approaching the resistivity of graphite (10^{-5} Ω m)[424] and two orders of magnitude lower than that of rGO annealed at 200 °C in Ar/H_2 or UHV (10^{-2} Ω m)[410]. In contrast, the thermal reduction of GO under air shows a constant decrease in film resistivity from 1 Ω m at 130 °C to 10^{-3} Ω m at 250 °C. Conversely, at 300 °C, an increase in the resistivity of TrGO is observed, which could be ascribed to the partial oxidation of the GO layers since its ignition temperature is 317 °C[425]. Moreover, the differences in the kinetics obtained from the film resistivity measurements may suggest structural reorganization of Csp^3–O to Csp^2–O taking place, it determines a transition of the electrical nature of GO from insulating to conductive.

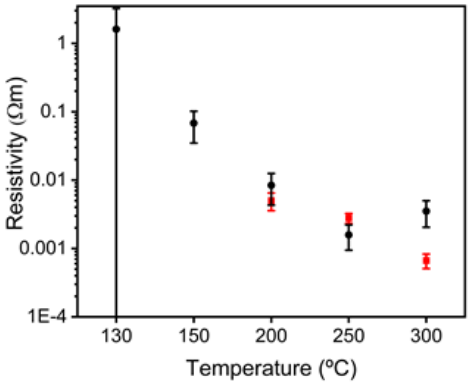

Fig. 59 *Resistivity measurements for TrGO in air (black dots) and argon (red dots) for 4 hours.*

Lastly the surface area, pore size and oxygen content play a key role in the electrical conductivity performance. On the Figure 60 are presented correlations between aforementioned factors toward electrical conductivity.

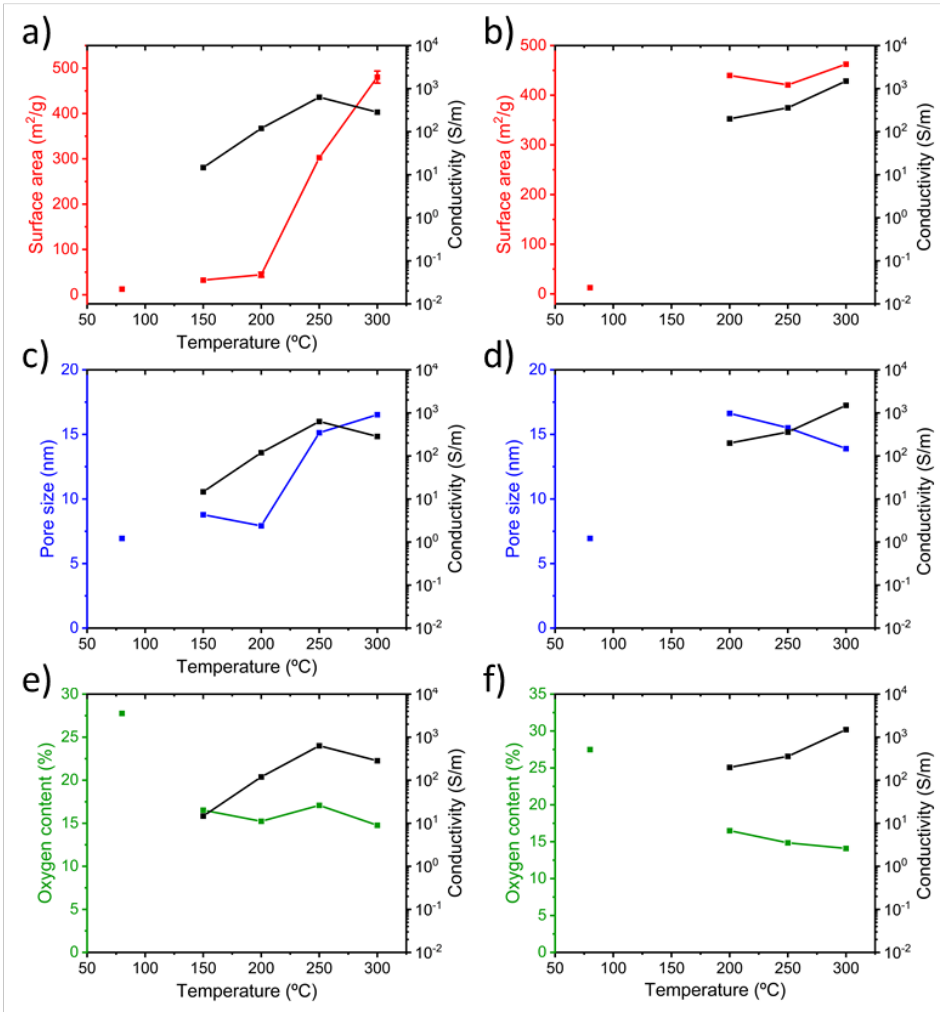

Fig. 60 *Film conductivity (a, c, e) under air and (b, d, f) under argon compared with their corresponding (a, b) surface area, (c, d) pore size and (e, f) oxygen content.*

In the present case, during removal of OFGs, the mechanism is governed by the decrease in the oxygen content of the GO and the increase in film conductivity in both cases under air and argon conditions. That dependence is attributed to restoration of sp^2 network which is presented in pristine graphene. Moreover, an increase in the interface electrical resistance arises from the overlap of graphene sheets. When the reduction is performed under argon, the increase in film conductivity with the annealing temperature is followed by the increase of surface area. Same trend is observed under air condition. Differently, when the reduction is carried out under air the same trend in case of pore size (increase in pore size is accompanied by the increase in the conductivity). However, this tendency is not observed for argon condition, where the trend is revered. That feature clearly indicate that in case of thermal reduction there is no significant correlation between pore size and the performance of conductivity in the material. Moreover, it can be concluded that the increase of pore size has a higher effect on the electrical conductivity performance of TrGO under air, while under argon the effect of pore size and film conductivity cannot be distinguished.

4.3 Conclusions

In summary, it is presented an optimized, scalable, easily controllable, and low-temperature (<300 °C) annealing procedure without chemical treatments for the production of reduced graphene oxide with electrical properties at will. The use of multiple techniques made it possible to gain an unprecedented insight and control over the compositional, structural and electrical characteristics of the materials. The oxygen atoms' reorganization on the GO surface to promote H_2O and CO_2 release is favoured in a range of temperatures between 130 and 200 °C as shown from the XPS and ssNMR analyses. Therefore, it is possible to achieve the elimination of OFGs without promoting the ignition of the carbon framework when the reduction is performed in air. The main OFG formed during the annealing is Csp^2–O, which does not result in any mass loss, yet it determines a variation of the electrical nature of GO from insulating to conductive. Moreover, it has been demonstrated that film resistivities of $\sim 10^{-2}$–10^{-4} Ω m can be achieved by annealing under air between 150 and 200 °C for 24 and 4 hours, respectively, and under an inert atmosphere from 200 °C for 4 hours. Such results indicate the viability of GO reduction upon annealing at temperatures as low as 150 °C, compatible with the use of plastic substrates. Interestingly, films supported on plastic substrates showed unaltered resistance when subjected to 2000 bending cycles. This represents an important

step forward for application in wearable and flexible electronics. Moreover, the loss of OFGs is detrimental to the electrical conductivity performance, it is compensated with a high gain in the surface area and general oxygen content yielding material with ~450 m^2 g^{-1} and 103 S m^{-1}. Moreover, this presented protocol of reduction of GO is suitable for both laboratory and industrial application.

Chapter 5 Graphene-based hybrid as active material for strain and pressure sensor device

5.1 Introduction

In general pressure sensors are devices that can produce electrical signals when there is a change in pressure[104, 105]. These devices have significant technological potential, as they can serve as crucial components for wearable bioelectronics applications, such as monitoring the health of the wearer and their environment[106, 108, 111, 426-428]. A variety of electroactive materials have been utilized as active components, including graphene[107, 323], conductive elastomers[122], and nanoparticles[121]. Among these materials, graphene has been the most extensively researched because of its outstanding electrical and mechanical properties. Moreover, it is worth mentioning that graphene can be safely used in devices that come into direct contact with human skin, allowing for applications such as tattoo sensors[429]. Pressure sensors with high sensitivities can detect extremely small pressure changes and can be used to convert muscle movements and subtle sound vibrations into electrical signals[430, 431]. In case of strain sensors, these are devices that detect small mechanical deformations and convert them into electrical signals. Over the past few years, these sensors have been incorporated into flexible and wearable electronic devices, adapting them for use in health monitoring applications[211], motion detection[432] and soft robotic[433]. Compared to complex fabrication methods like microelectromechanical systems and microfluidic techniques, designing the structure of the active material is the simplest and most straightforward approach for creating pressure sensors. In those method, a small applied pressure can cause subtle structural changes in the electroactive material. Moreover, the application of pressure can induce the formation of cracks and structural defects, which in turn modify the percolation pathways for charge transport. Consequently, this can cause substantial variations in the electrical output[112, 434]. Thus, the LbL method of pressure sensing preparation seems the most suitable technique for active material preparation for pressure sensing device.

Pressure and strain sensors based 2D materials typically exhibit minimal hysteresis, good linearity in response, and high sensitivity[435]. For instance, an ultrafast dynamic pressure sensor based on a hybrid graphene structure has been reported[153]. In this case, a GO/graphene composite film is created by vacuum filtration of a solution

containing graphene oxide and graphene. Here, the 2D graphene layers serve as the conductive component, while GO acts as a surfactant to prevent graphene from restacking and aggregating in the aqueous solution. The pressure sensor utilizes a lateral structure, where the planar GO/graphene film is placed on the surface of the electrodes. Moreover, this pressure sensor has shown excellent sensitivity (0.032 kPa^{-1}) in the low-pressure range (<1 kPa) and a very low detection limit (approximately 0.15 g). Additionally, it demonstrated outstanding cycling stability (>8000 cycles) and impressive response time, capable of detecting dynamic pressure signals as high as 10 kHz. In another notable example, a novel graphene-based strain and pressure sensor was fabricated by dip-coating a polyimide foam template, followed by chemical reduction and thermal reduction processes[111]. This graphene-based strain and pressure sensor exhibits high sensitivity and excellent linearity, making it suitable for applications in health monitoring and human motion detection. The advancement of sensors based on graphene, offering high performance with facile and inexpensive fabrication, is crucial for building smart sensing systems for the IoMT. However, low-dimensional materials such as nanoparticles and nanowires[203, 432, 436-438] and CNT[107, 439] also have been utilized for fabrication high performance sensors. Among these materials, AuNPs have been utilized as the active sensing material in strain sensors due to the ease of controlling their composition, shape, and size[440, 441]. Additionally, their properties can be tailored through molecular functionalization, and their simple and cost-effective fabrication makes them highly attractive for technological applications. The mechanism of these AuNPs-based strain sensors relies on the relationship between strain and electron tunneling among neighboring nanoparticles within the films or networks. While some efforts have been made to enhance the sensing capabilities of AuNPs-based strain sensors by employing various organic ligands such as 8-mercaptooctanoic acid[442], 1,9-nonadithiol[443], and mercaptopropionic acid[444], the complete potential of the inherent mechanical properties of the organic linker has yet to be fully realized.

Combining two excellent materials such as graphene and gold nanoparticles into a single active material could be the beginning of a new generation of high-performance strain and pressure sensors. In this Chapter I will discuss novel graphene-based material doped with gold nanoparticles and evaluated for performance as strain and pressure sensors.

5.2 Results

5.2.1 Characterization of gold nanoparticles

The AuNPs were synthesized by protocol described in section 5.2. To determine the size of the AuNPs the UV-Vis spectroscopy was utilized. The obtained UV-Vis spectrum of synthesized nanoparticles is presented on Figure 61. As shown in Figure 61 the wavelength at 520.5 nm of the sample corresponds well with the value found in the literature[445]. Because of λ_{max} = 520.5 nm this value is attributed to 17.6 ± 1.2 nm of diameter of AuNPs and 1.9 10^{-12} NPs mL^{-1}. As the rGO produce by thermal annealing in 150 °C and above (see Chapter 4) does not reach pore size higher than average 20 nm, this diameter is suitable to penetrate the defects in the rGO structure.

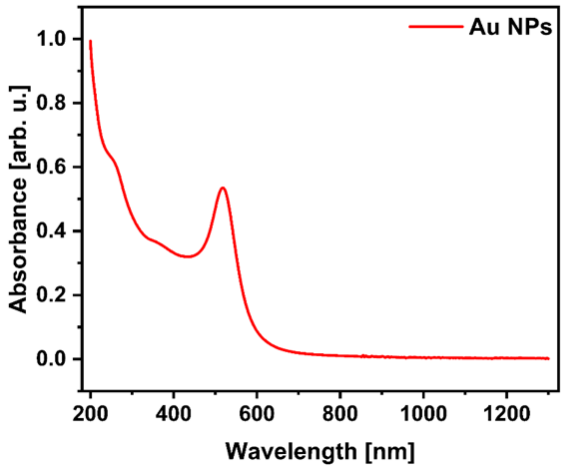

Fig. 61 *The UV-Vis spectrum of synthesized AuNPs.*

Moreover, the crystallinity of synthesized AuNPs was investigated by XRD technique, and corresponding XRD patterns are shown on Figure 62. The gold nanocrystals exhibited four distinct peaks at 2θ = 38.1 and 44.3, which is value found in the literature [446]. Furthermore, these peaks corresponded to standard Bragg reflections (111) and (200) respectively. The intense diffraction at 38.1 peak shows that the preferred growth orientation of zero valent gold was fixed in (111) direction. This refers to molecular-sized solids formed with a repeating 3D pattern of atoms or molecules with an equal distance between each part. This XRD pattern is typical of pure Au nanocrystals[446, 447].

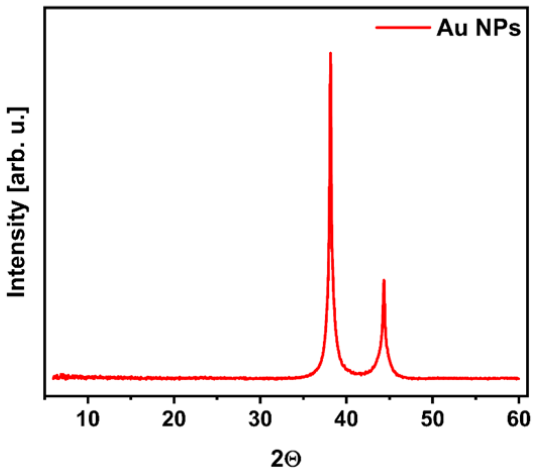

Fig. 62 *The XRD spectrum of synthesized AuNPs.*

5.2.2 Characterization of prepared layer material

The multiscale characterization of various physicochemical properties of the GO-based hybrid structures was conducted using different experimental techniques. By precisely identifying the layers of the obtained materials, it is possible to track changes in the chemical composition of individual layers and estimate the quality of the applied reduction process. XPS offered quantitative insights into the chemical composition of the layered material. Specifically, the notable differences between the carbon, oxygen, nitrogen and sulfur peaks indicated the formation of a chemical bond between the OFGs on the surface of GO and the amine and thiol groups from the other component. On Figure 63 is presented obtained survey spectra for GO(L1), GO(L2) and rGO(L1).

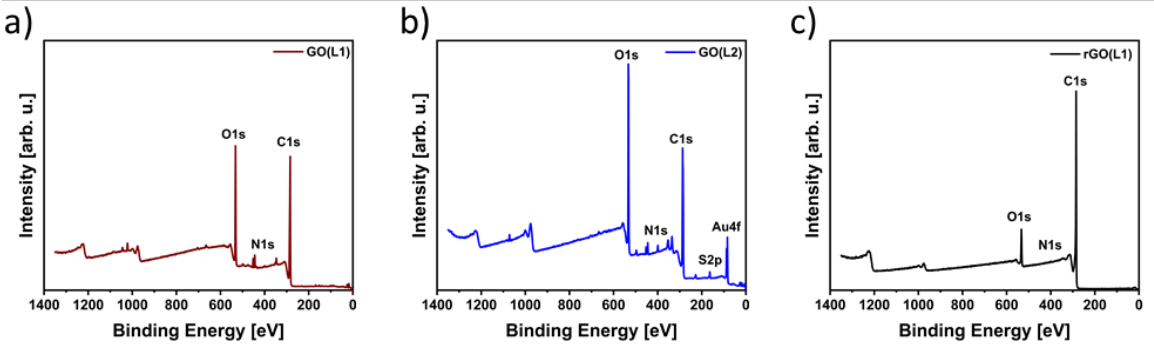

Fig. 63 *Survey spectra of obtained a) GO(L1) b) GO(L2) and c) rGO(L1) layers.*

As it is illustrated on Figure 63 (a) and (c) the thermal reduction process occurred with expected from Chapter 4 efficiency. From Figure 63 (b) the appearing of S 2p and Au 4f

peaks attributed to 164.08 eV and 84.08 eV respectively, clearly indicate presence of 4-aminotiophenol (corresponds to sulfur peak presence) and AuNPs (attributed to Au 4f peak). That feature is not observed in GO(L1) layer as well as in rGO(L1). The absence of these peaks in rGO(L1) layer can explained by the thickness of the deposited top layer, which XPS beam is not able to penetrate. The data obtained from profilometer indicate that the thickness of layer deposited from GO solution is ~300 nm, where the ability of penetration of material by XPS beam is limited to from 10 to 100 nm. In the other hand, from XPS survey data the atomic percentage of all element present in the sample. On Table 8 is shown of atomic percentage obtained from XPS spectra. From the atomic percentage from XPS data, it can be inferred that the nitrogen content in the sample increased by approximately 0.6%, which corresponds to the presence of 4-aminotiophenol in the material. Moreover, to have better insight into the changes during LbL deposition the C 1s XPS spectra was deconvoluted. The deconvoluted spectra are presented on Figure 64.

Tab. 8 The atomic percentage obtained from XPS survey spectra.

Sample	%C	%O	%N	%S	%Au
GO(L1)	67.59	30.97	1.44	-	-
GO(L2)	66.88	28.99	1.97	1.67	0.99
rGO(L1)	86.41	12.49	1.11	-	-

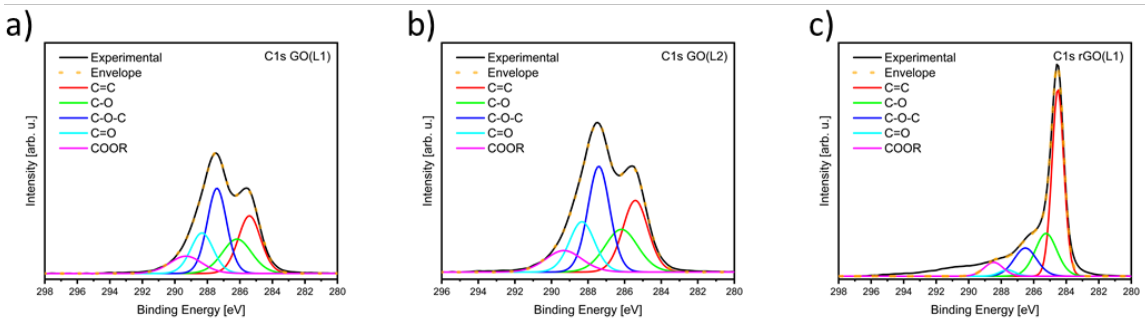

Fig. 64 *Fitted XPS C 1s spectra for a) GO(L1) b) GO(L2) and c) rGO(L1).*

As it is shown on Figure 64 the high-resolution C 1s spectrum is fitted with five Gaussian-Lorentzian curves representing five chemical environments such as: at 284.4 eV C–C (Csp^2–Csp^2), 285.15 eV C–O (including Csp^2–O–Csp^2, Csp^3– OH and Csp^2–OH), 286.48 eV C–O–C (Csp^3–O–Csp^3), 287.38 eV C=O, and 288.50 eV COOR (including COOH and lactone). However, there is no significant difference observed between the samples GO(L1) and GO(L2), which can be explained by dominance the GO in the layer structure.

Because of, the XPS spectrometer collected average data form surface area of these layers, where the atomic percentage that content of sulfur form 4-aminotiophenol is 1.67% and the pristine GO layer contain some trace amount of nitrogen in the sample it is difficult to track the functionalization of the GO layer by this method. Same problem was observed in case of deconvolution of N 1s spectra, where due to presence of nitrogen bond in GO layer is hard to estimate the influence of amine group from 4-aminotiophenol on GO surface modification. However, the lack of significant changes in binding energy data obtained from GO(L2) layer may suggest that AuNPs and 4-aminotiophenol are attracted to GO layer by the supramolecular interactions. In the other hand the difference in C 1s spectra on Figure 64 between (a), (b) and (c) clearly indicate that reduction of GO layer was conducted efficiently.

Moreover, to have better insight into the chemical composition and crystallinity of prepared layer the Raman experiment was conducted. The obtained Raman spectrum for all samples is presented on Figure 65.

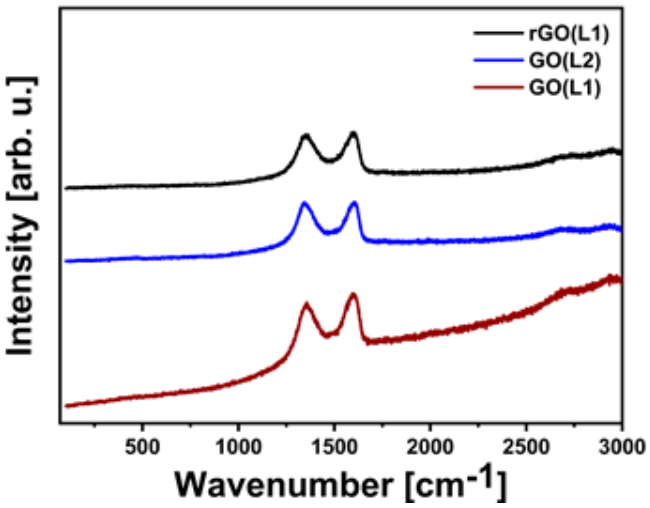

Fig. 65 *Raman spectra of GO(L1), GO(L2) and rGO(L1).*

Through the analysis of the D and G peaks characteristics around 1350 cm^{-1} and 1600 cm^{-1}, it provides information on the defect associated to vacancies and grain boundaries of the material. while the latter gives insight into the chemical state of the carbon through the scattering of the E_{2G} phonon of the sp^2 carbon bond. Considering the G-peak of the GO(L1) measured at 1603 cm^{-1}, its value shifts to a lower wavenumber, reaching 1590 cm^{-1} for the GO(L2), which is consistent with the observed effect of the functionalization of graphitic materials[448, 449]. Moreover, the intensity ratio I_D/I_G is commonly used to

quantify the disorder level in GO based materials. After a certain degree of disorder, which is much lower than the defect density found in GO(L1), adding more defects causes peak attenuation and a subsequent decrease in the I_D/I_G ratio[406]. Thus, this value does not significantly change from I_D/I_G = 1.52 for GO(L1) to deposited layer of GO(L2) I_D/I_G = 1.65, as the anchoring groups for this functionalization are already present on GO and are counted as defects. However, during the reduction step of deposited layer on substrate, the elimination of defects that did not react in the previous step leads to an increase in the I_D/I_G to 1.73 for rGO(L1) ratio is observed, which states in agreement with Chapter 4 results.

Moreover, to validate the changes in crystallinity of deposited layers the XRD measurement were provided. However, due to weak interactions between deposited 4-aminotiophenol with AuNPs and GO layers, the changes in XRD spectrum for GO(L1) and GO(L2) where not observed. For this reason, to compere the deposited layer on Figure 66 are presented XRD spectra for GO(L1), pure rGO layer without any organic and AuNPs deposition and rGO(L1).

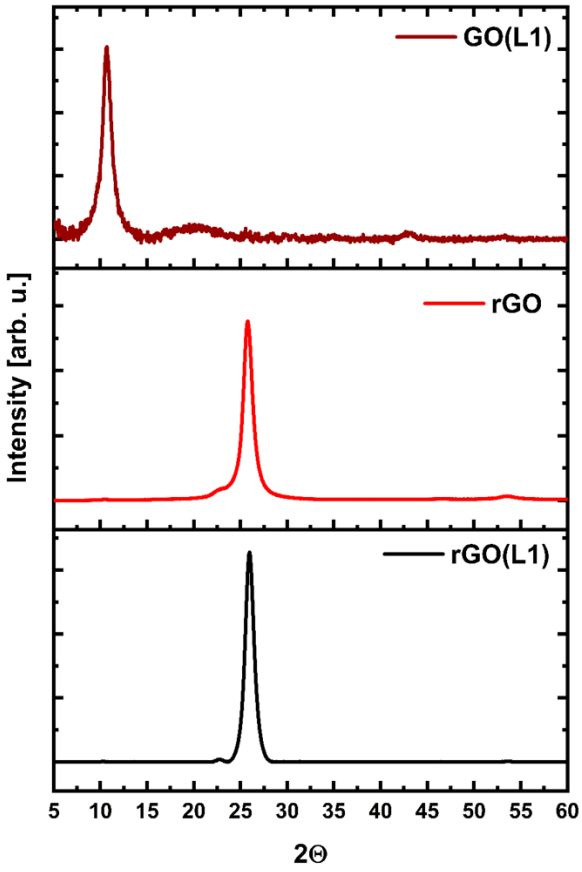

Fig. 66 *The XRD spectrum of layers GO(L1) (top), pure rGO (middle) and rGO(L1) bottom.*

As it shown of Figure 66 the characteristic peak of GO on 2Θ = 10.68 is disappearing and not observed in both case of post reduction layers rGO and rGO(L1). Moreover, the characteristic peak for rGO based materials 2Θ = (25-27) is appearing after reduction process in both causes, which is another indicator efficiency of thermal reduction of these layers. Furthermore, in comparison pure rGO and rGO(L1) it is observed the increase of 2Θ value from 2Θ = 25.75 for pure rGO to 2Θ = 26.08 for rGO(L1) (the better illustration of this phenomena is shown on Figure 67).

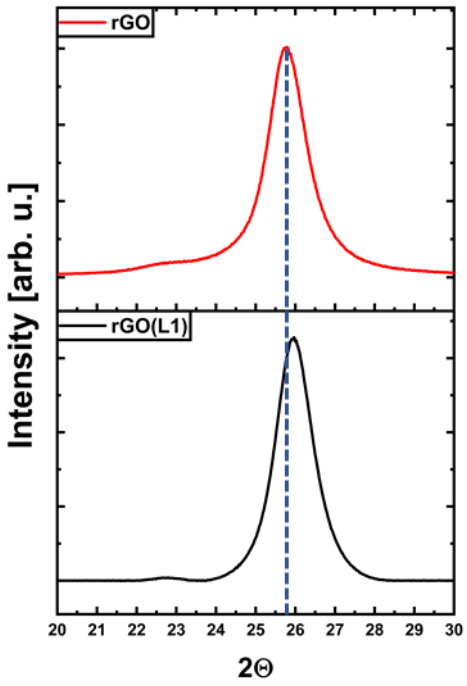

Fig. 67 *The XRD spectra of pure rGO layer (top) and rGO(L1) (bottom).*

This feature indicates that implementation of organic molecules and AuNPs increased interlayer distance between GO sheets and they are stacked during the reduction process in the built by LbL method structure of active material.

Moreover, to investigate the deposition quality the SEM imagines of prepared layer were performed, which are presented on Figure 68. From SEM imagines it is clear that deposited AuNPs on the top layer of GO create irregular aggregates on the whole plane of GO layer surface. Moreover, the reduction process has significant impact on the top layer of GO. From the morphology it is shown that the GO layer under thermal annealing has changed its flat layer into irregular plane.

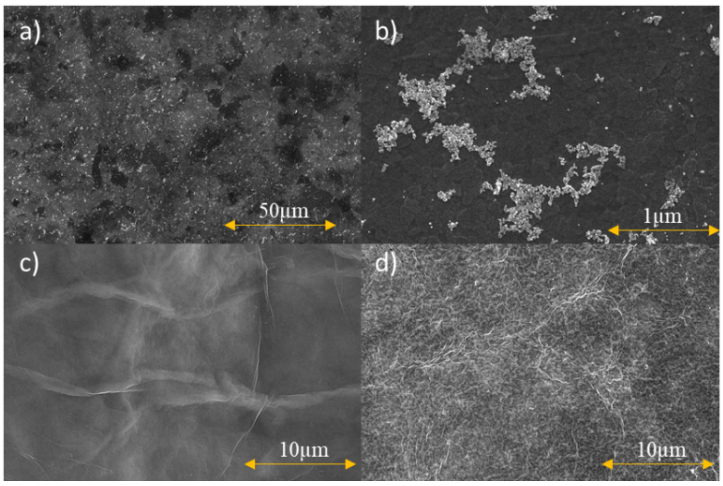

Fig. 68 *The SEM imagines of a), b) GO(L2), c) GO(L1) and d) rGO(L1) layers.*

5.2.3 Pressure sensing application

The prepared by LbL method active material on the ITO-glass was tested according to the application as pressure senor. The performance of pressure sensor was evaluated using a force gauge with a movement-control stand, combined with a sourcemeter to provide a steady bias voltage. A step force ranging from 0.005 to 1 N was applied to the device (with a contact area of 1 cm^2). Mechanical displacement was converted into an electrical signal by measuring the current change under different applied forces. The sensitivity of the pressure sensor was calculated using the Equation 15:

$$S = \delta((R_1 - R_0)/R_0)/\delta P \qquad Eq.\ 15$$

where R_1 and R_0 are the resistance with and without applied pressure (P), respectively and it shows sensitivity of 0.613 kPa^{-1}, which much higher than sensitivity of pure rGO which reach 0.052 kPa^{-1}. On the Figure 69 the performance of pressure sensor device is presented.

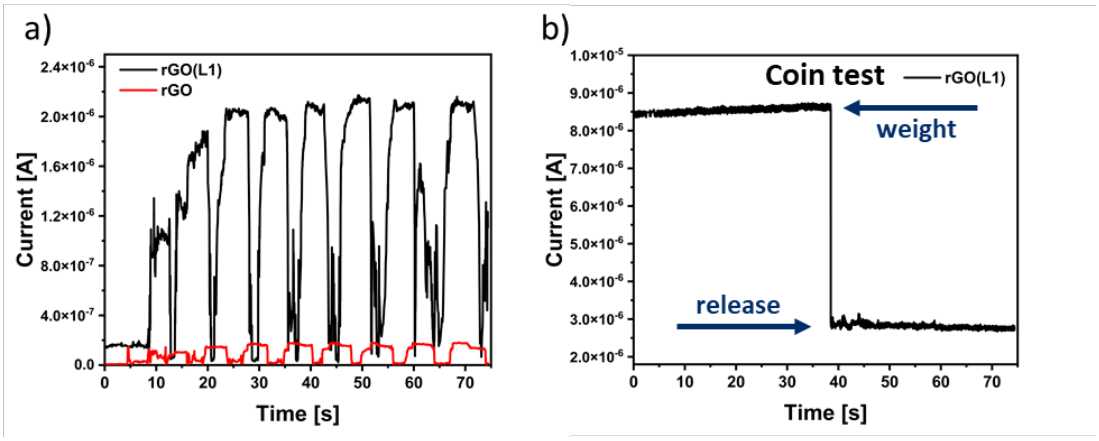

Fig. 69 *Respond of pressure sensor device for a) 0.4 kPa and b) coin 6.24 g (~0.061N).*

As it is shown on Figure 69 (a) the obtained layers as active material stands out in the performance with comparison of pure rGO prepared by similar protocol. The observed differences in sensitivities can be attributed to the fact that the current passing through the rGO-based vertical junction is highly influenced by extremely small changes in the interlayer distance between the rGO sheets, which is, in turn, determined by the applied pressure. Moreover, to present effectiveness of obtained sensor the fatigue experiment was provided, which are illustrated on Figure 70. The test was conducted for 0.1 kPa with 0.2 V of bias voltage. The presented results clearly indicate the stability of the obtained pressure sensor. Furthermore, the device exhibits a superior performance, in which the working current is stable even after 2500 times of press-release circles. Both respond and recovery time has been calculated. As it is shown on Figure 70 and all previously presented figures attributed to performance of sensing device the signal has to stabilize. Then, the respond time was calculated from minimal sensitivity to the highest peak and reach 127 ms. Due to, 1 s off applied pressure and the stability of system in case of individual peak, recovery time was calculated form the point of release pressure to obtaining stable signal and is attributed to value of 496 ms.

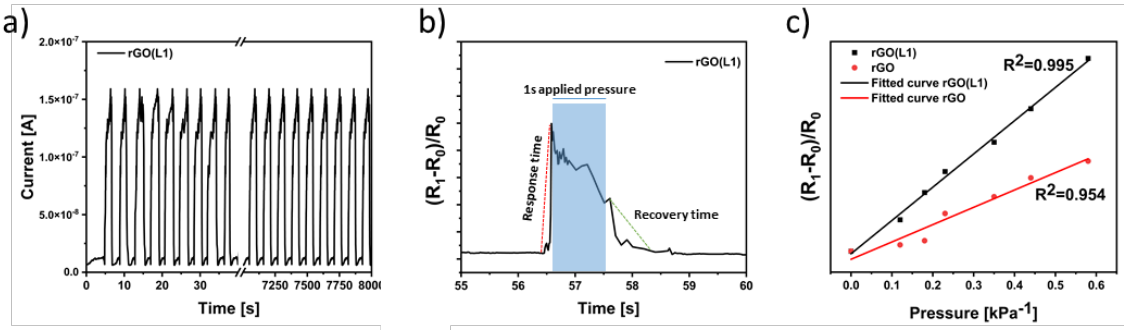

Fig. 70 *a) the fatigue test of obtained pressure sensor and b) response and recovery time c) Relative resistance as function of the pressure applied for sensor.*

Finally, the linearity was calculated. From obtained results (see Figure 70 (c)) the linearity of rGO(L1) as pressure sensors corresponds to $R^2 = 0.995$ which is much better considering the rGO response with the value $R^2 = 0.954$. However, such linearity is attributed to the low range of pressure for presented pressure senor. Which it can be concluded that higher rate of applied pressure destroys the built structure of layer to that level than it cannot be restored again.

5.2.4 Strain sensing application

The prepared by LbL method active material on the ITO-PET was also tested according to the application as strain senor. To determine the gauge factor, the key parameter for quantifying the sensitivity of a strain sensor, the relative resistance change (R_1 - R_0) under different strains (ε) was measured. Here, R_0 represents the baseline resistance recorded when the strain sensor is under no stress. The strain ε is calculated by the equation c = h/2r, where h is the thickness of the ITO-PET sheet (125 μm) and r is the bending radius of the substrate. The radius was determined by follow in the changes of α angle[197], which is created during the bending process as it illustrated on Figure 71.

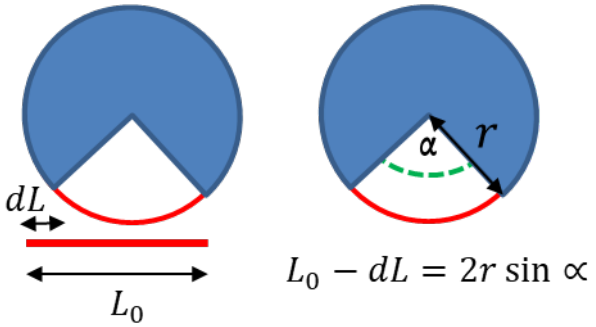

Fig. 71 *The graphical illustration of creation the α angle during bending.*

Subsequently, the angle α was substituted into the equation along with the difference in substrate length before (L_0) and after (dL) bending. The relative resistance change ((R_1-R_0)/R_0) is determined by measuring the current change under different stresses, and the GF is calculated by fitting the plot of ((R_1- R_0)/R_0 ≈ ε)[450]. To examine the effect of bending direction on strain sensing performance, the configuration of vertical was tested by aligning the electrodes on the PET substrate. The strain sensor's response was measured under a very low operating voltages, with a bias voltages of 0.1 and 0.2 V applied. The whole data was collected towards inward bending performance. The sensor was measured with the small strain form -0.5% to -0.08%. The GF for rGO(L1) was calculated to 12.57 value which much higher than the 6.21 for pure rGO. The performance of obtained rGO based sensor is presented on Figure 72. As it is presented on Figure 72 the resistance of sensor device depends on applied strain. With the increase of the strain the resistance of sensor also is increasing, which puts the device into the positive manner. Typically, for AuNPs based strain sensors it is observed the decreasing of resistance by higher strains. That feature can be explained by compressive consequences, where the AuNPs usually overlapped and arranged closer together, shortening the charge transfer distance and increasing the charge percolation paths, which resulted in a decrease in the strain sensor's resistance[197, 451]. However, in rGO(L1) strain sensor are the rGO layers. AuNPs, as metallic nanoparticles, typically exhibit high conductivity, acting as effective conductors. In contrast, rGO obtained through the thermal reduction of GO displays semiconductor properties, resulting in higher resistance than the AuNPs present in the sample. In a resting state, the system remains undisturbed; however, during inward bending, the rGO layers and functionalized AuNPs move closer together. Nevertheless, due to the atomic content of gold in the sample being around 1%, the rGO layers dominate and prevent the AuNPs from coming into proximity. Furthermore, the temporary bending induces structural changes in the rGO layer, causing it to stretch and alter its conductivity[323].

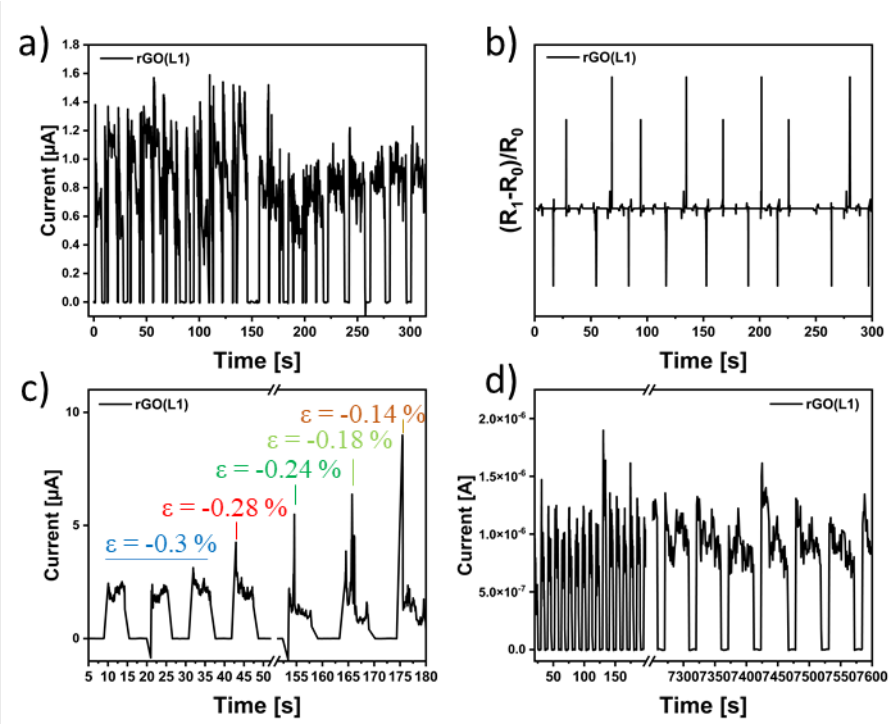

Fig. 72 *The performance of strain sensor a) the response of the strain sensor to ε = -0.3%, b) relative resistance for respond of sensor at ε = -0.3%, c) respond of the strain sensor at different bending states by applying different inward strains form ε = -0.3% to 0.1% , d) Fatigue test of strain sensor at ε = -0.3%.*

On the Figure 72 (c) is presented the dynamic test, where the strain sensor response is corresponding to various strain used. That test, clearly indicate the increasing of resistance during the increasing of strain value. As it is shown, the sensor corresponds to strain change with high, sharp signal on the beginning of peak. However, after the strain the system must relax to back to based resistance. That feature significantly affect the respond and recovery time which is calculated to 1.11 s for responded time and 2.79 s of recovery time, as it presented on Figure 73. Moreover, on the Figure 72 (d) is presented the fatigue test of strain sensor which indicate that the device stays stable after even 2000 cycles. Finally on the Figure 73 (b) is illustrated the obtained calibration curve for rGO(L1) strain sensor and pure rGO layer.

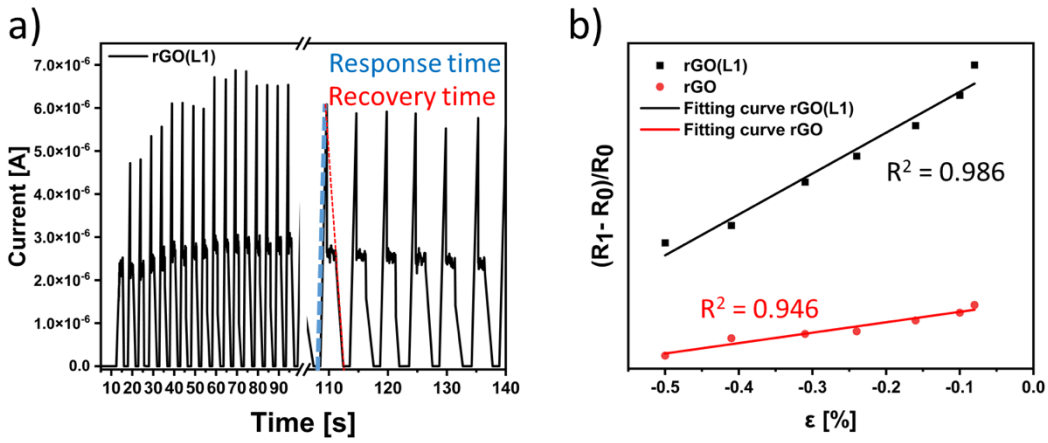

Fig. 73 *Graphical presentation of calculation of a) respond and recovery time of strain sensor of rGO(L1) and b) relative resistance change versus strain.*

Taking into consideration linearity of strain sensor response the rGO(L1) sensor R^2 = 0.986 which is acceptable value of linearity in comparison with R^2 = 0.946 for rGO layer without 4-aminothiphenol and AuNPs.

5.3 Conclusions

In summary, it has been described a novel method to tune and boost the sensitivity of both pressure and strain sensors by LbL method with utilization of organic linker and AuNPs. In particular, the sensitivity of pressure and strain sensor is significantly increased by implementation of functionalized AuNPs between its sheets. The pressure sensor based on graphene exhibits a sensitivity as high as 0.613 kPa^{-1}, short response time 127 ms, high durability (over 2500 times). Whereas the strain sensor based on the same material exhibits GF = 12.57, 1.11 s of time respond and high durability (over 2500 times). The high differences in the respond and recovery time for both pressure and strain sensors can be explained by the nature of substrate. While ITO glass is a rigid material and does not need to return to its original shape after contact and release, the respond and recovery time are not affected by the substrate. In the case of ITO on PET, especially considering higher strain values, the substrate behaves like a shape-memory material and must return to its original position. This significantly affects the signal recovery time in strain sensing applications. Moreover, in both cases the obtained signals turn into positivity system in general, which means that during implementation of factors on the sensors the resistance is increasing. That, feature clearly indicate that the whole sensing is affected by the rGO sheet and not so much by functionalized AuNPs. This phenomenon can be explained by semiconductor properties of obtained rGO layer, the abundance of

AuNPs in the structure of sensor and the structure changes presented on XRD spectra, where the interlayer distance of rGO sheet slightly changed (form 2Θ = 25.75 to 26.08), which has significant consequences on the strain and pressure devices. Moreover, the presence of functionalized by 4-aminotiophenol AuNPs increase the performance of both strain and pressure devices.

In general, in this Chapter is presented the preparation of active material by LbL method with utilization of rules of green chemistry (no toxic solvent was used, and the reduction of GO was conducted by thermal annealing). Moreover, the presented active material exhibits high potential properties as strain and pressure senor applications.

Chapter 6 Graphene-based hybrid as active material for humidity sensor

6.1 Introduction

The standards and legal norms governing the monitoring of the environment, industry, and agriculture have a significant impact on the development of humidity sensor technology[452, 453]. Commercially available sensors made from ceramics (such as Al_2O_3 and Si_3N_4), metal oxides like SnO_2 and GaN, polyelectrolytes, and conducting polymers have significant drawbacks[454, 455]. The main reasons for the need to explore alternative solutions include the low signal to noise ratio at low analyte concentrations, degradation during prolonged exposure to operational conditions, and lengthy response and recovery times. The ideal strategy for implementing new nanocomposites in humidity sensor applications involves utilizing materials that possess high porosity, a high surface to volume ratio, conductivity, and hydrophilicity. Consequently, carbon-based materials such as CNT[456], GO[457, 458], and rGO[459, 460] have become highly relevant. Sensor devices based on these graphene derivatives are promising due to their superior mechanical and chemical stability, faster response times, and greater scalability compared to traditional solutions. Additionally, the chemical composition of GO and rGO, which includes oxygen in hydroxyl, ether, and carbonyl groups at the sheet edges, enables a detection mechanism based on supramolecular interactions such as hydrogen bonding, π-π stacking, and van der Waals forces. These properties make them ideal for ultra-sensitive and selective sensing, as the reversible and repeatable processes meet the requirements for rapid response and detection of low water concentrations. However, despite the strength of these interactions, GO-based sensors suffer from significant hysteresis and inconsistent performance over time[262]. Moreover, GO the conductivity of the GO-based devices is quite low (1×10^{-4} and lower)[461] which is unfavorable feature. This limitation is critical for humidity sensor applications, making rGO a more suitable choice for electrochemical devices. However, both GO and rGO-based sensors have significant drawbacks. GO sensors exhibit slow response and recovery times as well as poor stability. Although rGO shows greater stability than GO, it remains insufficiently stable and demonstrates low sensitivity to humidity due to its hydrophobic nature[462]. Thus, to enhance stability and sensitivity the graphene-based materials are functionalized to new hybrids components which perform higher sensitivity and better stability because of functional moieties received from other compounds. Moreover, rGO electrical properties

with combination of water swellable material is promising idea for enhance features of humidity sensors as a result of functionalization of rGO *via* supramolecular interactions with WSM. In last few years superabsorbent polymers (SAP) and hydrogels were investigated towards improvement of properties of pristine graphene and graphene-based devices. SAP represent a class of hydrophilic polymeric hydrogels that can swell, absorb and retain a large volume of water or other biological fluids. Components such as poly(vinyl alcohol), N-isopropylacrylamide, poly(acrylic acid) and poly(vinylpyrrolidone) were used for fabrication of hydrogels with high swelling ratio[463-466]. Another class of SAP are WSM. In contrast to hydrogels, the WSM are specified in absorption of water molecules. Generally, WSM are made with two different parts: hydrophobic rubber and hydrophilic polymer or SAP. Usually, the WSM are prepared using two main methods: i) in blending method the two components are simply mixed by means of mechanical agitation, rolls and mills; ii) the second method relies on grafting - in this case two parts, *i.e.* hydrophilic and hydrophobic are covalently bonded by chemical reaction. The type of chemical reaction depends on organic moieties contained in parts. The most commonly used is polymerization *via* radical or irradiation mechanism. The main advantage of grafting method is forming of covalent bonds on hydrophobic surface of rubber. That means irreversible modification of surface which cannot be washed or eliminated during material exposition. Despite the history of WSM has about 25 years there is no reported correlation between structure, preparation method and humidity senor response. The most common application of WSM are sealants. Although, high volume change during being exploited on water molecules WSM are not significantly studied in humidity sensors.

In this Chapter there is presentation of synthesis the WSM based on itaconic acid and divinylbenzene and its implementation into the rGO based humidity sensors device. The illustration of concept is presented on Figure 74.

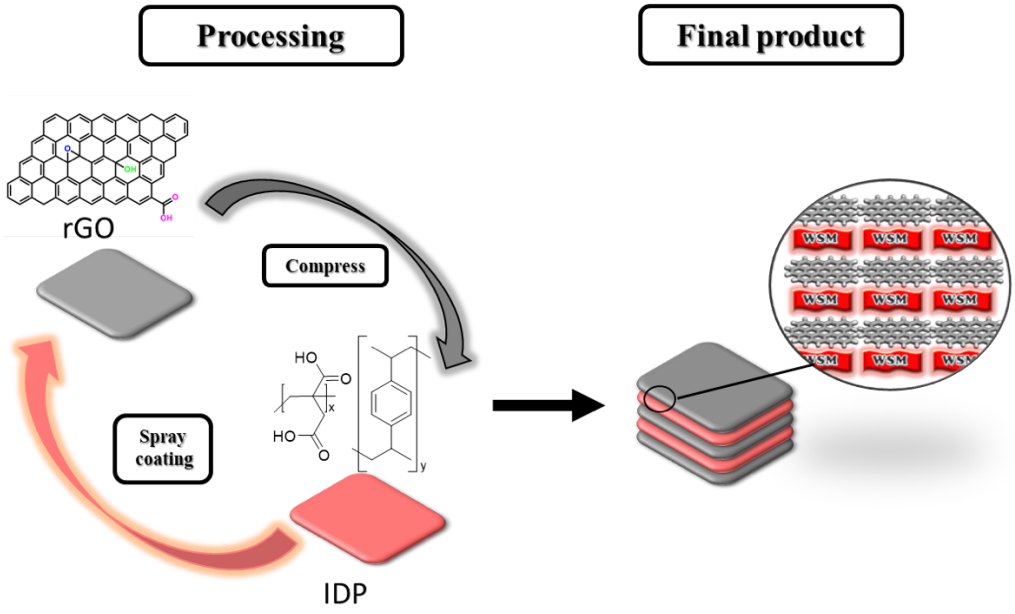

Fig. 74 *The illustration of the concept.*

6.2 Results

6.2.1 Identification of synthesized material

The composition and the structure of synthesized IDP was investigated by various methods. To identify the polymerization process the FT-IR spectrum was performed. On the Figure 75 is presented FT-IR spectra for substrates and product.

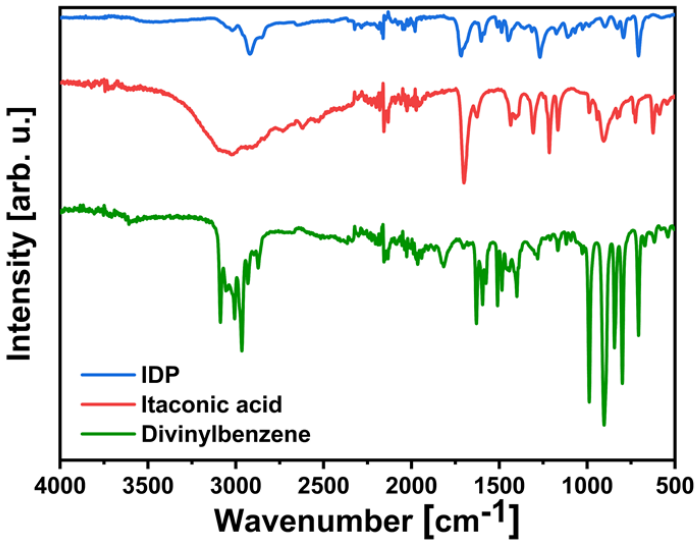

Fig 75 *The FT-IR spectra of IDP, itaconic acid and divinylbenzene.*

The blue curve displays the distinctive vibration bands of IDP including: the stretching absorption bands at 1717 cm^{-1} (C=O), 1400–1500 cm^{-1} (C–O), and at 2850–2925 cm^{-1} (C–H aliphatic). Moreover, the stretching absorption bands at 3000–3100 cm^{-1} (C–H aromatic) and 1510–1605 cm^{-1} (C=C aromatic) could be related to DVB, which confirms the polymerization. Furthermore, the broad absorption peak observed at 2500–3500 cm^{-1} (OH stretching vibration) from itaconic is losing intensity. The absorption peak present in DVB at 1650 cm^{-1}, which corresponds to vinyl group is no longer observed in the IDP spectrum.

Moreover, to have better insight into chemical composition the XPS spectra and EA were performed. Figure 76 (a) depicts the obtained XPS spectra. The atomic percentage obtained from XPS for IDP sample was 88.12% for C and 11.88% for O, whereas the EA gives values of: 77.39% for C, 6.75% for H and 15.86% for O. That oxygen content in the XPS and EA analysis suggests that divinylbenzene predominates in the polymer composition. This allows to estimate the monomer composition, indicating that for every 2 parts derived from IA, there are 4 parts from DVB. This ratio can be simplified to 2:1. This relationship also explains the decrease in OH band intensity for the polymer compared to IA in the IR spectrum. Furthermore, the presented ratio is consistent with the masses obtained from MALDI-TOF High – Resolution Mass Spectrometry (HRMS) analysis, as shown in Figure 77. Moreover, to have better insight into the crystallinity of IDP polymer the XRD spectrum was performed. From XRD spectra (see Figure 76 (b)) the broad peak in range 2Θ = 13.76 to 2Θ = 24.85 clearly indicate the amorphous nature of synthesize polymer, which was expected for this type of polymer.

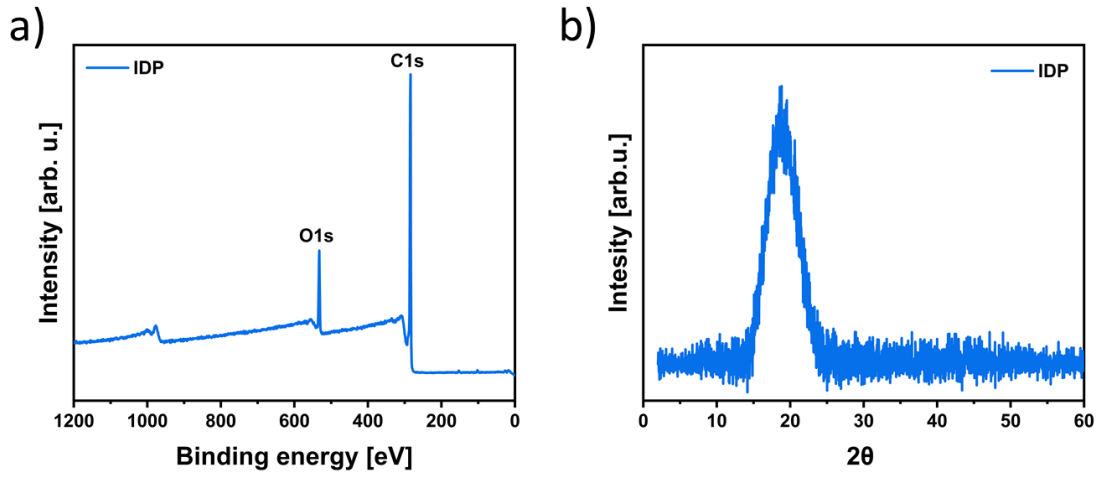

Fig. 76 *The a) XPS spectra and b) XRD spectrum obtained from IDP sample.*

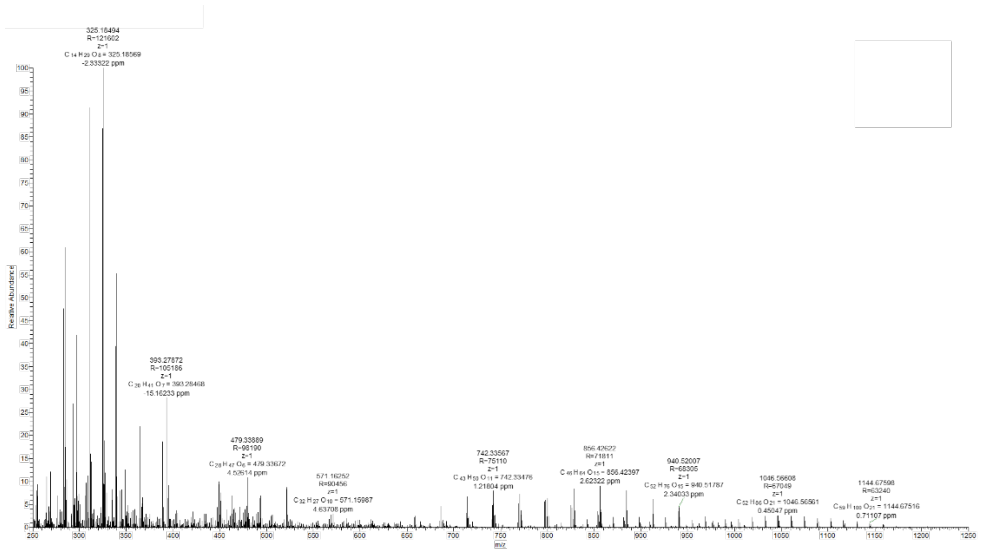

Fig. 77 *The MALDI – TOF – HRMS obtained spectrum for IDP sample.*

Furthermore, to gain deeper knowledge into the deposition quality and investigate the changes into morphology of rGO the SEM imagines has been performed, which are presented on Figure 78. As it is shown on Figure 78, the compression of rGO does not affect drastically the original layer of deposited rGO. Furthermore, after deposition of IDP into the rGO surface by spray-coating method the deposited particles are evenly distributed.

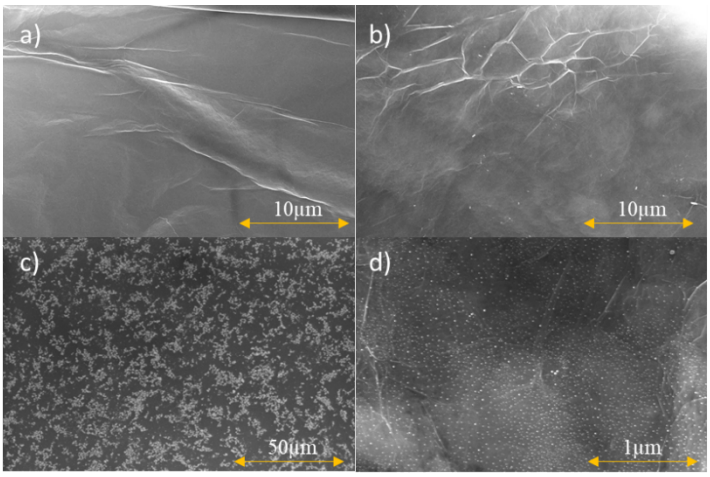

Fig. 78 *The SEM imagines of a) rGO before compress, b) rGO after compress, c) IDP and d) IDP deposited and compressed on rGO.*

6.2.2 Humidity sensor application

After assembling the senor (rGO(IDP)) performance of the humidity sensor was evaluated by connecting the two electrical contacts to a Keithley 2636A Source Measure Unit (SMU). To measure sensitivity, response time, and recovery time, a constant bias of

0.1 V was applied to the device, and the current intensity was recorded for 120 seconds with a sampling frequency of 80 Hz while a pulsed flow of humid air was directed onto the sample. This was achieved by cyclically and manually opening a glass stopcock connected to a balloon filled with humid air, positioned 10 cm from the sample. The initial humidity values ranged between 36% and 42% RH. The RH values inside the chamber were measured using two independent commercial hygrometers. The device's response was calibrated by recording the resistance and the corresponding RH values indicated by the hygrometers, while the humidity level inside the chamber was varied from 10% to 90% RH and then back to 10% RH. On Figure 79 is presented the respond of sensor to RH%.

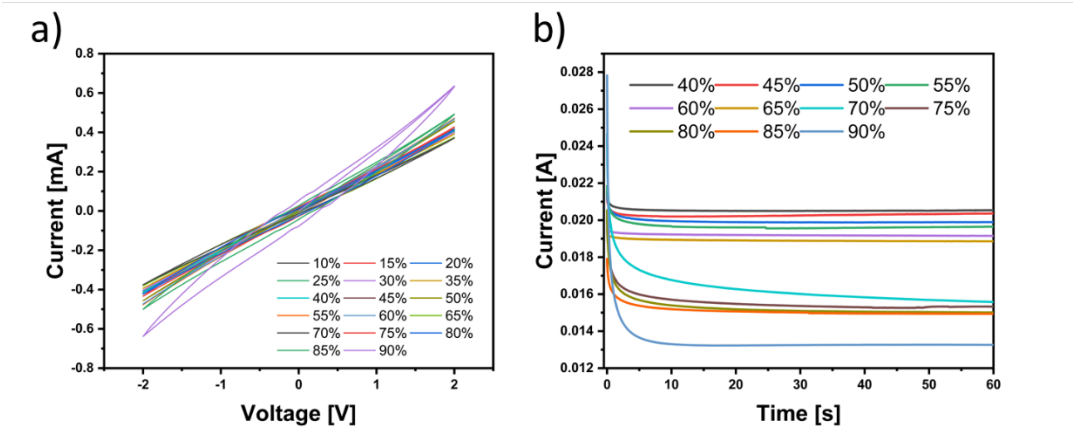

Fig. 79 *a) I to V curves for various RH% for rGO(IDP) an b) respond of rGO(IDP) for various humidity.*

As depicted in the Figure 79 (b), from 40% to 65% RH, the response is proportional to the increase in humidity. However, upon reaching 70% RH, there is a significant jump in the response. The signal then becomes proportional again within the range of 70% to 85% RH, followed by another abrupt increase at 90% RH. This behavior can be explained by the volumetric expansion of the WSM. From 40% to 65% RH, the volume increases gradually, but at 70% RH, the volumetric expansion of the WSM is rapid, causing a strong compression of the graphene layers. A slow swelling is observed again up to 85% RH, but at 90% RH, the volume reaches its peak, potentially to the extent of disrupting the graphene layers. This is evidenced by the difficulty in regenerating the system after re-drying the test chamber post 90% RH, unlike the lower RH values, where the volumetric expansion of the WSM does not damage the structure, allowing easy regeneration of the system. On Figure 80 is presented relative resistance in the function of RH%. To verify the linearity of the sensor's response, the relative resistance was plotted against RH%.

From Figure XX (a), two distinct trends are evident, caused by the sharp increase in conductivity between 65% and 70% RH. Consequently, the sensor responses were divided into two groups: from 40% to 65% RH and from 70% to 85% RH. The value of R^2 for 40% - 65% was 0.995 and for 70 - 85% R^2 = 0.932. This indicates that the highest linearity is maintained before the volumetric expansion of the IDP.

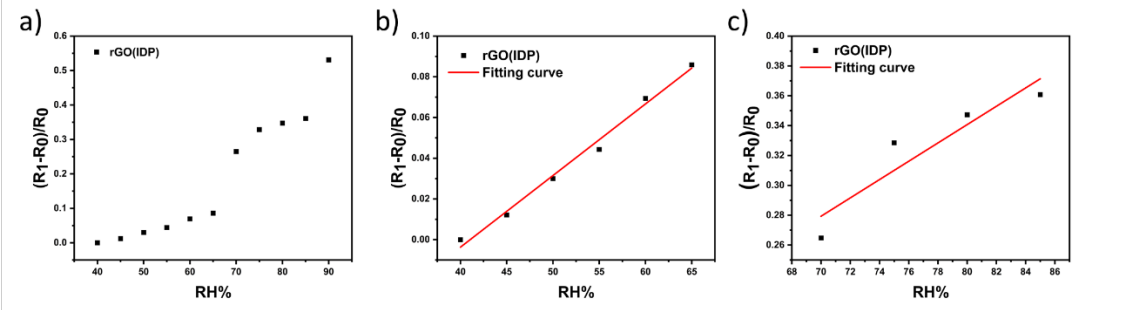

Fig. 80 *Relative resistance in function of RH% applied for a) 40-90% b) 40-65% and c) 70 – 85% rGO(IDP) humidity sensor.*

Dynamic tests were conducted to calculate the response and recovery times, which are presented on Fig. 81. The response time was measured at 0.4 seconds, while the recovery time was 17.9 seconds. However, these high values may result from the stabilization of humidity within the test chamber, making it challenging to accurately determine these parameters in the experiment due to the difficulty in evenly distributing humidity throughout the chamber's volume. Furthermore, from Figure 81 (b), it can be observed that in the range of 10% to 70% RH, the sensor's response is fully dynamic, allowing for real-time tracking of humidity changes in the measurement system. Additionally, it is possible to return to the initial value of 20% RH even after exposure to 70% RH, where a single abrupt increase in resistance occurs. This recovery is not observed at 90% RH, where the second abrupt increase takes place.

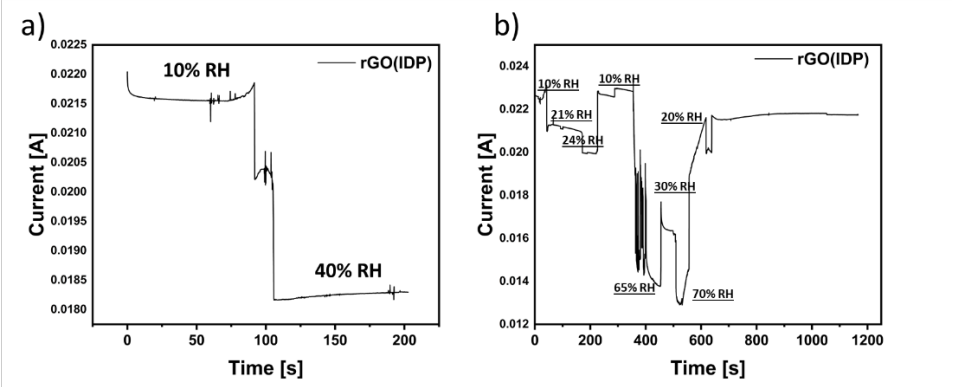

Fig. 81 *Dynamic tests of obtained humidity sensor a) and b).*

6.3 Conclusions

In this chapter, a WSM material synthesized from the reaction of itaconic acid and divinylbenzene was characterized. It was determined that the resulting polymer predominantly contains divinylbenzene components in a molar ratio of 2:1 relative to itaconic acid. The synthesized WSM was then implemented into rGO layers using a hydraulic press, thereby creating an active material that was tested for humidity sensing. The presented humidity sensor exhibits high linearity in sensor response within the 40% to 65% RH range and a rapid response time of 0.4 seconds, allowing for dynamic monitoring of humidity changes in the system

Chapter 7 General conclusion and outlook

In summary, the presented thesis systematically investigates the properties of obtaining rGO through chemical and thermal reduction methods. It outlines the relationships and differences between the reduction conditions and the properties and characteristics of the resulting materials, which are crucial for the potential application of rGO in electronics. In case of chemical reduction of GO he study presented, developed, and optimized a scalable, easily controllable, and energy-efficient method for producing chemically reduced CrGO with tailored electrical properties. Moreover, this research, supported by ssNMR, indicates that the peak area associated with Csp^2–O species is an excellent measure of the reduction strength of the employed reducing agents. Specifically, the observed trend $Na_2S_2O_4 \approx N_2H_4 > AA > NaBH_4$, which corresponds with the findings from FTIR analysis, elemental analysis, and XPS analysis. Moreover, the peak area of the Csp^2–O species demonstrated the impact of reaction time on GO reduction for three of the reducing agents: $Na_2S_2O_4$, AA, and $NaBH_4$. Additionally, investigations using EA and XPS revealed that employing N_2H_4 in the GO reduction process led to nitrogen contamination and pyrazole formation. Likewise, $NaBH_4$ caused sodium contamination, whereas AA induced a supramolecular interaction with DHA within the CrGO structure. Significantly, these findings demonstrate that CrGO with exceptional electrical conductivity (>1800 S m^{-1}) can be synthesized using AA (with a 12-hour reaction time), $Na_2S_2O_4$, or N_2H_4 (regardless of reaction time). CrGO produced with AA or N_2H_4 exhibited reduced hydrophilicity, enabling the fabrication of films on flexible plastic substrates that maintained resistance even after 2000 bending cycles. This characteristic clearly indicates that CrGO can be utilized for flexible pressure and humidity sensing electronics. Moreover, skin irritation tests showed that all forms of CrGO could be classified as non-irritating materials, confirming that the reduction process does not compromise their biocompatibility on the skin. These findings represent a notable progress in the utilization of rGO, especially in wearable and flexible electronics designed for direct interaction with the skin.

In case of thermal reduction GO, this study introduces an optimized, scalable, easily controllable, and low-temperature (<300 °C) annealing process, devoid of chemical treatments, for producing rGO with customizable electrical properties. The application of various techniques enabled unprecedented insights into and control over the compositional, structural, and electrical characteristics of the materials. The

reorganization of oxygen atoms on the GO surface to facilitate the release of H_2O and CO_2 is favored within the temperature range of 130 to 200 °C, as indicated by XPS and ssNMR analyses. Therefore, it is possible to remove OFGs without causing the carbon framework to ignite when the reduction is carried out in air. The primary OFG formed during annealing is Csp^2–O, which does not lead to any mass loss but significantly alters the electrical properties of GO from insulating to conductive. Furthermore, it has been shown that film resistivities ranging from approximately 10^{-2}–10^{-4} Ω m can be achieved through annealing in air at temperatures between 150 and 200 °C for 24 and 4 hours, respectively, and under an inert atmosphere at 200 °C for 4 hours. These results indicate that reducing GO through annealing at temperatures as low as 150 °C is feasible, making it compatible with the use of plastic substrates. Interestingly, films on plastic substrates maintained unchanged resistance after undergoing 2000 bending cycles. This marks a significant advancement for applications in wearable and flexible electronics. Furthermore, although the loss of OFGs adversely affects electrical conductivity, it is offset by a substantial increase in surface area and overall oxygen content, resulting in a material with approximately 450 $m^2\ g^{-1}$ and 103 S m^{-1}. Furthermore, this proposed reduction protocol for GO is suitable for both laboratory and industrial applications.

Moreover, the investigation of the efficiency of the reduction method allows to construct highly sensitive pressure and strain sensors based on rGO. Furthermore, a novel method has been described to adjust and enhance the sensitivity of both pressure and strain sensors using the LbL technique, incorporating an organic linker and AuNPs. Specifically, the sensitivity of the pressure and strain sensor is notably enhanced by integrating functionalized AuNPs between its layers. The graphene-based pressure sensor demonstrates a sensitivity as high as 0.613 kPa^{-1}, with a short response time of 127 ms and exceptional durability (over 2500 cycles). Similarly, the strain sensor based on graphene exhibits a GF of 12.57, a response time of 1.11 seconds, and high durability (over 2500 cycles). The significant differences in response and recovery times for both pressure and strain sensors can be attributed to the substrate's nature. Unlike ITO glass, which is rigid and maintains its shape after contact and release, the response and recovery times are independent of the substrate. The substantial variations in response and recovery times between the pressure and strain sensors can be attributed to the characteristics of the substrate. Unlike ITO glass, which remains rigid and retains its shape after contact and release, the response and recovery times are unaffected by the substrate. Furthermore,

in both cases, the signals obtained generally exhibit a positive response system, indicating that the resistance increases with the application of external factors on the sensors. This characteristic clearly indicates that the overall sensing is predominantly influenced by the rGO sheet rather than the functionalized AuNPs. This phenomenon can be attributed to the semiconductor properties of the resulting rGO layer, the incorporation of abundant AuNPs within the sensor structure, and structural changes observed in XRD spectra, where the interlayer distance of the rGO sheet has slightly shifted (from $2\theta = 25.75$ to 26.08). These changes have significant implications for the performance of strain and pressure devices. Furthermore, the presence of AuNPs functionalized with 4-aminotiophenol enhances the performance of both strain and pressure sensors. In this Chapter (Chapter 5), the preparation of the active material using the LbL method is presented, adhering to the principles of green chemistry (no toxic solvents were used, and GO reduction was achieved through thermal annealing). Furthermore, the active material demonstrated promising properties for applications in strain and pressure sensors.

Furthermore, the knowledge gained from tracking the progress of GO reduction was also utilized to develop a humidity sensor. In Chapter 6, a WSM synthesized from the reaction of itaconic acid and divinylbenzene was characterized. It was found that the resulting polymer predominantly consists of divinylbenzene components in a molar ratio of 2:1 relative to itaconic acid. Subsequently, the synthesized WSM was incorporated into rGO layers using a hydraulic press, creating an active material that was evaluated for humidity sensing. The humidity sensor presented demonstrates high linearity in its response within the 40% to 65% RH range and achieves a rapid response time of 0.4 seconds, enabling dynamic monitoring of humidity fluctuations within the system.

References

1. Kim, K.S., et al., *Large-scale pattern growth of graphene films for stretchable transparent electrodes.* Nature, 2009. **457**(7230): p. 706-10.
2. Zhu, Y., et al., *Carbon-based supercapacitors produced by activation of graphene.* Science, 2011. **332**(6037): p. 1537-41.
3. Liu, M., et al., *A graphene-based broadband optical modulator.* Nature, 2011. **474**(7349): p. 64-7.
4. Wang, Q.H., et al., *Electronics and optoelectronics of two-dimensional transition metal dichalcogenides.* Nat Nanotechnol, 2012. **7**(11): p. 699-712.
5. Geim, A.K. and K.S. Novoselov, *The rise of graphene.* Nature Materials, 2007. **6**(3): p. 183-191.
6. Novoselov, K.S., et al., *Two-dimensional gas of massless Dirac fermions in graphene.* Nature, 2005. **438**(7065): p. 197-200.
7. Singh, V., et al., *Graphene based materials: Past, present and future.* Progress in Materials Science, 2011. **56**(8): p. 1178-1271.
8. Schafhaeutl, C., *Ueber die Verbindungen des Kohlenstoffes mit Silicium, Eisen und andern Metallen, welche die verschiedenen Arten von Gusseisen, Stahl und Schmiedeeisen bilden.* Journal für praktische Chemie, 1840. **19**(1): p. 159-174.
9. Brodie, B.C., *XIII. On the atomic weight of graphite.* Philosophical transactions of the Royal Society of London, 1859(149): p. 249-259.
10. Boehm, H.P., et al., *Das Adsorptionsverhalten sehr dünner Kohlenstoff-Folien.* Zeitschrift für anorganische und allgemeine Chemie, 1962. **316**(3-4): p. 119-127.
11. Morgan, A.E. and G.A. Somorjai, *Low energy electron diffraction studies of gas adsorption on the platinum (100) single crystal surface.* Surface Science, 1968. **12**(3): p. 405-425.
12. Morgan, A.E. and G.A. Somorjai, *Low-Energy Electron-Diffraction Studies of the Adsorption of Unsaturated Hydrocarbons and Carbon Monoxide on the Platinum (111) and (100) Single-Crystal Surfaces.* The Journal of Chemical Physics, 1969. **51**(8): p. 3309-3320.
13. Blakely, J.M., J.S. Kim, and H.C. Potter, *Segregation of Carbon to the (100) Surface of Nickel.* Journal of Applied Physics, 1970. **41**(6): p. 2693-2697.
14. Van Bommel, A.J., J.E. Crombeen, and A. Van Tooren, *LEED and Auger electron observations of the SiC(0001) surface.* Surface Science, 1975. **48**(2): p. 463-472.
15. Lu, X., et al., *Patterning of highly oriented pyrolytic graphite by oxygen plasma etching.* Applied Physics Letters, 1999. **75**(2): p. 193-195.
16. Xuekun, L., et al., *Tailoring graphite with the goal of achieving single sheets.* Nanotechnology, 1999. **10**(3): p. 269.
17. Novoselov, K.S., et al., *Electric field effect in atomically thin carbon films.* Science, 2004. **306**(5696): p. 666-9.
18. Cranford, S.W. and M.J. Buehler, *Mechanical properties of graphyne.* Carbon, 2011. **49**(13): p. 4111-4121.
19. Long, M., et al., *Electronic Structure and Carrier Mobility in Graphdiyne Sheet and Nanoribbons: Theoretical Predictions.* ACS Nano, 2011. **5**(4): p. 2593-2600.
20. Song, Q., et al., *Graphenylene, a unique two-dimensional carbon network with nondelocalized cyclohexatriene units.* Journal of Materials Chemistry C, 2013. **1**(1): p. 38-41.
21. Mermin, N.D., *Crystalline Order in Two Dimensions.* Physical Review, 1968. **176**(1): p. 250-254.
22. Novoselov, K.S., et al., *Two-dimensional atomic crystals.* Proceedings of the National Academy of Sciences, 2005. **102**(30): p. 10451-10453.

23. Zhang, Y., et al., *Experimental observation of the quantum Hall effect and Berry's phase in graphene.* Nature, 2005. **438**(7065): p. 201-4.
24. Naguib, M., et al., *Two-Dimensional Nanocrystals Produced by Exfoliation of Ti3AlC2.* Advanced Materials, 2011. **23**(37): p. 4248-4253.
25. Naguib, M., et al., *25th Anniversary Article: MXenes: A New Family of Two-Dimensional Materials.* Advanced Materials, 2014. **26**(7): p. 992-1005.
26. Cao, J., et al., *Realization of 2D crystalline metal nitrides via selective atomic substitution.* Science Advances, 2020. **6**(2): p. eaax8784.
27. Park, J.-H., et al., *Large-Area Monolayer Hexagonal Boron Nitride on Pt Foil.* ACS Nano, 2014. **8**(8): p. 8520-8528.
28. Zhang, K., et al., *Two dimensional hexagonal boron nitride (2D-hBN): synthesis, properties and applications.* Journal of Materials Chemistry C, 2017. **5**(46): p. 11992-12022.
29. Ly, T.H., et al., *Dynamical observations on the crack tip zone and stress corrosion of two-dimensional MoS2.* Nature Communications, 2017. **8**(1): p. 14116.
30. Georgantzinos, S., et al., *Mechanical properties of hexagonal boron nitride monolayers: Finite element and analytical predictions.* Proceedings of the Institution of Mechanical Engineers, Part C: Journal of Mechanical Engineering Science, 2020. **234**(20): p. 4126-4135.
31. Lee, C., et al., *Measurement of the elastic properties and intrinsic strength of monolayer graphene.* Science, 2008. **321**(5887): p. 385-8.
32. Weiss, N.O., et al., *Graphene: an emerging electronic material.* Adv Mater, 2012. **24**(43): p. 5782-825.
33. Stankovich, S., et al., *Graphene-based composite materials.* Nature, 2006. **442**(7100): p. 282-286.
34. Morozov, S.V., et al., *Giant Intrinsic Carrier Mobilities in Graphene and Its Bilayer.* Physical Review Letters, 2008. **100**(1): p. 016602.
35. Van Khai, T., et al., *Significant enhancement of blue emission and electrical conductivity of N-doped graphene.* Journal of Materials Chemistry, 2012. **22**(34): p. 17992-18003.
36. Lee, K.H., et al., *Large-Scale Synthesis of High-Quality Hexagonal Boron Nitride Nanosheets for Large-Area Graphene Electronics.* Nano Letters, 2012. **12**(2): p. 714-718.
37. Sun, C., et al., *N-doped WS2 nanosheets: a high-performance electrocatalyst for the hydrogen evolution reaction.* Journal of Materials Chemistry A, 2016. **4**(29): p. 11234-11238.
38. Gao, H., et al., *Tuning Electrical Conductance of MoS2 Monolayers through Substitutional Doping.* Nano Letters, 2020. **20**(6): p. 4095-4101.
39. Ma, Y., et al., *Electronic and magnetic properties of perfect, vacancy-doped, and nonmetal adsorbed MoSe2, MoTe2 and WS2 monolayers.* Physical Chemistry Chemical Physics, 2011. **13**(34): p. 15546-15553.
40. Yoo, E., et al., *Large Reversible Li Storage of Graphene Nanosheet Families for Use in Rechargeable Lithium Ion Batteries.* Nano Letters, 2008. **8**(8): p. 2277-2282.
41. Stoller, M.D., et al., *Graphene-Based Ultracapacitors.* Nano Letters, 2008. **8**(10): p. 3498-3502.
42. Yang, F., et al., *2D Organic Materials for Optoelectronic Applications.* Advanced Materials, 2018. **30**(2): p. 1702415.
43. Naumis, G.G., et al., *Electronic and optical properties of strained graphene and other strained 2D materials: a review.* Reports on Progress in Physics, 2017. **80**(9): p. 096501.
44. Guo, F., et al., *Graphene-based environmental barriers.* Environ Sci Technol, 2012. **46**(14): p. 7717-24.
45. Pierleoni, D., et al., *Selective Gas Permeation in Graphene Oxide–Polymer Self-Assembled Multilayers.* ACS Applied Materials & Interfaces, 2018. **10**(13): p. 11242-11250.

46. Wang, E.N. and R. Karnik, *Graphene cleans up water.* Nature Nanotechnology, 2012. **7**(9): p. 552-554.
47. Yang, L., et al., *Mass production of two-dimensional materials beyond graphene and their applications.* Nano Research, 2021. **14**(6): p. 1583-1597.
48. Hass, J., W.A. de Heer, and E.H. Conrad, *The growth and morphology of epitaxial multilayer graphene.* Journal of Physics: Condensed Matter, 2008. **20**(32): p. 323202.
49. Yi, M. and Z. Shen, *A review on mechanical exfoliation for the scalable production of graphene.* Journal of Materials Chemistry A, 2015. **3**(22): p. 11700-11715.
50. Bhuyan, M.S.A., et al., *Synthesis of graphene.* International Nano Letters, 2016. **6**(2): p. 65-83.
51. Li, X., et al., *Large-area synthesis of high-quality and uniform graphene films on copper foils.* Science, 2009. **324**(5932): p. 1312-4.
52. Somani, P.R., S.P. Somani, and M. Umeno, *Planer nano-graphenes from camphor by CVD.* Chemical Physics Letters, 2006. **430**(1): p. 56-59.
53. Cao, H., et al., *Large-scale graphitic thin films synthesized on Ni and transferred to insulators: Structural and electronic properties.* Journal of Applied Physics, 2010. **107**(4).
54. Penuelas, J., et al., *Surface morphology and characterization of thin graphene films on SiC vicinal substrate.* Physical Review B, 2009. **79**(3): p. 033408.
55. Varchon, F., et al., *Electronic Structure of Epitaxial Graphene Layers on SiC: Effect of the Substrate.* Physical Review Letters, 2007. **99**(12): p. 126805.
56. Wintterlin, J. and M.L. Bocquet, *Graphene on metal surfaces.* Surface Science, 2009. **603**(10): p. 1841-1852.
57. Vázquez de Parga, A.L., et al., *Periodically Rippled Graphene: Growth and Spatially Resolved Electronic Structure.* Physical Review Letters, 2008. **100**(5): p. 056807.
58. Sutter, P.W., J.-I. Flege, and E.A. Sutter, *Epitaxial graphene on ruthenium.* Nature Materials, 2008. **7**(5): p. 406-411.
59. Yang, S., et al., *Emerging 2D Materials Produced via Electrochemistry.* Advanced Materials, 2020. **32**(10): p. 1907857.
60. Zeng, Z., et al., *An effective method for the fabrication of few-layer-thick inorganic nanosheets.* Angew Chem Int Ed Engl, 2012. **51**(36): p. 9052-6.
61. Lin, Z., et al., *Solution-processable 2D semiconductors for high-performance large-area electronics.* Nature, 2018. **562**(7726): p. 254-258.
62. Parvez, K., et al., *Exfoliation of Graphite into Graphene in Aqueous Solutions of Inorganic Salts.* Journal of the American Chemical Society, 2014. **136**(16): p. 6083-6091.
63. Cohen-Karni, T., et al., *Graphene and Nanowire Transistors for Cellular Interfaces and Electrical Recording.* Nano Letters, 2010. **10**(3): p. 1098-1102.
64. Banadaki, Y.M., K.M. Mohsin, and A. Srivastava. *A graphene field effect transistor for high temperature sensing applications*. in *Proceedings of SPIE - The International Society for Optical Engineering*. 2014.
65. Li, J., et al., *Photosensitive Graphene Transistors.* Advanced Materials, 2014. **26**(31): p. 5239-5273.
66. Wang, H., et al., *Graphene-Based Ambipolar RF Mixers.* Electron Device Letters, IEEE, 2010. **31**: p. 906-908.
67. Wang, H., A.L. Hsu, and T. Palacios, *Graphene electronics for RF applications.* IEEE Microwave Magazine, 2012. **13**(4): p. 114-125.
68. Hummers, W.S., Jr. and R.E. Offeman, *Preparation of Graphitic Oxide.* Journal of the American Chemical Society, 1958. **80**(6): p. 1339-1339.
69. Marcano, D.C., et al., *Improved Synthesis of Graphene Oxide.* ACS Nano, 2010. **4**(8): p. 4806-4814.
70. Peng, L., et al., *An iron-based green approach to 1-h production of single-layer graphene oxide.* Nature Communications, 2015. **6**(1): p. 5716.

71. Szabó, T., et al., *Evolution of Surface Functional Groups in a Series of Progressively Oxidized Graphite Oxides.* Chemistry of Materials, 2006. **18**(11): p. 2740-2749.
72. Hofmann, U. and R. Holst, *Über die Säurenatur und die Methylierung von Graphitoxyd.* Berichte der deutschen chemischen Gesellschaft (A and B Series), 1939. **72**(4): p. 754-771.
73. Ruess, G., *Über das Graphitoxyhydroxyd (Graphitoxyd).* Monatshefte für Chemie und verwandte Teile anderer Wissenschaften, 1947. **76**(3): p. 381-417.
74. Scholz, W. and H.P. Boehm, *Untersuchungen am Graphitoxid. VI. Betrachtungen zur Struktur des Graphitoxids.* Zeitschrift für anorganische und allgemeine Chemie, 1969. **369**(3-6): p. 327-340.
75. Nakajima, T. and Y. Matsuo, *Formation process and structure of graphite oxide.* Carbon, 1994. **32**(3): p. 469-475.
76. Lerf, A., et al., *Structure of Graphite Oxide Revisited.* The Journal of Physical Chemistry B, 1998. **102**(23): p. 4477-4482.
77. Yang, Y.-K., et al., *Graphene-based materials with tailored nanostructures for energy conversion and storage.* Materials Science and Engineering: R: Reports, 2016. **102**: p. 1-72.
78. Anichini, C., et al., *Chemical sensing with 2D materials.* Chemical Society Reviews, 2018. **47**(13): p. 4860-4908.
79. Song, Y., et al., *Role of interfacial oxide in high-efficiency graphene-silicon Schottky barrier solar cells.* Nano Lett, 2015. **15**(3): p. 2104-10.
80. Joshi, S., et al., *Green synthesis of peptide functionalized reduced graphene oxide (rGO) nano bioconjugate with enhanced antibacterial activity.* 2020. **10**(1): p. 9441.
81. Pakulski, D., et al., *High-sorption terpyridine–graphene oxide hybrid for the efficient removal of heavy metal ions from wastewater.* Nanoscale, 2021. **13**(23): p. 10490-10499.
82. Dai, L., *Functionalization of Graphene for Efficient Energy Conversion and Storage.* Accounts of Chemical Research, 2013. **46**(1): p. 31-42.
83. Zhao, J., et al., *Efficient Preparation of Large-Area Graphene Oxide Sheets for Transparent Conductive Films.* ACS Nano, 2010. **4**(9): p. 5245-5252.
84. Becerril, H.A., et al., *Evaluation of solution-processed reduced graphene oxide films as transparent conductors.* ACS Nano, 2008. **2**(3): p. 463-70.
85. Sim, H.J., et al., *The Influence of Lateral Size and Oxidation of Graphene Oxide on Its Chemical Reduction and Electrical Conductivity of Reduced Graphene Oxide.* Molecules, 2022. **27**(22): p. 7840.
86. Stankovich, S., et al., *Synthesis of graphene-based nanosheets via chemical reduction of exfoliated graphite oxide.* Carbon, 2007. **45**(7): p. 1558-1565.
87. Chudziak, T., et al., *A comparative investigation of the chemical reduction of graphene oxide for electrical engineering applications.* Nanoscale, 2023. **15**(44): p. 17765-17775.
88. Mao, S., et al., *A new reducing agent to prepare single-layer, high-quality reduced graphene oxide for device applications.* Nanoscale, 2011. **3**(7): p. 2849-2853.
89. Zhou, X., et al., *Reducing Graphene Oxide via Hydroxylamine: A Simple and Efficient Route to Graphene.* The Journal of Physical Chemistry C, 2011. **115**(24): p. 11957-11961.
90. Shin, H.-J., et al., *Efficient Reduction of Graphite Oxide by Sodium Borohydride and Its Effect on Electrical Conductance.* Advanced Functional Materials, 2009. **19**(12): p. 1987-1992.
91. Zhang, J., et al., *Reduction of graphene oxide vial-ascorbic acid.* Chemical Communications, 2010. **46**(7): p. 1112-1114.
92. De Silva, K.K.H., H.-H. Huang, and M. Yoshimura, *Progress of reduction of graphene oxide by ascorbic acid.* Applied Surface Science, 2018. **447**: p. 338-346.

93. Fernández-Merino, M.J., et al., *Vitamin C Is an Ideal Substitute for Hydrazine in the Reduction of Graphene Oxide Suspensions.* The Journal of Physical Chemistry C, 2010. **114**(14): p. 6426-6432.
94. Li, C.-J. and B.M. Trost, *Green chemistry for chemical synthesis.* Proceedings of the National Academy of Sciences, 2008. **105**(36): p. 13197-13202.
95. Pelaez-Fernandez, M., et al., *Detailed thermal reduction analyses of graphene oxide via in-situ TEM/EELS studies.* Carbon, 2021. **178**: p. 477-487.
96. Afanas'ev, V.P., et al., *Studying Thermally Reduced Graphene Oxide by X-Ray Photoelectron Spectroscopy.* Journal of Structural Chemistry, 2020. **61**(5): p. 803-810.
97. Kumar, P., et al., *Graphene produced by radiation-induced reduction of graphene oxide.* International Journal of Nanoscience, 2011. **10**(04n05): p. 559-566.
98. Mohandoss, M., et al., *Solar mediated reduction of graphene oxide.* RSC Advances, 2017. **7**(2): p. 957-963.
99. Gao, W., et al., *New insights into the structure and reduction of graphite oxide.* Nature Chemistry, 2009. **1**(5): p. 403-408.
100. Li, H. and C. Bubeck, *Photoreduction processes of graphene oxide and related applications.* Macromolecular Research, 2013. **21**(3): p. 290-297.
101. Iskandar, F., et al., *Microwave-assisted reduction method under nitrogen atmosphere for synthesis and electrical conductivity improvement of reduced graphene oxide (rGO).* RSC Advances, 2017. **7**(83): p. 52391-52397.
102. Lundie, M., Ž. Šljivančanin, and S. Tomić, *Electronic and optical properties of reduced graphene oxide.* Journal of Materials Chemistry C, 2015. **3**(29): p. 7632-7641.
103. Güçlü, A.D., P. Potasz, and P. Hawrylak, *Excitonic absorption in gate-controlled graphene quantum dots.* Physical Review B, 2010. **82**(15): p. 155445.
104. Zang, Y., et al., *Advances of flexible pressure sensors toward artificial intelligence and health care applications.* Mater. Horiz., 2014. **2**.
105. Hammock, M.L., et al., *25th Anniversary Article: The Evolution of Electronic Skin (E-Skin): A Brief History, Design Considerations, and Recent Progress.* Advanced Materials, 2013. **25**(42): p. 5997-6038.
106. Jung, S., et al., *Reverse-micelle-induced porous pressure-sensitive rubber for wearable human-machine interfaces.* Adv Mater, 2014. **26**(28): p. 4825-30.
107. Lipomi, D.J., et al., *Skin-like pressure and strain sensors based on transparent elastic films of carbon nanotubes.* Nat Nanotechnol, 2011. **6**(12): p. 788-92.
108. Schwartz, G., et al., *Flexible polymer transistors with high pressure sensitivity for application in electronic skin and health monitoring.* Nature Communications, 2013. **4**(1): p. 1859.
109. Mannsfeld, S.C.B., et al., *Highly sensitive flexible pressure sensors with microstructured rubber dielectric layers.* Nature Materials, 2010. **9**(10): p. 859-864.
110. Yeom, C., et al., *Large-Area Compliant Tactile Sensors Using Printed Carbon Nanotube Active-Matrix Backplanes.* Advanced Materials, 2015. **27**(9): p. 1561-1566.
111. Lou, Z., et al., *An ultra-sensitive and rapid response speed graphene pressure sensors for electronic skin and health monitoring.* Nano Energy, 2016. **23**: p. 7-14.
112. Kang, D., et al., *Ultrasensitive mechanical crack-based sensor inspired by the spider sensory system.* Nature, 2014. **516**(7530): p. 222-226.
113. Tee, B.C.-K., et al., *A skin-inspired organic digital mechanoreceptor.* Science, 2015. **350**(6258): p. 313-316.
114. Kollosche, M., et al., *Strongly enhanced sensitivity in elastic capacitive strain sensors.* J. Mater. Chem., 2011. **21**: p. 8292-8294.
115. Someya, T., et al., *A large-area, flexible pressure sensor matrix with organic field-effect transistors for artificial skin applications.* Proceedings of the National Academy of Sciences, 2004. **101**(27): p. 9966-9970.

116. Bockenhauer, D., *Pulse wave velocity, blood pressure and bicycle tyres.* Pediatric Nephrology, 2011. **26**(8): p. 1343-1343.
117. Huang, C.-B., et al., *Molecule–Graphene Hybrid Materials with Tunable Mechanoresponse: Highly Sensitive Pressure Sensors for Health Monitoring.* Advanced Materials, 2019. **31**(1): p. 1804600.
118. Zhang, Z., et al., *Functional nanogenerators as vibration sensors enhanced by piezotronic effects.* Nano Research, 2014. **7**(2): p. 190-198.
119. Yao, H.B., et al., *A flexible and highly pressure-sensitive graphene-polyurethane sponge based on fractured microstructure design.* Adv Mater, 2013. **25**(46): p. 6692-8.
120. Wang, Q., W. Hong, and L. Dong, *Graphene "microdrums" on a freestanding perforated thin membrane for high sensitivity MEMS pressure sensors.* Nanoscale, 2016. **8**(14): p. 7663-7671.
121. Zhong, Y.-N., et al., *Heterojunction effect on contact resistance minimization in staggered pentacene thin-film transistors.* Applied Physics Express, 2016. **9**(11): p. 111601.
122. Pan, L., et al., *An ultra-sensitive resistive pressure sensor based on hollow-sphere microstructure induced elasticity in conducting polymer film.* Nat Commun, 2014. **5**: p. 3002.
123. Chou, H.H., et al., *A chameleon-inspired stretchable electronic skin with interactive colour changing controlled by tactile sensing.* Nat Commun, 2015. **6**: p. 8011.
124. Stampfer, C., et al., *Fabrication of Single-Walled Carbon-Nanotube-Based Pressure Sensors.* Nano Letters, 2006. **6**(2): p. 233-237.
125. Gong, S. and W. Cheng, *One-Dimensional Nanomaterials for Soft Electronics.* Advanced Electronic Materials, 2016. **3**: p. 1600314.
126. Maheshwari, V. and R. Saraf, *Tactile Devices To Sense Touch on a Par with a Human Finger.* Angewandte Chemie International Edition, 2008. **47**(41): p. 7808-7826.
127. Di, C.-a., F. Zhang, and D. Zhu, *Multi-Functional Integration of Organic Field-Effect Transistors (OFETs): Advances and Perspectives.* Advanced Materials, 2013. **25**(3): p. 313-330.
128. Guo, Y., G. Yu, and Y. Liu, *Functional Organic Field-Effect Transistors.* Advanced Materials, 2010. **22**(40): p. 4427-4447.
129. Di, C.-a., et al., *Interface Engineering: An Effective Approach toward High-Performance Organic Field-Effect Transistors.* Accounts of Chemical Research, 2009. **42**(10): p. 1573-1583.
130. Ke, K., et al., *Highly sensitive capacitive pressure sensors based on elastomer composites with carbon filler hybrids.* Composites Part A: Applied Science and Manufacturing, 2019. **126**: p. 105614.
131. Miao, P., et al., *Graphene Nanostructure-Based Tactile Sensors for Electronic Skin Applications.* Nano-Micro Letters, 2019. **11**: p. 71.
132. Xia, Y., et al., *Practical and Durable Flexible Strain Sensors Based on Conductive Carbon Black and Silicone Blends for Large Scale Motion Monitoring Applications.* Sensors, 2019. **19**(20): p. 4553.
133. Kou, H., et al., *Wireless wide-range pressure sensor based on graphene/PDMS sponge for tactile monitoring.* Scientific Reports, 2019. **9**(1): p. 3916.
134. He, Z., et al., *Capacitive Pressure Sensor with High Sensitivity and Fast Response to Dynamic Interaction Based on Graphene and Porous Nylon Networks.* 2018. **10**(15): p. 12816-12823.
135. Park, K.-I., et al., *Highly-Efficient, Flexible Piezoelectric PZT Thin Film Nanogenerator on Plastic Substrates.* Advanced Materials, 2014. **26**(16): p. 2514-2520.
136. Xu, S., et al., *Self-powered nanowire devices.* Nat Nanotechnol, 2010. **5**(5): p. 366-73.
137. Lin, L., et al., *Triboelectric active sensor array for self-powered static and dynamic pressure detection and tactile imaging.* ACS Nano, 2013. **7**(9): p. 8266-74.

138. Ong, M.T., K.-A.N. Duerloo, and E.J. Reed, *The Effect of Hydrogen and Fluorine Coadsorption on the Piezoelectric Properties of Graphene.* The Journal of Physical Chemistry C, 2013. **117**(7): p. 3615-3620.
139. Duerloo, K.-A.N., M.T. Ong, and E.J. Reed, *Intrinsic Piezoelectricity in Two-Dimensional Materials.* The Journal of Physical Chemistry Letters, 2012. **3**(19): p. 2871-2876.
140. Li, X. and H. Zhu, *Two-dimensional MoS2: Properties, preparation, and applications.* Journal of Materiomics, 2015. **1**(1): p. 33-44.
141. Cui, X., et al., *Multi-terminal transport measurements of MoS2 using a van der Waals heterostructure device platform.* Nature Nanotechnology, 2015. **10**(6): p. 534-540.
142. Li, W. and J. Li, *Piezoelectricity in two-dimensional group-III monochalcogenides.* Nano Research, 2015. **8**(12): p. 3796-3802.
143. Choong, C.L., et al., *Highly stretchable resistive pressure sensors using a conductive elastomeric composite on a micropyramid array.* Adv Mater, 2014. **26**(21): p. 3451-8.
144. Guo, Y., M. Zhong, and Z. Fang, *A Wearable Transient Pressure Sensor Made with MXene Nanosheets for Sensitive Broad-Range Human-Machine Interfacing.* 2019. **19**(2): p. 1143-1150.
145. Park, Y.J., et al., *All MoS(2)-Based Large Area, Skin-Attachable Active-Matrix Tactile Sensor.* 2019. **13**(3): p. 3023-3030.
146. Zheng, Y., et al., *Conductive MXene/cotton fabric based pressure sensor with both high sensitivity and wide sensing range for human motion detection and E-skin.* Chemical Engineering Journal, 2021. **420**: p. 127720.
147. He, X., et al., *Microstructured capacitive sensor with broad detection range and long-term stability for human activity detection.* npj Flexible Electronics, 2021. **5**(1): p. 17.
148. Yang, Z., et al., *Superhydrophobic MXene@ carboxylated carbon nanotubes/carboxymethyl chitosan aerogel for piezoresistive pressure sensor.* Chemical Engineering Journal, 2021. **425**: p. 130462.
149. You, X., et al., *Stretchable capacitive fabric electronic skin woven by electrospun nanofiber coated yarns for detecting tactile and multimodal mechanical stimuli.* Journal of Materials Chemistry C, 2018. **6**(47): p. 12981-12991.
150. Li, P., et al., *A wearable and sensitive graphene-cotton based pressure sensor for human physiological signals monitoring.* Scientific Reports, 2019. **9**(1): p. 14457.
151. Shadmand, Z., J. Rahbar Shahrouzi, and H. Hosseinzadeh Chaboki, *Design and fabrication of a graphene-based microcantilever flow sensor for liquid flow measurement.* Sensors and Actuators A: Physical, 2021. **317**: p. 112438.
152. Jian, M., et al., *Flexible and Highly Sensitive Pressure Sensors Based on Bionic Hierarchical Structures.* Advanced Functional Materials, 2017. **27**(9): p. 1606066.
153. Liu, S. and X. Wu, *Ultrafast Dynamic Pressure Sensors Based on Graphene Hybrid Structure.* 2017. **9**(28): p. 24148-24154.
154. Li, X.-P., et al., *Highly sensitive, reliable and flexible piezoresistive pressure sensors featuring polyurethane sponge coated with MXene sheets.* Journal of Colloid and Interface Science, 2019. **542**: p. 54-62.
155. Yue, Y., et al., *3D hybrid porous Mxene-sponge network and its application in piezoresistive sensor.* Nano Energy, 2018. **50**: p. 79-87.
156. Rinaldi, A., et al., *A Flexible and Highly Sensitive Pressure Sensor Based on a PDMS Foam Coated with Graphene Nanoplatelets.* Sensors, 2016. **16**(12): p. 2148.
157. Ma, Y., et al., *A highly flexible and sensitive piezoresistive sensor based on MXene with greatly changed interlayer distances.* Nature Communications, 2017. **8**(1): p. 1207.
158. Ma, Y., et al., *3D Synergistical MXene/Reduced Graphene Oxide Aerogel for a Piezoresistive Sensor.* ACS Nano, 2018. **12**(4): p. 3209-3216.
159. Cai, Y., et al., *Stretchable Ti(3)C(2)T(x) MXene/Carbon Nanotube Composite Based Strain Sensor with Ultrahigh Sensitivity and Tunable Sensing Range.* 2018. **12**(1): p. 56-62.

160. Li, M., et al., *Pressure sensing element based on the BN–graphene–BN heterostructure.* Applied Physics Letters, 2018. **112**(14).
161. Smith, A.D., et al., *Electromechanical Piezoresistive Sensing in Suspended Graphene Membranes.* Nano Letters, 2013. **13**(7): p. 3237-3242.
162. Hurst, A., et al., *A transconductive graphene pressure sensor*. 2013. 586-589.
163. Kwon, O.K., et al., *Developing ultrasensitive pressure sensor based on graphene nanoribbon: Molecular dynamics simulation.* Physica E: Low-dimensional Systems and Nanostructures, 2013. **47**: p. 6-11.
164. Smith, A.D., et al., *Piezoresistive Properties of Suspended Graphene Membranes under Uniaxial and Biaxial Strain in Nanoelectromechanical Pressure Sensors.* ACS Nano, 2016. **10**(11): p. 9879-9886.
165. Davaji, B., et al., *A patterned single layer graphene resistance temperature sensor.* Scientific Reports, 2017. **7**(1): p. 8811.
166. Zhu, S.-E., et al., *Graphene based piezoresistive pressure sensor.* Applied Physics Letters, 2013. **102**(16).
167. Milovanović, S.P., M.Ž. Tadić, and F.M. Peeters, *Graphene membrane as a pressure gauge.* Applied Physics Letters, 2017. **111**(4).
168. Nag, S., et al., *CNN Based Approach for Post Disaster Damage Assessment*, in *Proceedings of the 21st International Conference on Distributed Computing and Networking*. 2020, Association for Computing Machinery: Kolkata, India. p. Article 35.
169. Sanaeepour, M., A. Abedi, and M.J. Sharifi, *Performance Analysis of Nanoscale Single Layer Graphene Pressure Sensors.* IEEE Transactions on Electron Devices, 2017. **64**(3): p. 1300-1304.
170. Liu, D., S. Wei, and D. Wang, *Improving the Sensing Properties of Graphene MEMS Pressure Sensor by Low-Temperature Annealing in Atmosphere.* Sensors, 2022. **22**(20): p. 8082.
171. Jia, J., et al., *Skin-inspired flexible and high-sensitivity pressure sensors based on rGO films with continuous-gradient wrinkles.* Nanoscale, 2019. **11**(10): p. 4258-4266.
172. Gilanizadehdizaj, G., et al., *Facile fabrication of flexible piezo-resistive pressure sensor array using reduced graphene oxide foam and silicone elastomer.* Sensors and Actuators A: Physical, 2022. **340**: p. 113549.
173. Toropov, N., et al., *Review of biosensing with whispering-gallery mode lasers.* Light: Science & Applications, 2021. **10**(1): p. 42.
174. Han, D.-D., et al., *Bioinspired Graphene Actuators Prepared by Unilateral UV Irradiation of Graphene Oxide Papers.* Advanced Functional Materials, 2015. **25**(28): p. 4548-4557.
175. Xu, L., et al., *Self-powered ultrasensitive pulse sensors for noninvasive multi-indicators cardiovascular monitoring.* Nano Energy, 2021. **81**: p. 105614.
176. Shih, B., et al., *Electronic skins and machine learning for intelligent soft robots.* Science Robotics, 2020. **5**(41): p. eaaz9239.
177. Zhang, H., et al., *Metallic Sandwiched-Aerogel Hybrids Enabling Flexible and Stretchable Intelligent Sensor.* Nano Letters, 2020. **20**(5): p. 3449-3458.
178. Araromi, O.A., et al., *Ultra-sensitive and resilient compliant strain gauges for soft machines.* Nature, 2020. **587**(7833): p. 219-224.
179. Lee, S. and S. Franklin, *Nanomesh pressure sensor for monitoring finger manipulation without sensory interference.* 2020. **370**(6519): p. 966-970.
180. Zhang, L., et al., *Fully organic compliant dry electrodes self-adhesive to skin for long-term motion-robust epidermal biopotential monitoring.* Nature Communications, 2020. **11**(1): p. 4683.
181. Gao, Y., et al., *Flexible Hybrid Sensors for Health Monitoring: Materials and Mechanisms to Render Wearability.* Advanced Materials, 2020. **32**(15): p. 1902133.
182. Li, S.-X., et al., *Perovskite Single-Crystal Microwire-Array Photodetectors with Performance Stability beyond 1 Year.* Advanced Materials, 2020. **32**(28): p. 2001998.

183. Han, D.-D., et al., *Light-Mediated Manufacture and Manipulation of Actuators.* Advanced Materials, 2016. **28**(38): p. 8328-8343.
184. Sekitani, T. and T. Someya, *Stretchable, Large-area Organic Electronics.* Advanced Materials, 2010. **22**(20): p. 2228-2246.
185. Sekitani, T., et al., *A rubberlike stretchable active matrix using elastic conductors.* Science, 2008. **321**(5895): p. 1468-72.
186. Lee, C.-Y., et al., *Development of graphene-based sensors on paper substrate for the measurement of pH value of analyte.* BioChip Journal, 2016. **10**(3): p. 182-188.
187. Liao, X., et al., *Flexible, Cuttable, and Self-Waterproof Bending Strain Sensors Using Microcracked Gold Nanofilms@Paper Substrate.* ACS Applied Materials & Interfaces, 2017. **9**(4): p. 4151-4158.
188. Rim, Y.S., et al., *Recent Progress in Materials and Devices toward Printable and Flexible Sensors.* Advanced Materials, 2016. **28**(22): p. 4415-4440.
189. Ginley, D., *Handbook of Transparent Conductors*. 2011.
190. Barsan, N., D. Koziej, and U. Weimar, *Metal oxide-based gas sensor research: How to?* Sensors and Actuators B: Chemical, 2007. **121**(1): p. 18-35.
191. Coleman, J.N., et al., *Two-dimensional nanosheets produced by liquid exfoliation of layered materials.* Science, 2011. **331**(6017): p. 568-71.
192. Zhang, X., et al., *Black Phosphorus Quantum Dots.* Angewandte Chemie International Edition, 2015. **54**(12): p. 3653-3657.
193. Compton, O.C. and S.T. Nguyen, *Graphene Oxide, Highly Reduced Graphene Oxide, and Graphene: Versatile Building Blocks for Carbon-Based Materials.* Small, 2010. **6**(6): p. 711-723.
194. Zhang, D., et al., *Transparent, conductive, and flexible carbon nanotube films and their application in organic light-emitting diodes.* Nano Lett, 2006. **6**(9): p. 1880-6.
195. Chung, C.-H., et al., *Solution-processed flexible transparent conductors composed of silver nanowire networks embedded in indium tin oxide nanoparticle matrices.* Nano Research, 2012. **5**(11): p. 805-814.
196. Petronienė, J.J., et al., *Flexible strain sensors: Recent progress 2016-2023.* Sensors and Actuators A: Physical, 2024. **366**: p. 114950.
197. Xu, X.-L., et al., *High-performance strain sensor for detection of human motion and subtle strain by facile fabrication.* Measurement, 2022. **189**: p. 110658.
198. Geng, W., T.J. Cuthbert, and C. Menon, *Conductive Thermoplastic Elastomer Composite Capacitive Strain Sensors and Their Application in a Wearable Device for Quantitative Joint Angle Prediction.* ACS Applied Polymer Materials, 2021. **3**(1): p. 122-129.
199. Kim, Y.-G., et al., *Piezoelectric strain sensor with high sensitivity and high stretchability based on kirigami design cutting.* npj Flexible Electronics, 2022. **6**(1): p. 52.
200. Persano, L., et al., *High performance piezoelectric devices based on aligned arrays of nanofibers of poly(vinylidenefluoride-co-trifluoroethylene).* Nature Communications, 2013. **4**(1): p. 1633.
201. Chiappim, W., et al., *The status and perspectives of nanostructured materials and fabrication processes for wearable piezoresistive sensors.* Microsystem Technologies, 2022. **28**(7): p. 1561-1580.
202. Wang, L., et al., *Mechanically durable and amphiphobic rubber foam composites for strain/pressure sensors.* Composites Communications, 2023. **40**: p. 101590.
203. Amjadi, M., et al., *Highly Stretchable and Sensitive Strain Sensor Based on Silver Nanowire–Elastomer Nanocomposite.* ACS Nano, 2014. **8**(5): p. 5154-5163.
204. Chen, S., et al., *Transparent and Waterproof Ionic Liquid-Based Fibers for Highly Durable Multifunctional Sensors and Strain-Insensitive Stretchable Conductors.* ACS Applied Materials & Interfaces, 2018. **10**(4): p. 4305-4314.
205. Feng, W., et al., *Sensitive Electronic-Skin Strain Sensor Array Based on the Patterned Two-Dimensional α-In2Se3.* Chemistry of Materials, 2016. **28**(12): p. 4278-4283.

206. Wang, C., et al., *Synthesis of atomically thin GaSe wrinkles for strain sensors.* Frontiers of Physics, 2016. **11**(2): p. 116802.
207. Xu, M., et al., *Highly stretchable strain sensors with reduced graphene oxide sensing liquids for wearable electronics.* Nanoscale, 2018. **10**(11): p. 5264-5271.
208. Pang, Y., et al., *Flexible, Highly Sensitive, and Wearable Pressure and Strain Sensors with Graphene Porous Network Structure.* ACS Appl Mater Interfaces, 2016. **8**(40): p. 26458-26462.
209. Deng, C., et al., *High-performance capacitive strain sensors with highly stretchable vertical graphene electrodes.* Journal of Materials Chemistry C, 2020. **8**(16): p. 5541-5546.
210. Sun, Q., et al., *Active Matrix Electronic Skin Strain Sensor Based on Piezopotential-Powered Graphene Transistors.* Advanced Materials, 2015. **27**(22): p. 3411-3417.
211. Park, M., et al., *MoS2-Based Tactile Sensor for Electronic Skin Applications.* Advanced Materials, 2016. **28**(13): p. 2556-2562.
212. Zheng, Q., et al., *Sliced graphene foam films for dual-functional wearable strain sensors and switches.* Nanoscale Horizons, 2018. **3**(1): p. 35-44.
213. Cai, Y., et al., *Stretchable Ti3C2Tx MXene/Carbon Nanotube Composite Based Strain Sensor with Ultrahigh Sensitivity and Tunable Sensing Range.* ACS Nano, 2018. **12**(1): p. 56-62.
214. Yang, Y., et al., *Strain Sensors with a High Sensitivity and a Wide Sensing Range Based on a Ti3C2Tx (MXene) Nanoparticle–Nanosheet Hybrid Network.* Advanced Functional Materials, 2019. **29**(14): p. 1807882.
215. Zhang, Y.-Z., et al., *MXenes stretch hydrogel sensor performance to new limits.* Science Advances, 2018. **4**(6): p. eaat0098.
216. Liao, H., et al., *Conductive MXene Nanocomposite Organohydrogel for Flexible, Healable, Low-Temperature Tolerant Strain Sensors.* Advanced Functional Materials, 2019. **29**(39): p. 1904507.
217. Chen, L., et al., *Ultrasensitive and robust two-dimensional indium selenide flexible electronics and sensors for human motion detection.* Nano Energy, 2020. **76**: p. 105020.
218. Yan, W., et al., *Giant gauge factor of Van der Waals material based strain sensors.* Nature Communications, 2021. **12**(1): p. 2018.
219. Qin, Y., et al., *Lightweight, Superelastic, and Mechanically Flexible Graphene/Polyimide Nanocomposite Foam for Strain Sensor Application.* ACS Nano, 2015. **9**(9): p. 8933-8941.
220. Bae, S.-H., et al., *Graphene-based transparent strain sensor.* Carbon, 2013. **51**: p. 236-242.
221. Tian, H., et al., *Scalable fabrication of high-performance and flexible graphene strain sensors.* Nanoscale, 2014. **6**(2): p. 699-705.
222. Bandi, S. and A.K. Srivastav, *Chapter Seven - Graphene-based chemiresistive gas sensors*, in *Comprehensive Analytical Chemistry*, C.M. Hussain, Editor. 2020, Elsevier. p. 149-173.
223. Sun, Y.-F., et al., *Metal Oxide Nanostructures and Their Gas Sensing Properties: A Review.* Sensors, 2012. **12**(3): p. 2610-2631.
224. Janata, J. and M. Josowicz, *Conducting polymers in electronic chemical sensors.* Nature Materials, 2003. **2**(1): p. 19-24.
225. Yun, W. and J. Yeow, *A Review of Carbon Nanotubes-Based Gas Sensors.* Journal of Sensors, 2009. **2009**.
226. Ponzoni, A., et al., *Metal Oxide Gas Sensors, a Survey of Selectivity Issues Addressed at the SENSOR Lab, Brescia (Italy).* Sensors, 2017. **17**(4): p. 714.
227. Fine, G.F., et al., *Metal Oxide Semi-Conductor Gas Sensors in Environmental Monitoring.* Sensors, 2010. **10**(6): p. 5469-5502.
228. Liu, H., et al., *Phosphorene: An Unexplored 2D Semiconductor with a High Hole Mobility.* ACS Nano, 2014. **8**(4): p. 4033-4041.

229. Mayorga-Martinez, C.C., Z. Sofer, and M. Pumera, *Layered Black Phosphorus as a Selective Vapor Sensor.* Angewandte Chemie International Edition, 2015. **54**(48): p. 14317-14320.
230. Mak, K.F., et al., *Atomically Thin ${\mathrm{MoS}}_{2}$: A New Direct-Gap Semiconductor.* Physical Review Letters, 2010. **105**(13): p. 136805.
231. Li, H., et al., *Fabrication of single- and multilayer MoS2 film-based field-effect transistors for sensing NO at room temperature.* Small, 2012. **8**(1): p. 63-7.
232. Yue, Q., et al., *Adsorption of gas molecules on monolayer MoS2 and effect of applied electric field.* Nanoscale Research Letters, 2013. **8**(1): p. 425.
233. Perkins, F.K., et al., *Chemical Vapor Sensing with Monolayer MoS2.* Nano Letters, 2013. **13**(2): p. 668-673.
234. Mannix, A.J., et al., *Synthesis and chemistry of elemental 2D materials.* Nature Reviews Chemistry, 2017. **1**(2): p. 0014.
235. Choi, W., et al., *Recent development of two-dimensional transition metal dichalcogenides and their applications.* Materials Today, 2017. **20**(3): p. 116-130.
236. Järvinen, T., et al., *WS2 and MoS2 thin film gas sensors with high response to NH3 in air at low temperature.* Nanotechnology, 2019. **30**(40): p. 405501.
237. O'Brien, M., et al., *Plasma assisted synthesis of WS2 for gas sensing applications.* Chemical Physics Letters, 2014. **615**: p. 6-10.
238. Yao, Y., et al., *Humidity sensing behaviors of graphene oxide-silicon bi-layer flexible structure.* Sensors and Actuators B: Chemical, 2012. **161**(1): p. 1053-1058.
239. Bi, H., et al., *Ultrahigh humidity sensitivity of graphene oxide.* Scientific Reports, 2013. **3**(1): p. 2714.
240. Ghosh, S., et al., *Humidity Sensor Based on High Proton Conductivity of Graphene Oxide.* Nanotechnology, IEEE Transactions on, 2015. **14**: p. 931-937.
241. Zhang, S.-L., et al., *Efficient exfoliation of MoS2 with volatile solvents and their application for humidity sensor.* Journal of nanoscience and nanotechnology, 2014. **14**(11): p. 8518-8522.
242. Jha, R.K. and P.K. Guha, *Liquid exfoliated pristine WS2 nanosheets for ultrasensitive and highly stable chemiresistive humidity sensors.* Nanotechnology, 2016. **27**(47): p. 475503.
243. Su, P.-G. and C.-F. Chiou, *Electrical and humidity-sensing properties of reduced graphene oxide thin film fabricated by layer-by-layer with covalent anchoring on flexible substrate.* Sensors and Actuators B: Chemical, 2014. **200**: p. 9-18.
244. Smith, A.D., et al., *Resistive graphene humidity sensors with rapid and direct electrical readout.* Nanoscale, 2015. **7**(45): p. 19099-19109.
245. Feng, J., et al., *Giant moisture responsiveness of VS 2 ultrathin nanosheets for novel touchless positioning interface.* Advanced materials, 2012. **15**(24): p. 1969-1974.
246. Shaukat, R.A., et al., *All range highly linear and sensitive humidity sensor based on 2D material TiSi2 for real-time monitoring.* Sensors and Actuators B: Chemical, 2021. **345**: p. 130371.
247. Al-Hamry, A., et al., *Ultra-Sensitive and Fast Humidity Sensors Based on Direct Laser-Scribed Graphene Oxide/Carbon Nanotubes Composites.* Nanomaterials, 2023. **13**(9): p. 1473.
248. Pereira, N.M., et al., *Aerosol-Printed MoS(2) Ink as a High Sensitivity Humidity Sensor.* 2022. **7**(11): p. 9388-9396.
249. Shaukat, R.A., et al., *Two dimensional Zirconium diselenide based humidity sensor for flexible electronics.* Sensors and Actuators B: Chemical, 2022. **358**: p. 131507.
250. Li, N., et al., *High-Performance Humidity Sensor Based on Urchin-Like Composite of Ti(3)C(2) MXene-Derived TiO(2) Nanowires.* 2019. **11**(41): p. 38116-38125.
251. Jia, G., et al., *Flexible, biocompatible and highly conductive MXene-graphene oxide film for smart actuator and humidity sensor.* Sensors and Actuators B: Chemical, 2021. **346**: p. 130507.

252. Wehling, T.O., et al., *Molecular Doping of Graphene.* Nano Letters, 2008. **8**(1): p. 173-177.
253. Leenaerts, O., B. Partoens, and F.M. Peeters, *Adsorption of CO, and NO on graphene: A first-principles study.* Physical Review B, 2008. **77**(12): p. 125416.
254. Schedin, F., et al., *Detection of individual gas molecules adsorbed on graphene.* Nature Materials, 2007. **6**(9): p. 652-655.
255. Recum, P. and T. Hirsch, *Graphene-based chemiresistive gas sensors.* Nanoscale Advances, 2024. **6**(1): p. 11-31.
256. Wheeler, S. and J. Bloom, *Towards a More Complete Understanding of Non-Covalent Interactions Involving Aromatic Rings.* The journal of physical chemistry. A, 2014. **118**.
257. Georgakilas, V., et al., *Functionalization of graphene: covalent and non-covalent approaches, derivatives and applications.* Chem Rev, 2012. **112**(11): p. 6156-214.
258. Tai, Y., et al., *Combining the converse humidity/resistance response behaviors of rGO films for flexible logic devices.* Journal of Materials Chemistry C, 2017. **5**(15): p. 3848-3854.
259. Rathi, K. and K. Pal, *Impact of Doping on GO: Fast Response–Recovery Humidity Sensor.* ACS Omega, 2017. **2**(3): p. 842-851.
260. Teradal, N.L., et al., *Porous graphene oxide chemi-capacitor vapor sensor array.* Journal of Materials Chemistry C, 2017. **5**(5): p. 1128-1135.
261. Anichini, C., et al., *Ultrafast and Highly Sensitive Chemically Functionalized Graphene Oxide-Based Humidity Sensors: Harnessing Device Performances via the Supramolecular Approach.* ACS Applied Materials & Interfaces, 2020. **12**(39): p. 44017-44025.
262. Naik, G. and S. Krishnaswamy, *Room-Temperature Humidity Sensing Using Graphene Oxide Thin Films.* Graphene, 2016. **05**: p. 1-13.
263. Papamatthaiou, S., et al., *The Effect of Thermal Reduction and Film Thickness on fast Response Transparent Graphene Oxide Humidity Sensors.* Procedia Engineering, 2016. **168**: p. 301-304.
264. Kim, S.G., et al., *Kinetics of hydrazine reduction of thin films of graphene oxide and the determination of activation energy by the measurement of electrical conductivity.* RSC Advances, 2015. **5**(124): p. 102567-102573.
265. Zhang, Y., et al., *Dendritic, Transferable, Strictly Monolayer MoS2 Flakes Synthesized on SrTiO3 Single Crystals for Efficient Electrocatalytic Applications.* ACS Nano, 2014. **8**(8): p. 8617-8624.
266. Xu, W., et al., *Large Dendritic Monolayer MoS2 Grown by Atmospheric Pressure Chemical Vapor Deposition for Electrocatalysis.* ACS Applied Materials & Interfaces, 2018. **10**(5): p. 4630-4639.
267. Bellunato, A., et al., *Chemistry at the Edge of Graphene.* ChemPhysChem, 2016. **17**(6): p. 785-801.
268. Jia, X., et al., *Graphene edges: a review of their fabrication and characterization.* Nanoscale, 2011. **3**(1): p. 86-95.
269. Lee, D., et al., *Scalable exfoliation process for highly soluble boron nitride nanoplatelets by hydroxide-assisted ball milling.* Nano Lett, 2015. **15**(2): p. 1238-44.
270. Lei, W., et al., *Boron nitride colloidal solutions, ultralight aerogels and freestanding membranes through one-step exfoliation and functionalization.* Nature Communications, 2015. **6**(1): p. 8849.
271. Xu, J., et al., *Edge-Selectively Halogenated Graphene Nanoplatelets (XGnPs, X = Cl, Br, or I) Prepared by Ball-Milling and Used as Anode Materials for Lithium-Ion Batteries.* Advanced Materials, 2014. **26**(43): p. 7317-7323.
272. Chen, X., et al., *Functionalization of Two-Dimensional MoS2: On the Reaction Between MoS2 and Organic Thiols.* Angewandte Chemie International Edition, 2016. **55**(19): p. 5803-5808.

273. Yu, Z., et al., *Towards intrinsic charge transport in monolayer molybdenum disulfide by defect and interface engineering.* Nat Commun, 2014. **5**: p. 5290.
274. Ippolito, S., et al., *Covalently interconnected transition metal dichalcogenide networks via defect engineering for high-performance electronic devices.* 2021. **16**(5): p. 592-598.
275. Makarova, M., Y. Okawa, and M. Aono, *Selective Adsorption of Thiol Molecules at Sulfur Vacancies on MoS2(0001), Followed by Vacancy Repair via S–C Dissociation.* The Journal of Physical Chemistry C, 2012. **116**(42): p. 22411-22416.
276. Kuila, T., et al., *Chemical Functionalization of graphene and its applications.* Progress in Materials Science, 2012. **57**: p. 1061-1105.
277. Kosynkin, D.V., et al., *Longitudinal unzipping of carbon nanotubes to form graphene nanoribbons.* Nature, 2009. **458**(7240): p. 872-876.
278. Wang, X., et al., *N-doping of graphene through electrothermal reactions with ammonia.* Science, 2009. **324**(5928): p. 768-71.
279. Elias, D.C., et al., *Control of graphene's properties by reversible hydrogenation: evidence for graphane.* Science, 2009. **323**(5914): p. 610-3.
280. Ohta, T., et al., *Controlling the Electronic Structure of Bilayer Graphene.* Science, 2006. **313**(5789): p. 951-954.
281. Niyogi, S., et al., *Spectroscopy of covalently functionalized graphene.* Nano Lett, 2010. **10**(10): p. 4061-6.
282. Criado, A., et al., *The Covalent Functionalization of Graphene on Substrates.* Angewandte Chemie International Edition, 2015. **54**(37): p. 10734-10750.
283. Soni, H.R., J. Gebhardt, and A. Görling, *Reactivity of Substrate-Supported Graphene: A Case Study of Hydrogenation.* The Journal of Physical Chemistry C, 2018. **122**(5): p. 2761-2772.
284. Farjadian, F., et al., *Recent Developments in Graphene and Graphene Oxide: Properties, Synthesis, and Modifications: A Review.* ChemistrySelect, 2020. **5**(33): p. 10200-10219.
285. Copetti, G., et al., *Reversibility of Graphene Photochlorination.* The Journal of Physical Chemistry C, 2018. **122**(28): p. 16333-16338.
286. Sarkar, S., E. Bekyarova, and R.C. Haddon, *Chemistry at the Dirac point: Diels-Alder reactivity of graphene.* Acc Chem Res, 2012. **45**(4): p. 673-82.
287. Sarkar, S., et al., *Diels–Alder Chemistry of Graphite and Graphene: Graphene as Diene and Dienophile.* Journal of the American Chemical Society, 2011. **133**(10): p. 3324-3327.
288. Jiang, D.E., B.G. Sumpter, and S. Dai, *How do aryl groups attach to a graphene sheet?* J Phys Chem B, 2006. **110**(47): p. 23628-32.
289. Hossain, M.Z., M.A. Walsh, and M.C. Hersam, *Scanning Tunneling Microscopy, Spectroscopy, and Nanolithography of Epitaxial Graphene Chemically Modified with Aryl Moieties.* Journal of the American Chemical Society, 2010. **132**(43): p. 15399-15403.
290. Samaddar, P., et al., *Progress in graphene-based materials as superior media for sensing, sorption, and separation of gaseous pollutants.* Coordination Chemistry Reviews, 2018. **368**: p. 93-114.
291. Peng, W., et al., *A review on heavy metal ions adsorption from water by graphene oxide and its composites.* Journal of Molecular Liquids, 2017. **230**: p. 496-504.
292. Navalón, S., et al., *Covalently Modified Graphenes in Catalysis, Electrocatalysis and Photoresponsive Materials.* Chemistry – A European Journal, 2017. **23**(61): p. 15244-15275.
293. Bottari, G., et al., *Chemical functionalization and characterization of graphene-based materials.* Chemical Society Reviews, 2017. **46**(15): p. 4464-4500.
294. Park, S., et al., *Graphene Oxide Sheets Chemically Cross-Linked by Polyallylamine.* The Journal of Physical Chemistry C, 2009. **113**(36): p. 15801-15804.
295. Liu, Z., et al., *PEGylated Nanographene Oxide for Delivery of Water-Insoluble Cancer Drugs.* Journal of the American Chemical Society, 2008. **130**(33): p. 10876-10877.

296. Xu, Y., et al., *A Graphene Hybrid Material Covalently Functionalized with Porphyrin: Synthesis and Optical Limiting Property.* Advanced Materials, 2009. **21**(12): p. 1275-1279.
297. Veca, L.M., et al., *Polymer functionalization and solubilization of carbon nanosheets.* Chemical Communications, 2009(18): p. 2565-2567.
298. Stankovich, S., et al., *Synthesis and exfoliation of isocyanate-treated graphene oxide nanoplatelets.* Carbon, 2006. **44**(15): p. 3342-3347.
299. Hermawan, A., et al., *Advanced Strategies to Improve Performances of Molybdenum-Based Gas Sensors.* Nano-Micro Letters, 2021. **13**(1): p. 207.
300. Huang, Y., et al., *Ultrasensitive room temperature ppb-level NO2 gas sensors based on SnS2/rGO nanohybrids with P–N transition and optoelectronic visible light enhancement performance.* Journal of Materials Chemistry C, 2019. **7**(28): p. 8616-8625.
301. Lu, C.H., et al., *A graphene platform for sensing biomolecules.* Angew Chem Int Ed Engl, 2009. **48**(26): p. 4785-7.
302. Zhang, D., et al., *Room-temperature high-performance acetone gas sensor based on hydrothermal synthesized SnO2-reduced graphene oxide hybrid composite.* RSC Advances, 2015. **5**(4): p. 3016-3022.
303. Pargoletti, E., et al., *An electrochemical outlook upon the gaseous ethanol sensing by graphene oxide-SnO2 hybrid materials.* Applied Surface Science, 2019. **483**: p. 1081-1089.
304. Wang, J., et al., *Dielectrophoretic assembly of Pt nanoparticle-reduced graphene oxide nanohybrid for highly-sensitive multiple gas sensor.* Sensors and Actuators B: Chemical, 2015. **220**: p. 755-761.
305. Cittadini, M., et al., *Graphene oxide coupled with gold nanoparticles for localized surface plasmon resonance based gas sensor.* Carbon, 2014. **69**: p. 452-459.
306. Yang, T., et al., *Copper nanoparticle/graphene oxide/single wall carbon nanotube hybrid materials as electrochemical sensing platform for nonenzymatic glucose detection.* Journal of Electroanalytical Chemistry, 2016. **761**: p. 118-124.
307. Zhang, D., J. Liu, and B. Xia, *Layer-by-Layer Self-Assembly of Zinc Oxide/Graphene Oxide Hybrid Toward Ultrasensitive Humidity Sensing.* IEEE Electron Device Letters, 2016. **37**(7): p. 916-919.
308. Yang, Y. and H.E. Katz, *Hybrid of P3HT and ZnO@GO nanostructured particles for increased NO2 sensing response.* Journal of Materials Chemistry C, 2017. **5**(8): p. 2160-2166.
309. Albaris, H. and G. Karuppasamy, *Investigation of NH3 gas sensing behavior of intercalated PPy–GO–WO3 hybrid nanocomposite at room temperature.* Materials Science and Engineering: B, 2020. **257**: p. 114558.
310. Mishra, S.K., et al., *SPR based fibre optic ammonia gas sensor utilizing nanocomposite film of PMMA/reduced graphene oxide prepared by in situ polymerization.* Sensors and Actuators B: Chemical, 2014. **199**: p. 190-200.
311. Si, W., et al., *Electrodeposition of graphene oxide doped poly(3,4-ethylenedioxythiophene) film and its electrochemical sensing of catechol and hydroquinone.* Electrochimica Acta, 2012. **85**: p. 295-301.
312. Huang, X., et al., *Reduced graphene oxide–polyaniline hybrid: Preparation, characterization and its applications for ammonia gas sensing.* Journal of Materials Chemistry, 2012. **22**(42): p. 22488-22495.
313. Hou, X., et al., *Hierarchical three-dimensional MoS2/GO hybrid nanostructures for triethylamine-sensing applications with high sensitivity and selectivity.* Sensors and Actuators B: Chemical, 2020. **317**: p. 128236.
314. Lee, S.H., et al., *Room-Temperature, Highly Durable Ti3C2Tx MXene/Graphene Hybrid Fibers for NH3 Gas Sensing.* ACS Applied Materials & Interfaces, 2020. **12**(9): p. 10434-10442.

315. Zhou, C., et al., *Techniques for wearable gas sensors fabrication.* Sensors and Actuators B: Chemical, 2022. **353**: p. 131133.
316. Yu, H.-D., et al., *Chemical routes to top-down nanofabrication.* Chemical Society Reviews, 2013. **42**(14): p. 6006-6018.
317. Noah, N.M. and S.-J. Young, *Design and Synthesis of Nanostructured Materials for Sensor Applications.* J. Nanomaterials, 2020. **2020**: p. 20.
318. Zhu, R., et al., *Wireless Oxygen Sensors Enabled by Fe(II)-Polymer Wrapped Carbon Nanotubes.* ACS Sensors, 2017. **2**(7): p. 1044-1050.
319. Zheng, Y., et al., *Wearable electronic nose for human skin odor identification: A preliminary study.* Sensors and Actuators A: Physical, 2019. **285**: p. 395-405.
320. Wu, C., et al., *Interface-Regulated Contact Electrification for Power-Free and Highly Selective Gas Sensing.* Advanced Intelligent Systems, 2019. **1**(6): p. 1900066.
321. Hassinen, J., et al., *Low-cost reduced graphene oxide-based conductometric nitrogen dioxide-sensitive sensor on paper.* Analytical and Bioanalytical Chemistry, 2013. **405**(11): p. 3611-3617.
322. Lee, J., et al., *Highly Mobile Palladium Thin Films on an Elastomeric Substrate: Nanogap-Based Hydrogen Gas Sensors.* Angewandte Chemie International Edition, 2011. **50**(23): p. 5301-5305.
323. Ho, D.H., et al., *Stretchable and Multimodal All Graphene Electronic Skin.* Advanced Materials, 2016. **28**(13): p. 2601-2608.
324. Wang, B., et al., *A Highly Sensitive Diketopyrrolopyrrole-Based Ambipolar Transistor for Selective Detection and Discrimination of Xylene Isomers.* Advanced Materials, 2016. **28**(21): p. 4012-4018.
325. Guo, Y., et al., *Hierarchical graphene-polyaniline nanocomposite films for high-performance flexible electronic gas sensors.* Nanoscale, 2016. **8**(23): p. 12073-12080.
326. Kumar, L., et al., *Flexible room temperature ammonia sensor based on polyaniline.* Sensors and Actuators B: Chemical, 2017. **240**: p. 408-416.
327. Alrammouz, R., et al., *Highly porous and flexible capacitive humidity sensor based on self-assembled graphene oxide sheets on a paper substrate.* Sensors and Actuators B: Chemical, 2019. **298**: p. 126892.
328. Lutkenhaus, J.L. and P.T. Hammond, *Electrochemically enabled polyelectrolyte multilayer devices: from fuel cells to sensors.* Soft Matter, 2007. **3**(7): p. 804-816.
329. Ariga, K., *Nanoarchitectonics: a navigator from materials to life.* Materials Chemistry Frontiers, 2017. **1**(2): p. 208-211.
330. Borges, J. and J.F. Mano, *Molecular Interactions Driving the Layer-by-Layer Assembly of Multilayers.* Chemical Reviews, 2014. **114**(18): p. 8883-8942.
331. Hammond, P.T., *Engineering materials layer-by-layer: Challenges and opportunities in multilayer assembly.* AIChE Journal, 2011. **57**(11): p. 2928-2940.
332. Islam, M.M., et al., *Self-Assembled Multifunctional Hybrids: Toward Developing High-Performance Graphene-Based Architectures for Energy Storage Devices.* ACS Central Science, 2015. **1**(4): p. 206-216.
333. Decher, G., *Fuzzy Nanoassemblies: Toward Layered Polymeric Multicomposites.* Science, 1997. **277**(5330): p. 1232-1237.
334. Pomerantseva, E. and Y. Gogotsi, *Two-dimensional heterostructures for energy storage.* Nature Energy, 2017. **2**(7): p. 17089.
335. Richardson, J.J., M. Björnmalm, and F. Caruso, *Technology-driven layer-by-layer assembly of nanofilms.* Science, 2015. **348**(6233): p. aaa2491.
336. Ali Salman, A., *Application of Nanomaterials in Environmental Improvement*, in *Nanotechnology and the Environment*, S. Mousumi, Editor. 2020, IntechOpen: Rijeka. p. Ch. 2.

337. Gurzęda, B., et al., *Graphene material preparation through thermal treatment of graphite oxide electrochemically synthesized in aqueous sulfuric acid.* RSC Advances, 2017. **7**(32): p. 19904-19911.
338. Trikkaliotis, D.G., A.C. Mitropoulos, and G.Z. Kyzas, *Low-cost route for top-down synthesis of over- and low-oxidized graphene oxide.* Colloids and Surfaces A: Physicochemical and Engineering Aspects, 2020. **600**: p. 124928.
339. Wilson, N.R., et al., *Graphene Oxide: Structural Analysis and Application as a Highly Transparent Support for Electron Microscopy.* ACS Nano, 2009. **3**(9): p. 2547-2556.
340. Kariminejad, B., M. Salami-Kalajahi, and H. Roghani-Mamaqani, *Thermophysical behaviour of matrix-grafted graphene/poly(ethylene tetrasulphide) nanocomposites.* RSC Advances, 2015. **5**(121): p. 100369-100377.
341. Roghani-Mamaqani, H., et al., *Polystyrene-grafted graphene nanoplatelets with various graft densities by atom transfer radical polymerization from the edge carboxyl groups.* RSC Advances, 2014. **4**(47): p. 24439-24452.
342. Steinhardt, R. and E. Serfass, *X-Ray Photoelectron Spectrometer for Chemical Analysis.* Analytical Chemistry, 1951. **23**(11): p. 1585-1590.
343. Cushman, C., et al., *Trends in Advanced XPS Instrumentation. 1. Overview of the Technique, Automation, High Sensitivity, Imaging, Snapshot Spectroscopy, Gas Cluster Ion Beams, and Multiple Analytical Techniques on the Instrument.* Vacuum Technology & Coating, 2016.
344. Pei, S. and H.-M. Cheng, *The reduction of graphene oxide.* Carbon, 2012. **50**(9): p. 3210-3228.
345. Park, S., et al., *Graphene Oxide Papers Modified by Divalent Ions—Enhancing Mechanical Properties via Chemical Cross-Linking.* ACS Nano, 2008. **2**(3): p. 572-578.
346. Ren, P.-G., et al., *Temperature dependence of graphene oxide reduced by hydrazine hydrate.* Nanotechnology, 2011. **22**(5): p. 055705.
347. Kudin, K.N., et al., *Raman Spectra of Graphite Oxide and Functionalized Graphene Sheets.* Nano Letters, 2008. **8**(1): p. 36-41.
348. Manouchehri, M., et al., *Porphyrin-functionalized graphene oxide sheets: An efficient nanomaterial for micro solid phase extraction of non-steroidal anti-inflammatory drugs from urine samples.* Journal of Chromatography A, 2019. **1607**: p. 460387.
349. Tuinstra, F. and J.L. Koenig, *Raman Spectrum of Graphite.* The Journal of Chemical Physics, 1970. **53**(3): p. 1126-1130.
350. Perumbilavil, S., et al., *White light Z-scan measurements of ultrafast optical nonlinearity in reduced graphene oxide nanosheets in the 400–700 nm region.* Applied Physics Letters, 2015. **107**: p. 051104.
351. Harris, W. and G. Norman White, *X-ray Diffraction Techniques for Soil Mineral Identification*, in *Methods of Soil Analysis Part 5—Mineralogical Methods*. 2008. p. 81-115.
352. Trikkaliotis, D.G., et al., *Graphene Oxide Synthesis, Properties and Characterization Techniques: A Comprehensive Review.* ChemEngineering, 2021. **5**(3): p. 64.
353. Stan, C.V., et al., *X-Ray Diffraction under Extreme Conditions at the Advanced Light Source.* Quantum Beam Science, 2018. **2**(1): p. 4.
354. Zhao, B., et al., *Supercapacitor performances of thermally reduced graphene oxide.* Journal of Power Sources, 2012. **198**: p. 423-427.
355. Oliveira, E.H.C.d., et al., *Removal of toxic dyes from aqueous solution by adsorption onto highly recyclable xGnP® graphite nanoplatelets.* Journal of Environmental Chemical Engineering, 2019. **7**(2): p. 103001.
356. Wang, H., et al., *Synthesis of 3D graphite oxide-exfoliated carbon nanotube carbon composite and its application as catalyst support for fuel cells.* Journal of Power Sources, 2014. **260**: p. 338-348.

357. Perez, J.V.D., et al., *Response surface methodology as a powerful tool to optimize the synthesis of polymer-based graphene oxide nanocomposites for simultaneous removal of cationic and anionic heavy metal contaminants.* RSC Advances, 2017. **7**(30): p. 18480-18490.
358. Kyzas, G.Z., N.A. Travlou, and E.A. Deliyanni, *The role of chitosan as nanofiller of graphite oxide for the removal of toxic mercury ions.* Colloids and Surfaces B: Biointerfaces, 2014. **113**: p. 467-476.
359. Mendes, E. and N. Duarte, *Mid-Infrared Spectroscopy as a Valuable Tool to Tackle Food Analysis: A Literature Review on Coffee, Dairies, Honey, Olive Oil and Wine.* Foods, 2021. **10**(2): p. 477.
360. Blum, M.M. and H. John, *Historical perspective and modern applications of Attenuated Total Reflectance-Fourier Transform Infrared Spectroscopy (ATR-FTIR).* Drug Test Anal, 2012. **4**(3-4): p. 298-302.
361. Fale, P.L.V. and K.L.A. Chan, *Preventing damage of germanium optical material in attenuated total reflection-Fourier transform infrared (ATR-FTIR) studies of living cells.* Vibrational Spectroscopy, 2017. **91**: p. 59-67.
362. Haas, J. and B. Mizaikoff, *Advances in Mid-Infrared Spectroscopy for Chemical Analysis.* Annu Rev Anal Chem (Palo Alto Calif), 2016. **9**(1): p. 45-68.
363. Zare-Dorabei, R., et al., *Highly efficient simultaneous ultrasonic-assisted adsorption of Pb(II), Cd(II), Ni(II) and Cu (II) ions from aqueous solutions by graphene oxide modified with 2,2'-dipyridylamine: Central composite design optimization.* Ultrasonics Sonochemistry, 2016. **32**: p. 265-276.
364. Kaniyoor, A. and S. Ramaprabhu, *Thermally exfoliated graphene based counter electrode for low cost dye sensitized solar cells.* Journal of Applied Physics, 2011. **109**(12).
365. Lee, X.J., et al., *Review on graphene and its derivatives: Synthesis methods and potential industrial implementation.* Journal of the Taiwan Institute of Chemical Engineers, 2019. **98**: p. 163-180.
366. Fusco, L., et al., *Skin irritation potential of graphene-based materials using a non-animal test.* Nanoscale, 2020. **12**(2): p. 610-622.
367. Voiry, D., et al., *High-quality graphene via microwave reduction of solution-exfoliated graphene oxide.* Science, 2016. **353**(6306): p. 1413-1416.
368. Backes, C., et al., *Production and processing of graphene and related materials.* 2D Materials, 2020. **7**(2): p. 022001.
369. Reina, G., et al., *Promises, facts and challenges for graphene in biomedical applications.* Chemical Society Reviews, 2017. **46**(15): p. 4400-4416.
370. Bonaccorso, F., et al., *Graphene photonics and optoelectronics.* Nature Photonics, 2010. **4**(9): p. 611-622.
371. Eigler, S., et al., *Graphene oxide: efficiency of reducing agents.* Chemical Communications, 2013. **49**(67): p. 7391-7393.
372. Eigler, S. and A. Hirsch, *Chemistry with Graphene and Graphene Oxide—Challenges for Synthetic Chemists.* Angewandte Chemie International Edition, 2014. **53**(30): p. 7720-7738.
373. Wang, X., L. Zhi, and K. Müllen, *Transparent, Conductive Graphene Electrodes for Dye-Sensitized Solar Cells.* Nano Letters, 2008. **8**(1): p. 323-327.
374. Agarwal, V. and P. Zetterlund, *Strategies for reduction of graphene oxide – A comprehensive review.* Chemical Engineering Journal, 2021. **405**: p. 127018.
375. Guex, L.G., et al., *Experimental review: chemical reduction of graphene oxide (GO) to reduced graphene oxide (rGO) by aqueous chemistry.* Nanoscale, 2017. **9**(27): p. 9562-9571.
376. De Silva, K.K.H., et al., *Chemical reduction of graphene oxide using green reductants.* Carbon, 2017. **119**: p. 190-199.

377. Gao, J., et al., *Environment-Friendly Method To Produce Graphene That Employs Vitamin C and Amino Acid.* Chemistry of Materials, 2010. **22**(7): p. 2213-2218.
378. Sui, Z., et al., *Easy and green synthesis of reduced graphite oxide-based hydrogels.* Carbon, 2011. **49**(13): p. 4314-4321.
379. Sarr, S., et al., *Vanadium dioxide sulphur-doped reduced graphene oxide composite as novel electrode material for electrochemical capacitor.* Journal of Energy Storage, 2022. **55**: p. 105666.
380. Bharathidasan, P., et al., *Enhanced capacitance properties of nitrogen doped reduced graphene oxide obtained by simultaneous reduction and nitrogen doping.* FlatChem, 2018. **11**: p. 24-31.
381. Bertóti, I., et al., *Nitrogen implantation into graphene oxide and reduced graphene oxides using radio frequency plasma treatment in microscale.* Carbon, 2022. **199**: p. 415-423.
382. Park, S., et al. *Chemical structures of hydrazine-treated graphene oxide and generation of aromatic nitrogen doping*. Nature communications, 2012. **3**, 638 DOI: 10.1038/ncomms1643.
383. Lee, A., et al., *Raman study of D* band in graphene oxide and its correlation with reduction.* Applied Surface Science, 2021. **536**: p. 147990.
384. Claramunt, S., et al., *The Importance of Interbands on the Interpretation of the Raman Spectrum of Graphene Oxide.* The Journal of Physical Chemistry C, 2015. **119**(18): p. 10123-10129.
385. Ferrari, A.C., et al., *Raman Spectrum of Graphene and Graphene Layers.* Physical Review Letters, 2006. **97**(18): p. 187401.
386. Cançado, L.G., et al., *Quantifying defects in graphene via Raman spectroscopy at different excitation energies.* Nano Lett, 2011. **11**(8): p. 3190-6.
387. López Díaz, D., et al., *The Evolution of the Raman Spectrum With the Chemical Composition of Graphene Oxide.* The Journal of Physical Chemistry C, 2017. **121**.
388. Eckmann, A., et al., *Probing the Nature of Defects in Graphene by Raman Spectroscopy.* Nano Letters, 2012. **12**(8): p. 3925-3930.
389. Zhou, T., et al., *A simple and efficient method to prepare graphene by reduction of graphite oxide with sodium hydrosulfite.* Nanotechnology, 2011. **22**(4): p. 045704.
390. Lesiak, B., et al., *Chemical and structural properties of reduced graphene oxide—dependence on the reducing agent.* Journal of Materials Science, 2021. **56**(5): p. 3738-3754.
391. Corsini, E. and C.L. Galli, *Cytokines and irritant contact dermatitis.* Toxicology Letters, 1998. **102-103**: p. 277-282.
392. Dalla Colletta, A., et al., *CARBON-BASED nanomaterials and SKIN: An overview.* Carbon, 2022. **196**: p. 683-698.
393. Pelin, M., et al., *Graphene and graphene oxide induce ROS production in human HaCaT skin keratinocytes: the role of xanthine oxidase and NADH dehydrogenase.* Nanoscale, 2018. **10**(25): p. 11820-11830.
394. Frontiñán-Rubio, J., et al., *Differential effects of graphene materials on the metabolism and function of human skin cells.* Nanoscale, 2018. **10**(24): p. 11604-11615.
395. Pulingam, T., et al., *Mechanistic actions and contributing factors affecting the antibacterial property and cytotoxicity of graphene oxide.* Chemosphere, 2021. **281**: p. 130739.
396. Shabbir, M.Z., A.-u. Rahman, and M. Munir, *A comprehensive global perspective on phylogenomics and evolutionary dynamics of Small ruminant morbillivirus.* Scientific Reports, 2020. **10**(1): p. 17.
397. Kim, H., et al., *Skin Corrosion and Irritation Test of Nanoparticles Using Reconstructed Three-Dimensional Human Skin Model, EpiDerm™.* Toxicological Research, 2016. **32**(4): p. 311-316.

398. Geim, A.K., *Graphene prehistory.* Physica Scripta, 2012. **2012**(T146): p. 014003.
399. Guerrero-Contreras, J. and F. Caballero-Briones, *Graphene oxide powders with different oxidation degree, prepared by synthesis variations of the Hummers method.* Materials Chemistry and Physics, 2015. **153**: p. 209-220.
400. Zaaba, N.I., et al., *Synthesis of Graphene Oxide using Modified Hummers Method: Solvent Influence.* Procedia Engineering, 2017. **184**: p. 469-477.
401. Chen, D., H. Feng, and J. Li, *Graphene Oxide: Preparation, Functionalization, and Electrochemical Applications.* Chemical Reviews, 2012. **112**(11): p. 6027-6053.
402. Agarwal, V. and P.B. Zetterlund, *Strategies for reduction of graphene oxide – A comprehensive review.* Chemical Engineering Journal, 2021. **405**: p. 127018.
403. Suk, J.W., et al., *Mechanical Properties of Monolayer Graphene Oxide.* ACS Nano, 2010. **4**(11): p. 6557-6564.
404. Zhu, Y., et al., *Graphene and Graphene Oxide: Synthesis, Properties, and Applications.* Advanced Materials, 2010. **22**(35): p. 3906-3924.
405. Eda, G. and M. Chhowalla, *Chemically Derived Graphene Oxide: Towards Large-Area Thin-Film Electronics and Optoelectronics.* Advanced Materials, 2010. **22**(22): p. 2392-2415.
406. Abdolhosseinzadeh, S., H. Asgharzadeh, and H. Seop Kim, *Fast and fully-scalable synthesis of reduced graphene oxide.* Scientific Reports, 2015. **5**(1): p. 10160.
407. Lee, K.H., et al., *Large scale production of highly conductive reduced graphene oxide sheets by a solvent-free low temperature reduction.* Carbon, 2014. **69**: p. 327-335.
408. Tu, N.D.K., et al., *Remarkable Conversion Between n- and p-Type Reduced Graphene Oxide on Varying the Thermal Annealing Temperature.* Chemistry of Materials, 2015. **27**(21): p. 7362-7369.
409. Jung, I., et al., *Tunable Electrical Conductivity of Individual Graphene Oxide Sheets Reduced at "Low" Temperatures.* Nano Letters, 2008. **8**(12): p. 4283-4287.
410. Mattevi, C., et al., *Evolution of Electrical, Chemical, and Structural Properties of Transparent and Conducting Chemically Derived Graphene Thin Films.* Advanced Functional Materials, 2009. **19**(16): p. 2577-2583.
411. Jung, I., et al., *Reduction Kinetics of Graphene Oxide Determined by Electrical Transport Measurements and Temperature Programmed Desorption.* The Journal of Physical Chemistry C, 2009. **113**(43): p. 18480-18486.
412. Chen, W. and L. Yan, *Preparation of graphene by a low-temperature thermal reduction at atmosphere pressure.* Nanoscale, 2010. **2**(4): p. 559-563.
413. Yin, K., et al., *Thermodynamic and Kinetic Analysis of Lowtemperature Thermal Reduction of Graphene Oxide.* Nano-Micro Letters, 2011. **3**(1): p. 51-55.
414. Kumar, P.V., et al., *Scalable enhancement of graphene oxide properties by thermally driven phase transformation.* Nature Chemistry, 2014. **6**(2): p. 151-158.
415. Slobodian, O.M., et al., *Low-Temperature Reduction of Graphene Oxide: Electrical Conductance and Scanning Kelvin Probe Force Microscopy.* Nanoscale Research Letters, 2018. **13**(1): p. 139.
416. Vacchi, I.A., et al., *Chemical reactivity of graphene oxide towards amines elucidated by solid-state NMR.* Nanoscale, 2016. **8**(28): p. 13714-13721.
417. Guo, S., et al., *Is carboxylation an efficient method for graphene oxide functionalization?* Nanoscale Advances, 2020. **2**(9): p. 4085-4092.
418. Lucherelli, M.A., et al., *A Straightforward Approach to Multifunctional Graphene.* Chemistry – A European Journal, 2019. **25**(57): p. 13218-13223.
419. Vacchi, I.A., et al., *Strategies for the Controlled Covalent Double Functionalization of Graphene Oxide.* Chemistry – A European Journal, 2020. **26**(29): p. 6591-6598.
420. King, A.A.K., et al., *A New Raman Metric for the Characterisation of Graphene oxide and its Derivatives.* Scientific Reports, 2016. **6**(1): p. 19491.

421. Wu, J.-B., et al., *Raman spectroscopy of graphene-based materials and its applications in related devices.* Chemical Society Reviews, 2018. **47**(5): p. 1822-1873.
422. Vollebregt, S., et al., *Influence of the growth temperature on the first and second-order Raman band ratios and widths of carbon nanotubes and fibers.* Carbon, 2012. **50**(10): p. 3542-3554.
423. Sengupta, I., et al., *Thermal reduction of graphene oxide: How temperature influences purity.* Journal of Materials Research, 2018. **33**(23): p. 4113-4122.
424. Tyler, W.W. and A.C. Wilson, *Thermal Conductivity, Electrical Resistivity, and Thermoelectric Power of Graphite.* Physical Review, 1953. **89**(4): p. 870-875.
425. Woll, K., et al., *Rapid Thermal Characterization of Graphene Oxide—Nanocalorimetry as a Pathway for Novel Insights in Tribology.* Lubricants, 2019. **7**(11): p. 96.
426. Wang, S., et al., *Skin electronics from scalable fabrication of an intrinsically stretchable transistor array.* Nature, 2018. **555**(7694): p. 83-88.
427. Liu, M., et al., *Large-Area All-Textile Pressure Sensors for Monitoring Human Motion and Physiological Signals.* Advanced Materials, 2017. **29**(41): p. 1703700.
428. Wang, X., et al., *Silk-Molded Flexible, Ultrasensitive, and Highly Stable Electronic Skin for Monitoring Human Physiological Signals.* Advanced Materials, 2014. **26**(9): p. 1336-1342.
429. Kabiri Ameri, S., *Graphene Electronic Tattoo Sensors.* 2017. **11**(8): p. 7634-7641.
430. Gong, S., et al., *A wearable and highly sensitive pressure sensor with ultrathin gold nanowires.* Nat Commun, 2014. **5**: p. 3132.
431. Wang, X., et al., *Full Dynamic-Range Pressure Sensor Matrix Based on Optical and Electrical Dual-Mode Sensing.* Advanced Materials, 2017. **29**(15): p. 1605817.
432. Lee, J., et al., *A stretchable strain sensor based on a metal nanoparticle thin film for human motion detection.* Nanoscale, 2014. **6**(20): p. 11932-11939.
433. Yeo, J.C., et al., *Flexible and Stretchable Strain Sensing Actuator for Wearable Soft Robotic Applications.* Advanced Materials Technologies, 2016. **1**.
434. Huang, T., et al., *Porous Fibers Composed of Polymer Nanoball Decorated Graphene for Wearable and Highly Sensitive Strain Sensors.* Advanced Functional Materials, 2019. **29**(45): p. 1903732.
435. Luo, Z., et al., *Structure-Property Relationships in Graphene-Based Strain and Pressure Sensors for Potential Artificial Intelligence Applications.* Sensors, 2019. **19**(5): p. 1250.
436. Zheng, M., et al., *Strain sensors based on chromium nanoparticle arrays.* Nanoscale, 2014. **6**(8): p. 3930-3933.
437. Farcau, C., et al., *Tunable Conductive Nanoparticle Wire Arrays Fabricated by Convective Self-Assembly on Nonpatterned Substrates.* ACS Nano, 2010. **4**(12): p. 7275-7282.
438. Segev-Bar, M. and H. Haick, *Flexible Sensors Based on Nanoparticles.* ACS nano, 2013. **7**.
439. Roh, E., et al., *Stretchable, Transparent, Ultrasensitive, and Patchable Strain Sensor for Human–Machine Interfaces Comprising a Nanohybrid of Carbon Nanotubes and Conductive Elastomers.* ACS Nano, 2015. **9**(6): p. 6252-6261.
440. Yi, L., et al., *Nanoparticle monolayer-based flexible strain gauge with ultrafast dynamic response for acoustic vibration detection.* Nano Research, 2015. **8**(9): p. 2978-2987.
441. Schlicke, H., et al., *Tuning the Elasticity of Cross-Linked Gold Nanoparticle Assemblies.* The Journal of Physical Chemistry C, 2019. **123**(31): p. 19165-19174.
442. Ly, T.N. and S. Park, *Wearable strain sensor for human motion detection based on ligand-exchanged gold nanoparticles.* Journal of Industrial and Engineering Chemistry, 2020. **82**: p. 122-129.
443. Ketelsen, B., et al., *Nanoparticle-Based Strain Gauges: Anisotropic Response Characteristics, Multidirectional Strain Sensing, and Novel Approaches to Healthcare Applications.* Advanced Functional Materials, 2023. **33**(7): p. 2210065.
444. Moreira, H., et al., *Electron transport in gold colloidal nanoparticle-based strain gauges.* Nanotechnology, 2013. **24**: p. 095701.

445. Bastús, N.G., J. Comenge, and V. Puntes, *Kinetically controlled seeded growth synthesis of citrate-stabilized gold nanoparticles of up to 200 nm: size focusing versus Ostwald ripening.* Langmuir, 2011. **27**(17): p. 11098-105.
446. Sneha, K., et al., *Yucca-derived synthesis of gold nanomaterial and their catalytic potential.* Nanoscale research letters, 2014. **9**: p. 627.
447. Sneha, K., et al., *Counter ions and temperature incorporated tailoring of biogenic gold nanoparticles.* Process Biochemistry, 2010. **45**(9): p. 1450-1458.
448. Tang, G., et al., *Simultaneous functionalization and reduction of graphene oxide with polyetheramine and its electrically conductive epoxy nanocomposites.* Chinese Journal of Polymer Science, 2014. **32**(8): p. 975-985.
449. Chakraborty, S., et al., *High yield synthesis of amine functionalized graphene oxide and its surface properties.* RSC Advances, 2016. **6**(72): p. 67916-67924.
450. Zhang, Z. and T. Si, *Controllable assembly of silver nanoparticles based on the coffee-ring effect for high-sensitivity flexible strain gauges.* Sensors and Actuators A: Physical, 2017. **264**: p. 188-194.
451. Huang, C.-B., et al., *Highly Sensitive Strain Sensors Based on Molecules–Gold Nanoparticles Networks for High-Resolution Human Pulse Analysis.* Small, 2021. **17**(8): p. 2007593.
452. Chen, Z. and C. Lu, *Humidity sensors: a review of materials and mechanisms.* Sensor letters, 2005. **3**(4): p. 274-295.
453. Ruiz-Garcia, L., et al., *A review of wireless sensor technologies and applications in agriculture and food industry: state of the art and current trends.* Sensors (Basel), 2009. **9**(6): p. 4728-50.
454. Kuang, Q., et al., *High-Sensitivity Humidity Sensor Based on a Single SnO 2 Nanowire.* Journal of the American Chemical Society, 2007. **129**: p. 6070-1.
455. Sakai, Y., Y. Sadaoka, and M. Matsuguchi, *Humidity sensors based on polymer thin films.* Sensors and Actuators B: Chemical, 1996. **35**(1): p. 85-90.
456. Kim, W., et al., *Hysteresis caused by water molecules in carbon nanotube field-effect transistors.* Nano Letters, 2003. **3**(2): p. 193-198.
457. Borini, S., et al., *Ultrafast Graphene Oxide Humidity Sensors.* ACS Nano, 2013. **7**(12): p. 11166-11173.
458. Karim, M.R., et al., *Graphene oxide nanosheet with high proton conductivity.* J Am Chem Soc, 2013. **135**(22): p. 8097-100.
459. Singh, E., M. Meyyappan, and H.S. Nalwa, *Flexible Graphene-Based Wearable Gas and Chemical Sensors.* ACS Applied Materials & Interfaces, 2017. **9**(40): p. 34544-34586.
460. Basu, S. and P. Bhattacharyya, *Recent developments on graphene and graphene oxide based solid state gas sensors.* Sensors and Actuators B: Chemical, 2012. **173**: p. 1-21.
461. Gilje, S., et al., *A Chemical Route to Graphene for Device Applications.* Nano Letters, 2007. **7**(11): p. 3394-3398.
462. Montes-García, V. and P. Samorì, *Humidity Sensing with Supramolecular Nanostructures.* Advanced Materials, 2024. **36**(12): p. 2208766.
463. Nayak, S. and L.A. Lyon, *Soft Nanotechnology with Soft Nanoparticles.* Angewandte Chemie International Edition, 2005. **44**(47): p. 7686-7708.
464. Brazel, C.S. and N.A. Peppas, *Modeling of drug release from swellable polymers.* Eur J Pharm Biopharm, 2000. **49**(1): p. 47-58.
465. Ito, T., et al., *Water-Absorbing Bioadhesive Poly(Acrylic Acid)/Polyvinylpyrrolidone Complex Sponge for Hemostatic Agents.* 2022. **9**(12).
466. Brazel, C.S. and N.A. Peppas, *Dimensionless analysis of swelling of hydrophilic glassy polymers with subsequent drug release from relaxing structures.* Biomaterials, 1999. **20**(8): p. 721-32.

List of abbreviations

in order of usage

0D zero-dimensional

1D one-dimensional

2D two-dimensional

3D three-dimensional

G – graphene

GO – graphene oxide

rGO – reduced graphene oxide

TMDC – transition metal dichalcogenides

h-BN – hexagonal boron nitride

2DMs – two-dimensional materials

CVD – chemical vapor deposition

HOPG – highly oriented pyrolytic graphite

RF – radio frequency

OFGs – oxygen functional groups

ESSs – energy storage systems ESSs

CrGO – chemically reduced graphene oxide

AA – L-ascorbic acid

DOS – density of states

GQDs – graphene quantum dots GQDs

MEMS – microelectromechanical systems

IoMT – Internet of Medical Things

SWCNT – single walled carbon nanotubes

OFET – organic field-effect transistor

GF – gauge factor

PET – polyethylene terephthalate

PI – polyimide

PU – polyurethane

PDMS – polydimethylsiloxane

PEN – polyethylene

HOMO – highest occupied molecular orbital

LUMO – lowest unoccupied molecular orbital

EDL – electron depletion layer

LOD – the limit of detection

EDC – 1-ethyl-3-(3-dimethylaminopropyl)-carbodiimide

DCC – N,N'-dicyclohexylcarbodiimide

LbL – Layer by Layer

RH – relative humidity

SEM – scanning electron microscopy

EDS – Energy Dispersive X-ray Spectroscopy

XPS – X-ray photoelectron spectroscopy

RS – Raman spectroscopy

XRD – X-ray diffraction

FTIR – Fourier Transform Infrared Spectroscopy

ATR – attenuated total reflectance

EA – Elemental Analysis

NMR – nuclear magnetic resonance

RhE – reconstructed human epidermis

RT – room temperature

SD – standard error

CP/MAS – cross-polarization magic angle spinning

DP/MAS – direct polarization with magic angle spinning

TrGO – thermally reduced graphene oxide

CrGO – chemically reduced graphene oxide

AuNPs – gold nanoparticles

WSM – water swellable material

IA – itaconic acid

DVB – divinylbenzene

PTFE – polytetrafluoroethylene

FWHM – Full-Width at Half Maximum

DHA – dehydroascorbic acid

FPP – four-point probe

ssNMR-MAS – solid-state NMR magic angle spinning

SAP – superabsorbent polymers

HRMS – High – Resolution Mass Spectrometry

Scientific Achievements

Publications

1. **Chudziak T**, Montes-García V, Czepa W, Pakulski D, Musial A, Valentini C, Bielejewski M, Carlin M, Tubaro A, Pelin M, Samorì P, Ciesielski A *"A comparative investigation of the chemical reduction of graphene oxide for electrical engineering applications"* **Nanoscale**, 2023, 15, 17765-17775, IF = 6.8

2. Valentini C, Montes-García V, Livio PA, **Chudziak T**, Raya J, Ciesielski A, Samorì P *"Tuning the electrical properties of graphene oxide through low-temperature thermal annealing"* **Nanoscale**, 2023, 15, 5743-5755, IF = 6.8

3. Pakulski D, Gorczynski A, Marcinkowski D, Czepa W, **Chudziak T**, Witomska S, Nishina Y, Patroniak V, Ciesielski A, Samorì P*"High-sorption terpyridine-graphene oxide hybrid for the efficient removal of heavy metal ions from wastewater"* **Nanoscale**, 2021, 13, 10490-10499, IF = 6.8

4. Pakulski D, Montes-García V, Gorczynski A, Czepa W, **Chudziak T**, Samorì P, Ciesielski A *"Thiol-decorated covalent organic frameworks as multifunctional materials for high-performance supercapacitors and heterogeneous catalysis"* **Journal of Materials Chemistry A**, 2022, 10, 16685-16696, IF = 11.6

5. Pakulski D, Montes-García V, Gorczynski A, Czepa W, **Chudziak T**, Bielejewski M, Musial A, Pérez-Juste I, Samorì P, Ciesielski A *"Two-dimensional metal-organic polymers as cathode hybrid materials for high-performance Al-batteries"* **Journal of Materials Chemistry A**, 2022, 12, 440-450, IF = 11.6

6. Pakulski D, Montes-García V, Czepa W, Marcinkowski D**,** Peng HJ, **Chudziak T**, Gorczynski A, Kukulka W, Valentini C, Patroniak V, Samorì P, Ciesielski A "*MOF (UiO-66-NH_2)@COF (TFP-TABQ) hybrids via on-surface condensation reactions for sustainable energy storage"* **Chemical Communications,** 2024, 60, 412-415, IF = 4.9

Conferences and Internships

A. Participation in scientific conferences:

PhD student is the author and co-author of several oral and poster presentations on international conferences throughout his academic career. All conferences held during PhD studies are presented below.

Nanotech France 2022 Int. Conference and Exhibition 15-17/06/2022 Paris, France. (Poster)

Chem2DMat 2023 Int. Conference and Exhibition 15-18/05/2023 Bologna, Italy. (Oral presentation)

Smart Materials and Surfaces 2023 Int. Conference and Exhibition 23-5/10/2023 Albuferia-Algavre, Portugal. (Oral presentation)

B. International internships:

- **Country**: France

Institution: Université de Strasbourg, Institut de Science et d'Ingenerie Supramoleculaire (I.S.I.S.)

Duration time: 01.11.2021-30.11.2021 and 01.09.2023–30.11.2023

Description of activities:

During an internship at the Institut de science et d'ingénierie supramoléculaires in Strasbourg, France, a library of hybrid materials based on graphene was obtained. The synthesized materials were fully characterized using spectroscopic methods and scanning electron microscopy. Additionally, the prepared components were implemented into working devices such as humidity and pressure sensors. The resulting chemiresistor devices were analyzed for their humidity detection properties and piezoelectric properties.

Supervisor: Prof. Paolo Samori

Auxiliary supervisor: Dr. Artur Ciesielski (HDR)

Grants

PhD student is the participator in various grants presented below:

2019/35/B/ST5/01568 OPUS “Supramolecularly engineered sensors based on 2D materials for detection of gases and pressure” financed by NCN (contractor)

2021/41/N/ST5/01112 PRELUDIUM “New generation of humidity sensors based on graphene-functionalized materials” financed by NCN (principal investigator)

Initiative of Excellence – Research University “rigidity of graphene-based hybrid materials and responsiveness of pressure sensors in piezoelectric systems” (principal investigator)